

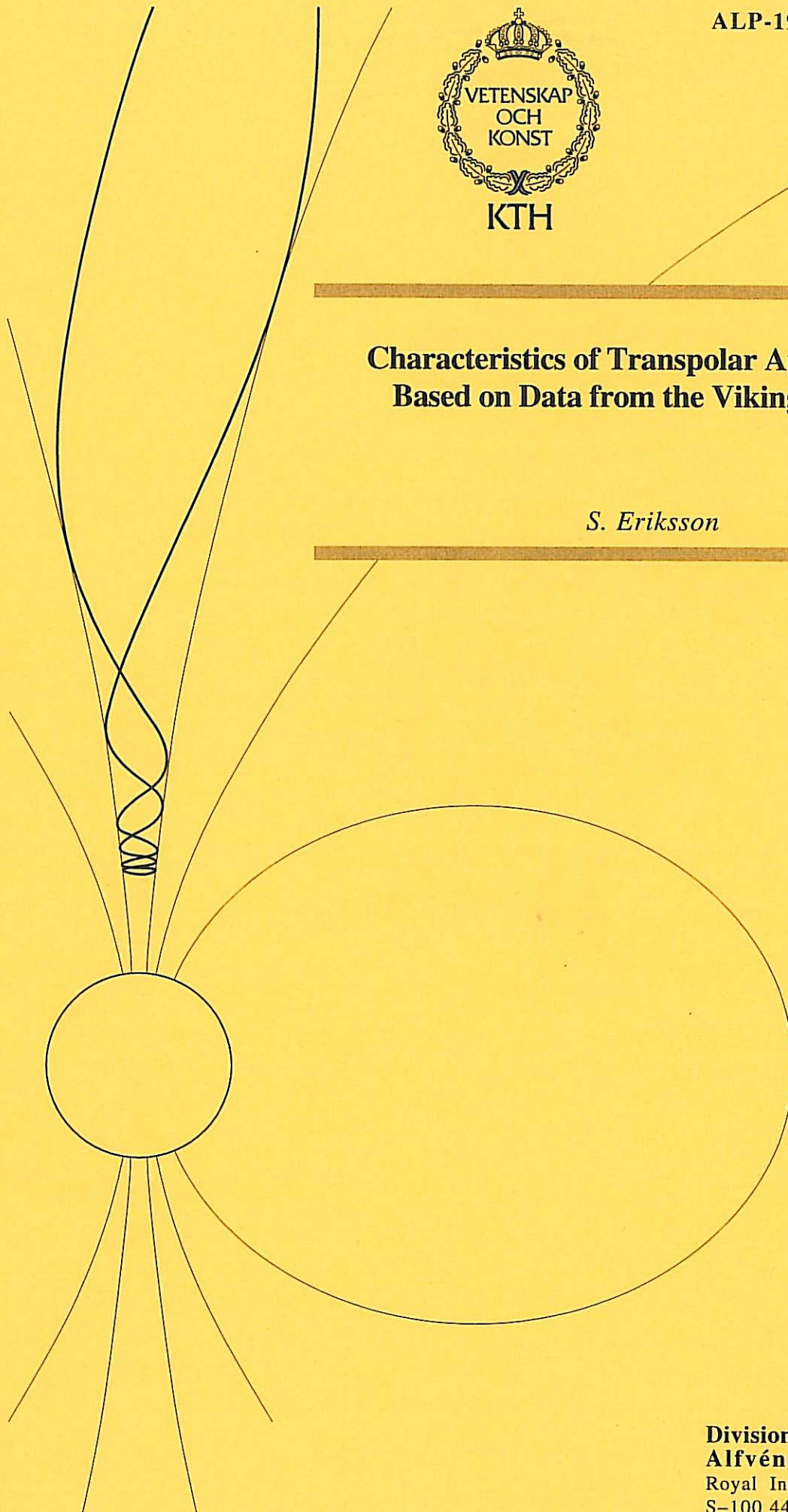


---

## Characteristics of Transpolar Auroral Arcs Based on Data from the Viking Satellite

*S. Eriksson*

---



**Division of Plasma Physics  
Alfvén Laboratory**  
Royal Institute of Technology  
S-100 44 Stockholm, Sweden





# Characteristics of Transpolar Auroral Arcs Based on Data from the Viking Satellite

Stefan Eriksson, Alfvén Laboratory  
Division of Plasma Physics  
Royal Institute of Technology  
Stockholm, Sweden

February 1996





## Contents

<b>1</b>	<b>Introduction</b>	<b>3</b>
1.1	The Ionosphere and the Magnetosphere . . . . .	4
1.2	Motion of Charged Particles in Electric and Magnetic Fields .	8
1.3	Current Density Distributions . . . . .	11
1.4	The Concept of Double Layers . . . . .	15
1.5	The Aurora . . . . .	17
1.6	The Transpolar Arc Phenomenon . . . . .	18
<b>2</b>	<b>Observational Results</b>	<b>22</b>
<b>3</b>	<b>Estimation of the Current Density</b>	<b>33</b>
<b>4</b>	<b>Discussion and Conclusion</b>	<b>36</b>
<b>A</b>	<b>Coordinate Systems</b>	<b>41</b>
<b>B</b>	<b>The Particle Gyration</b>	<b>42</b>
<b>C</b>	<b>The Convective Drift Motion</b>	<b>43</b>
<b>D</b>	<b>Basic Concepts</b>	<b>44</b>
<b>E</b>	<b>Fortran and IDL Programmes</b>	<b>45</b>
<b>F</b>	<b>Data Plots</b>	<b>46</b>





## Acknowledgements

I would like to thank my patient tutor, Lars Blomberg, for the many good proposals during this thesis, and also for letting me using his Fortran subroutines, without which I would have been completely lost. I would also like to thank Per-Arne Lindqvist, Bengt-Harald Nilsson and Ramesh Mehra at the Department of Plasma Physics for their valuable contributions when I needed it the most. Finally, I am very grateful to Ingrid Sandahl, Masatoshi Yamauchi, and the people of IRF in Kiruna for giving me the best possible introduction at IRF and also for making the rest of the week such a rewarding visit.





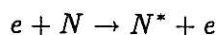
## 1 Introduction

"Some say that the northern lights are the glare of the Arctic ice and snow; And some say that it is electricity, and nobody seems to know".

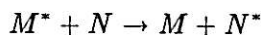
This is a quote from Robert W. Service [Ballad of the Northern Lights, 1909] and captures to some extent the struggle of this field of science from pure folkloristic views to present scientific conceptions with all of its current models and definitions.

This thesis undergraduate work has been conducted in order to establish and to possibly clarify the characteristics of the auroral phenomenon known as transpolar auroral arcs (or occasionally known as theta aurora from their characteristic geographical distribution over the poles, which together with the normal auroral oval resembles the Greek letter theta,  $\theta$ ) from the vast amount of data collected by different scientific instruments on the first Swedish satellite, Viking.

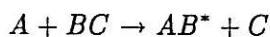
The transpolar aurora is a large-scale ( $>100$  km) region of auroral emission, which is generally sun-aligned and reaches contiguously across the polar cap from the dayside to the nightside sectors of the auroral oval. The optical emissions in the aurora result from light consisting of atomic line spectra and molecular band spectra. The ambient atmospheric particles are excited by impacting auroral particles, that convert their kinetic energy to optical and infrared emissions of discrete wavelengths through processes initiated by inelastic collisions. The atmospheric species may spontaneously relax to lower energy states directly while emitting radiation. Alternatively, they may undergo one or more chemical reactions, finally resulting in an excited product which also emits energy by spontaneous radiative decay. Thus, there are several mechanisms behind the auroral emission. The production of a given excited state may be the result of electron impact in inelastic collisions of the form



or the result of energy transfer



or the result of a chemiluminescent reaction



Here the asterisk indicates an excited state of the atom or molecule.

## 1.1 The Ionosphere and the Magnetosphere

The ultimate reasons why a beautiful physical phenomenon as the aurora takes place around the Earth's magnetic poles is the presence of the solar wind from the Sun, the existence of an atmosphere containing different molecular and atomic species and being threaded by a geomagnetic field.

The atmosphere is generally divided into layers according to different physical aspects, either by the thermal conditions prevailing at different altitudes or by the transport processes. The latter leads to an atmosphere divided into a lower layer, the homosphere, where turbulent mixing makes it rather homogenous. In the upper layer, the heterosphere, diffusive transport processes govern the motion of particles. The turbopause constitutes the border between these at an altitude about 110 km above the Earth's surface. In the heterosphere, molecular oxygen and nitrogen decrease in abundance, so that atomic oxygen dominates in the 200 km to 600 km altitude interval. At even higher altitudes, atomic hydrogen and helium take over.

In 1883, Stewart suggested the existence of an electrically conducting layer in the upper atmosphere in order to explain the daily variations of the Earth's magnetic field. This layer of ionized gases, which is tied by friction to the atmosphere, reaches roughly from 50 km to about 1000 km in altitude. It is called the ionosphere and it consists of free electrons and positive ions that are produced when the ultraviolet radiation (UV, wavelengths less than 240 nm) from the Sun is absorbed by the atoms and molecules in the atmosphere. The cosmic radiation, with extremely high energy, is responsible for ionization in the lowest altitude range of about 70 km. The altitude and character of the ionized layers depend on both the nature of the solar radiation and on the composition of the atmosphere.

The electron,  $n_e$ , and ion densities,  $n_i$ , in the individual ionized layers are essentially equal. This state of the conductive matter is generally phrased as quasineutrality, *i.e.*, the ionized gas is neutral on large enough scale sizes that one can take  $n_i \simeq n_e \simeq n$ , where  $n$  is a common density called the plasma density, but it is not so neutral that all the interesting electromagnetic forces vanish. When ionized gases fulfil this condition such that the gas locally is dense enough that the Debye length,

$$\lambda_D \equiv \sqrt{\frac{\epsilon_0 k_B T_e}{ne^2}}$$

is much smaller than a characteristic length  $\ell$ , they are being called a plasma. The Debye length is a measure of the shielding distance of a charged cloud,



outside of which it is by definition quasineutral.

A common definition made, is that the ionosphere ends without a sharp boundary at a level of 1000 to 2000 km, above which the hydrogen ion is the dominating ion species (during average conditions). This region of space, which is dominated by the geomagnetic field, is called the magnetosphere (see Figure 1). Its outer boundary is called the magnetopause, where an external magnetic field was found by Cahill. The reason for this boundary is the highly conducting plasma flow from the Sun, the solar wind, that reaches through interplanetary space and which carries with it electrical currents. The magnetopause develops as a consequence of the balance between the dynamic pressure of the solar wind flow and the magnetic pressure of the magnetospheric magnetic field.

Since the solar wind has a high enough conductivity to conserve magnetic fluxes, the magnetic field of the solar corona appears to follow the solar wind, *i.e.*, the magnetic field is coupled to the motion of matter in such a way that it is said to be "frozen-in" (after Hannes Alfvén). Thus, the solar wind

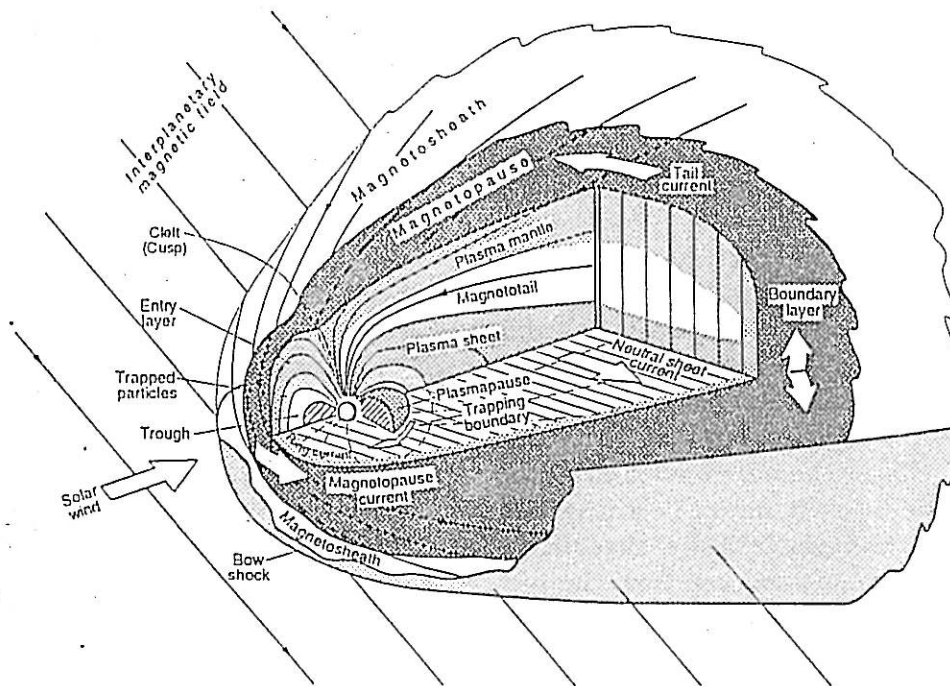


Figure 1: The Magnetosphere.

brings with it a magnetic field, generally called the IMF (interplanetary

magnetic field).

The geomagnetic field derives from the electric current systems in the interior of the Earth and it is roughly a dipole field at the surface. The largest magnetic field strength is found at the poles, where it reaches values of about  $62 \mu\text{T}$ . The magnetic dipole axis makes an angle of about eleven degrees with the rotation axis (from which it is also displaced about 350 km). Since the magnetic dipole axis is opposite to the rotation axis, the geographic northpole is close to the magnetic southpole and vice versa. Thus, the field is directed in the negative  $z_{GSM}$  direction (cf. Appendix A) in the northern polar cap, a region of open magnetic field lines, i.e., the magnetic field lines close so far away from the Earth, that they appear to be open from our point of view. Therefore, they are defined as "open".

The structure of the magnetosphere is today essentially known and its most important parts are illustrated in Figure 1. A couple of Earth radii in front of the magnetopause, a practically collisionless shock front (the phenomenon resembles the shock front that is created in front of an aircraft when it reaches the speed of sound), the bow shock, arises since the Earth's magnetosphere constitutes an obstacle to the supersonic flow of the solar wind. The bow shock represents a transition from supersonic to subsonic plasma flow. On the nightside, the solar wind causes the magnetosphere to be elongated in a tail-like manner and thus it is called the magnetotail. Inside the bow shock and outside the magnetopause, a region of subsonic plasma flow is found, called the magnetosheath.

Over the past years, two fundamental mechanisms for transferring energy to the magnetosphere from the solar wind have been suggested: the viscous interaction model [Axford and Hines, 1961] and the magnetic merging model [Dungey, 1961]. Both models explain many qualitative features of magnetospheric convection and auroral particle energization [Eastman *et al.*, 1976; Mozer *et al.*, 1979].

Since the solar wind is electrically conducting, it gives rise to an electric field when it moves in a magnetic field. This is a well known result of electromagnetic theory. Because of the rather low velocity of the solar wind, the formula deduced from the special relativity theory, transverse to the direction of motion

$$\vec{E}' = \gamma(u) \cdot (\vec{E} + \vec{u} \times \vec{B})$$

where  $\gamma(u)$  is

$$\gamma(u) = \frac{1}{\sqrt{1 - \frac{u^2}{c^2}}}$$

simplifies to

$$\vec{E}' = \vec{E} + \vec{u} \times \vec{B}$$

where primed quantities refer to the restframe of the solar wind. The electric field component parallel to the direction of motion is unaffected. Since the solar wind is a good conductor as mentioned, its electric field,  $\vec{E}'$ , will become approximately zero. Thus, in an Earth centred frame of reference (geocentric solar magnetic, cf. Appendix A), the generated electric field will be antiparallel to  $\vec{u} \times \vec{B}$ . When the IMF is southward, *i.e.*, opposite to the geomagnetic field in the equatorial plane, the energy injection becomes strong. This case corresponds to a positive interplanetary electric field (IEF), parallel to  $y_{GSM}$  (dawn-to-dusk). When, on the other hand, the IMF is directed northward, *i.e.*, parallel to the geomagnetic field in the equatorial plane, the energy injection becomes weak, corresponding to a negative IEF, antiparallel to  $y_{GSM}$ . The solar wind interaction with the magnetosphere thus shows a behaviour which is similar to a rectifier and it is said to act as a magnetohydrodynamic (MHD) generator.

In the magnetosphere, some well defined plasma populations have been identified. Vasyliunas [1979] defined magnetospheric boundary layers as regions of space threaded by geomagnetic field lines, but populated by plasma similar to that found in the magnetosheath. The plasma mantle *e.g.*, is found on open magnetic field lines, while the plasma sheet boundary layer is found in closed field line portions of the magnetosphere. The plasma mantle was first identified as a magnetosheath-like plasma flowing along magnetic field lines inside the magnetopause in the near-Earth lobes of the magnetotail [Rosenbauer *et al.*, 1975]. The plasma density and the spatial thickness of the mantle are greatest during periods of southward IMF [Sckopke *et al.*, 1976]. Mantle particles are believed to enter the magnetosphere near the dayside cusp. Pilipp and Morfill [1978] suggested that mantle particles may be one source of plasma sheet particles. The Earth's plasma sheet is the highly dynamical region of the magnetosphere that acts as a depository for auroral particles. It is a region of closed magnetic field lines which has a distinct inner edge that varies as a function of local time and the level of geomagnetic activity [Vasyliunas, 1968; Frank, 1971]. Figure 2 shows a view of the magnetotail portion of the plasma sheet as seen from two perspectives.

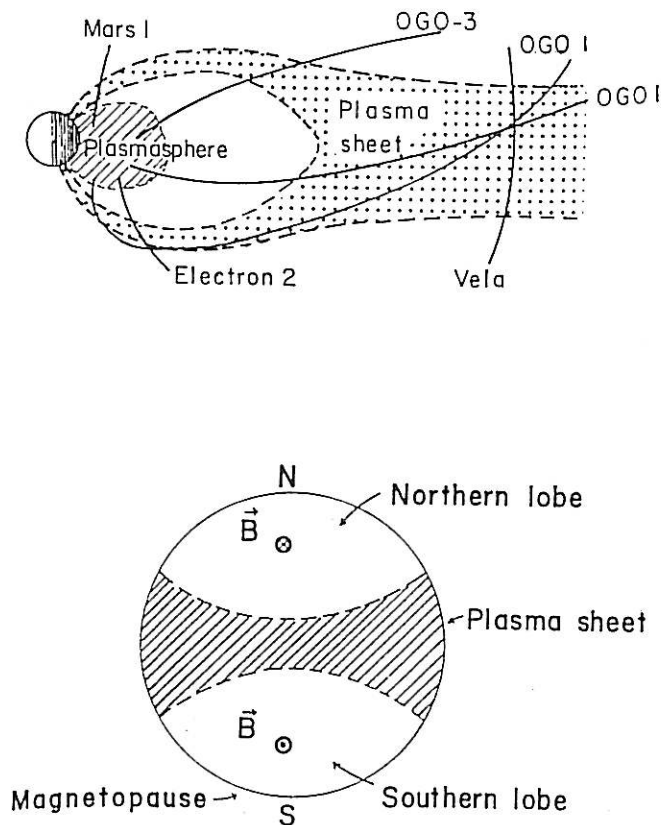


Figure 2: *top*; The distribution of nightside, plasma sheet electrons in meridional plane [Vasyliunas, 1968], *bottom*; Cross-sectional view of magnetotail looking Earthward (from the Handbook of Geophysics and the Space Environment, 1985).

## 1.2 Motion of Charged Particles in Electric and Magnetic Fields

In a neutral gas, the atoms and molecules move in straight ballistic orbits between practically instantaneous collisions and they are unaffected by electric and magnetic fields.

In a plasma, however, the charged particles are influenced not only by collisions with neutrals, but also by "equivalent" collisions with other charged particles governed by the long ranged Coulomb force. This means that they are affected by the electric and magnetic fields at all times.

When a charged particle enters a homogenous magnetic field,  $\vec{B}$ , it will perform a circular motion with constant angular velocity (the gyro(angular) frequency),  $\omega_g$ , transverse to the magnetic field. This is due to the balance between the centrifugal and the magnetic force (cf. Appendix B). Along the magnetic field, the particle moves with constant velocity,  $\vec{v}_{||}$ . The final motion in a homogenous magnetic field is thus a spiral.

When an electric field,  $\vec{E}$ , is superimposed on the magnetic field, the particle will start drifting transverse to both the magnetic and the electric field (cf. Appendix C). This drift velocity,  $\vec{u}_{\perp}$ , gives the plasma convection as seen in the ionosphere over the poles in the presence of the geomagnetic field and the ionospheric, electric field. During southward IMF, this convective drift motion, the  $\vec{E} \times \vec{B}$ -drift, is generally in the antisunward direction ( $-x_{GSM}$ ) at high latitudes. According to this convective drift motion, particles of different charge will drift in the same direction, therefore they will not carry any current. Along the magnetic field, the particles will be accelerated by the parallel component of the electric field (see the section about double layers below).

The magnetic field is in reality usually inhomogenous, which means that a gradient is present in the magnetic field. In regions of larger magnetic field strengths, the gyroradii of the particles decrease, while they increase in regions of smaller magnetic field strength. This leads to a drift motion, the gradient drift, in opposite directions for positive and negative particles, *i.e.*, a current is established. The magnetic force, averaged over the gyro-orbit, is given by

$$\vec{F}_m = -\mu \cdot \nabla B$$

Here,  $\mu$  is the magnetic moment, whose magnitude is the product of the area of the gyrocircle and the average current, carried by the gyrating particle. The average force has the same effect on the particle as an electric field,  $\vec{F}_m/q$ . When this equivalent electric field is used in the expression for the  $\vec{E} \times \vec{B}$ -drift, the motion transverse to the magnetic field is given. When the same force is combined with Newton's equation of motion, the acceleration along  $\vec{B}$  is given as

$$-\frac{\mu}{m} \cdot (\nabla B)_{||}$$

Thus, the particle will experience a decelerating force field when entering a region of larger magnetic field strength. If the particle's pitch angle is



larger than some threshold value, the particle might turn at a point called the magnetic mirror point.

The most important drift motions are illustrated in Figure 3.

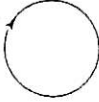
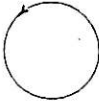
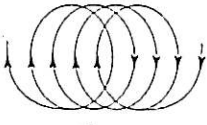
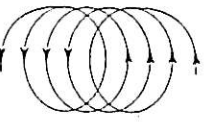
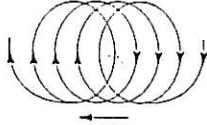
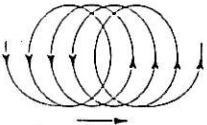
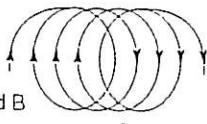
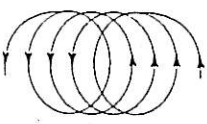
	Positive particles	Negative particles
Homogeneous magnetic field No disturbing force	$\odot B$ 	$\odot B$ 
Homogeneous magnetic field Homogeneous electric field	$\odot B$ $\downarrow E$  $\leftarrow$ Drift	$\odot B$  $\rightarrow$ Drift
Homogeneous magnetic field Gravitation	$\odot B$ $\downarrow g$  $\leftarrow$ Drift	$\odot B$  $\rightarrow$ Drift
Inhomogeneous magnetic field	$\odot B$ $\downarrow \text{grad } B$  $\rightarrow$ Drift	$\odot B$  $\leftarrow$ Drift

Figure 3: Drift motions of electrically charged particles (after Alfvén and Fälthammar, 1963)

### 1.3 Current Density Distributions

Before discussing the electrodynamics of the high-latitude ionosphere, it is worth mentioning the theory of magnetosphere/ionosphere coupling, put forward by Vasyliunas [1970]. This model illustrates the physical laws describing how magnetospheric convection may couple with the ionosphere. It is presented in Figure 4 in the form of a loop of equations (straight lines) and of quantities to be determined (boxes). External sources of particles, cross-magnetospheric potentials etc are imposed boundary conditions. The

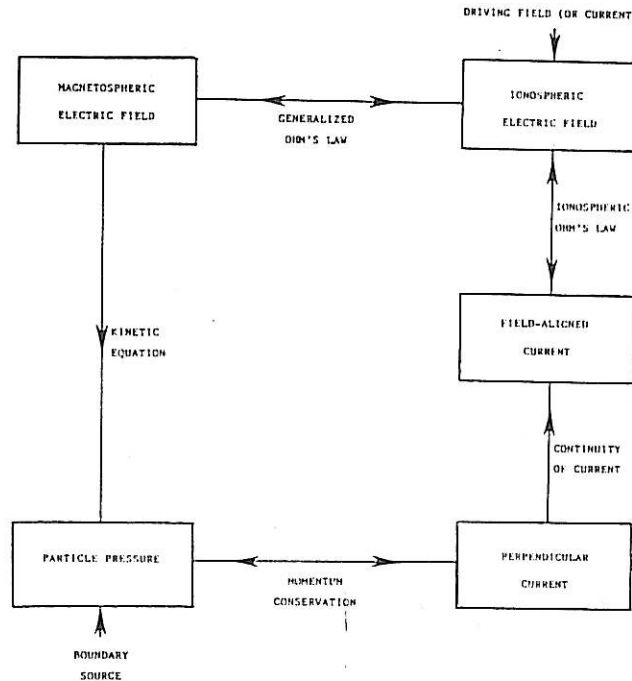


Figure 4: Outline of self consistent calculation of magnetospheric convection [Vasyliunas,1970].

loop is self-consistently closed which means that it may be entered at any point. Suppose that we have an initial idea about the distribution of magnetospheric electric fields and particles. Now, with knowledge of the electric field, the motion and distribution of charged particles in the magnetosphere and hence the total plasma pressure at any point may be calculated. From

the plasma pressure gradients, the components of the electric current perpendicular to the magnetic field may be deduced. The force balance equation

$$\nabla p = \vec{j} \times \vec{B}$$

leads to

$$\vec{j}_\perp = \frac{\vec{B} \times \nabla p}{B^2}$$

Here, the pressure is assumed to be isotropic for simplicity. When calculating the divergence of this perpendicular current and averaging over each flux tube, we obtain  $(j_\parallel)$  the field-aligned currents (FAC) flowing between the magnetosphere and the ionosphere.

$$\frac{\partial}{\partial s} \left( \frac{j_\parallel}{B} \right) = -\frac{1}{B} \nabla_\perp \cdot \vec{j}_\perp$$

From the requirement that these FACs be closed by perpendicular currents in the ionosphere, we obtain the configuration of the electric current in the ionosphere. The continuity of ionospheric current requires that

$$\nabla \cdot \vec{I} = j_\parallel \cdot \sin \chi$$

where  $\vec{I}$  is the height integrated current and  $\chi$  the inclination of magnetic field lines. In the ionosphere, Ohm's law

$$\vec{I} = \underline{\Sigma} \cdot (\vec{E} + \vec{v}_n \times \vec{B})$$

where  $\underline{\Sigma}$  is the height integrated conductivity tensor and  $\vec{v}_n$  is the neutral wind velocity (usually unknown), finally gives the ionospheric electric field. There is empirical evidence suggesting a functional relationship between FAC in discrete auroral arcs and field-aligned potential drops (double layers) [Lyons *et al.*, 1979].

It is clear from the derivation above, that measurements of  $\vec{E}$  and  $j_\parallel$  are very important to the understanding of the magnetosphere/ionosphere circuit. Measurements of precipitating particle fluxes are also needed to identify the dominant carriers of  $j_\parallel$ , to calculate field-aligned potential drops and to understand spatial variations in the height integrated conductivity tensor.

The concept of FACs in the polar regions was introduced by Birkeland [1908], but not until 1966 did satellite observations of magnetic disturbances

transverse to the main geomagnetic field provide direct evidence for their existence. The FAC density is determined from such measurements by using the Maxwell equation (Ampère's law)

$$\nabla \times \vec{B} = \mu_0 \vec{j}$$

FACs are important because of the role they play in the coupling between the magnetosphere and the ionosphere, for the transfer of energy and momentum from interplanetary space and also for their relationship to auroral phenomena and geomagnetic storms due to increased solar activity [Boström,1974]. The distribution of FAC in the northern auroral region has been determined *e.g.*, through analysis of magnetometer data obtained by the Triad satellite [Iijima and Potemra,1976]. They are directed into the ionosphere at the poleward boundary and away from the ionosphere at the equatorward boundary of the FAC region during the morning hours. These directions are the opposite for the evening hours, as seen in Figure 5. The two principal regions of FAC which have been distinguished encircling the geomagnetic poles, are reminiscent of the so called auroral oval defined from optical studies of the aurora [Feldstein,1966]. The auroral oval is an annular region, eccentric with respect to the magnetic pole (displaced toward the nightside) and essentially fixed in space, while the Earth rotates under it, where the geographic distribution of the aurora is given at an instant in time.

The region at the poleward side of the auroral oval is denoted as region 1 (R1) and the equatorward region as region 2 (R2) as illustrated in Figure 6. The current density in R1 statistically exceeds the current density in R2 at all local times except near the midnight hours (2100-0300 MLT, magnetic local time), when the most active auroral electrojets are frequently observed. The R1 currents appear to persist even during very low geomagnetic activity.

A new magnetic disturbance region, poleward of R1, was observed by the MAGSAT satellite during periods of strongly northward IMF and was shown to increase in amplitude as  $B_z$  increased. This pattern was interpreted in terms of Birkeland currents (FAC) by Iijima *et al.* [1984]. The stable, well-defined FAC system has been referred to as the "NBZ" system for its characteristic "northward  $B_z$ " dependence. This NBZ FAC system flows into the polar ionosphere on the duskside and flows away from the polar ionosphere on the dawnside (opposite to the usual R1 FACs) [Iijima and Shibaji,1987].

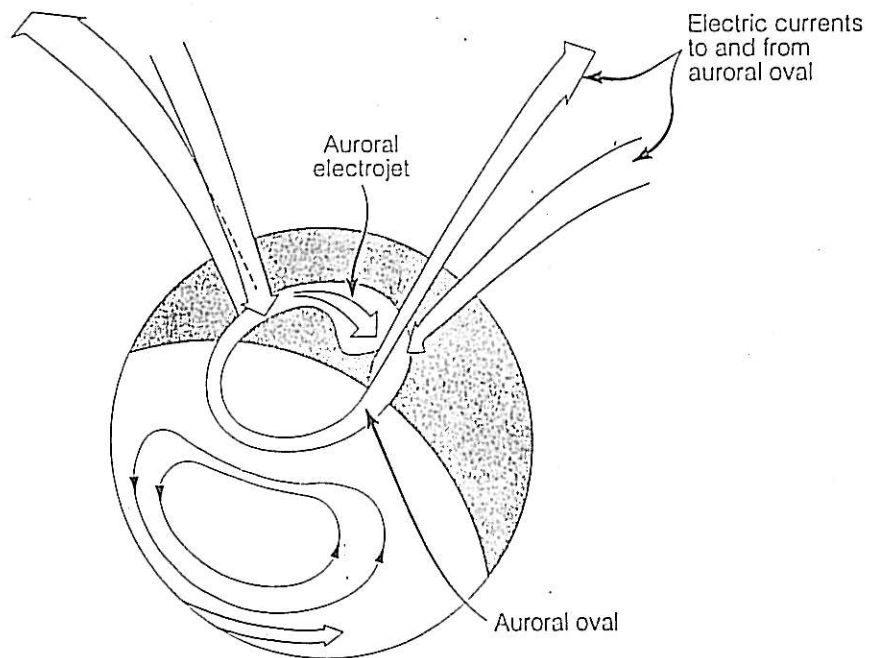


Figure 5: Sketch of the electric current system to and from the auroral oval (after Lanzerotti 1988).

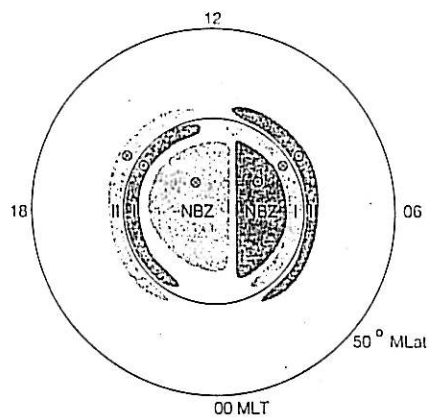


Figure 6: Geometry of the current system used in the model by Blomberg and Marklund [1991].

#### 1.4 The Concept of Double Layers

A wide variety of observations of auroral particle spectra, both upward flowing ions and downward accelerated electrons, have been interpreted in terms of potential drops along the magnetic field (henceforth called parallel potential drops). The magnetic field-aligned potential drop may be estimated by three independent methods that are found to give similar results [Burch, 1988; Reiff *et al.*, 1988]. Weimer [1988] shows results that indicate very strongly that electron and ion acceleration on auroral field lines can, to first order, be explained by a dc potential drop. It is possible that these parallel electric fields are concentrated in double layers (DL). Since quasineutrality is not valid locally in a DL, it can be thought of as a low-density region that separates two plasmas from one another. Electrons from one of the plasmas are reflected by the layer and ions are accelerated to a beam into the other plasma. The roles of particles from the other plasma are reversed. The potential distribution for a DL is depicted in Figure 7, as well as the phase space for the ions and the electrons.

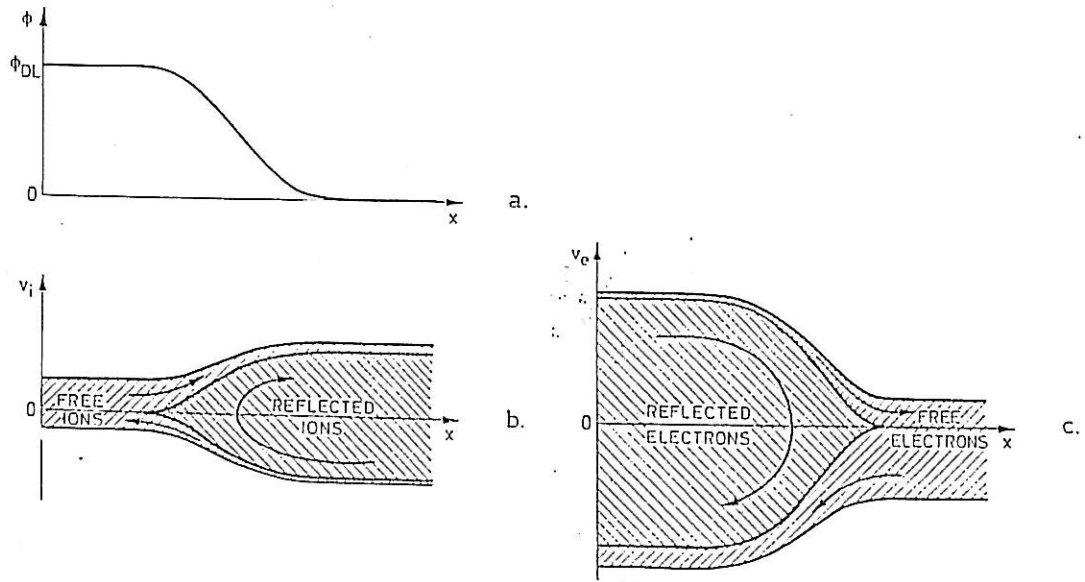


Figure 7: Schematic picture of a) the potential distribution, b) phase space for the ions, and c) phase space for the electrons in a double layer (after Carlqvist [1979]).

In space, the sources of these plasmas consist of the ionosphere and the magnetospheric convection, that supplies plasma from the magnetotail to the auroral field lines, while simultaneously generating the necessary potential difference and this available circuit voltage may well be shared by several layers in series [Block,1972; Lennartsson,1977] .

The interior of a (laboratory) DL shows a monotonic potential variation from investigations made *e.g.*, by Baker *et al.* [1981]. In this article, it was also shown that the radial (perpendicular to the magnetic field direction) electric field partly turned towards the central (parallel) axis. As a consequence of current continuity with the upward directed FAC, inward directed electric fields usually prevail in the ionosphere. Thus, the 3-D potential is distributed with U-shaped equipotentials, oriented as is observed above auroras (illustrated in Figure 8).

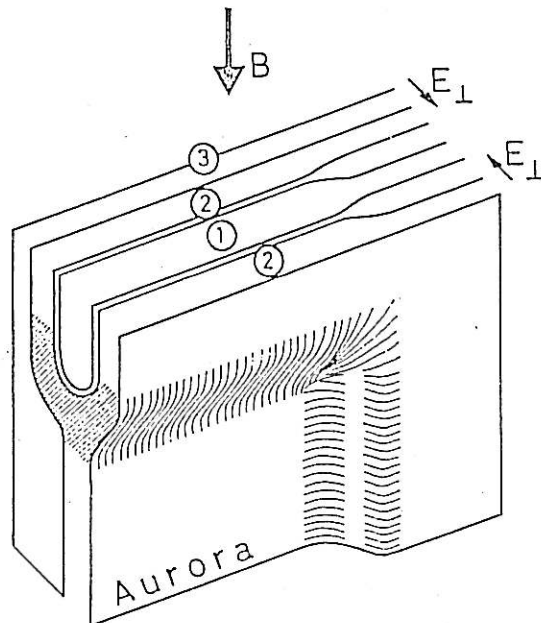


Figure 8: Suggested equipotential surfaces above an auroral arc at a perpendicular electric field reversal. Electrons injected in region (1) will fall through the entire DL potential drop. Electrons drifting along surfaces in regions (2) at shaded altitudes will fall through part of the drop. Electrons on surface (3) will not see any parallel electric field (from [Block,1981]).

The reason is understood, as mentioned, to be associated with the particle budget. To balance perpendicular losses of electrons and ions, the electric field must be directed towards the center with, but away without, a magnetic field. As pointed out by Block [1969] the electrostatic equipotentials in a DL must turn upwards to become field-aligned around the FAC. The first direct *in situ* measurements, made on the S3-3 satellite [Temerin *et al.*, 1982], found a large number of small DLs, each with a net potential drop of the order of 1 V. The frequency of occurrence of these layers indicated that there are thousands of them in series along auroral field lines. They can therefore account for the kilovolt potential drops required to explain acceleration of auroral electrons and upward ion beams in terms of parallel electric fields.

### 1.5 The Aurora

Aurora is the name given to the light resulting from the precipitation of electrons and protons from the magnetosphere into the Earth's atmosphere. The flow of particles gives rise to the Birkeland currents (FAC) and the emitted light consists of atomic line spectra and molecular band spectra characteristic principally of oxygen and nitrogen, the chief constituents of the upper atmosphere, which are ionized or excited by collisions with the precipitating particles. The most intense visible feature of the aurora is the atomic oxygen 557.7 nm auroral green line.

The auroral features are distinguished according to their spatial structures, where the structured component is known as the discrete aurora while the unstructured formation is known as the diffuse (or continuous) aurora. The latter is often neglected because its faintness and absence of contrast makes it difficult to observe. The discrete aurora results from electrons alone, while the diffuse aurora may result from both electron and proton precipitation. The frequency of occurrence of the aurora has been determined by all-sky cameras (ASCA) [Feldstein, 1966] to be statistically distributed in a band encircling the pole. This region is, as mentioned above, called the auroral oval, the high and low latitude borders of which are the average locations of the edges of auroral luminosity seen in ASCA photographs. With increasing magnetic activity, the oval expands and moves equatorward. A coordinate system often used to describe the oval is the corrected geomagnetic latitude and the corrected geomagnetic local time (MLT).

Winningham and Heikkila [1974] identified three classes of low energy electron precipitation: polar rain, polar showers and polar squalls. Polar



rain is a relatively uniform type of precipitation that can fill the entire polar cap. Particles have mean thermal energies of about 100 eV and are isotropically distributed outside the atmospheric loss cone. Polar showers are characterized by locally enhanced fluxes of precipitating electrons with mean energies of about 1 keV and are usually embedded in broader regions of polar rain. They are thought to be responsible for sun-aligned arcs in the polar cap. Polar squalls are described as localized, intense fluxes of electrons that have undergone field-aligned accelerations of several kV. They are found in the polar cap during geomagnetic substorms.

## 1.6 The Transpolar Arc Phenomenon

The transpolar auroral arc (or theta aurora) is a configuration of auroral and polar cap luminosities for which a generally sun-aligned transpolar arc extends contiguously from the dayside to the nightside sectors of the auroral oval. During periods of a relatively bright transpolar arc the plasma convection, due to  $\vec{E} \times \vec{B}$ -drift, in the polar cap region associated with the transpolar arc is usually sunward. Elsewhere over the polar cap, the convection is antisunward. The convection pattern over the auroral zones and polar cap is suggestive of the existence of four cells of plasma convection [Frank *et al.*, 1986]. Field-aligned electron acceleration into the polar atmosphere and FAC sheets are present in the transpolar arc plasmas.

There are probably two general states of the polar cap, as suggested by Frank *et al.* [1986]: a bright, well-developed transpolar arc and a dim or even absent transpolar arc. When the feature is dim or at its initial stages of brightening, there is a severe corresponding change in the character of luminosities, convection electric fields and plasmas over the polar cap region. The plasma convection is then generally turbulent or sunward in the polar cap and exhibits no longer the signature of a simple four-cell convection pattern. During periods of a relatively dim arc or an absence of such an arc, the polar cap region is characterized by a simultaneous appearance of complex spatial distributions of polar arcs and of field-aligned electron acceleration into the atmosphere. The electric fields of the polar regions are suggestive of the existence of a four-cell convection pattern spanning the auroral zones and polar cap, with two cells located over the polar cap. The transpolar arc is positioned near the common boundary of these two cells in a region of sunward flow and it occurs during periods of persistent northwardly directed IMF. The auroral oval contracts and the luminosities in the oval remain relatively constant. The transpolar arc is distinguished from po-

lar arcs in that it traverses the *entire* polar cap. Sporadic, spatially narrow zones of electron precipitation are the signatures of polar showers. These electron distributions exhibit often the effects of field-aligned acceleration and are associated with the major luminosity features of the polar cap. Coincident with the observations of such field-aligned accelerations, the convection electric fields are directed inward, toward the acceleration region, *i.e.*,  $\nabla \cdot \vec{E} < 0$  (the divergence of a vector field  $\vec{A}$  at a point is defined as the net *outward* flux of  $\vec{A}$  per unit volume as the volume about the point tends to zero).

The detection of field-aligned electron acceleration into the atmosphere over the polar cap region is insufficient evidence to establish the existence of a transpolar arc, since such electron distributions often occur elsewhere over the polar cap. Usually, energetic ions in the energy range about 1-10 keV are present within the transpolar arc region and they are not observed in other regions of the polar cap when a bright, well-developed transpolar arc is present. This feature distinguishes the transpolar arc from other luminosity features in the polar cap. The region of energetic ions remains intact within the polar cap region during dimming of the polar arc.

During one of DE 1's passages through the polar region when a transpolar arc was developing, the Earth's magnetosphere was immersed within substantial intensities of solar electrons [Frank *et al.*, 1986]. These electrons were observed over the entire polar cap with the exception of the region associated with the transpolar arc. The magnetic field lines threading both the transpolar arc and poleward zones of the auroral oval thus displayed an absence of comparable intensities of solar electrons. This absence of solar electrons provides substantial, but not irrefutable evidence that the magnetic field lines in these two regions are closed, thus preventing direct particle entry from the magnetosheath and interplanetary medium. Substantial FACs were detected in the transpolar arc plasmas traversed by the DE 1 satellite and two pairs of oppositely directed current sheets were found. The orientations of these current sheets were also found to be approximately parallel to the transpolar arcs as determined by Frank *et al.* [1986].

Frank *et al.* [1982] suggested that the theta aurora is the signature of the bifurcation of magnetotail lobes by a region of upward flowing plasmas from the boundary layer of the plasma sheet in the distant magnetotail.

Potemra *et al.* [1984] have studied the IMF  $B_y$ -dependence of convection patterns over the poles during IMF  $B_z > 0$  conditions and they concluded that the convection patterns may be ordered principally by the IMF  $B_y$  component. This dependence is also well-described by Chiu *et al.* [1985].

During periods of weak IMF  $B_y$ , two polar convection cells are symmetrically located on either side of the noon-midnight meridian, thus producing sunward convection across the pole. As the IMF  $B_y$  becomes more and more positive (negative), the dawn (dusk) convection cell expands across the northern polar cap, whereas the other cell shrinks. The behaviour is the opposite across the southern polar cap. During strong IMF  $B_y$  ( $> 5$  nT) this cell expansion gives the appearance of a single convection cell in the polar region (see Figure 9). At the "collapsed" cell a large convective plasma flow

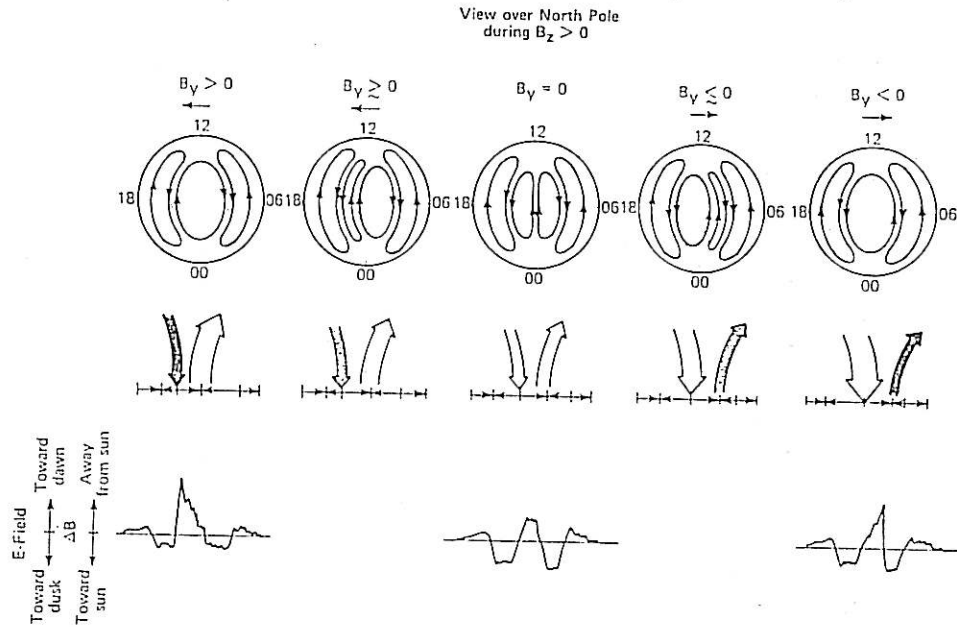


Figure 9: Schematic diagram of convection flow (along the top) and electric field and NBZ FACs distribution along the dawn-dusk meridian (in the middle) in the north polar regions for IMF  $B_z > 0$ . The R1 and R2 FAC systems have been omitted to avoid confusion [Potemra *et al.*, 1984].

gradient is developed where reversal of the NBZ FAC system, antisunward polar ionosphere current and the most intense polar cap electric fields are statistically observed. This convection gradient region is suggested [Potemra *et al.*, 1984] to be associated with sun-aligned arcs and the transpolar arc of the theta aurora. The convection patterns proposed are consistent with the antiparallel merging model [Crooker, 1979] in which the IMF merges with the geomagnetic field lines in the tail lobe during IMF  $B_z > 0$  conditions. This process divides the open field lines of the lobes and produces an area

of closed field lines in the polar cap associated with the transpolar arc of the theta aurora (illustrated in Figure 10).

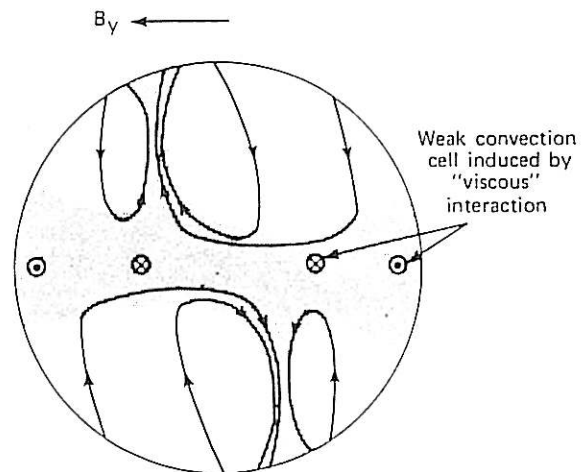


Figure 10: Cross section of the geomagnetic tail as viewed from the distant tail looking toward the Earth [Potemra *et al.*, 1984].



## 2 Observational Results

The first Swedish satellite project was the scientific satellite Viking, which was launched on 22 February 1986, from Kourou, French Guyana by an Ariane rocket into an 817 (perigee) by 13530 km (apogee) polar orbit with an inclination of  $98.8^\circ$  and an orbital period of 262 min. It carried five different instruments built by groups in Sweden, Denmark, France, Canada and the United States. The Alfvén Laboratory was responsible for the instrument measuring the electric field. The measurements were conducted by six probes mounted on four wire booms, each 40 m long and two rigid booms, 4 m each. The other experiments consisted of a magnetic field experiment with a tri-axial flux gate magnetometer, a hot plasma/energetic particle experiment, a low-frequency wave experiment and a high-frequency experiment and an auroral imaging experiment with wavelength ranges 124-150 nm and 133-190 nm (two CCD cameras). At apogee, one pixel covered 20 by 20 km<sup>2</sup>. The main scientific objective of the project was to investigate the auroral acceleration processes, by flying through the region where the acceleration is believed to take place. Operations ceased on 12 May 1987, after fifteen months of operation, well beyond the estimated nominal lifetime of eight months.

In this paper we will use the electric field data, the particle data and to some extent the magnetic field data in order to examine some properties of transpolar auroral arcs. Some of the data and plots used in this thesis are found on the pages following the appendices.

The strategy that was chosen incorporated the identification of as many polar orbits as possible, sharing the following criteria. The detected electric field for a particular orbit should have a clear peak ( $> 10$  mV/m) in the standard deviation of the dawn-to-dusk electric field poleward of the auroral oval, which was assumed never to exceed  $80^\circ$  invariant latitude (ILat). The standard deviation,  $\sigma$ , results from a least squares sine wave fit of the raw electric field data in the spinning satellite frame of reference and it is computed once per spin, or every 20 seconds. It has been shown that a high value in  $\sigma$  is, in most cases, a clear indicator of auroral activity on the magnetic field lines crossed by the satellite. In Figure 11 is shown two examples of this profile, where the poleward part of the auroral oval is displayed at 20:38:00 UT (ILat  $67.7^\circ$ ) and at 21:26:00 UT (ILat  $77.6^\circ$ ) for orbit 121 and at 11:58:00 UT (ILat  $75.9^\circ$ ) 12:55:00 UT (ILat  $81.1^\circ$ ) for orbit 328. The polar arc, possibly a transpolar feature, is assumed to be located at 21:18:00 UT and at 12:32:00 UT for the orbits 121 and 328 respectively.

The data acquired in this search amounted to 43 orbits. This number decreased further when the particle information was included, due to the fact that we wanted to study orbits which also showed a particle signature in the neighbourhood of the arc. Therefore, cases with a clear negative divergence in the dawn-to-dusk electric field (which has been shown to coincide with larger polar precipitation) where precipitating particles were absent, were excluded in this study. These cases were titled as type 3 events by Obara *et al.* [1993]. So, this study involves seventeen orbits. All data were obtained in the northern hemisphere (since there was no on-board storage and no receiving station in the Antarctic region) and the satellite moved in a dusk-to-dawn passage across the polar cap region in nearly all the seventeen orbits (see Figure 12), mainly from the evening to premidnight sector to the late morning to noon sector. The lines, fixed at the footprint of the satellite,

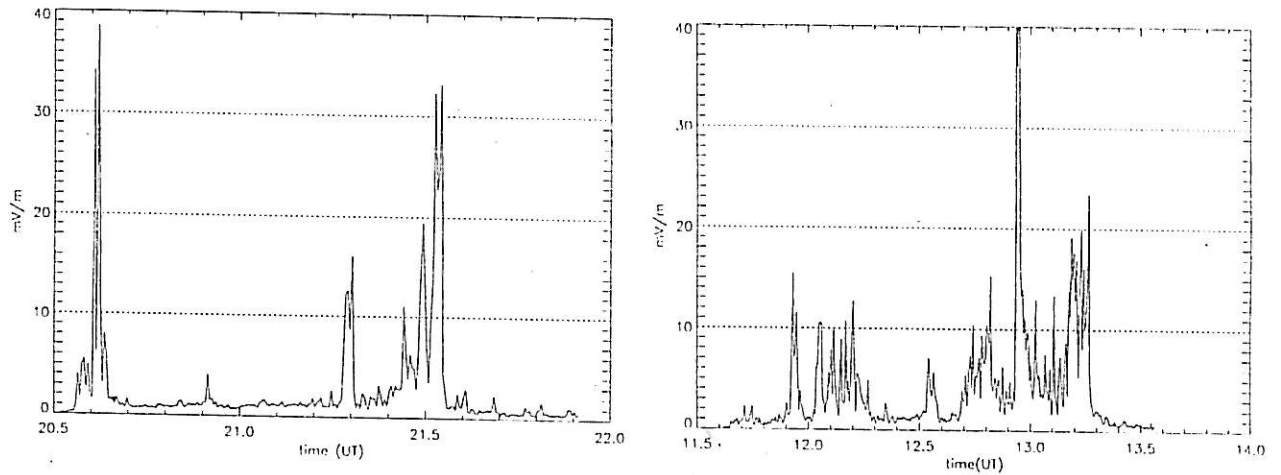


Figure 11: The  $\sigma$ -profiles of orbit 121 (left) and orbit 328 (right). Diagrams like these were used to locate possible transpolar auroral arcs. The peak is located at approximately 21:18:00 UT, invariant latitude  $81.4^\circ$  for orbit 121 and at 12:32:00 UT, invariant latitude  $85.3^\circ$  for orbit 328.

show whether the convection drift velocity is mostly sunward or antisunward. In this particular case (orbit 121), the site of the possible transpolar arc is located in a region of sunward convection (as shown with a black dot).





present. For cases 2 and 3, two equal but oppositely directed current sheets exist back to back. The upward FAC sheet is on the dawnside, while the downward one is located on the duskside for case 2. This configuration is reversed for case 3. All polar cap field-aligned currents are represented by a number of sun-aligned (in the local noon-midnight direction) current sheets. The reason being that polar arcs usually are sun-aligned during northward IMF conditions.

When performing the classification mentioned above on the signatures for the seventeen orbits (some orbits show more than one interesting feature in the  $\sigma$ -profile, which lead to a total of more than seventeen events) we found ten case 1, six case 2 and five case 3 events. The cases have been collected and tabulated after their most prominent features in Table 1. Now,

Current Density Cases			
Case 1	Case 2	Case 3	unknown
121	115	191	479
131	160	328	605
175	187	570	
235		584	
264			
460			
627			
812			

Table 1: The suggested cases, defined by Marklund and Blomberg [1991] as derived from particle precipitation. See this text for an explanation of the various cases.

since the currents existing back to back of case 2 and case 3 close in the ionosphere across the polar cap, then the local electric field is directed towards dawn for case 2 and towards dusk for case 3. This should result in local sunward convection between the current sheets for case 2 and local antisunward convection for case 3. If we compare this prediction for the different cases as estimated in Table 1 with the local convection as concluded in Table 6, we will find a good correlation for the case 2 and case 3 directions. Orbits 115, 160 and 187 have current signatures which are assumed to be case 2 events, and therefore they should have sunward convection. This is true

for all three events. Orbits 191, 328, 570 and 584 are estimated to be case 3 events. Here, all the events hold a convection which are antisunwardly directed as was expected, except for orbit 191, which is an “intermediate” state. This result shows that the procedure of classification which is used in this paper is acceptable, even if not irrefutable.

IMF values, all with IMF  $B_z > 0$ , were available for eight orbits. This is consistent with earlier results of the dependence on IMF  $B_z$  for the theta aurora. Six of these orbits also show a positive IMF  $B_y$  (see Table 2 below). According to theories of the possible IMF  $B_y$ -dependence over the polar cap, there should be a higher frequency of transpolar arc signatures on the dusk side of the polar cap, or very near to the magnetic pole, during IMF  $B_z > 0$  conditions when  $B_y$  is positive. These signatures should be located clearly towards dawn in the polar cap when  $B_y$  is negative. When we estimated the different locations of these signatures in convection velocity diagrams, three definite cases of a duskward location were found, while one case was located just on the dawn side and two cases were located clearly on the dawn side when  $B_y$  was positive. The definite case of a negative  $B_y$ , orbit 812, was found to be situated in the dawn side. The result put forward here is vaguely in favor of the present theories on the IMF  $B_y$ -dependence in the polar cap. However, it should be noted that the total amount of IMF  $B_y$  data in this study was too small to give any stronger evidence of this dependence.

IMF Dependencies		
IMF $B_z$	IMF $B_y$	Orbit number
> 0	> 0	131, 160, 264, 479, 570, 627
> 0	< 0	328, 812

Table 2: Table of IMF data as analysed in this paper.

The magnetic activity, as measured by the  $K_p$ -index (cf. Appendix D), was less than or equal to  $K_p=3$  for all orbits, which means that the magnetic activity was rather low, in agreement with a northward IMF (see Table 3). The energy injection into the Earth’s magnetosphere was probably weak during all these seventeen cases because of the northward IMF.

The electron energy spectra for the different orbits show that auroral emissions most probably were excited by precipitating electrons in the 100 eV to 1 keV range for all cases that were correlated with a clear peak in the

$\sigma$ -profile. The electron and ion energy *vs* time spectra for orbits 121 and 328 are shown in Figure 13. Both electrons and ions were measured in the 40 eV to 40 keV range on the particle experiment carried by Viking. The ion energies were distributed over a wider range than the electrons. In orbit

$K_p$ Values	
$K_p$	Orbit number
0	812
1	187, 235, 570, 584, 605, 627
2	115, 131, 187, 264, 328, 460, 479
3	121, 160, 175, 191

Table 3: Table of magnetic activity index. The larger the value, the more turbulent the magnetospheric conditions.

121, they were less than or equal to 8.6 keV, but in orbit 328 they were below 650 eV. In the ESP1 diagram of orbit 121, one can see a well-defined signature distributed around 21:18:00 UT at the 320 eV level. There are also some signatures of ions present as well in this region, that may carry some of the upward FAC. Both signatures are well correlated with the peak  $\sigma$ -value located at 21:18:00 UT.

There is an interesting declining feature in the PISP diagram from higher ion energies (to the left) to lower ion energies (to the right). This feature is not as clear for orbit 328, but it is still visible. This dependence has not been observed for the electron precipitation as far as this survey is concerned. A possible explanation could be the  $\vec{E} \times \vec{B}$ -drift. This would make faster ions arrive earlier to the satellite than slower ions, which would be deviated from their original velocity direction. This is similar to the velocity filter effect used to explain the magnetosheath ion dispersion observed poleward of the cusp.

In the ESP1 diagram of orbit 328, a similar structure as was found in the ESP1 diagram for orbit 121, is seen in the 390 eV level, but it is displaced to the right from the location of the peak  $\sigma$ -value. Both structures, as measured from ESP1 data, are distributed in approximately a 140 seconds broad region, which is within the calculated limits of the measured full width at base-values (180 seconds for orbit 121 and 225 seconds for orbit 328) from the  $\sigma$ -profiles.

When looking at the electron precipitation regions for all the orbits, after the peak in  $\sigma$ , we found that they were to a large extent located at the peak (approximately -60 to +55 seconds) or downward of the peak (approximately +40 to +110 seconds). This is being clarified in Table 4.

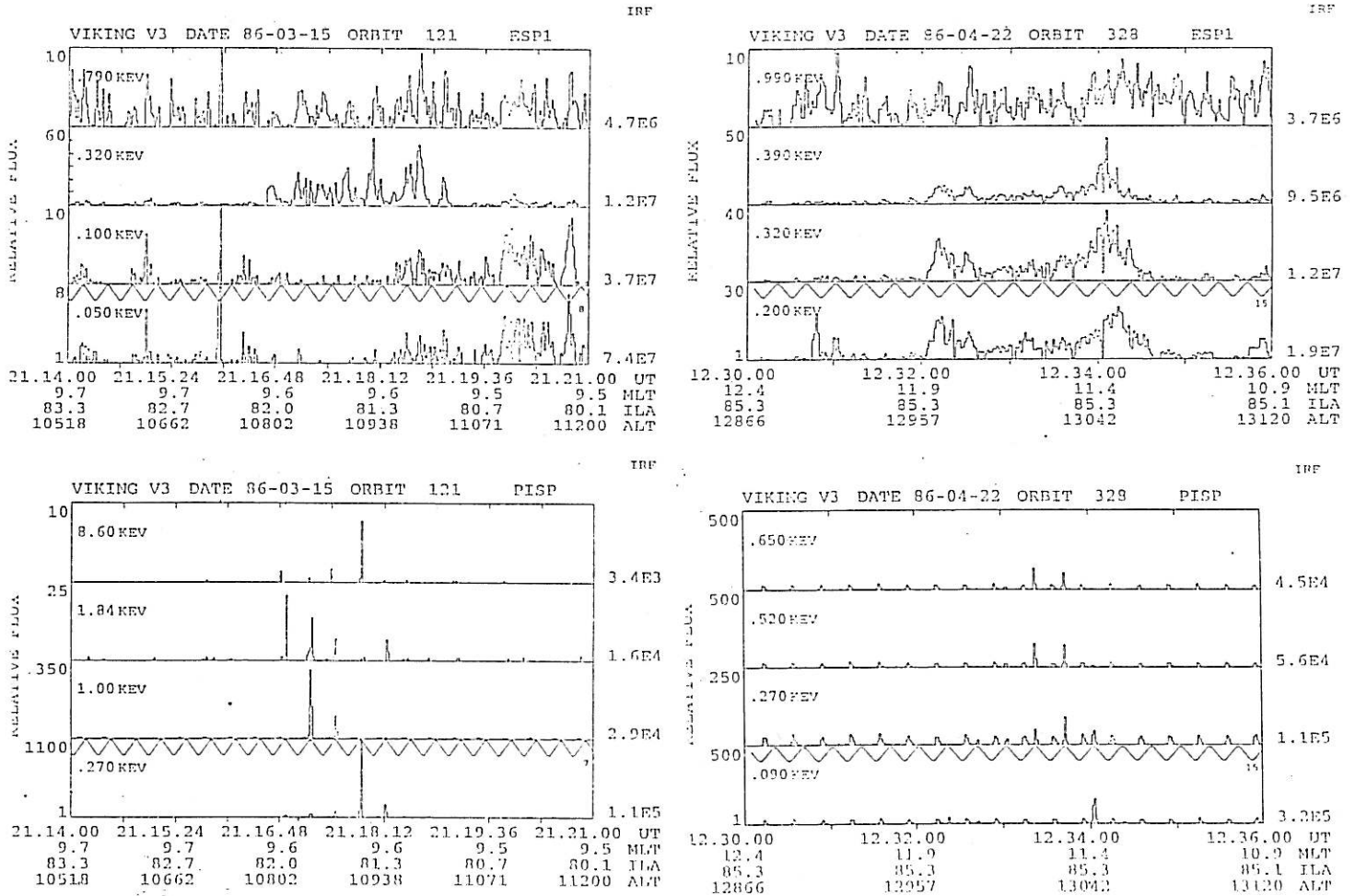


Figure 13: The electron (ESP1) and ion (PISP) energy spectra are shown for some different energy levels of orbits 121 and 328. The particles' pitch angles ( $0^{\circ}$ - $180^{\circ}$ ) are introduced in the lowest panel,  $0^{\circ}$  being a minimum in the plotted curve, i.e., the particles are moving into the ionosphere from above.

Now, from UV images taken from the Viking satellite during orbits 121 and 328, there is no theta aurora present for the former (where magnetospheric substorms are present, personal communication with R.D.Elphinstone of University of Calgary) but there is one nice theta aurora present for the latter one. In section 4 below, this difference will be discussed further.

The total acceleration voltage drops correlated with the time of possible polar cap auroras were calculated from the small deviations as seen in the potential profile along the dawn-to-dusk meridian and they were estimated never to exceed 3 kV, and the average potential drop was estimated to be 1 kV. The local electric potential drop is calculated by integrating the measured electric field at the specific altitude where the Viking satellite is passing. Since the electric potential is U-shaped and field-aligned and the electric field is directed radially inwards, it is only the positive ions, measured by the particle experiment, that are affected by the estimated potential drop of 3 kV. The energetic electrons which were measured by Viking must have been accelerated through a potential drop above the satellite if the local parallel electric fields did not change direction. The altitude for the approximate location of transpolar arc events ranged from 9.474 km to 13.524 km. This, and the relatively low energies of the electrons, which in-

Electron precipitation offset		
left	at peak	right
191 [-30,-10]	115 [-80,105]	131 [120,220]
570 [-130,-100]	121 [-80,40]	175 [-,60]
584 [-,-10]	160 [-20,50]	187 [40,50]
	235 [-60,30]	264 [-,120]
	460 [-50,50]	328 [10,125]
	479 [-60,50]	605 [15,35]
	627 [-155,65]	
	812 [-20,40]	

Table 4: The distribution of electron precipitation signatures as related to the  $\sigma$ -peak for all the seventeen orbits. The orbit is presented with its correlated electron precipitation interval location in seconds and marked around the peak.

dicare that they have not yet entered the parallel potential region, suggest

that the satellite was most oftenly passing above the acceleration regions. The energies of the electrons might correspond to the particular plasma population from where they originated.

Another intriguing result is the different cross polar cap potentials evaluated along the  $y_{GSM}$  direction as the difference between the duskward and the dawnward potential at the poleward side of the auroral oval. One would expect that most events would show a negative total cross potential, thereby giving mostly antisunward plasma flow across the polar cap. However, we discovered that a total of six orbits had a positive net value, while seven orbits showed the expected negative values (see Table 5). The remaining

Cross Polar Cap Potential	
$\Delta\Phi_{pc}$	
kV	Orbit number
-26.59	187
-25.58	175
-19.10	235
-7.04	131
-6.08	264
-3.01	605
-2.22	191
1.86	121
6.15	584
13.75	570
18.40	479
19.01	328
48.35	460

Table 5: The potential evaluated from the spin plane component of the electric field. The values were computed as the difference between the duskward potential and the dawnward potential at the poleward side of the auroral oval.

four satellite orbits did not cross the entire polar cap. Four examples of this cross polar cap potential are illustrated in Figure 15.

There is also found a nearly perfect match between the negative divergence in the dawn-to-dusk electric field and the occurrence of electron

precipitation (illustrated in Figure 14). A positive slope of the electric field curve indicates a negative divergence of the electric field, since the satellite moves in a dusk-to-dawn direction and the electric field is positive towards dusk. The peak in  $\sigma$  is clearly correlated with the peak in the electric field, and hence to the electron precipitation.

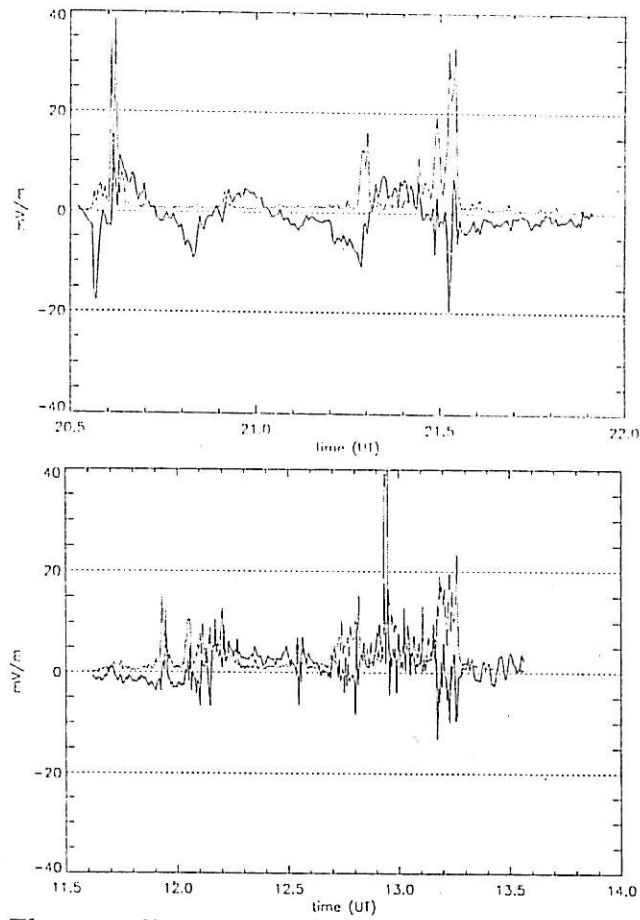


Figure 14: The  $\sigma$ -profile is displayed on top of the electric field in the dawn-to-dusk direction for orbit 121 (top) and orbit 328 (bottom), in order to show the correlation between them during a negative divergence of the electric field. A positive value in the electric field gives an antisunward convective flow and a negative value results in a sunward convection.

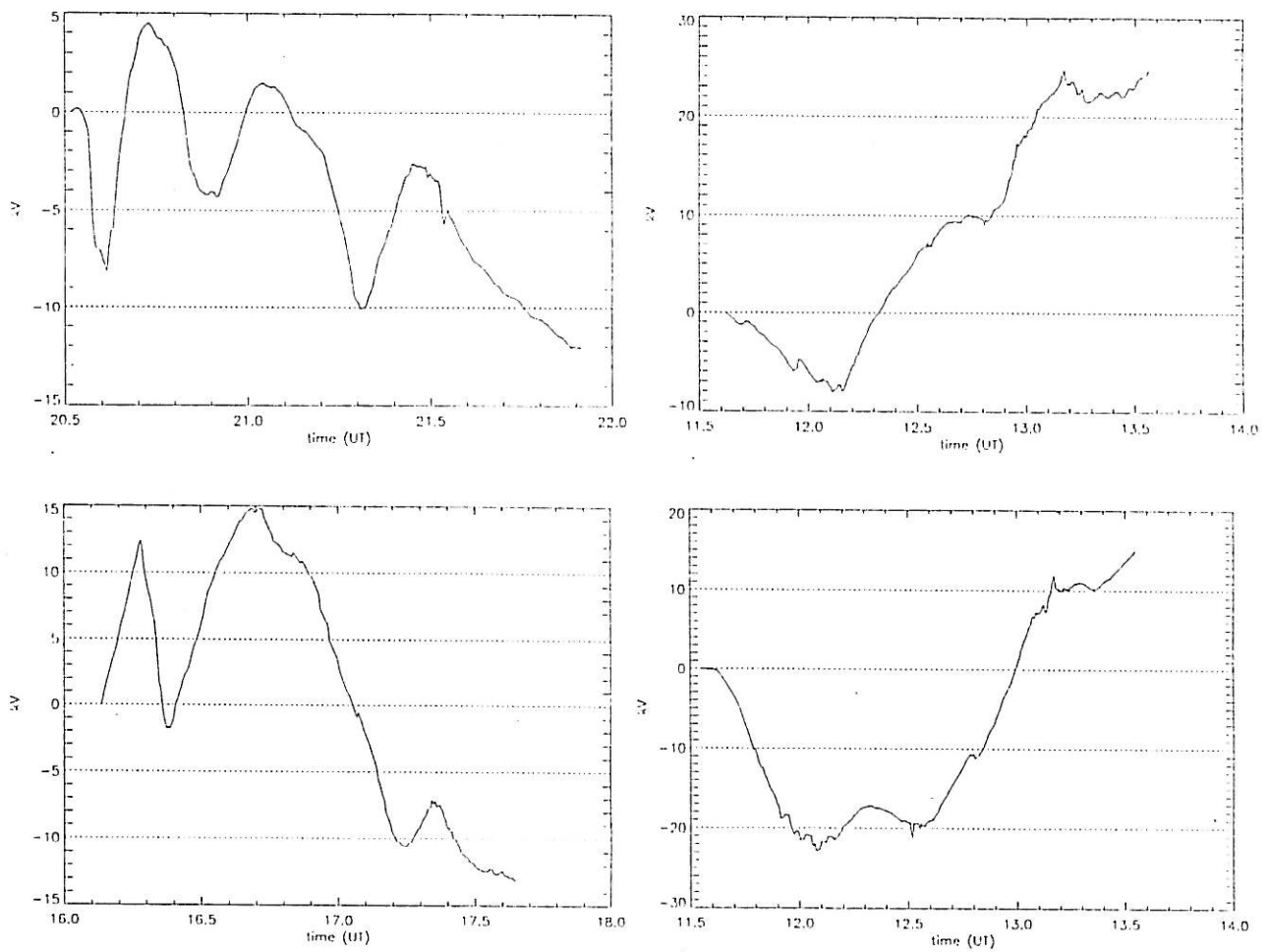


Figure 15: The polar cap electric potential integrated solely along the dawn-to-dusk electric field for orbits 121 (top left), 131 (bottom left), 328 (top right) and 350 (bottom right). Notice the higher frequencies of notches for orbit 350 than for orbit 121. These notches are assumed to coincide with particle precipitation and to give an estimate of the DC voltage drop. The respective locations of polar arcs are, in the same order as above: 21:18:00 UT, 17:08:00 UT, 12:32:00 UT and 12:30:00 UT.





### 3 Estimation of the Current Density

A great deal of attention has been paid to the Birkeland currents during the past decade or so. A lot of research has been done in order to measure these currents at different altitudes and during various conditions, such as magnetic substorms. The reason being to achieve a better understanding of phenomena like the aurora. But how do you measure these quantities? One suggestion would be to probe the particle flow *in situ*, by orbiting satellites, but this method is not as reliable as desired and usually gives doubtful results. The main cause for this is the difficulty in tracing low energy particles, whose contribution to the current may be of utmost importance. The derivation of FACs in the magnetosphere and ionosphere are today usually made through interpretations of magnetometer data, accumulated by satellites and to some extent by rockets. The interpretation is made on the assumption that the currents in the ionosphere are homogenous and stream through idealized sheets of constant width and infinite length. This method has been the most useful one when deducing current densities on the basis of magnetometer data.

We shall now deduce the analytical expression between a magnetic field,  $\vec{B}$ , and a current density,  $\vec{j}$ , in an infinite current sheet, limited along  $\hat{e}_x$  and parallel to  $\hat{e}_y$ . Let us assume that  $\vec{j} = j \hat{e}_z$ , i.e., the current density is homogenous. Then, the current density from magnetometer satellite data is derived using Ampère's law,  $\nabla \times \vec{B} = \mu_0 \vec{j}$ , where the effect of horizontal currents is being neglected as was assumed above. Then the field-aligned current density may be derived as

$$\frac{\partial B_y}{\partial x} - \frac{\partial B_x}{\partial y} = \mu_0 j_{||}$$

in the  $\hat{e}_z$  direction. When the satellite passes through an imaginary infinite current sheet assumed to be sun-aligned, measuring the magnetic field along its course in an inertial frame of reference, the sheet is generally crossed at an angle. If the sheet were crossed perpendicularly by the satellite, we would get the current density in a rather straightforward manner, using  $\frac{\partial B_y}{\partial x}$ , since the second term above is cancelled out using the infinite sheet assumption. The derivatives might be calculated as differences between nearby data points as  $\frac{\Delta B_y}{\Delta x}$ . However, when the satellite crosses the sheet at an angle you will need to introduce new assumptions, since information is missing about the rate of change of the magnetic field in the direction perpendicular to the orbit. The choice made here was to take the difference between every other data point,

*i.e.*,  $\Delta B_y(i) = B_y(i+1) - B_y(i-1)$ , at the particular data point  $i$ . This will give current density features in the approximate spatial range from 100 to 200 km, *i.e.*, large-scale phenomena. The model we decided to use in this thesis fixes the infinite current sheet direction to be sun-aligned throughout the orbit (all vectors in the model are displayed in the geocentric equatorial inertial, GEI, coordinate system, cf. Appendix A). Now, to extract the interesting variations in the magnetic field, the total magnetic field measured by the satellite can not be used right away. The IGRF model magnetic field, which is a static multipole magnetic field imitating the Earth's magnetic field at its surface, must be subtracted from the total measured magnetic field. Then we use this new field and project it onto the current sheet direction and then evaluate the magnetic field differences for nearby data points. The distance in the denominator is evaluated as the scalar product between the satellite velocity vector and  $\hat{e}_x$  multiplied by the time difference of the data points. Since we are interested in knowing the ionospheric current densities and the satellite measured the local magnitude, the evaluated currents are scaled down to ionospheric altitudes, as  $j_{||\text{iono}} = \frac{B_{\text{iono}}}{B_{\text{sat}}} \cdot j_{||\text{sat}}$ .

In Figure 16 below, the  $\sigma$ -profile is plotted on top of the current density for orbits 121, 131, 328 and 302 respectively. There seems to be a good correlation between the auroral oval signatures and the current density profiles for all orbits, reflecting the region 1 and region 2 FACs (in direction). This correlation is well depicted for orbit 302, a case of no polar arc disturbances. The FACs are directed as they should be, as illustrated in Figure 5. When it comes to verifying any correlation between possible transpolar arcs as derived from  $\sigma$ , magnetically deduced currents and particle precipitation data, it is not as obvious. For orbit 121, the precipitation spectrum indicates an upward current, a case 1 event in the model of Marklund and Blomberg [1991], carried by both electrons and positive ions around 21:18:00 UT. This feature seems to be reflected in the current density profile as a hump of approximately  $1.7 \mu\text{A}/\text{m}^2$  (peak value at 21:17:00 UT) flowing away from the ionosphere. Orbit 131 exhibits a highly varying electric field that possibly has to do with instrumental disturbances because of the periodic fluctuations as indicated by  $\sigma$ . The particle data indicate an upward flowing FAC two to three minutes to the right of the  $\sigma$ -peak. This feature is seen in the current density profile as well, located at 17:10:40 UT. The peak value is estimated to be approximately  $2.4 \mu\text{A}/\text{m}^2$ . For orbit 328, the features are more difficult to distinguish. From particle precipitation, we observe a smooth structure distributed two minutes to the right in the electron spectrum, but it is barely distinguishable in the current density profile ( $< 1 \mu\text{A}/\text{m}^2$ ).

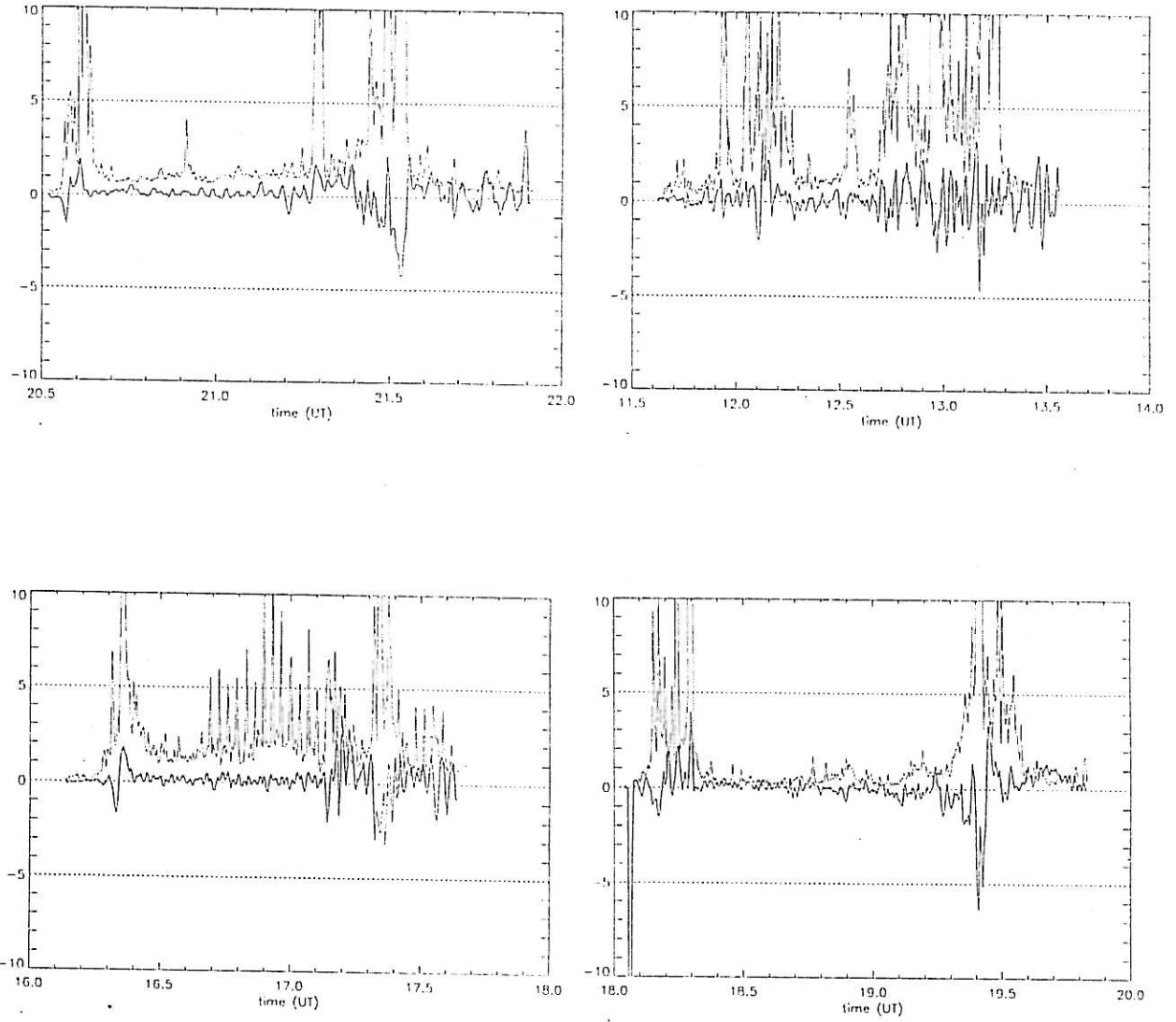


Figure 16: The current density profiles in  $\mu\text{A}/\text{m}^2$  for orbits 121 (top left), 131 (bottom left), 328 (top right) and 302 (reference case, bottom right). Positive values coincide with a current directed out of the ionosphere. The respective  $\sigma$ -profile in mV/m is distributed on top of each plot for correlation estimates.



## 4 Discussion and Conclusion

We have studied the possible relations between the electric field (and its standard deviation) in the dawn-to-dusk direction and the particle precipitation (mainly electrons) that might correspond to transpolar arcs in the northern hemisphere during a solar cycle minimum. The convective electric fields showed to large extent a negative divergence, coincident with possible observations of field-aligned accelerations. The inward directed electric fields usually prevail in the ionosphere in regions of FAC. This is a consequence of current continuity with the upward directed currents and it is also a necessary condition for the existence of arcs as formulated by a kinetic theory of arc formation.

The direction of the electric field was dawnward rather than duskward for the probable cases of polar arc activity, which corresponds to sunward convection. When comparing this result with the plots for the convection velocities based on the spin plane component of the electric field, the polar arcs are usually found in a region of sunward convection, as might have been expected (see Table 6). Sunward convective plasma motion may be

Convection Velocity Distribution		
antisunward	sunward	intermediate
328	115	191
570	121	264
584	131	460
812	160	605
	175	
	187	
	235	
	479	
	627	

Table 6: The main convection velocity state for the possible local, transpolar arcs for the different orbits as derived from the electric field in the dawn-to-dusk direction and as verified, too, by the convection velocity plots.

an indicator of precipitating electrons of plasma sheet origin as is suggested by Hoffman *et al.* [1985] and also to some extent by the measured electron

energies just below the 1 keV level found in this paper.

The question raised now, is whether the signatures we have studied in this paper really are parts of a transpolar arc or if they simply are isolated, sun-aligned polar arcs. From a personal communication with R.D.Elphinstone of University of Calgary, there were not so many theta auroras observed in the UV pictures as was expected from the  $\sigma$ -profiles. Orbit 121, for instance is interpreted as a magnetic substorm and not as a polar arc. Maybe, the signature is even a part of a so-called double auroral-oval on the morningside of the polar cap, partly because of its closeness to the auroral oval. When there is some kind of signature present in the polar cap, it is interpreted as a polar arc rather than as a theta aurora. The only clear case of theta aurora was found for orbit 328. In orbit 350, there are only some faint, quiet polar arcs present. Since orbit 328 and 350 were passing above regions of possible transpolar arcs at approximately the same altitude (the latter one was located about 150 km above the former one at 12.961 km), then this difference suggests that orbit 350 experienced a denser electric field than orbit 328 did, suggesting that the acceleration region for orbit 350 was located at a higher altitude than for orbit 328. Another conceivable explanation is that, from a physical phenomenon point of view, there may actually be polar arcs present, even if they are not glowing in the observable wavelength ranges as were chosen for the Viking satellite. The isolated particle signatures that are present for noticeable standard deviations of the electric field, though lacking a visible UV emission, are the suggestion of this and future studies of these typical signatures as measured by improved and extended UV auroral imagers might just reveal these particle signatures as really being parts of transpolar arcs.

We suggest that future studies of the transpolar auroral arc investigate the exact contribution of the various energy levels of the precipitating particles and especially the electron distribution functions in order to determine the role of low-energetic electrons for the Birkeland currents, since they probably carry the major part of the FACs and also as a way to deduce the magnetospheric origins of the precipitating electrons. The low-energetic electrons in the 100 eV range may originate in the magnetosheath.

Another interesting future assignment would be to compare the mentioned IMF  $B_y$ -dependence in this paper with the possible features of transpolar arcs in the UV-images and also to compare the events where no particle precipitation were present, though a clear negative divergence was found in the dawn-to-dusk electric field, with the UV-images. These events were excluded from the original 43 orbits and they may amount to as many as 26

orbits.

Yet another result put forward in this paper are the different profiles of the cross polar cap potentials and their odd shapes across the polar cap. As mentioned in this paper, there are some cases of a positive total cross polar cap potential as computed from dusk to dawn. This suggest a sunward convection during most of the orbit's passage. A good example of this is orbit 213 (see Figure 17 below), which also shows a strong northward IMF  $B_z$  (3.2 nT) and a positive IMF  $B_y$  (around 2.0 nT) component. The convection

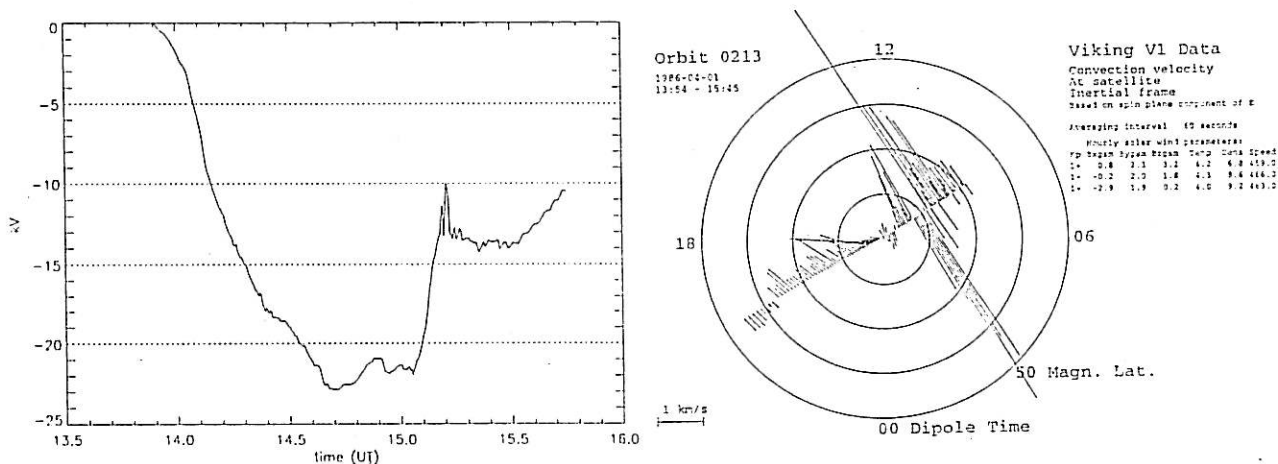


Figure 17: To the left is illustrated the "positive" potential profile as integrated along the dusk-to-dawn meridian for orbit 213. The convection across the northern hemisphere along the Viking orbit is illustrated to the right, showing a major sunward convection.

is sunward across the major part of the polar cap and a possible polar arc signature may be located near 15:03:00 UT, in a region between sunward and antisunward convection. Note also how close to the auroral oval (at 15:12:00 UT) this is.

It is important to remember that the evaluated potential does not represent a complete, true polar cap cross potential distribution, since it was calculated using only one component of the electric field. The potential along the three perpendicular GEI directions is proportional to the distance covered by the satellite. Then, we may define that the total potential is composed of the calculated potential in the dawn-to-dusk direction and a rest term, which will hold the values of the other two unknown quantities. Thus, if the distances from the remaining two directions are relatively small



compared to the dusk-to-dawn direction, then the rest term might be neglected and dismissed as a source of the odd shapes in the polar cap cross potential. In the case of orbit 213, the distances covered in the  $x_{GEI}$  and the  $y_{GEI}$  direction are of comparable magnitude, which makes the interpretation of the odd potential distribution in just one direction very uncertain.

The current density model that was employed in this paper utilizes the magnetic field data in an infinite current sheet approximation projected onto a plane perpendicular to the IGRF magnetic model direction. The infinite current sheet was supposed to be sun-aligned and limited in the dawn-to-dusk direction. This is the best possible assumption employed today as compared with a particle flux derivation. Our model seems to follow the signatures of the auroral oval fairly well, but the smaller the changes are the less reliable the model should be in terms of actual values of the current density. A further, possible development of the model would be to consider an averaging procedure over nearby data points rather than just taking the differences as was conducted and then to compare the directions of the FAC (into or away from the ionosphere) with the ones deduced applying the particle precipitation spectra. This is of particular importance when it comes to verifying the different cases as adopted by the model of Marklund and Blomberg [1991].

In conclusion, we have analyzed the data obtained by the Viking satellite in the northern polar cap region. Electron as well as some ion precipitation were found to be located, mostly to the right of a clear peak in the standard deviation of the dawn-to-dusk electric field (based on the component in the spin plane). The regions of precipitation were found to be well correlated to a negative divergence of this electric field, but the possible events of an electric field signature without any particle precipitation were not studied in this paper. This will become a logical future step in investigating the Viking data. In those cases where an interplanetary magnetic field had been evaluated by solar wind satellites, the IMF showed a northward component, as was expected. The electron energies were to a large extent found at levels below 1 keV, while the ion energies were seen to be spread in a wider range, though never exceeding the 10 keV level. Furthermore, Hoffman *et al.* [1985] reported that polar cap arcs show sunward flow superimposed on the antisunward convection and they inferred that the precipitating particles originate in the plasma sheet or plasma sheet boundary layer. Now, since the local convection velocity in the expected regions of a transpolar arc was sunward rather than antisunward, we suggest that the particles may be of plasma sheet origins. From the signatures of possible transpolar arcs, the

field-aligned currents were flowing away from the ionosphere. These current density sheets were interpreted as case 1 events according to the model of Marklund and Blomberg [1991], after the particle distributions rather than the estimated current density profiles evaluated from the magnetic disturbance data. This doubtful interpretation by using the particle precipitation should be looked into in the near future, and possibly be confirmed by an improved, averaging FAC model. Below are the main results found in this study:

- IMF  $B_z$  was positive when available.
- A negative divergence of the electric field was well correlated with a particle precipitation region.
- The particle precipitation region was located at the transpolar arc, as defined from the variance in the electric field data, or dawnward of it.
- Electron energies were most often below 1 keV.
- Ion energies were on average found at the 2 keV level and rarely exceeded 10 keV.
- Local sunward convection was found for locally balanced currents in the sense of case 2 events.
- Locally enhanced antisunward convection was found for locally balanced currents in the sense of case 3 events.
- The global plasma convection was sunward for almost as many orbits as it was antisunward. There were typically more cases of sunward convection early during the Viking mission than antisunward. This situation was the opposite in the late part of the mission.
- Particle precipitation regions are not always associated with visible arcs.



## A Coordinate Systems

In describing interactions between the solar wind and the Earth's magnetosphere, the geocentric solar magnetospheric (GSM) coordinate system is generally employed as a superior system for ordering data. It is a right-handed Cartesian system, with coordinates  $x_{GSM}$ ,  $y_{GSM}$  and  $z_{GSM}$  and its origin at the center of the Earth (see Figure 18). The positive  $x_{GSM}$  axis is

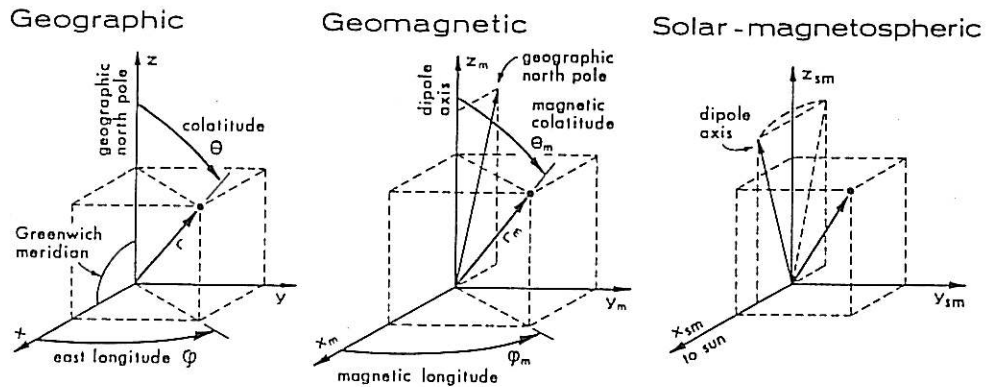


Figure 18: Some coordinate systems used in the description of geomagnetic phenomena. The geocentric solar magnetospheric system is described in the text (from Handbook of Geophysics and the Space Environment, 1985).

directed toward the sun. The  $z_{GSM}$  axis lies in the plane containing both the  $x_{GSM}$  axis and the geomagnetic dipole axis. The system not only rotates with the orbital period of the Earth around the sun, but also rocks back and forth through 23 degrees (a rotation about the  $x_{GSM}$  axis) with a period of one day. The system is particularly useful for referencing data from distant regions of the magnetosphere, since time-dependent features that result from the conical motion of the dipole axis are, to a large extent, eliminated; i.e., to a first approximation, the entire magnetosphere, in its main features, may be expected to rock back and forth in this way.

Another coordinate system, which was used for some Viking quantities, is

the geocentric equatorial inertial, GEI, coordinate system and it is defined as follows. The  $x_{GEI}$  axis is directed towards the vernal equinox, the  $z_{GEI}$  axis is parallel to the Earth's spin axis and the  $y_{GEI}$  axis completes the coordinate system. The directions of the infinite current sheet, in GEI coordinates,  $\hat{e}_y$  and  $\hat{e}_x$ , for the current model used in this thesis, are computed as follows. First you take the direction of the sun,  $\hat{s}$ , and then you evaluate the cross product with the IGRF model magnetic field,  $\vec{m}$ , at the position of the Viking satellite

$$\vec{w} = \hat{s} \times \vec{m}$$

This vector becomes parallel to the  $y_{GSM}$  direction. The employed, perpendicular, infinite sheet direction  $\hat{e}_x$  is given as

$$\hat{e}_x = -\frac{\vec{w}}{|\vec{w}|}$$

The parallel direction of the infinite current sheet is evaluated as the cross product between  $\vec{m}$  and  $\vec{w}$  as

$$\vec{r} = \vec{m} \times \vec{w}$$

Then,  $\hat{e}_y$  is given as

$$\hat{e}_y = \frac{\vec{r}}{|\vec{r}|}$$

The electric field and the potential integrated from it, utilizes a coordinate system based on the Viking satellite's spin plane. The  $x$  axis is in the spin plane, along the projection of the magnetic field,  $\vec{B}$ , onto the spin plane. The  $y$  axis is also in the spin plane, perpendicular to  $\vec{B}$  and the  $z$  axis is parallel to the spin axis.

## B The Particle Gyration

In the presence of a homogenous magnetic field,  $\vec{B}$ , the equation of motion of the charged particle becomes

$$m \frac{d\vec{v}}{dt} = q\vec{v} \times \vec{B}$$

where  $m$ ,  $q$  and  $\vec{v}$  are the particles mass, charge and velocity. If we look at the perpendicular motion, we get

$$m\omega^2 \vec{\rho} = q(\vec{v} \times \vec{B})_{\perp}$$

where  $\vec{\rho}$  is the momentary position vector of the particle, directed outwards from the center of gyration. This is what the expression looks like when the centrifugal force balances the magnetic force.  $\omega$  is the angular velocity at which the position vector rotates. Since

$$v_{\perp} = \omega \rho$$

the gyro(angular)frequency is easily calculated as

$$\omega = \omega_g = |q| \frac{B}{m}$$

Thus, the gyroradius is given as

$$\rho = \frac{mv_{\perp}}{|q|B}$$

## C The Convective Drift Motion

The equation of motion of a charged particle in a magnetic and electric field is given as

$$m \frac{d\vec{v}}{dt} = q(\vec{E} + \vec{v} \times \vec{B})$$

If the total transverse velocity is split into a sum of an initially unknown average velocity,  $\vec{u}_{\perp}$  and a superposed periodic velocity  $\vec{v}'_{\perp}$ , i.e

$$\vec{v}_{\perp} = \vec{u}_{\perp} + \vec{v}'_{\perp}$$

then, by inserting this expression in the equation of motion one gets

$$m \frac{d\vec{v}'_{\perp}}{dt} = q(\vec{v}'_{\perp} \times \vec{B}) + q\vec{E}_{\perp} + q(\vec{u}_{\perp} \times \vec{B}) - m \frac{d\vec{u}_{\perp}}{dt}$$

If the electric and magnetic fields are assumed to be constant in time and space, the last term is zero. If we now form the time average of the resulting

equation, terms containing  $\vec{v}'$  disappear, because  $\vec{v}'$  is periodic and hence has a zero average. Thus, we are left with

$$0 = q\vec{E}_{\perp} + q\vec{u}_{\perp} \times \vec{B}$$

If this equation is vector multiplied by  $\vec{B}$ , we get the final expression for the transverse drift motion

$$\vec{u}_{\perp} = \frac{\vec{E} \times \vec{B}}{B^2}$$

## D Basic Concepts

There are some concepts that you often run across when discussing phenomena related to space physics and especially to auroral physics. We will describe some of the most frequently encountered ones in this appendix.

The magnetograms and averaged data supplied by magnetic observatories are too detailed for many purposes. Therefore, some numerical parameters that indicate the level of general magnetic activity have been computed. The  $K_p$  index ("p" for planetary) is probably the most widely used of all indices. It is a measure of the worldwide average level of magnetic activity and it is very sensitive to auroral zone activity. It is based on the  $K$  indices from 12 ground stations longitudinally distributed. The  $K$  index is a measure of the irregular variations of standard magnetograms and it is an indicator of the general level of disturbance at a given observatory. The  $K_p$  index takes on integer values ranging from 0 to 9. A value in between two values is given a superscript: +, - or 0, depending on the relative closeness to this particular value. The higher the value, the higher the magnetic activity.

Three quantities are used to locate a specific phenomenon or a satellite's position. These are the universal time (UT), the corrected geomagnetic latitude (invariant latitude) and the corrected geomagnetic local time (MLT). The universal time is essentially equivalent to the Greenwich Mean Time. The invariant latitude is centred around the geomagnetic poles, having  $90^\circ$  at the northern geomagnetic pole and  $-90^\circ$  at the corresponding pole in the southern hemisphere. The invariant latitude and the MLT coordinates are well depicted in Figure 12 for the convection velocity.





## E Fortran and IDL Programmes

We have used three different programmes. First, we searched for interesting events with "Search.for", then we transferred the chosen data to data files with "Transz.for". The conversion from .dat-files to .ps-files was basically conducted interactively with "Read.pro" in an IDL environment.

```

1      program OrbitSearch
2      implicit none
3      integer*4 n,i,j,k,count,tic,start,finish,total,ok,check,high,low
4      parameter (n=1000)
5      integer*4 refy,refm,refd,sthrr,stmt,sphr,spmt,successtac
6      integer*4 orb(1:n),rec(1:n),pos(1:n),flag(1:n),kp,num(1:n),Q
7      integer*4 UTh(1:n),UTm(1:n),UTs(1:n),UTmil(1:n)
8      real*4 upper,lower,invlim
9      real*4 time(1:n),E1(1:n),E2(1:n),sigma(1:n),Bx(1:n),By(1:n),
10     1      Bz(1:n)
11     real*4 spinphi(1:n),DevVfg(1:n),Vfg(1:n),DevE1(1:n),DevE2(1:n)
12     real*4 DevElw(1:n),DevE2w(1:n),Devr3(1:n),Devrl(1:n)
13     real*4 Alt(1:n),IL(1:n),MLT(1:n),FLat(1:n),FLon(1:n)
14     real*4 PolLat,EqLat
15     real*8 reftime
16     logical cross
17
18 99    call aski('Give Viking startorbit',0,start)
19     call aski('Give Viking endorbit',0,finish)
20     if (start.eq.0.or.finish.eq.0) then
21         stop
22     endif
23     call askf('Sigma upper limit',0,upper)
24     call askf('Sigma lower limit',0,lower)
25     call askf('InvLat limit',0,invlim)
26     call aski('Higher limit of hits',0,high)
27     call aski('Lower limit of hits',0,low)
28     total=finish-start+1
29     if ((total.ge.1).and.(total.le.n)) then
30         orb(1)=start
31         rec(1)=1
32         pos(1)=1
33         tac=0
34         do 10 i=1,total
35             count=0
36             tic=0
37             Q=0
38             call get_info(orb(i),num(i),refy,refm,refd,
39             1      sthrr,stmt,sphr,spmt,reftime,ok)
40             if (ok.eq.1) then
41                 call get_kp(orb(i),pos(i),kp,check)
42                 if (check.eq.1.and.kp.gt.0) then
43                     Q=int(kp/10)
44                     do 20 j=1,num(i)
45                         call get_data(orb(i),rec(j),time(j),E1(j),E2(j),
46             1      sigma(j),Bx(j),By(j),Bz(j),spinphi(j),
47             2      DevVfg(j),Vfg(j),DevE1(j),DevE2(j),DevElw(j),
48             3      DevE2w(j),Devr3(j),Devrl(j),flag(j))
49                         UTh(j)=int(time(j)/3600.0)
50                         UTm(j)=int((time(j)-real(UTh(j)*3600.0))/60.0)
51                         UTs(j)=time(j)-UTh(j)*3600.0-UTm(j)*60.0
52                         UTmil(j)=UTs(j)/1000.0
53                         call get_orbitdata(orb(i),UTh(j),UTm(j),UTs(j),UTmil(j),
54             1      Alt(j),IL(j),MLT(j),FLat(j),FLon(j),flag(j))
55                         call oval_edges(Q,MLT(j),PolLat,EqLat,successtac)
56                         if (successtac.ne.1) then
57                             stop
58                         else
59                             if (IL(j).ge.PolLat) then
60                                 count=count+1
61                             endif
62                         endif
63                         rec(j+1)=rec(j)+1
64 20      continue
65         do 30 k=1,count
66             if (sigma(k).gt.upper) then
67                 cross=.true.
68             else
69                 cross=.false.
70             endif

```



```
71         if (.not.cross.and.IL(k).gt.invlm.and.
72             1         sigma(k).gt.lower) then
73                 tic=tic+1
74             endif
75     30         continue
76             if (tic.ge.low.and.tic.le.high) then
77                 write(*,*) orb(i)
78                 write(*,*) tic
79                 tac=tac+1
80             endif
81         endif
82     endif
83         orb(i+1)=orb(i)+1
84         pos(i+1)=pos(i)+1
85     10     continue
86     else
87         write(*,*) 'Bad input'
88         goto 99
89     endif
90     write(*,*) tac
91     stop
92     end
end
```



```

1      program FetchData
2      implicit none
3      integer*4 i,j,n,antal,start,slut,num
4      real*8 my0,reftime,pi
5      parameter (n=1000)
6      parameter (my0=12.56637061,pi=3.1415926535)
7      integer*4 ok1,ok2,ok3,ok4,ok5,ok6,ok7
8      integer*4 refy,refm,refd,sthhr,stmt,sphr,spmt
9      integer*4 orb,pos(1:n),flag1,flag2,flag3,flag4,flag5,flag6,flag7
10     integer*4 flag8,flag9,flag10,UTh(1:n),UTm(1:n),UTs(1:n),UTmil(1:n)
11     logical same
12     real*4 time(1:n),E1(1:n),E2(1:n),sigma(1:n),Bx(1:n),By(1:n),Bz(1:n)
13     real*4 IMFx(1:n),IMFy(1:n),IMFz(1:n),sx(1:n),sy(1:n),sz(1:n)
14     real*4 spinphi(1:n),DevVfg(1:n),Vfg(1:n),DevE1(1:n),DevE2(1:n)
15     real*4 DevE1w(1:n),DevE2w(1:n),Devr3(1:n),Devr1(1:n)
16     real*4 Alt(1:n),IL(1:n),MLT(1:n),FLat(1:n),FLon(1:n)
17     real*4 time1(1:n),time2(1:n),pot2(1:n),pot2c(1:n)
18     real*4 pot12(1:n),pot12c(1:n),pot123(1:n),pot123c(1:n)
19     real*4 ns(1:n),ew(1:n),scale(1:n),t(1:n)
20     ! real*4 sub1,sub2,t1,t2,ex(1:n),ey(1:n),ez(1:n),B(1:n),v(1:n),vreal(1:n)
21     real*4 mx(1:n),my(1:n),mz(1:n),vx(1:n),vy(1:n),vz(1:n)
22     real*4 rx(1:n),ry(1:n),rz(1:n),wx(1:n),wy(1:n),wz(1:n),E(1:n)
23     real*4 dump_dot,dt,Br2(1:n)
24     real*4 vxb1(1:n),vxb2(1:n),vxb3(1:n),vel(1:n)
25     real*4 dsw2(1:n),dE,divE(1:n)
26     real*4 ds(1:n),vw2(1:n),fac3(1:n),dBr2(1:n)
27     real*4 r1(1:n),r2(1:n),r3(1:n),w1(1:n),w2(1:n),w3(1:n),r,w
28     real*4 sum1,sum2,sum3,add1,add2,add3,L1,L2,L3,delta
29     call aski('Give Vikingorbit',0,orb)
30     call get_info(orb,num,refy,refm,refd,
31     1      sthhr,stmt,sphr,spmt,reftime,flag1)
32     999 write(*,200) 'Number of Data Records:',num
33     200 format(' ',T2,A,I5)
34     if (num.eq.0) then
35         stop
36     endif
37     call aski('Give startrecord ',0,start)
38     call aski('Give endrecord ',0,slut)
39     if (start.eq.0.or.slut.eq.0) then
40         stop
41     endif
42     antal=slut-start+1
43     if (antal.le.n.and.slut.le.num.and.start.le.slut) then
44         pos(1)=start
45         do i=1,antal
46             call get_data(orb,pos(i),time1(i),E1(i),E2(i),sigma(i),
47             1      Bx(i),By(i),Bz(i),spinphi(i),DevVfg(i),Vfg(i),DevE1(i),
48             2      DevE2(i),DevE1w(i),DevE2w(i),Devr3(i),Devr1(i),flag2)
49             call corotation_field(orb,pos(i),vxb1(i),vxb2(i),vxb3(i),
50             1      flag3)
51             call get_imf_gsm(orb,pos(i),IMFx(i),IMFy(i),IMFz(i),flag4)
52             call get_igrf(orb,pos(i),mx(i),my(i),mz(i),flag5)
53             call get_sundir(orb,pos(i),sx(i),sy(i),sz(i),flag6)
54             call get_velocity(orb,pos(i),vx(i),vy(i),vz(i),flag7)
55             call get_dipolescale(orb,pos(i),ns(i),ew(i),flag8)
56             call get_potential(orb,pos(i),time2(i),pot2(i),pot12(i),
57             1      pot123(i),pot2c(i),pot12c(i),pot123c(i),flag9)
58             if (time1(i).eq.time2(i)) then
59                 same=.true.
60             else
61                 same=.false.
62             endif
63             time(i)=time1(i)
64             t(i)=(time(i)/3600.0)
65             UTh(i)=int(t(i))
66             UTm(i)=int((time(i)-real(UTh(i)*3600.0))/60.0)
67             UTs(i)=time(i)-UTh(i)*3600.0-UTm(i)*60.0
68             UTmil(i)=UTs(i)/1000.0
69             call get_orbitdata(orb,UTh(i),UTm(i),UTs(i),UTmil(i),
70

```



```

71      1      Alt(i), IL(i), MLT(i), FLat(i), FLon(i), flag10)
72      call dump_cross(sx(i), sy(i), sz(i), mx(i), my(i), mz(i),
73      1      wx(i), wy(i), wz(i))
74      call dump_cross(mx(i), my(i), mz(i), wx(i), wy(i), wz(i),
75      1      rx(i), ry(i), rz(i))
76      !      call dump_cross(vx(i), vy(i), vz(i), Bx(i), By(i), Bz(i),
77      !      1      ex(i), ey(i), ez(i))
78      r=sqrt(rx(i)**2+ry(i)**2+rz(i)**2)
79      r1(i)=rx(i)/r
80      r2(i)=ry(i)/r
81      r3(i)=rz(i)/r
82      w=sqrt(wx(i)**2+wy(i)**2+wz(i)**2)
83      w1(i)=-wx(i)/w
84      w2(i)=-wy(i)/w
85      w3(i)=-wz(i)/w
86      E(i)=E2(i)+vxb2(i)
87      open(unit=91, file='sigma.dat', access='direct', status='new',
88      1      recl=25, err=30, recordtype='fixed', shared)
89      open(unit=92, file='time.dat', access='direct', status='new',
90      1      recl=25, err=30, recordtype='fixed', shared)
91      open(unit=93, file='e.dat', access='direct', status='new',
92      1      recl=25, err=30, recordtype='fixed', shared)
93      open(unit=94, file='alt.dat', access='direct', status='new',
94      1      recl=25, err=30, recordtype='fixed', shared)
95      open(unit=95, file='ilat.dat', access='direct', status='new',
96      1      recl=25, err=30, recordtype='fixed', shared)
97      open(unit=96, file='pot2c.dat', access='direct', status='new',
98      1      recl=25, err=30, recordtype='fixed', shared)
99      write(91, rec=i, err=30, iostat=ok1) sigma(i)
100     write(92, rec=i, err=30, iostat=ok2) time(i)/3600.0
101     write(93, rec=i, err=30, iostat=ok3) E(i)
102     write(94, rec=i, err=30, iostat=ok4) Alt(i)
103     write(95, rec=i, err=30, iostat=ok5) IL(i)
104     write(96, rec=i, err=30, iostat=ok6) pot2c(i)/1E3
105     Bx(i)=Bx(i)-mx(i)
106     By(i)=By(i)-my(i)
107     Bz(i)=Bz(i)-mz(i)
108     pos(i+1)=pos(i)+1
109 end do
110 if (.not.same) then
111     write(*,300) 'CAUTION: Times from routines get_data &'
112     write(*,400) 'get_potential are NOT the same.'
113     write(*,400) 'The times from get_data are chosen'
114 endif
115 300 format(' ', T2, A)
116 400 format(' ', T12, A)
117 do i=1, antal
118 !      vreal(i)=sqrt(vx(i)**2+vy(i)**2+vz(i)**2)
119 !      vel(i)=sqrt(vx(i)**2+vy(i)**2)
120 !      B(i)=sqrt(Bx(i)**2+By(i)**2+Bz(i)**2)
121     Br2(i)=dump_dot(Bx(i), By(i), Bz(i), r1(i), r2(i), r3(i))
122     vw2(i)=dump_dot(vx(i), vy(i), vz(i), w1(i), w2(i), w3(i))
123 end do
124 do i=2, antal-1
125     dBr2(i)=(Br2(i+1)-Br2(i-1))
126     dE=E(i+1)-E(i-1)
127     dsw2(i)=0
128     ds(i)=0
129     do j=i-1, i
130         dt=time(j+1)-time(j)
131         ds(i)=ds(i)+vel(j)*dt
132         dsw2(i)=dsw2(i)+vw2(j)*dt
133     end do
134     scale(i)=ns(i)*ew(i)
135     fac3(i)=scale(i)*1E4*(dBr2(i)/abs(dsw2(i)))/my0
136     divE(i)=-dE/abs(ds(i))
137     open(unit=99, file='fac3.dat', access='direct', status='new',
138     1      recl=25, err=30, recordtype='fixed', shared)
139     write(99, rec=i, err=30, iostat=ok7) fac3(i)
140 end do

```





```

141      sum1=0
142      sum2=0
143      sum3=0
144      do i=1,antal-1
145          delta=time(i+1)-time(i)
146          add1=vx(i)*delta
147          add2=vy(i)*delta
148          add3=vz(i)*delta
149          sum1=sum1+add1
150          sum2=sum2+add2
151          sum3=sum3+add3
152      end do
153      L1=sum1
154      L2=sum2
155      L3=sum3
156      write(*,*) L1,L2,L3
157      write(*,*) L1/L2,L3/L2
158 30      if (ok1.or.ok2.or.ok3.or.ok4.or.ok5.or.ok6.or.
159          1      ok7.gt.0) then
160          write(*,*) 'Error in transition to file'
161          write(*,*) ok1,ok2,ok3,ok4
162          write(*,*) ok5,ok6,ok7
163      else
164      !      call askf('Give time1',0,t1)
165      !      call askf('Give time2',0,t2)
166      !      do i=2,antal-1
167      !          sub1=t(i)-t1
168      !          sub2=t(i)-t2
169      !          if (abs(sub1).le.5E-3) then
170      !              write(*,*) 't1 =',pos(i)
171      !          endif
172      !          if (abs(sub2).le.5E-3) then
173      !              write(*,*) 't2 =',pos(i)
174      !          endif
175      !      end do
176      !      write(*,*) 'Transition to file completed'
177      !      endif
178      !      else
179      !          goto 999
180      !      endif
181      !      stop
182      !      end
end

```



```
FUNCTION Read, file
OpenR, lun, file, /Get_LUN
data=FltArr(1000)
temp=0.0
i=0
WHILE (NOT EOF(lun)) DO BEGIN
    ReadU, lun, temp
    data(i)=temp
    i=i+1
ENDWHILE
data=data(0:i-1)
Free_LUN, lun
RETURN, data
END
```







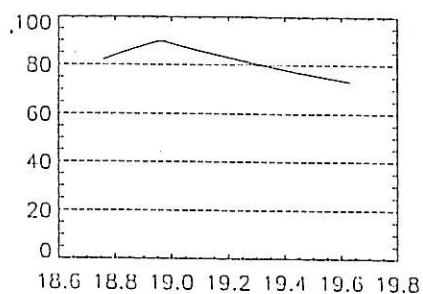
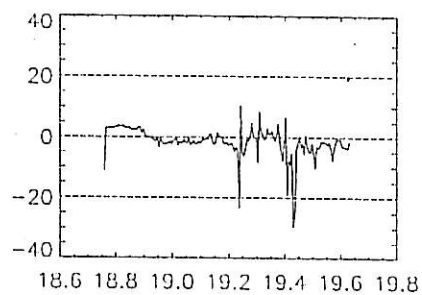
## F Data Plots

Three different data plots for all the orbits are given below. The orbits are 115, 121, 126, 131, 160, 175, 187, 191, 213, 235, 245, 252, 264, 292, 301, 302, 328, 341, 350, 353, 370, 423, 460, 467, 479, 484, 536, 569, 570, 573, 584, 595, 605, 627, 713, 725, 734, 742, 764, 798, 812, 836, 847 and 852. The plots depict, in order of appearance:

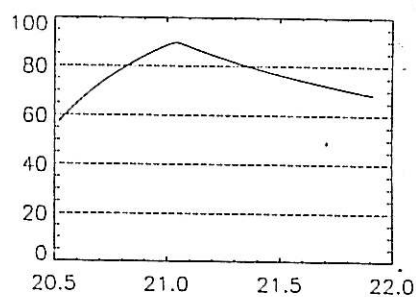
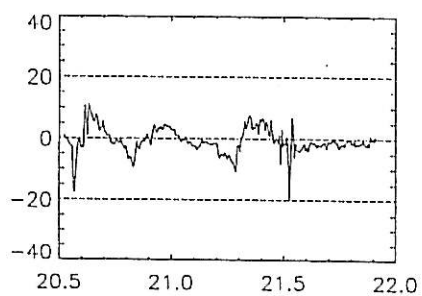
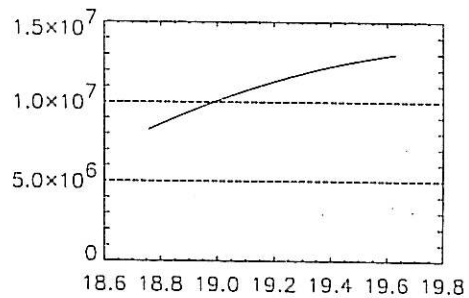
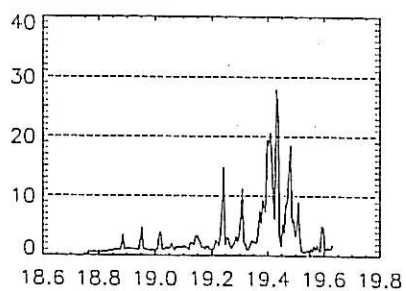
- Four small plots of the dawn-to-dusk electric field in mV/m (top left), the  $\sigma$ -profile in mV/m (bottom left), the invariant latitude (top right) and the altitude in m (bottom right).
- Three plots of (from top to bottom) the  $\sigma$ -profile (mV/m) on top of the dawn-to-dusk electric field (mV/m), the polar cap potential in the dawn-to-dusk direction (kV) and the  $\sigma$ -profile on top of the estimated current density ( $\mu\text{A}/\text{m}^2$ ).
- The convection velocity at the satellite in an inertial frame of reference.



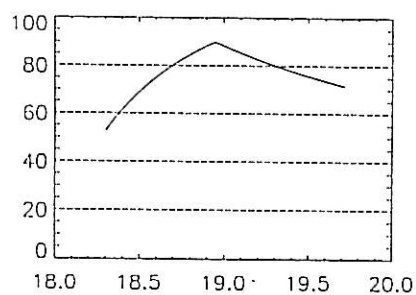
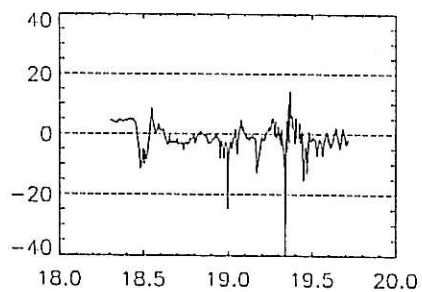
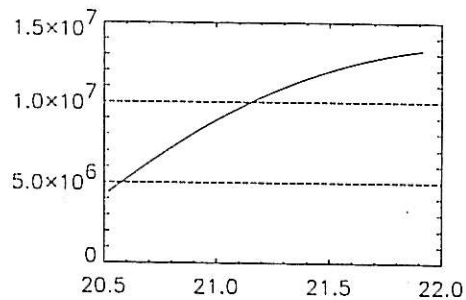
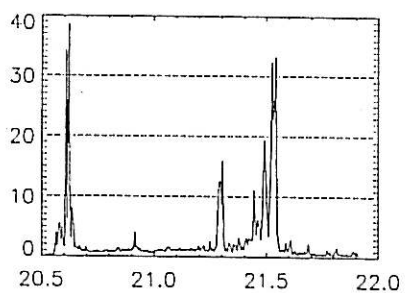




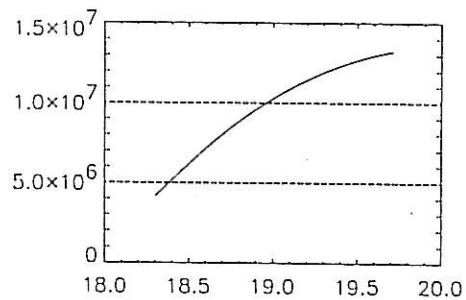
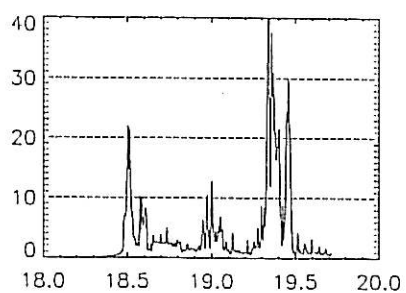
115



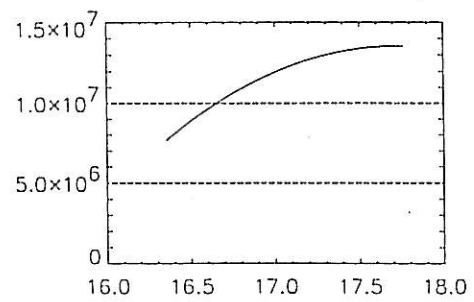
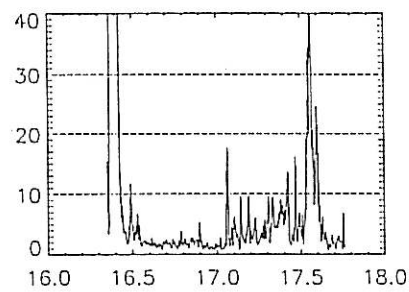
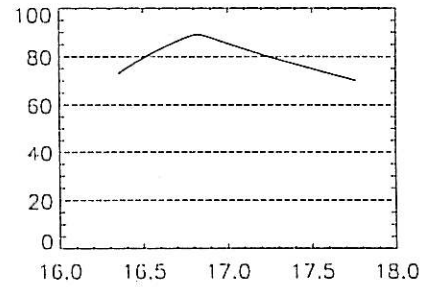
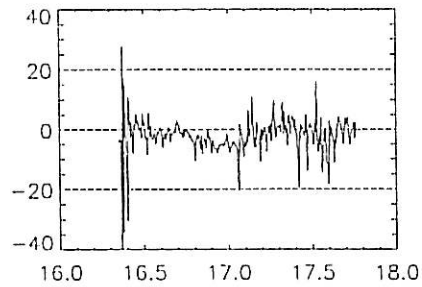
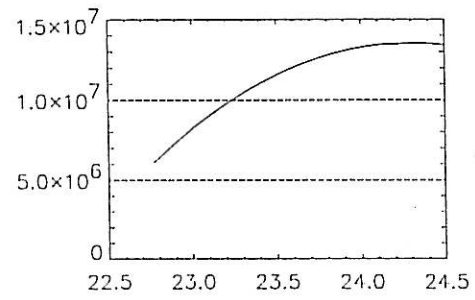
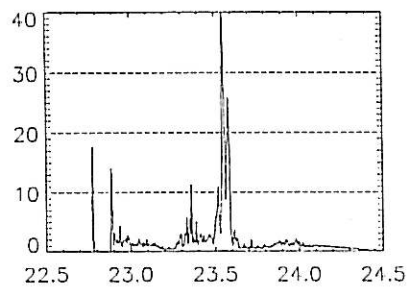
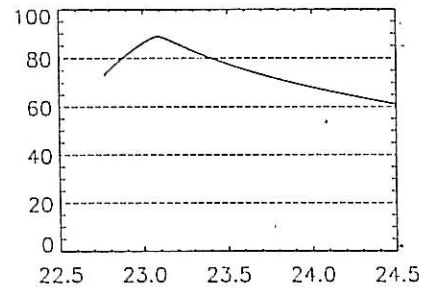
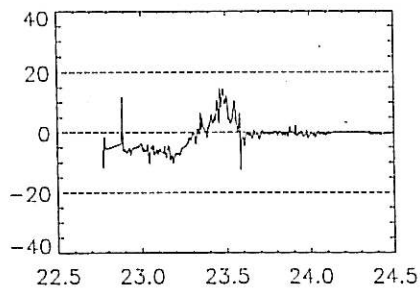
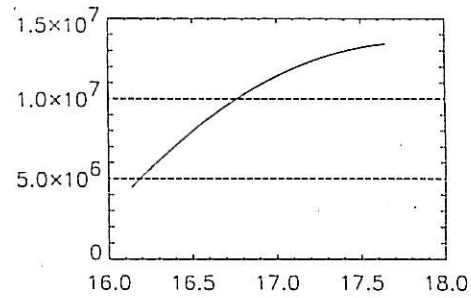
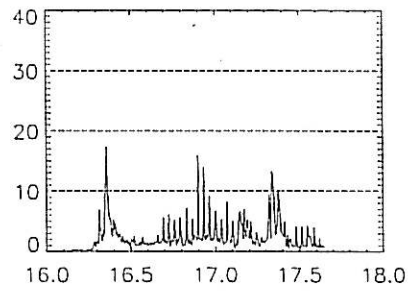
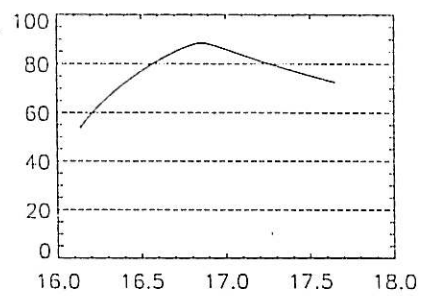
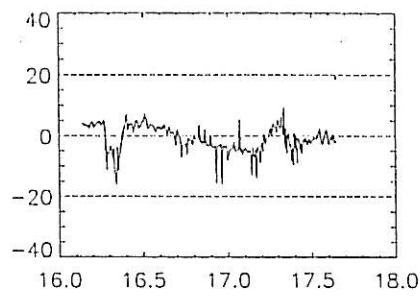
121



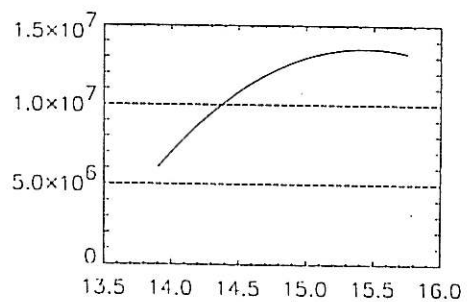
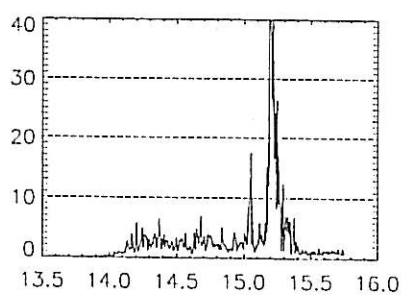
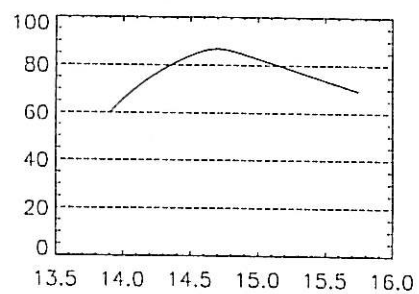
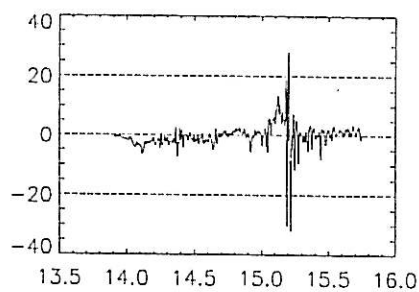
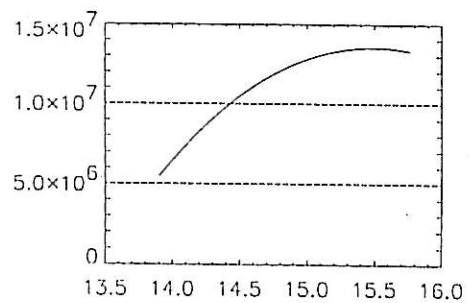
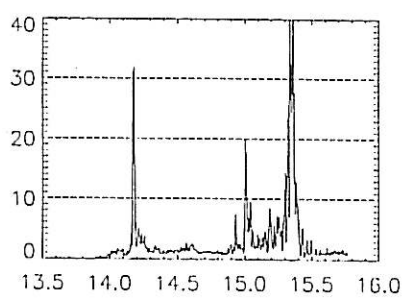
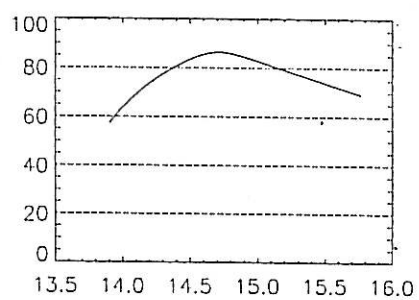
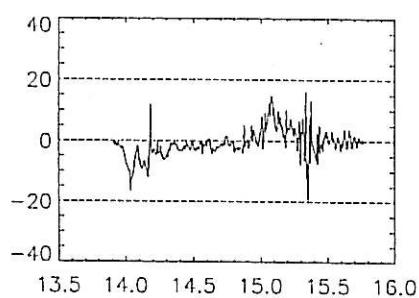
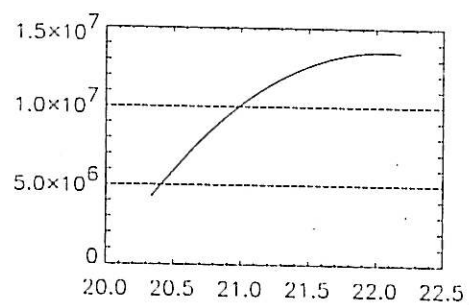
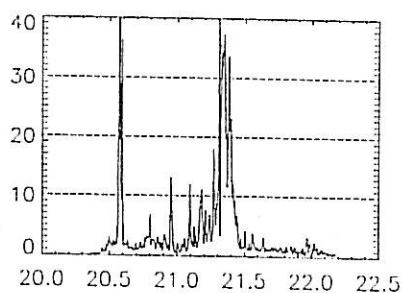
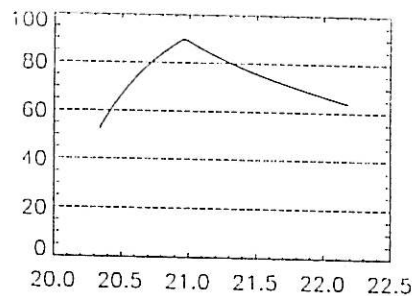
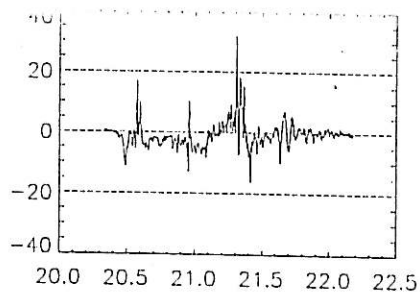
126



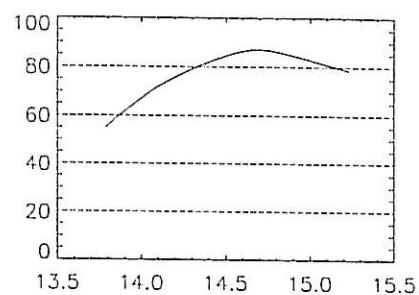
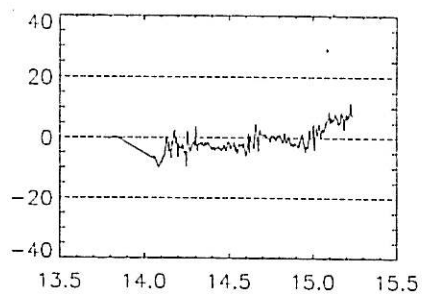




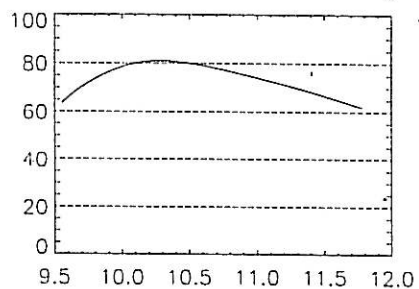
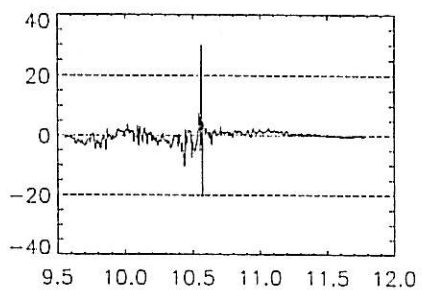
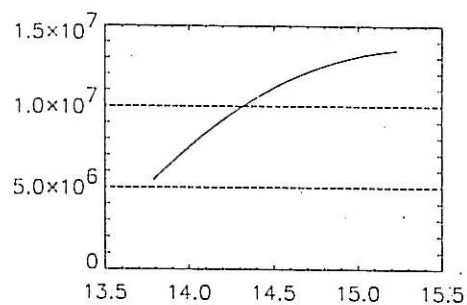
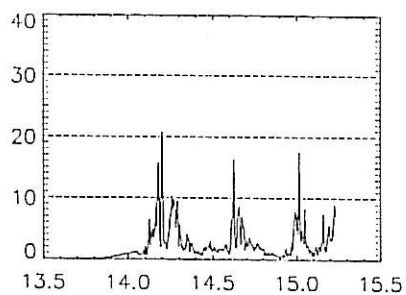




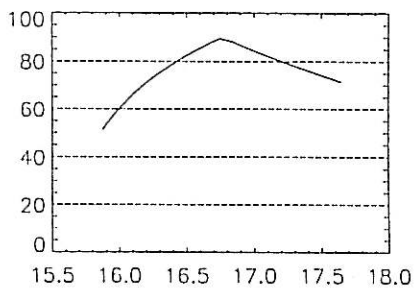
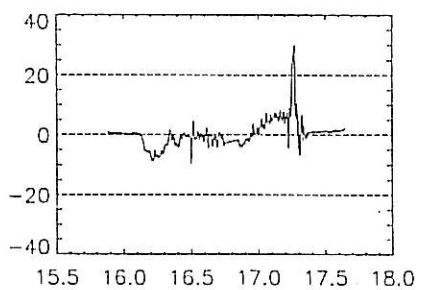
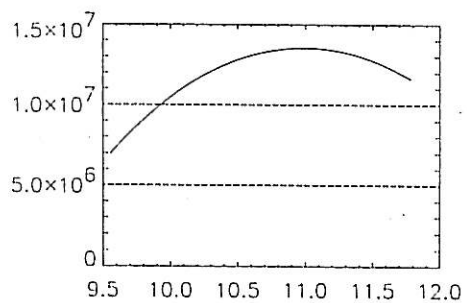
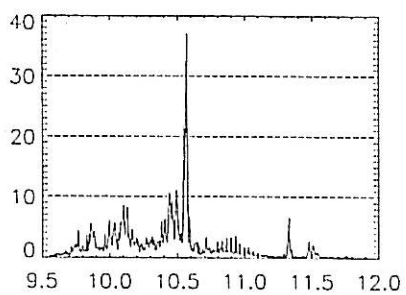




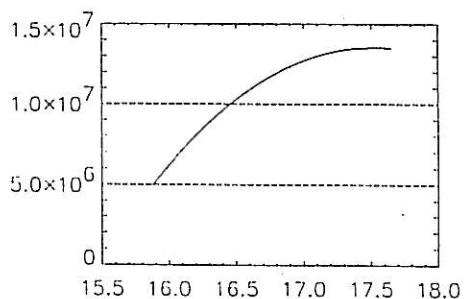
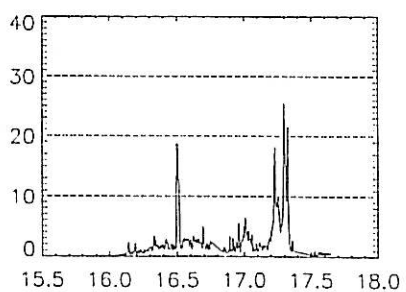
235



245

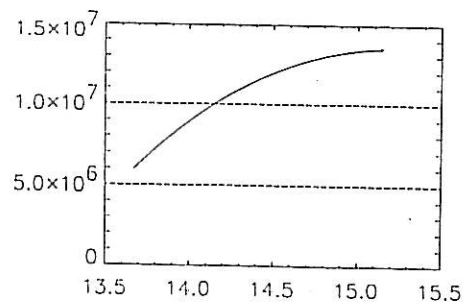
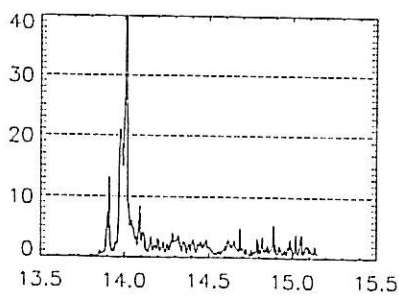
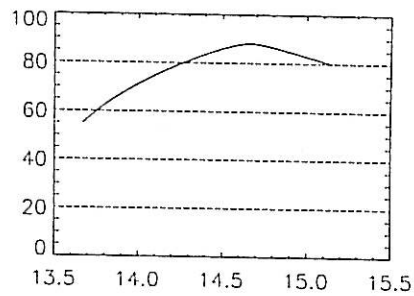
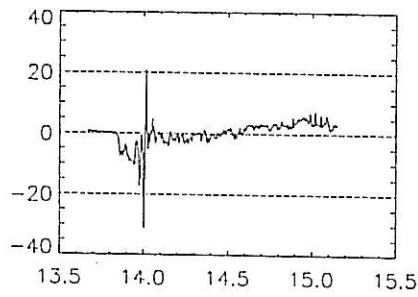
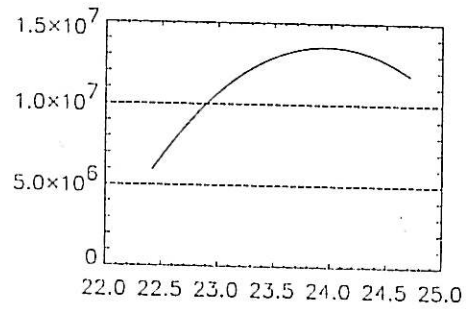
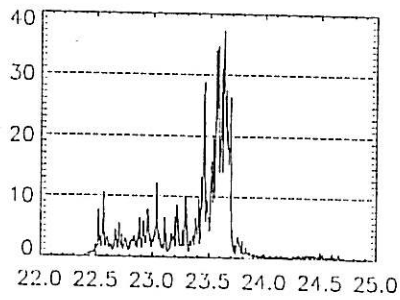
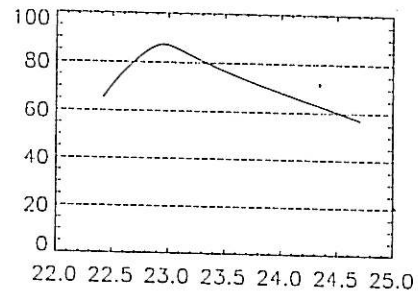
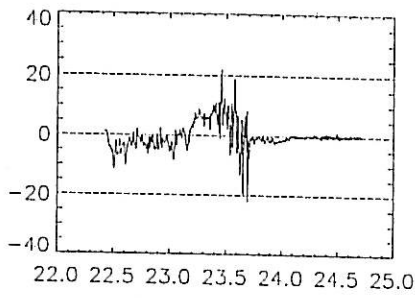
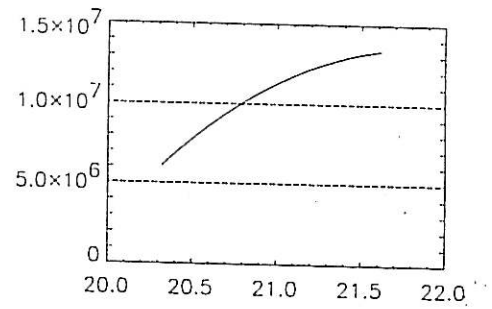
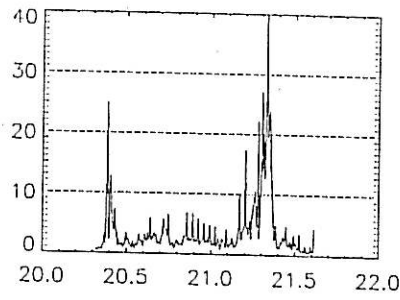
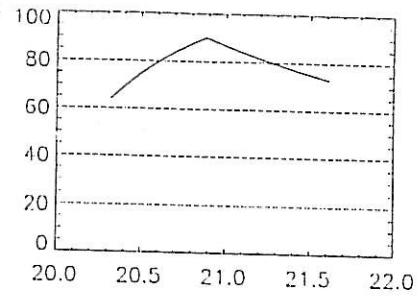
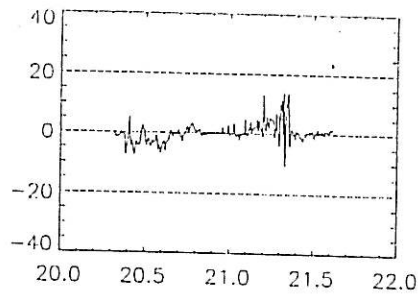


252

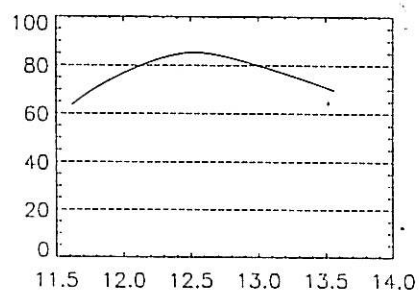
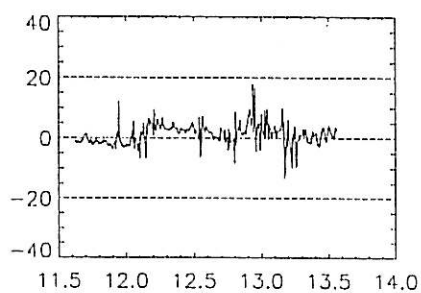
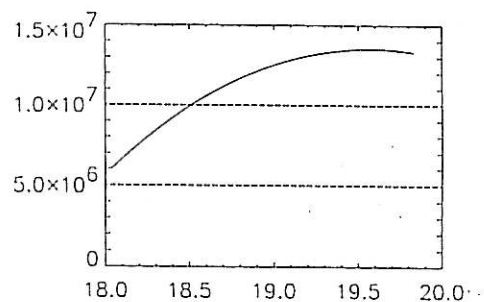
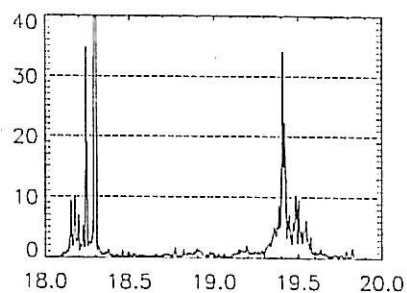
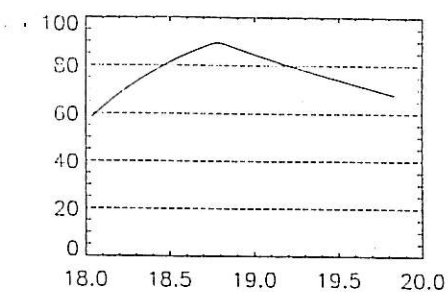
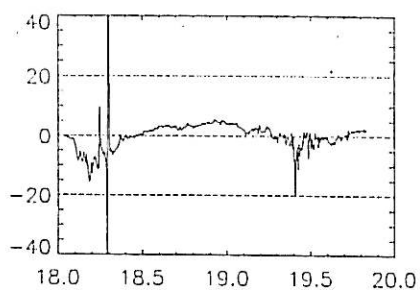




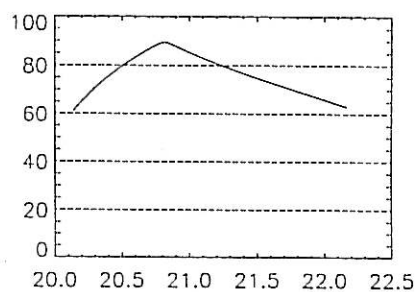
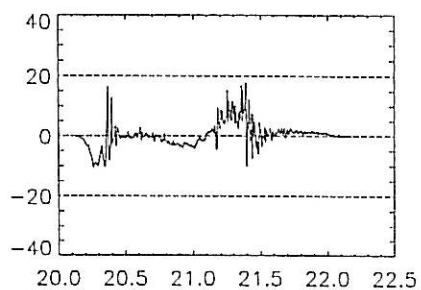
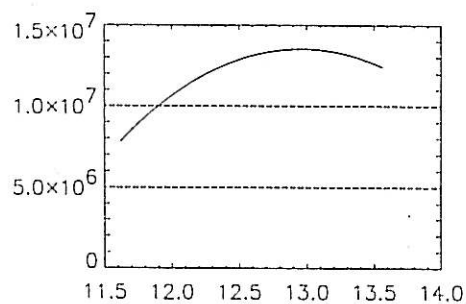
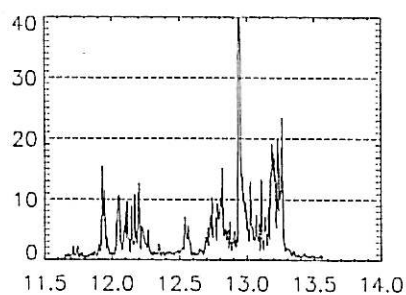




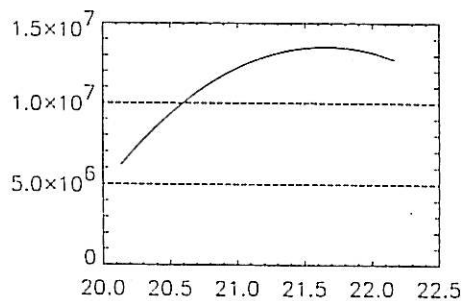
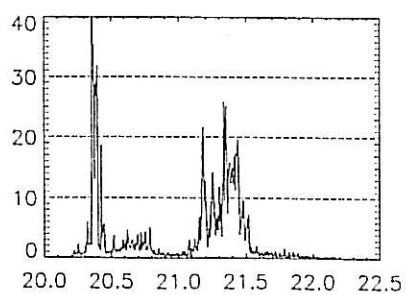




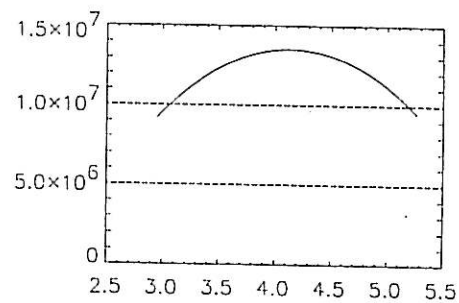
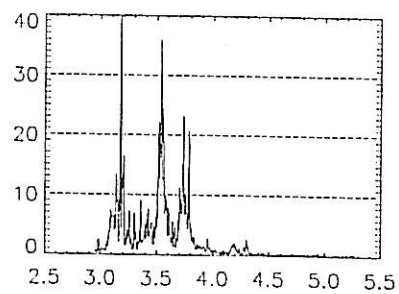
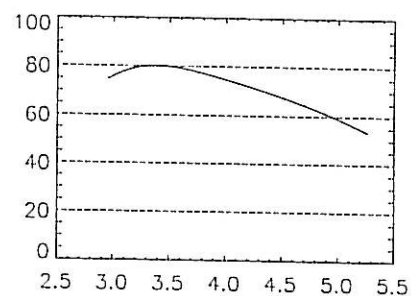
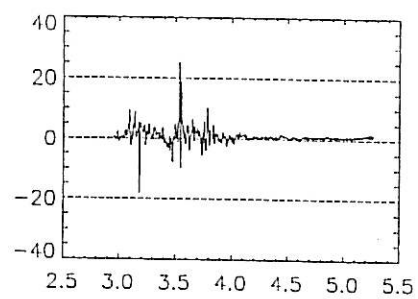
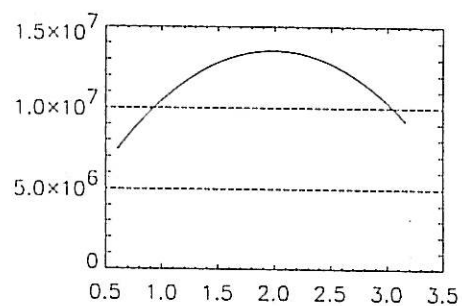
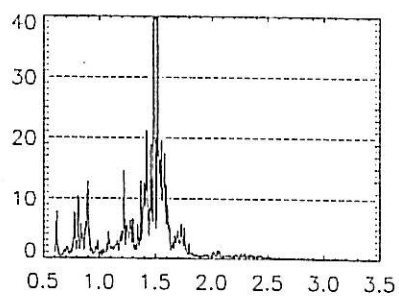
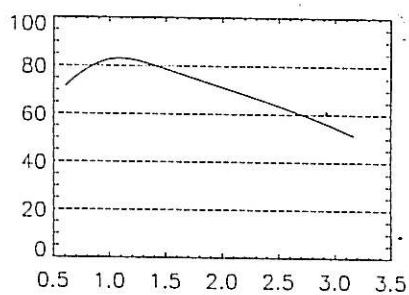
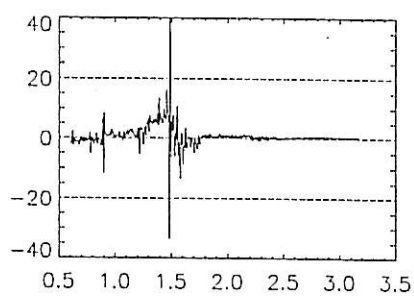
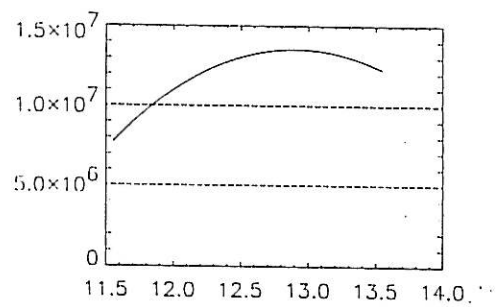
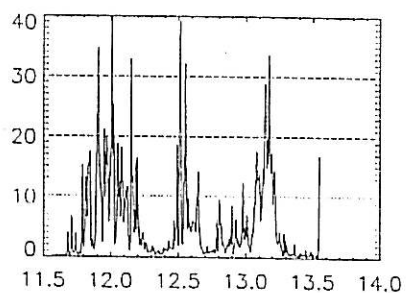
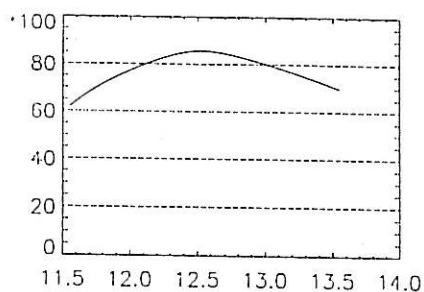
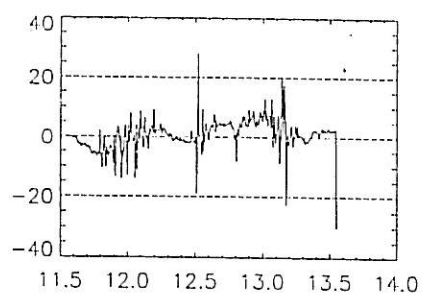
328



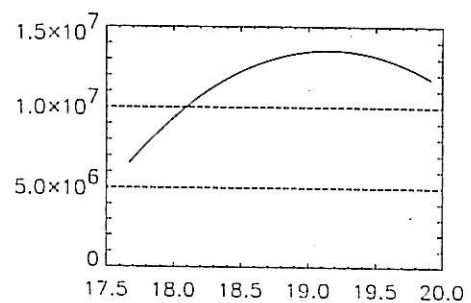
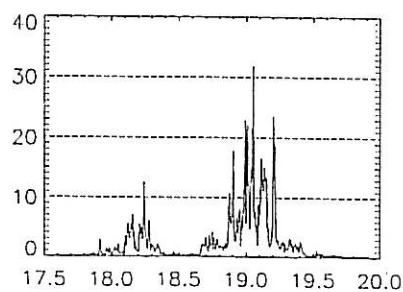
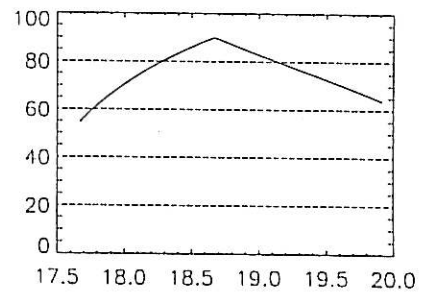
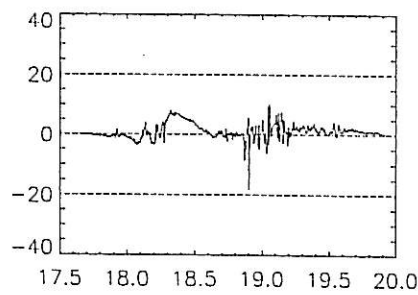
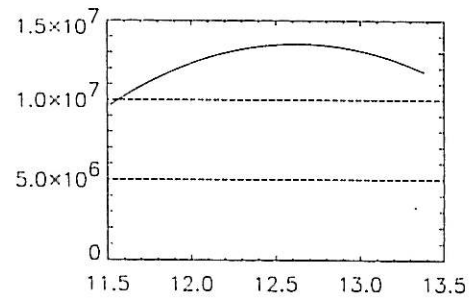
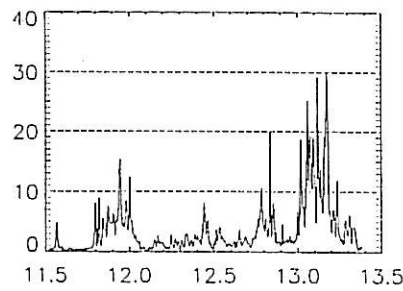
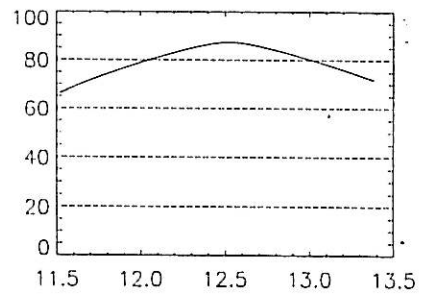
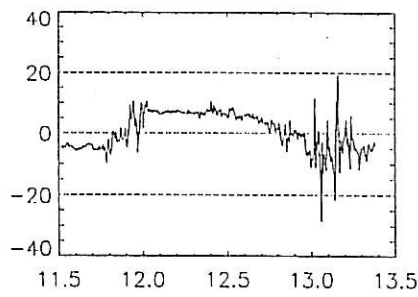
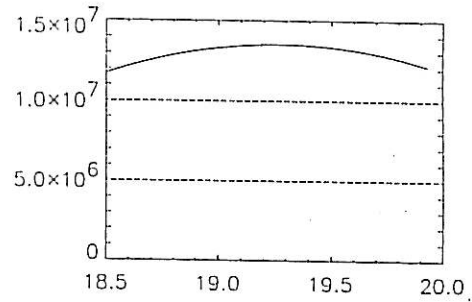
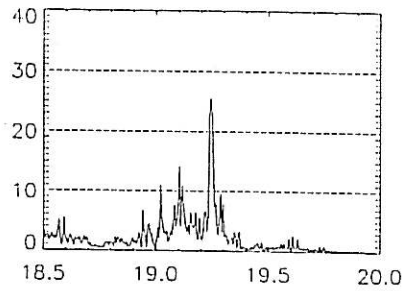
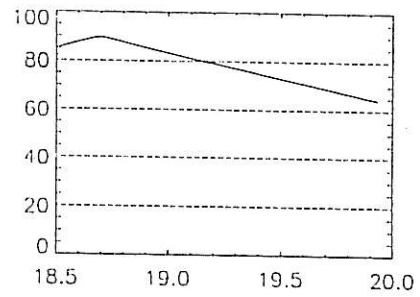
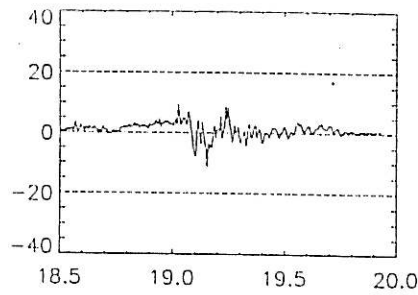
341







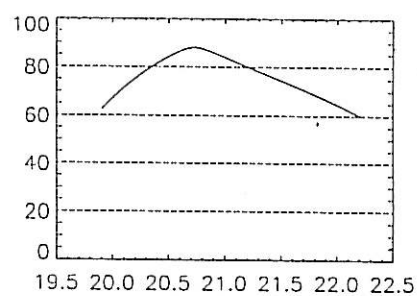
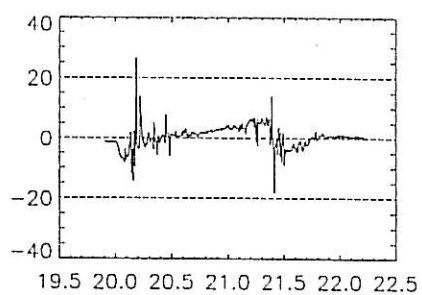
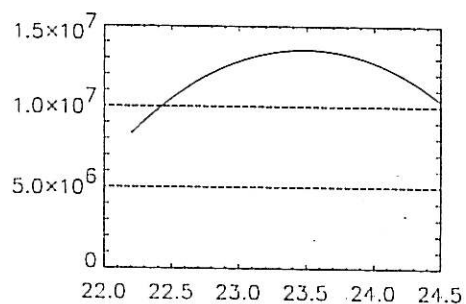
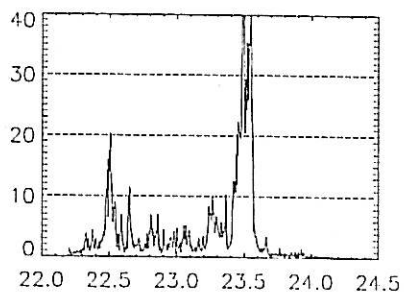
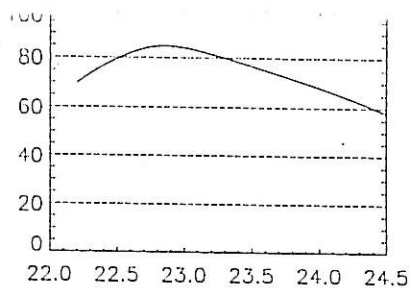
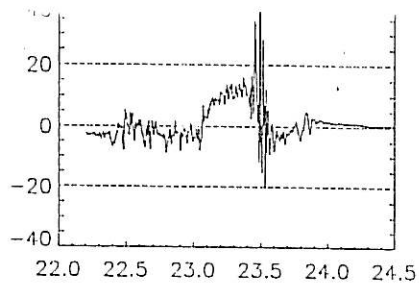




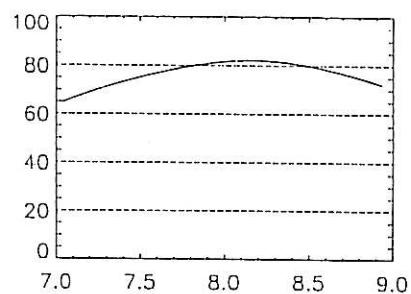
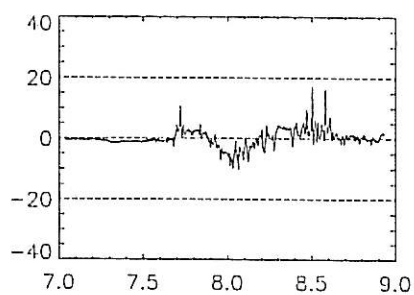
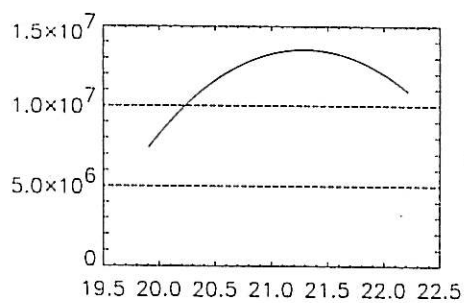
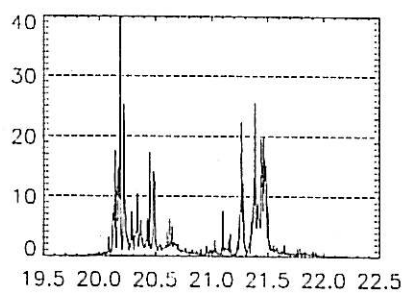




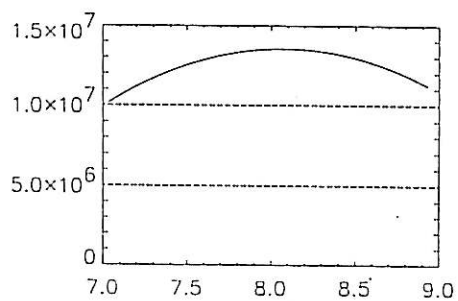
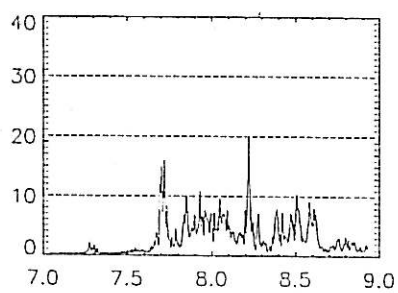
479



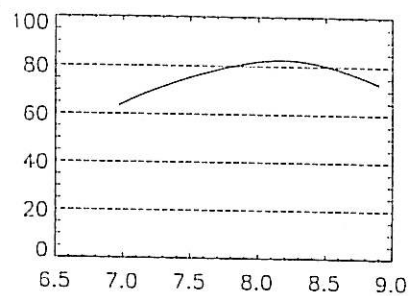
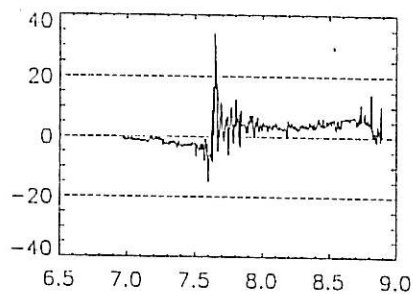
484



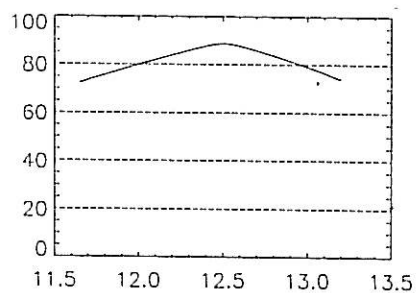
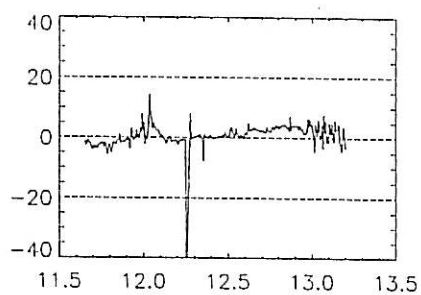
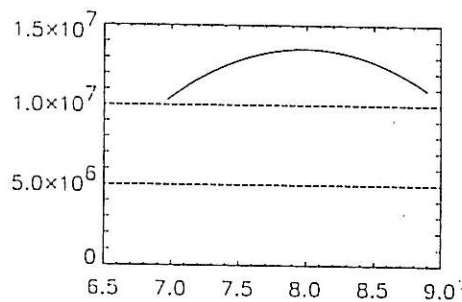
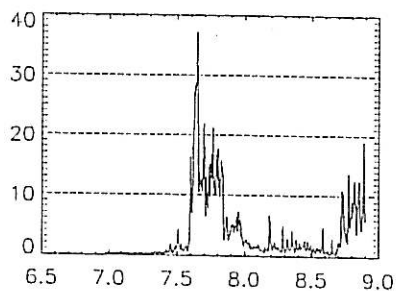
536



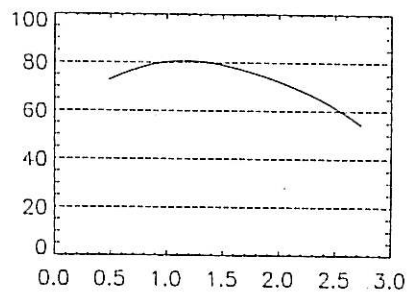
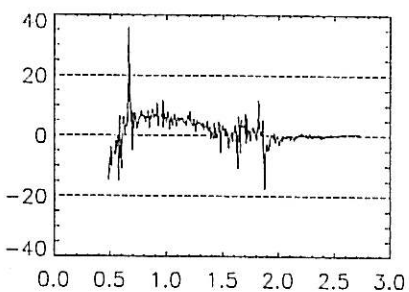
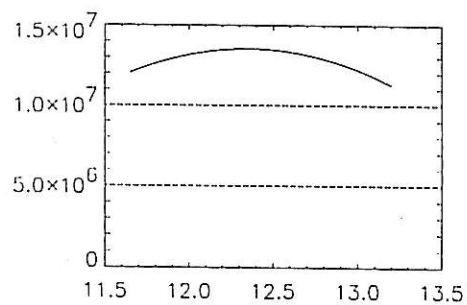
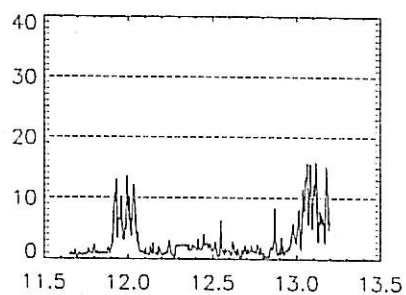




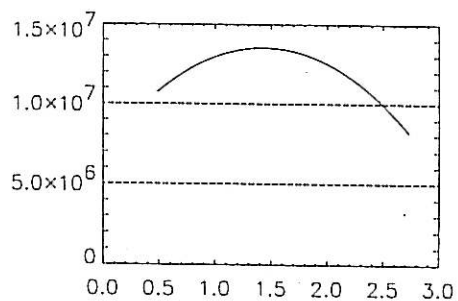
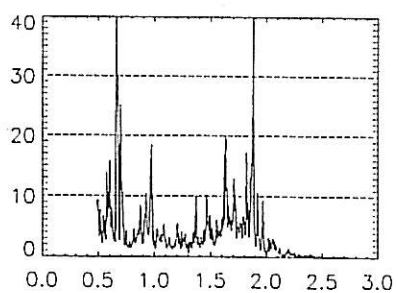
569



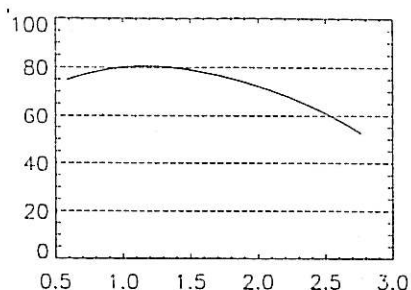
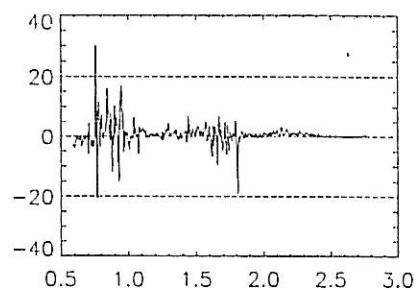
570



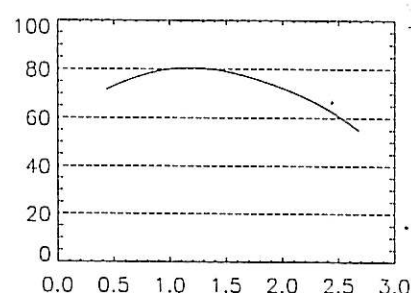
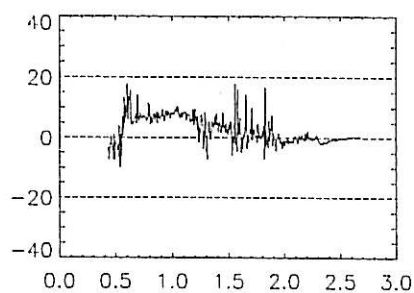
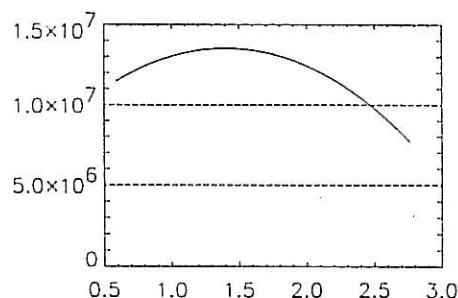
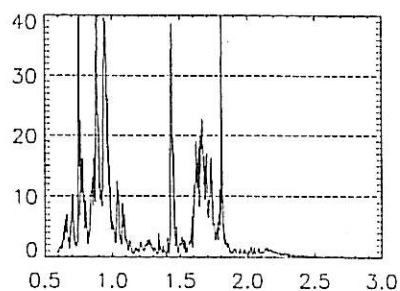
573



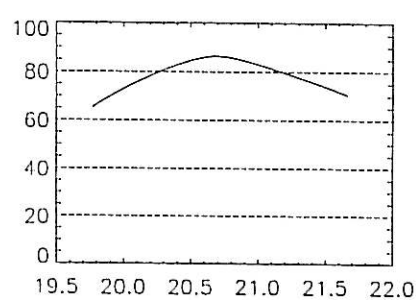
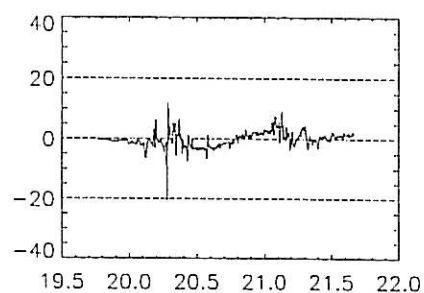
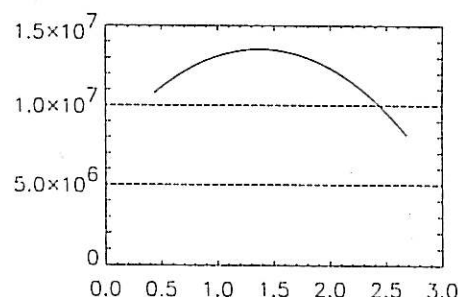
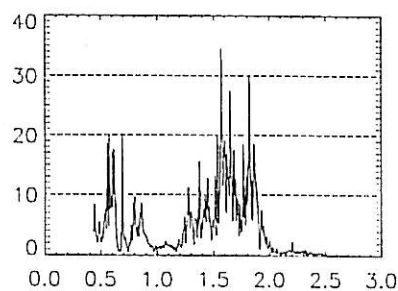




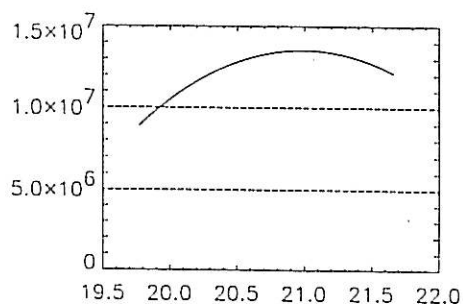
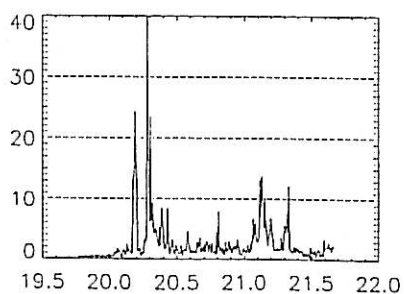
584



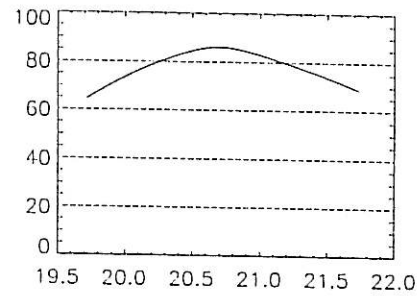
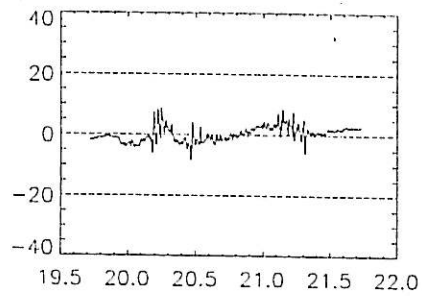
585



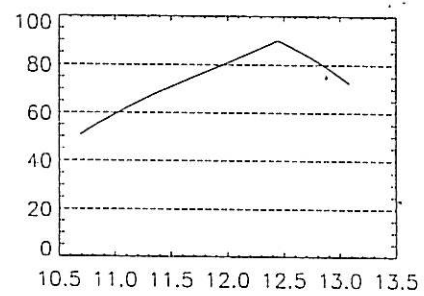
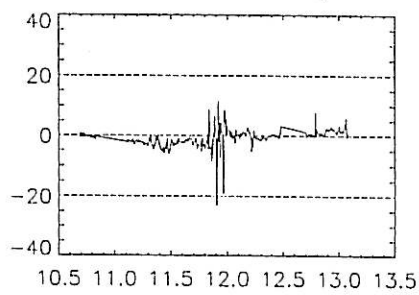
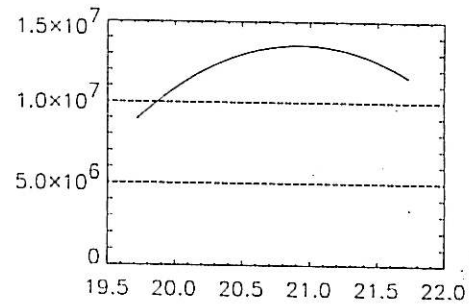
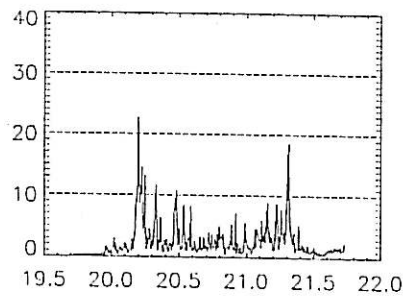
605



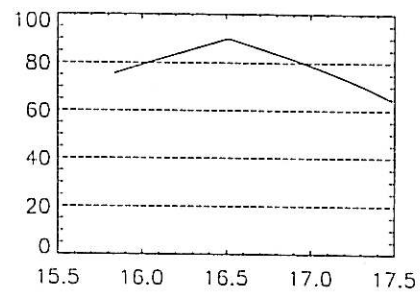
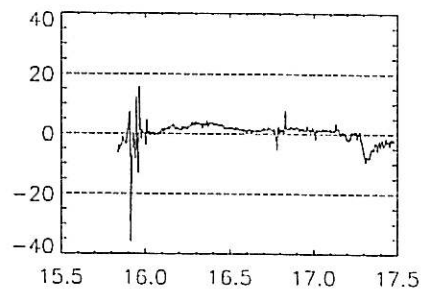
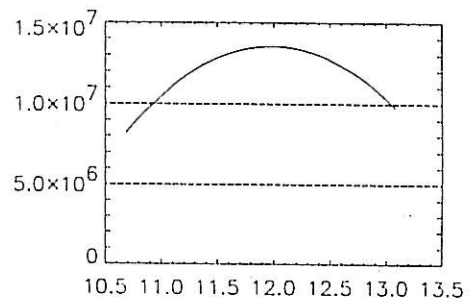
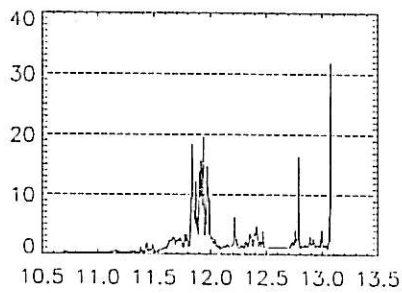




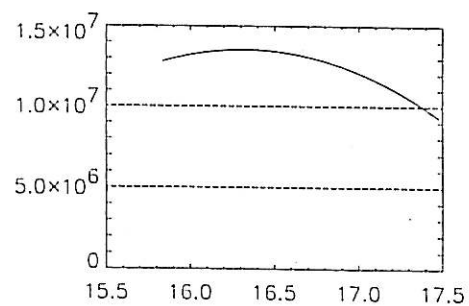
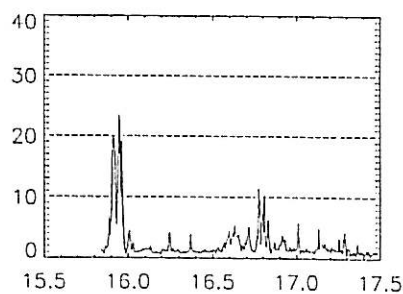
627



713



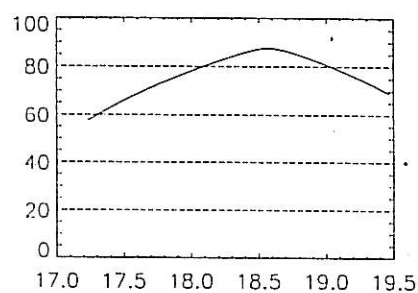
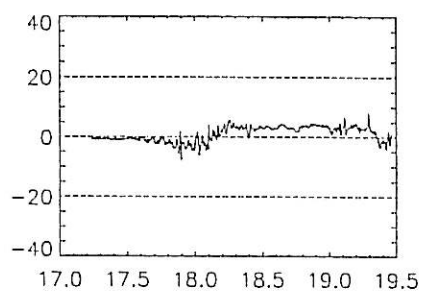
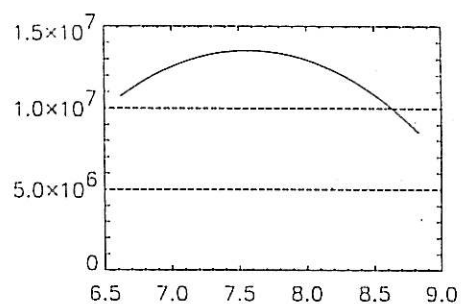
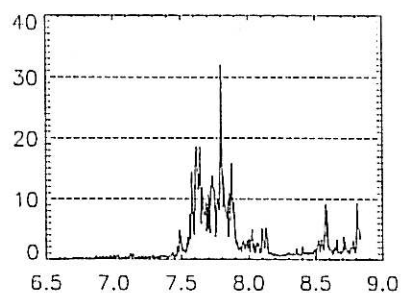
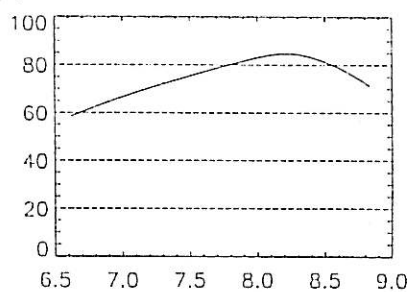
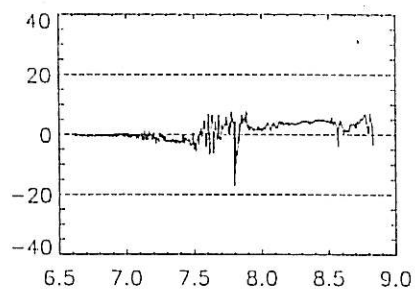
725



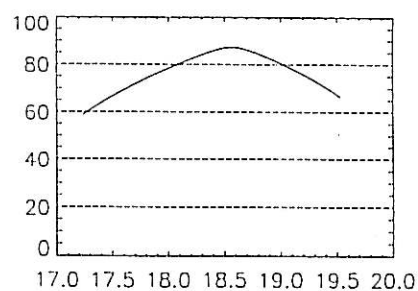
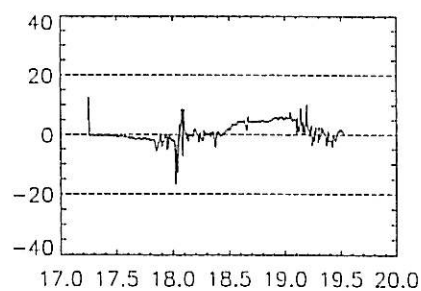
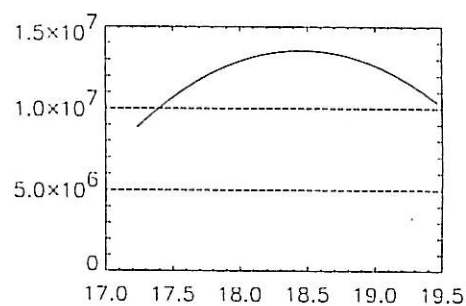
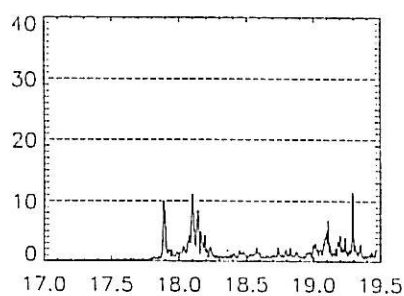




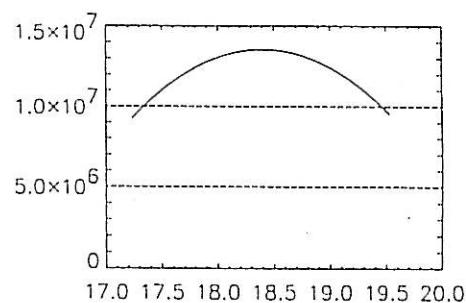
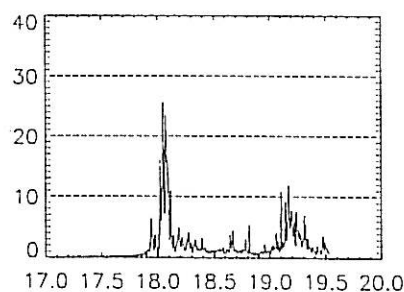
734



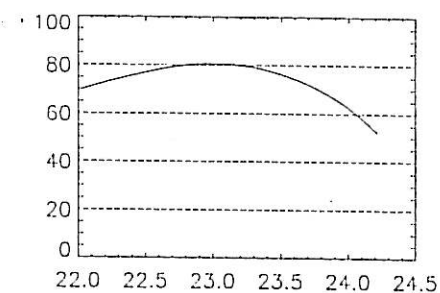
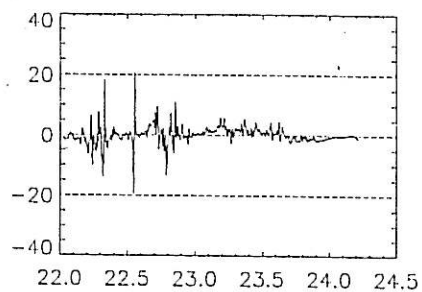
742



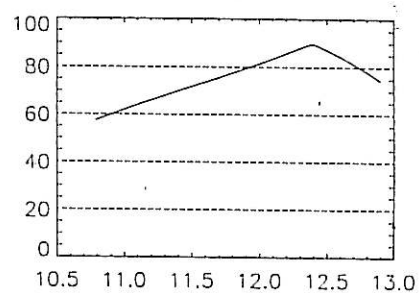
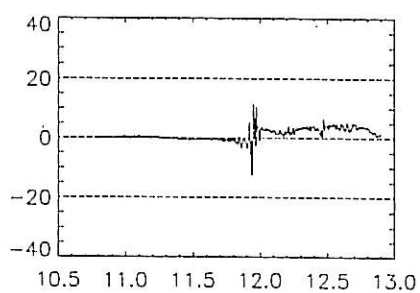
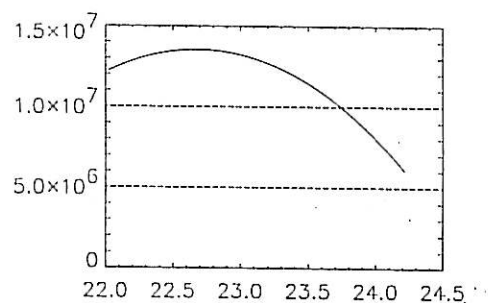
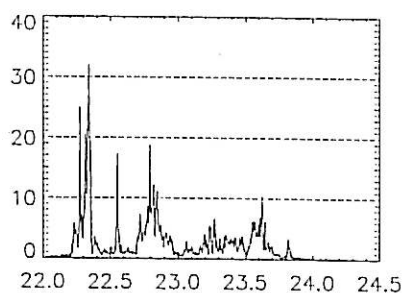
764



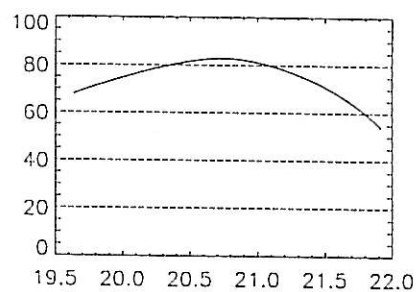
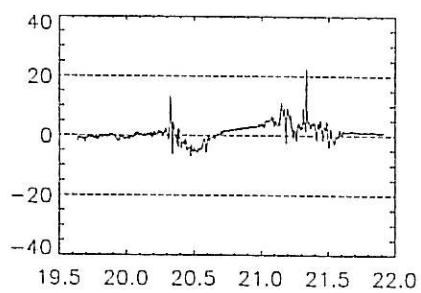
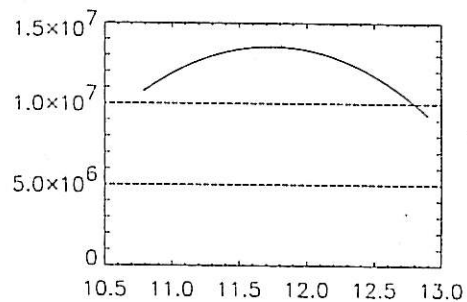
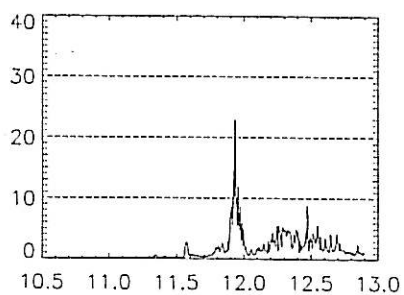




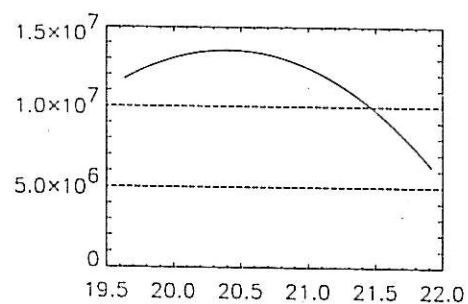
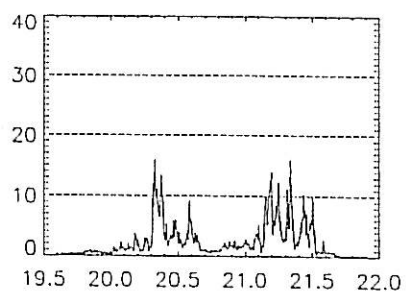
798



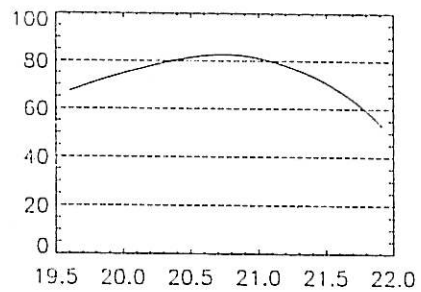
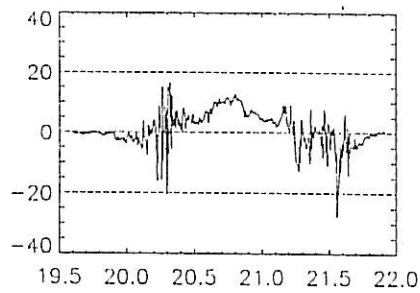
812



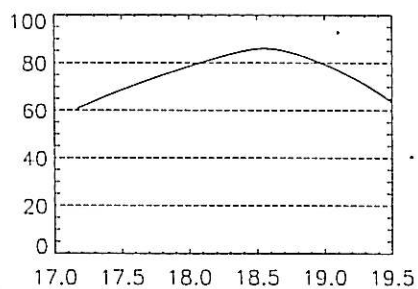
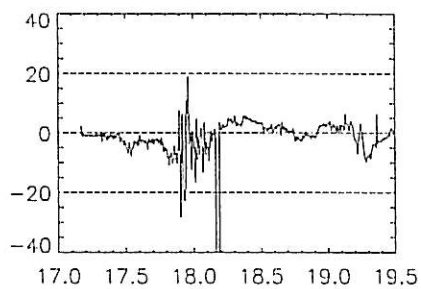
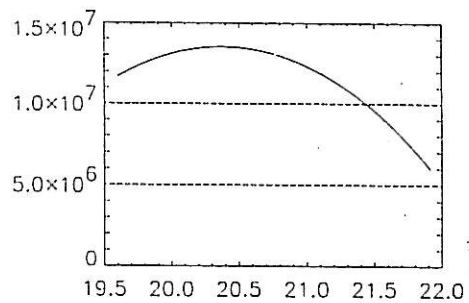
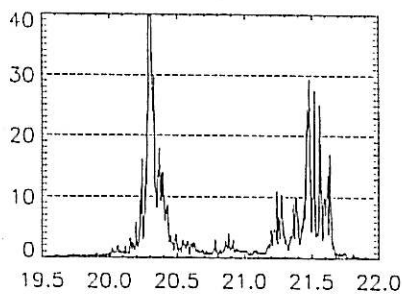
836



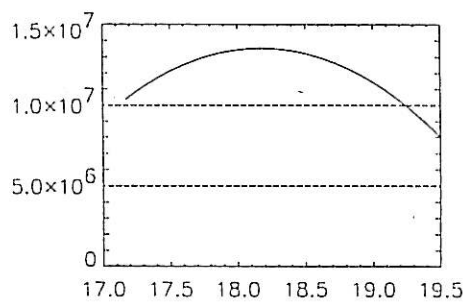
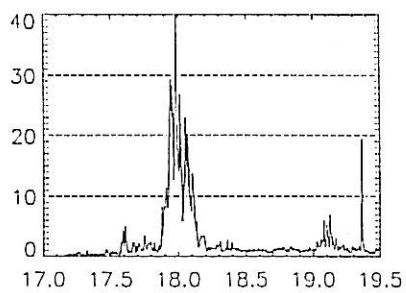




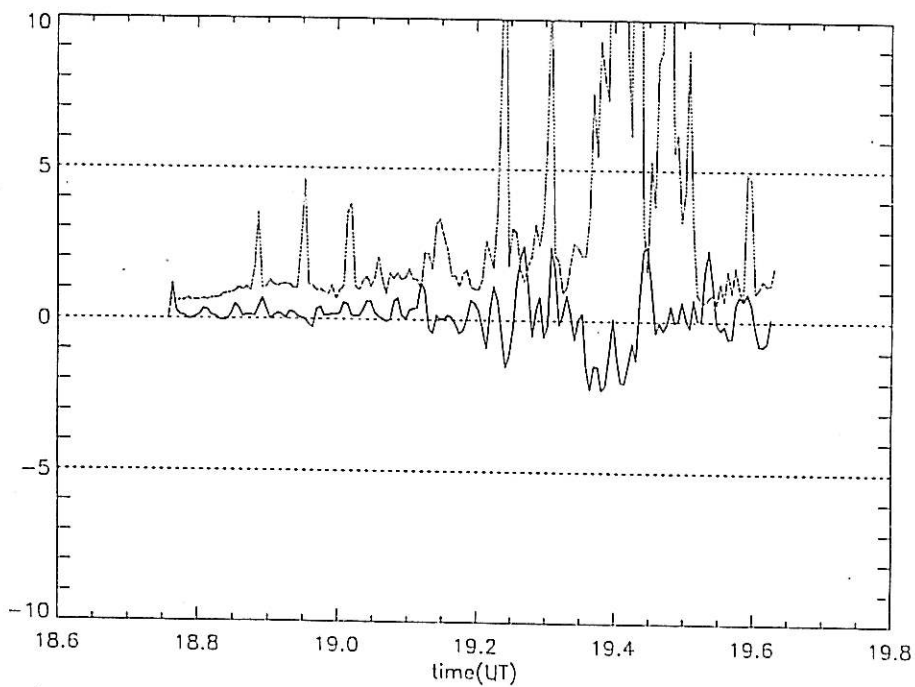
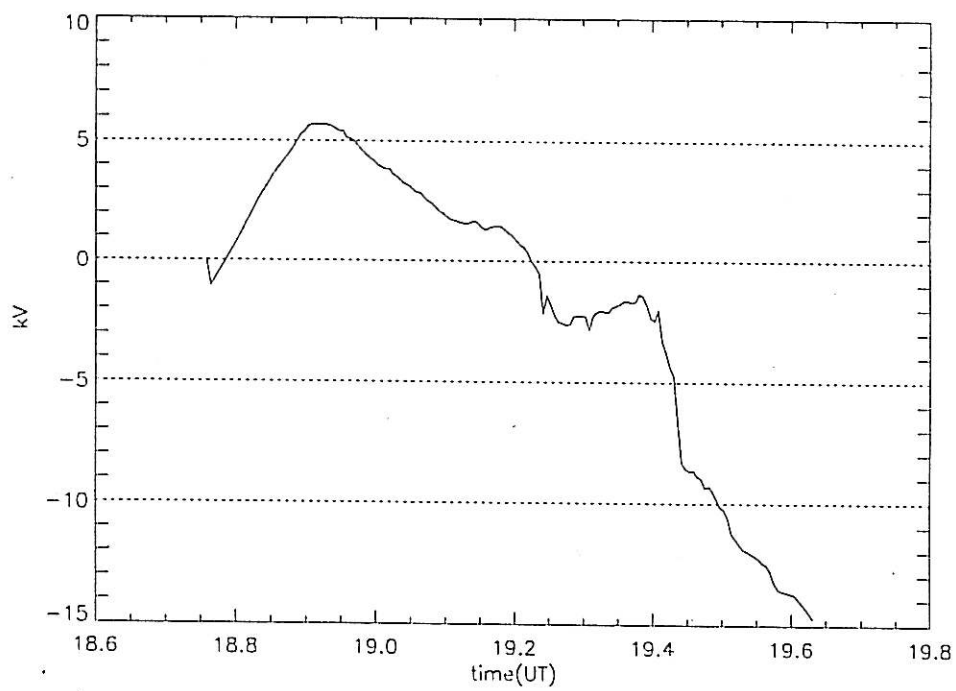
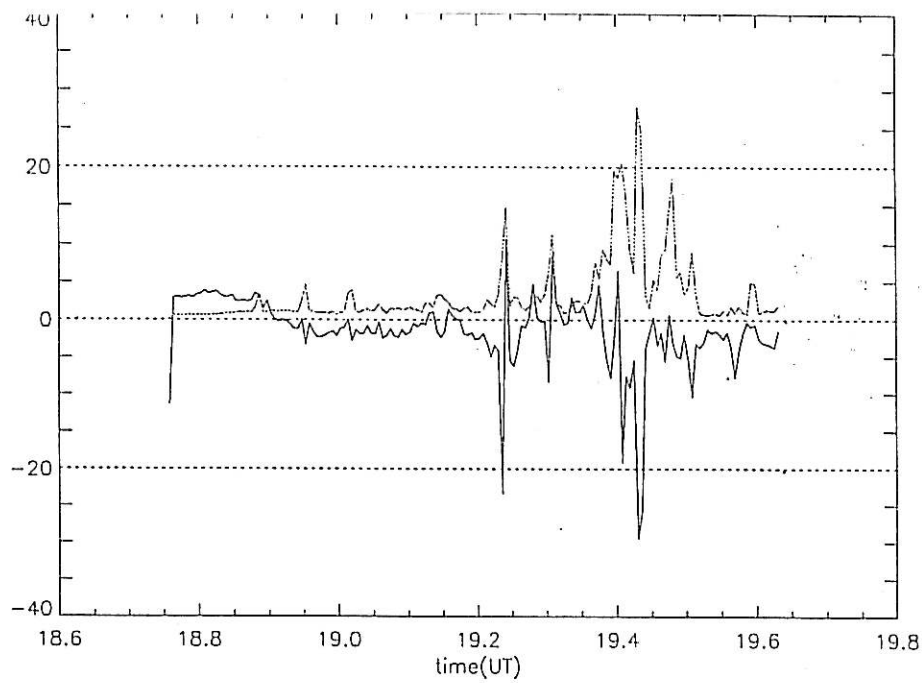
847



852

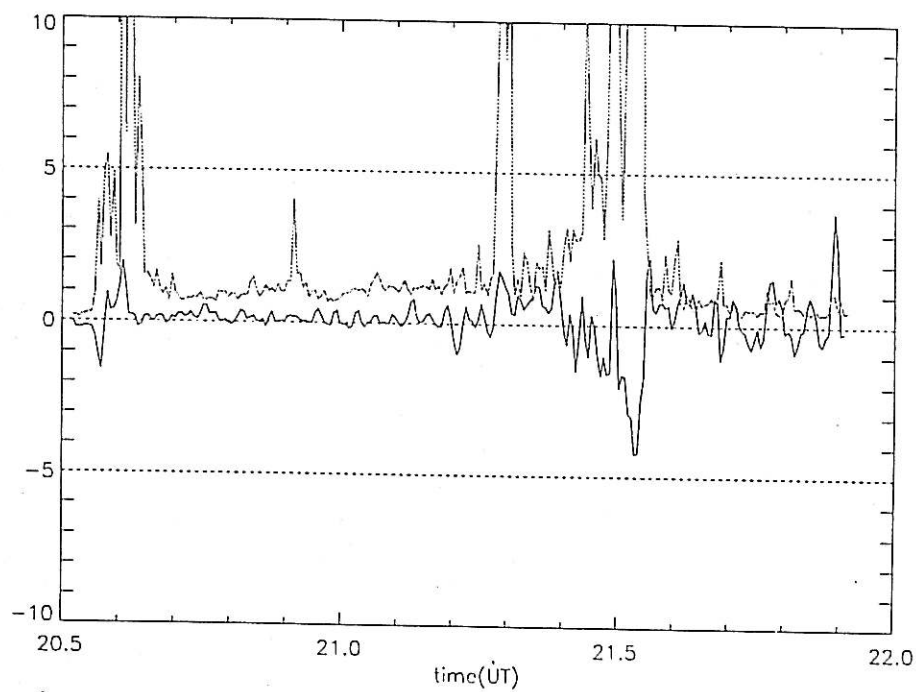
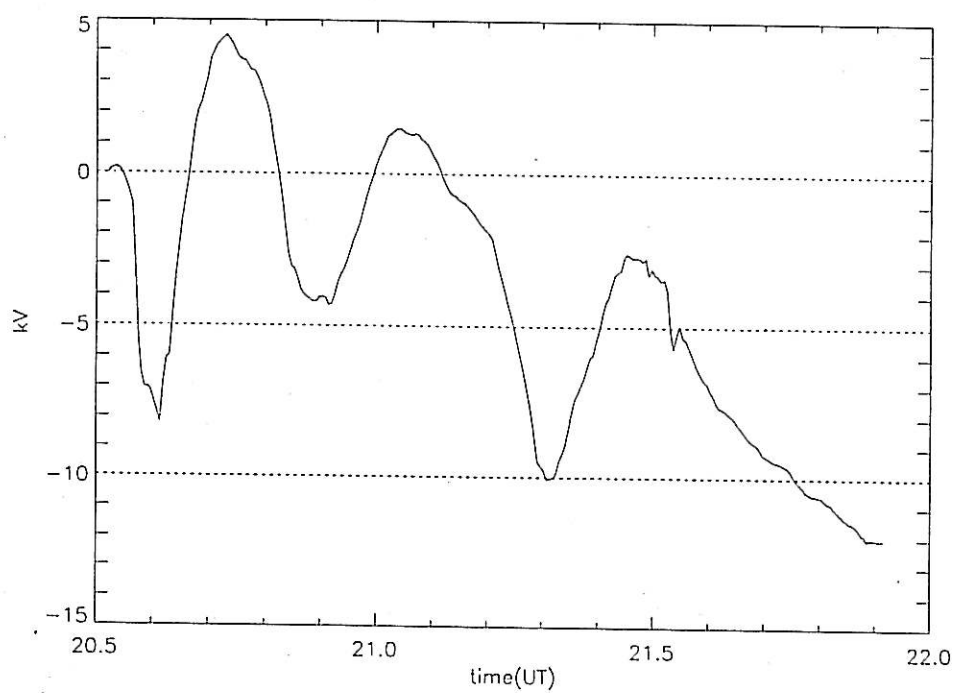
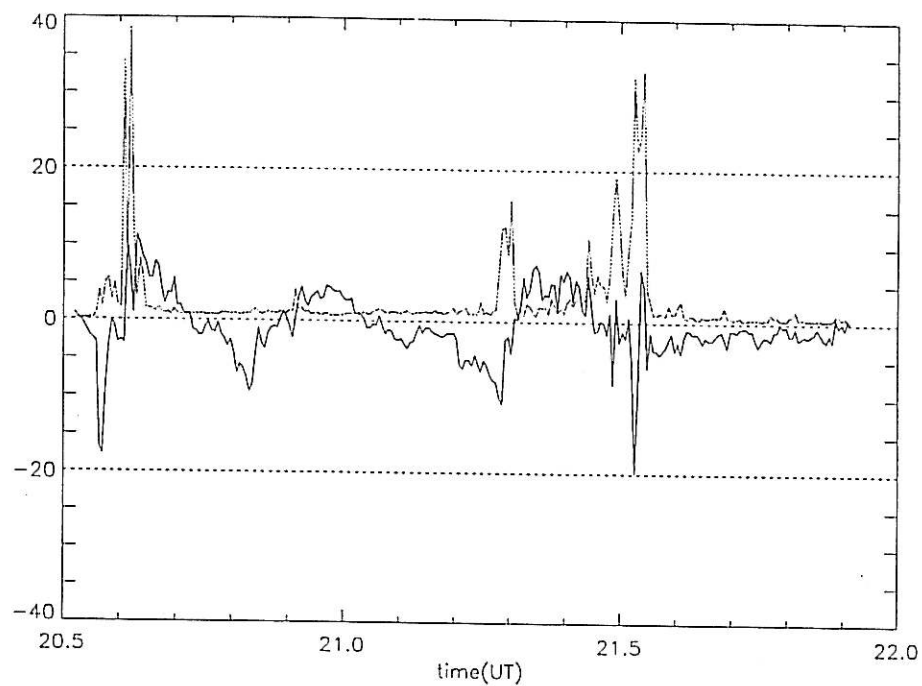




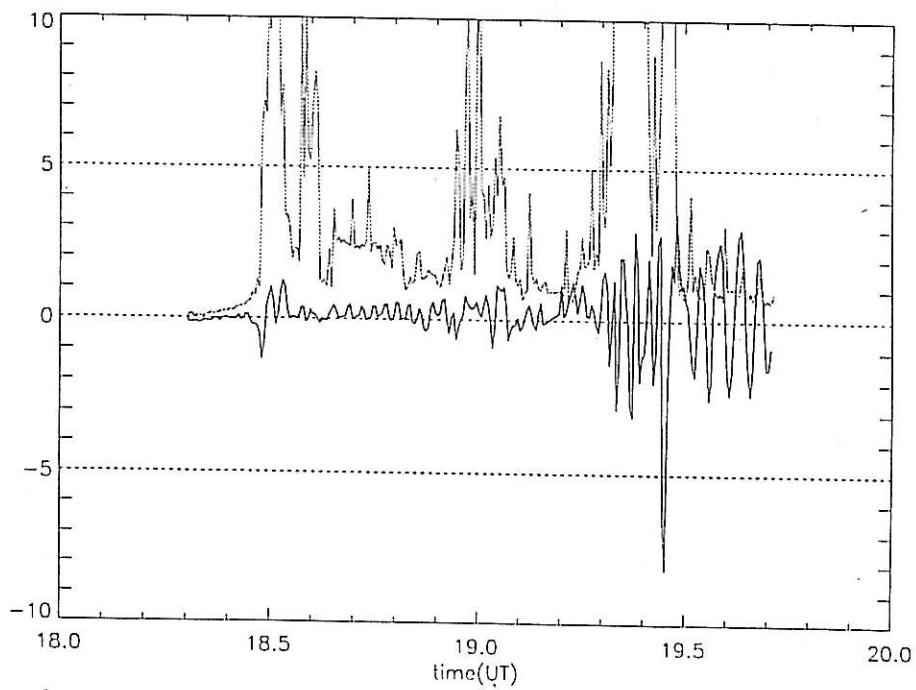
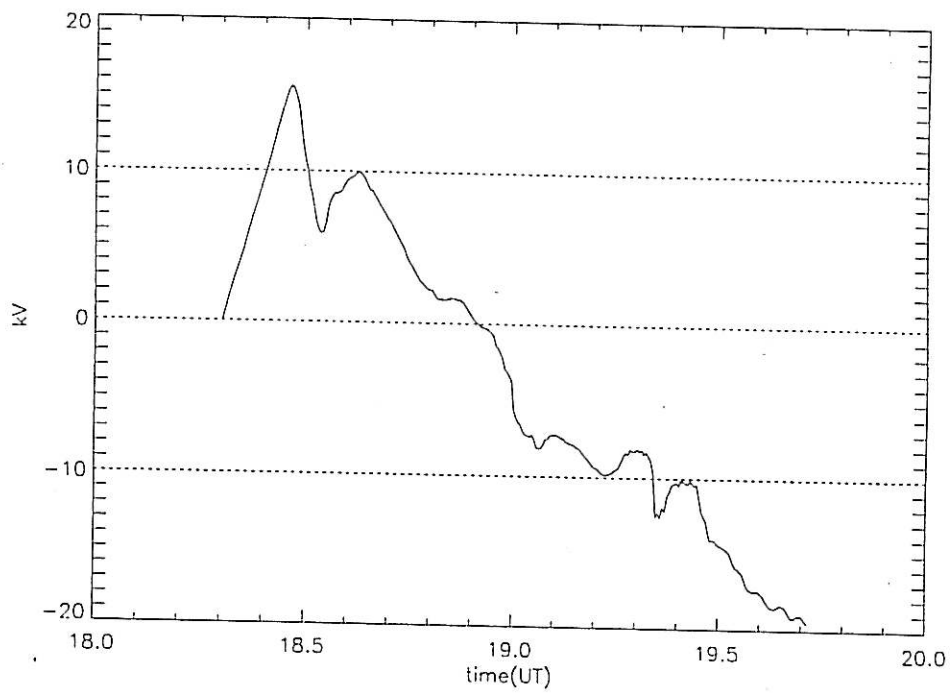
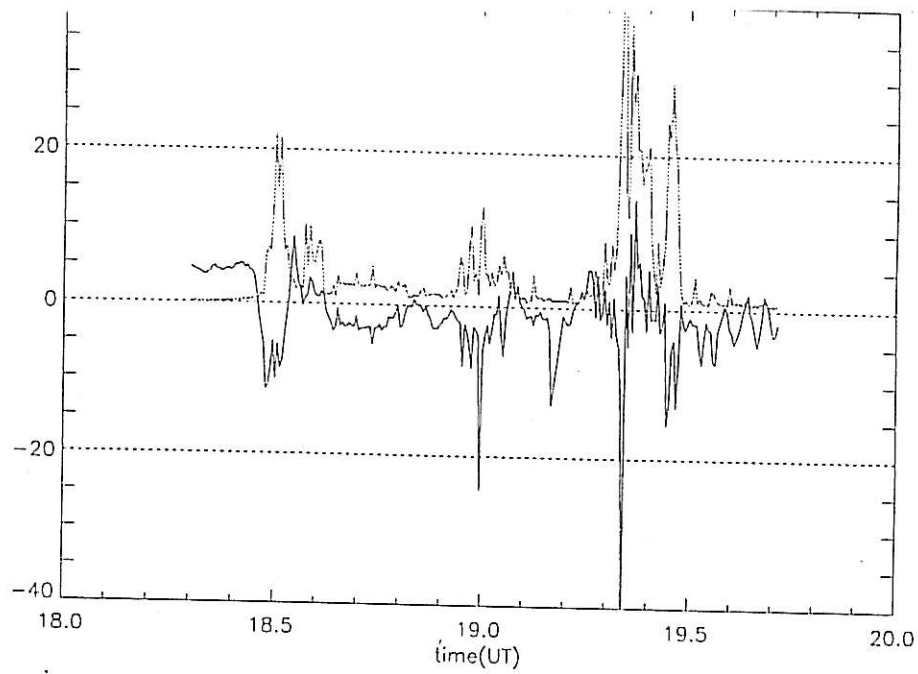




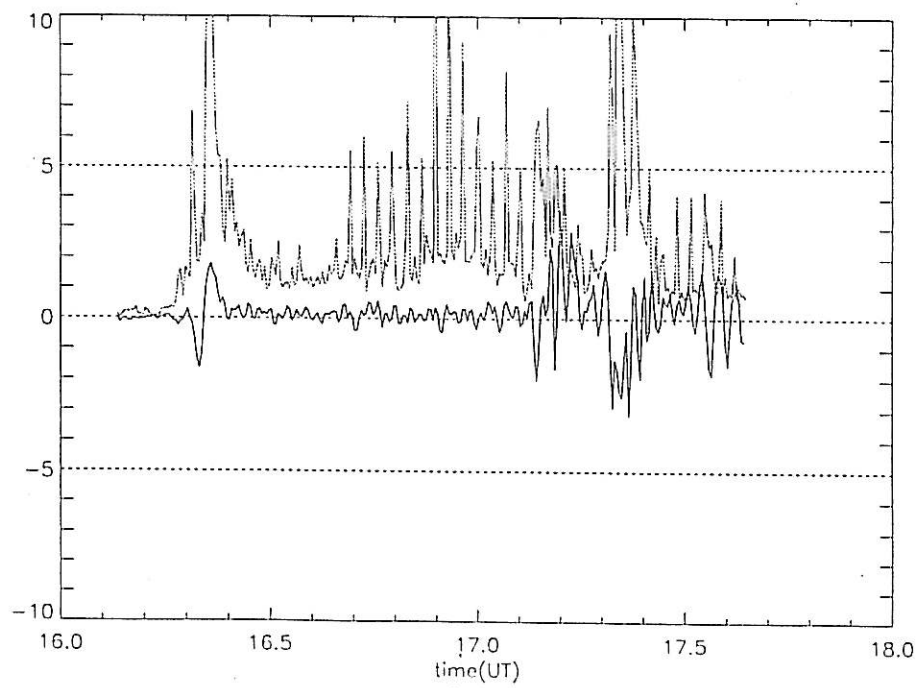
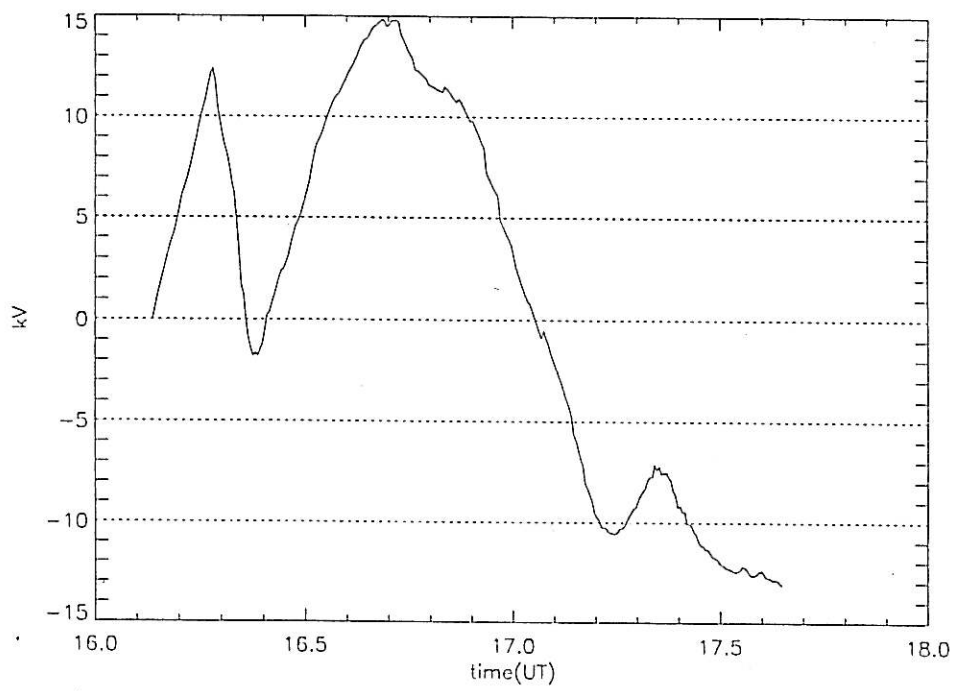
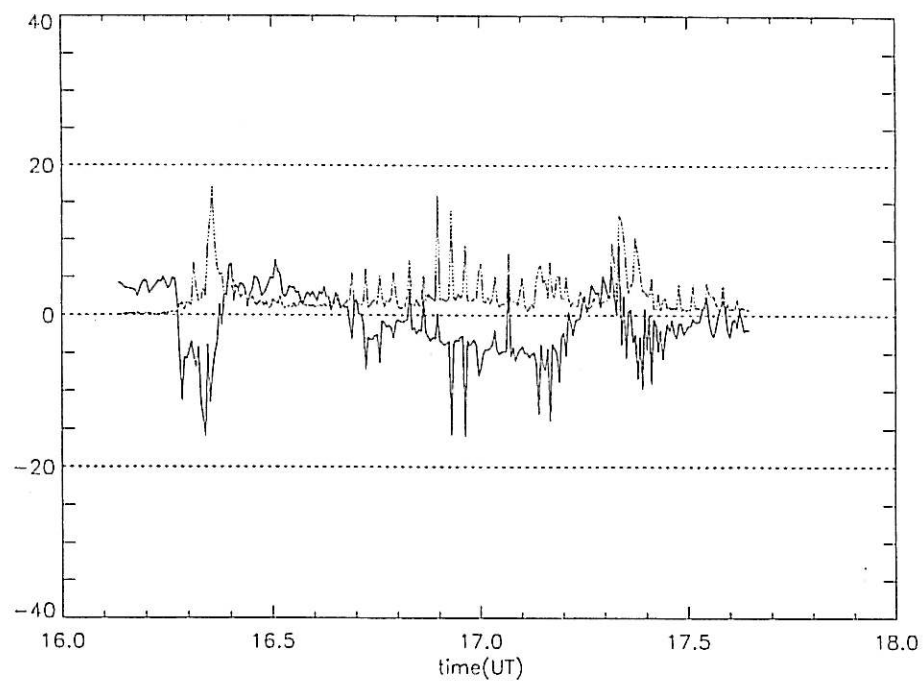




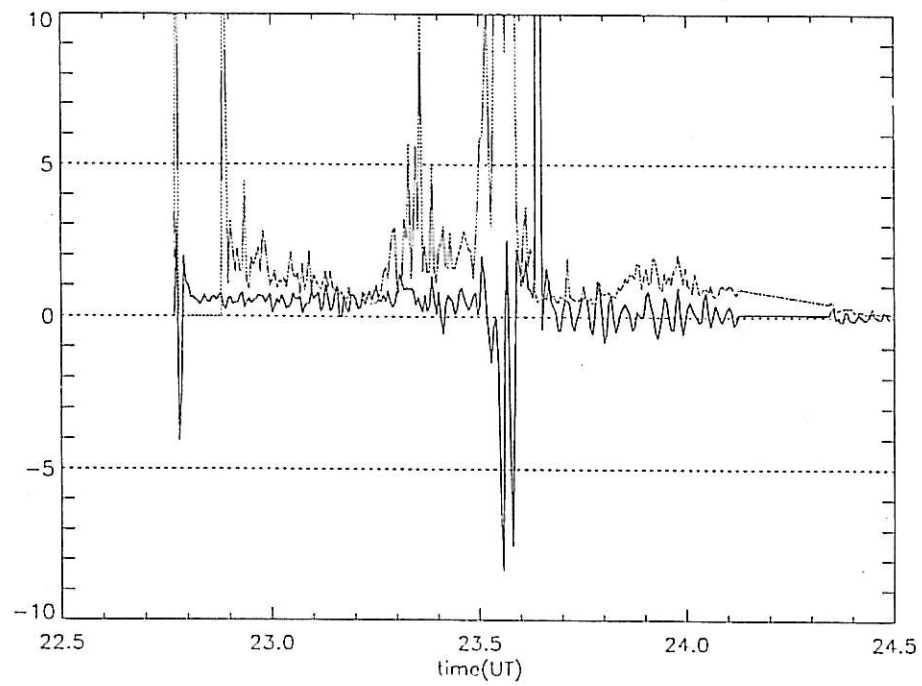
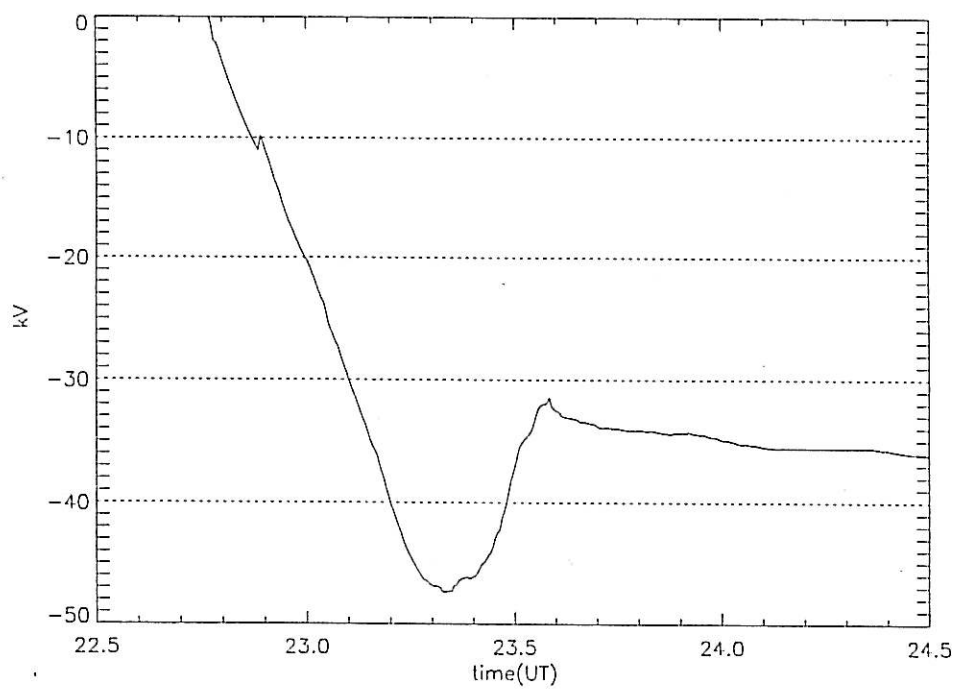
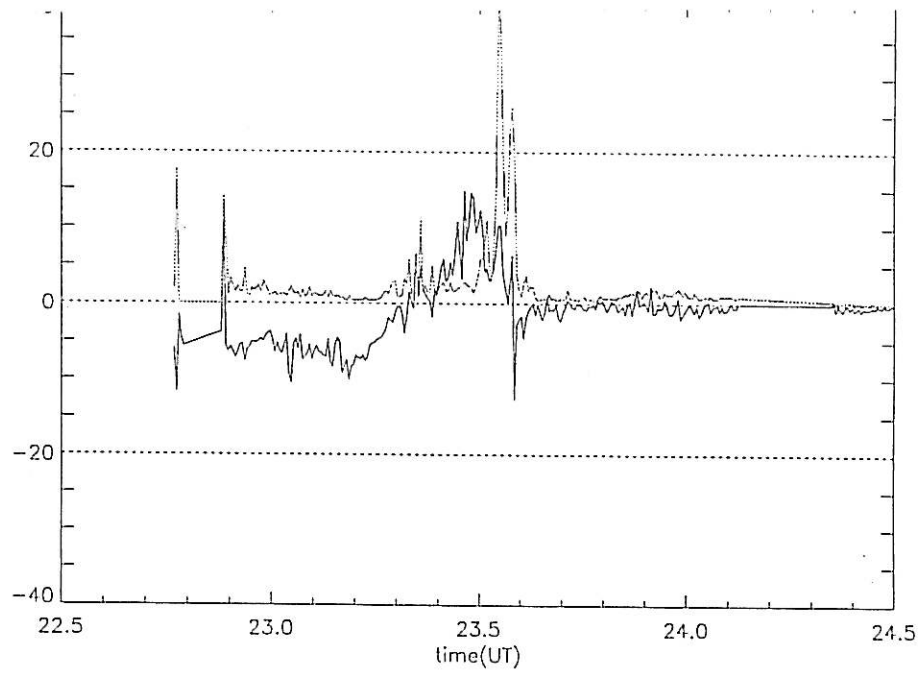






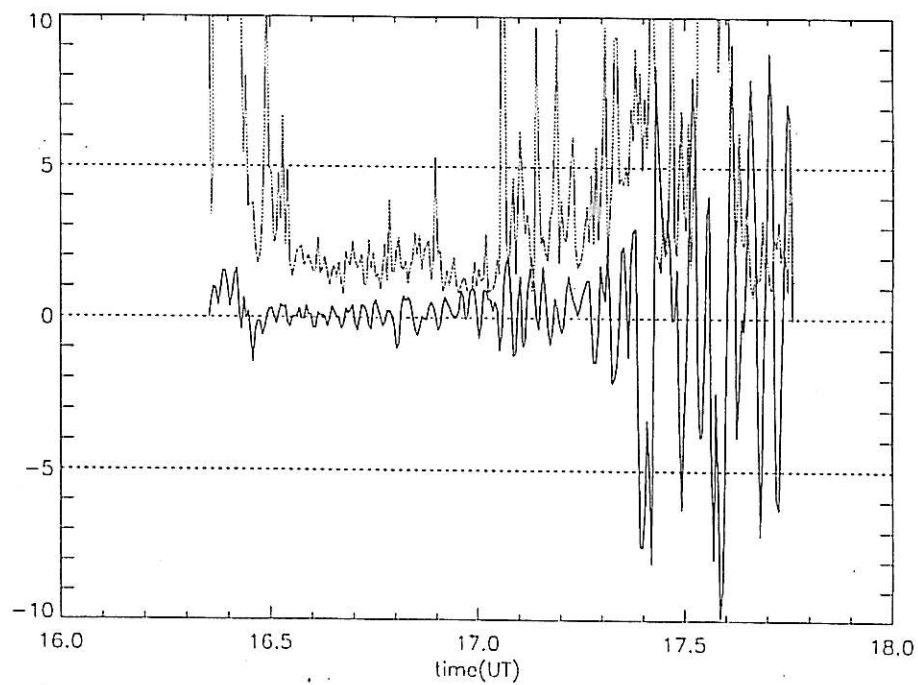
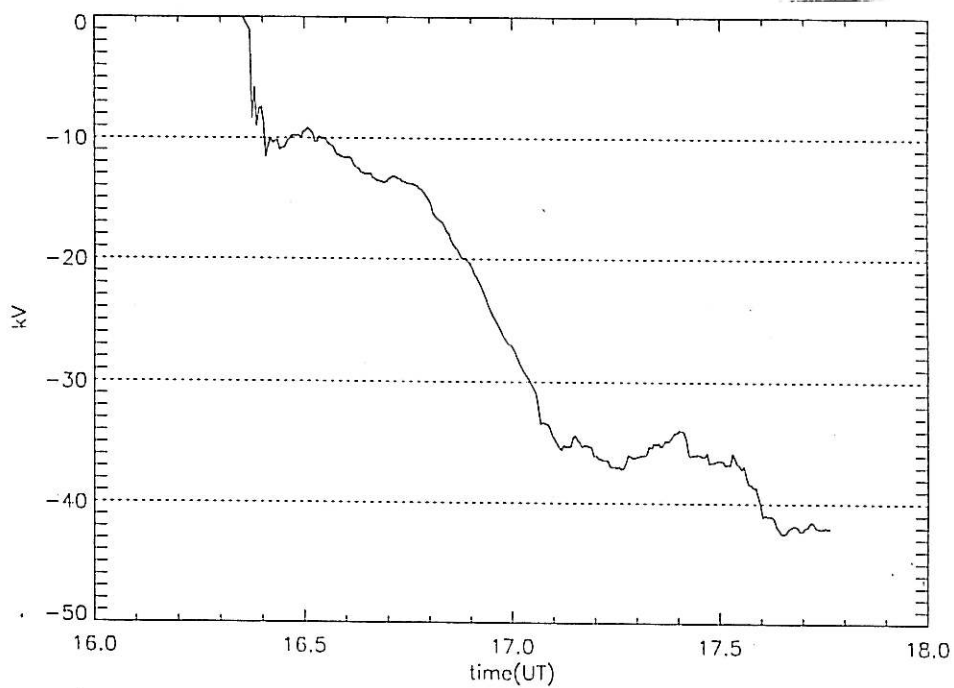
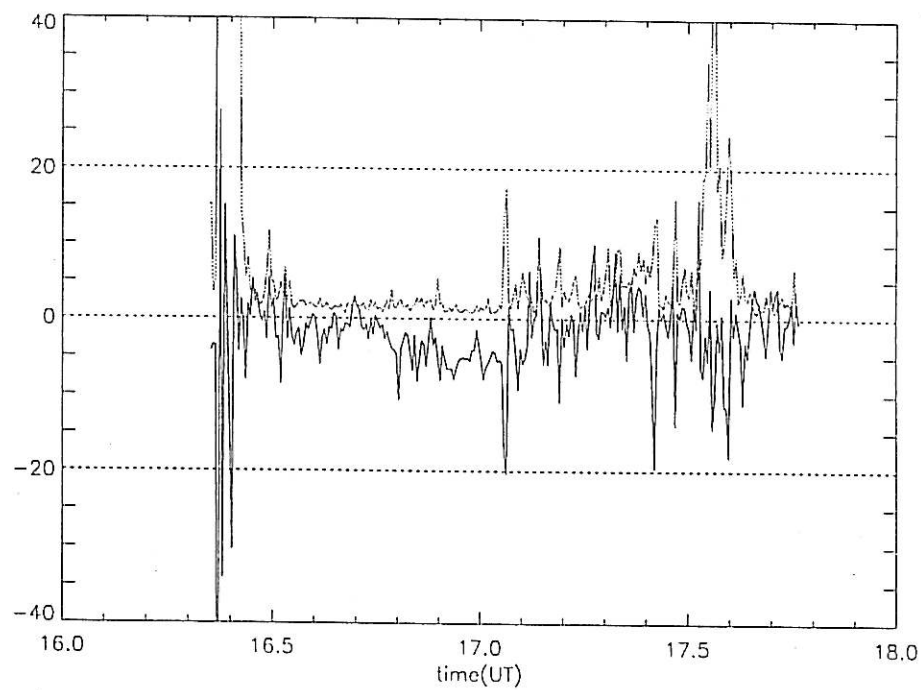




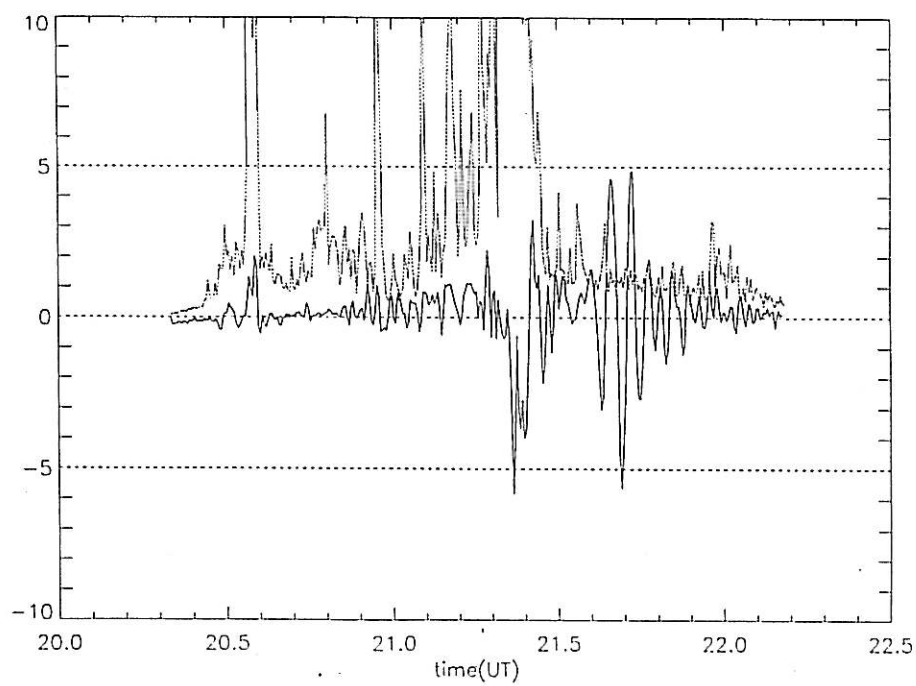
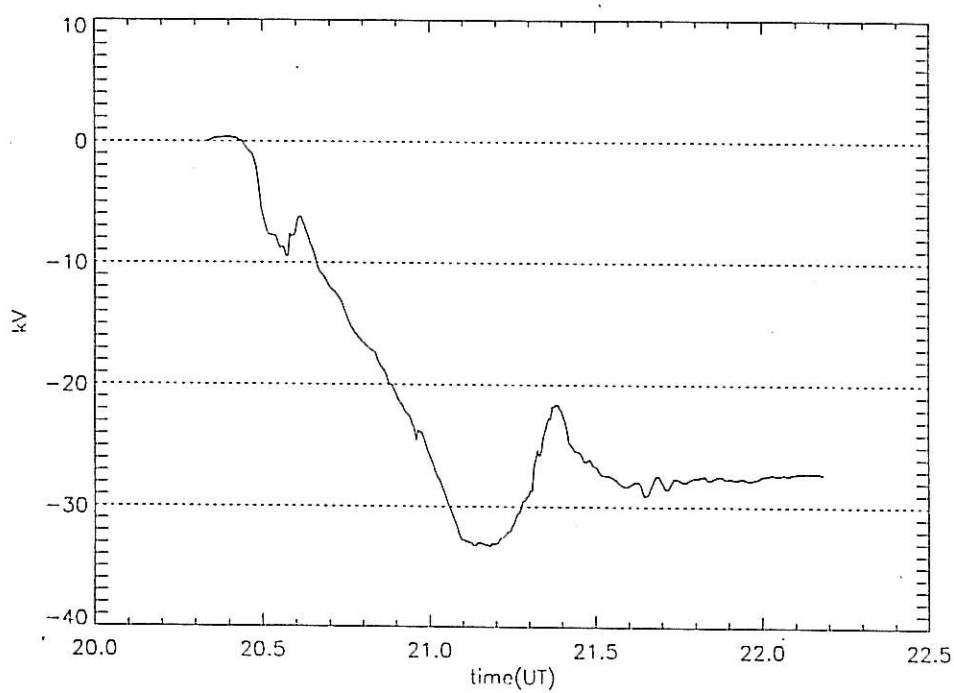
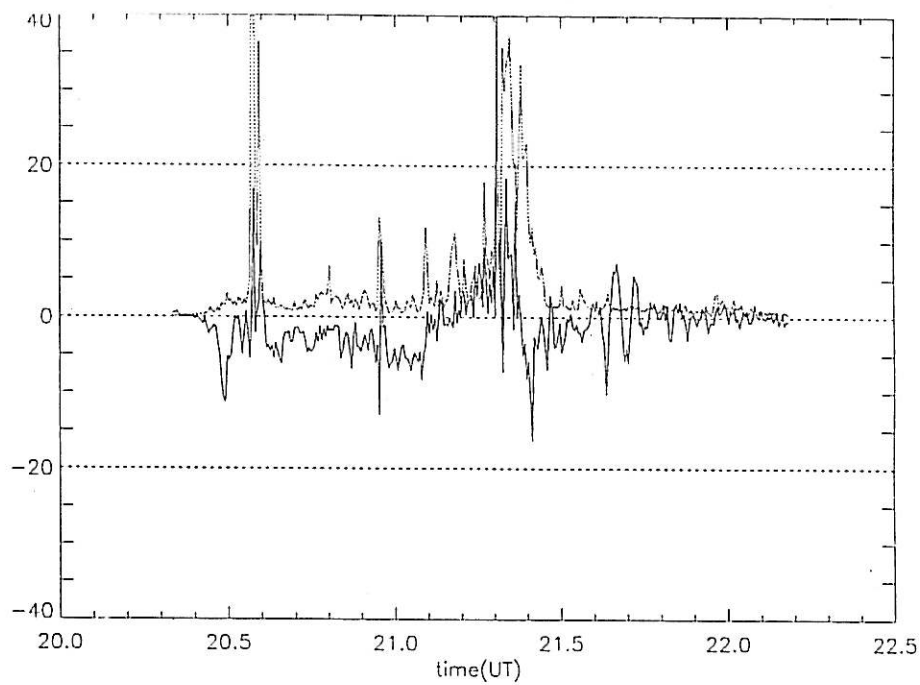




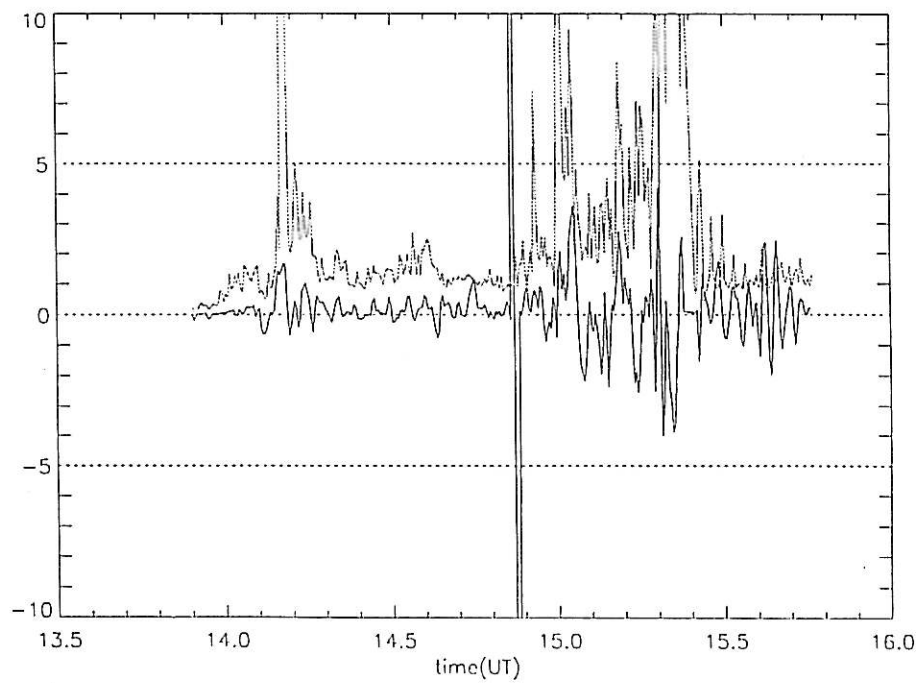
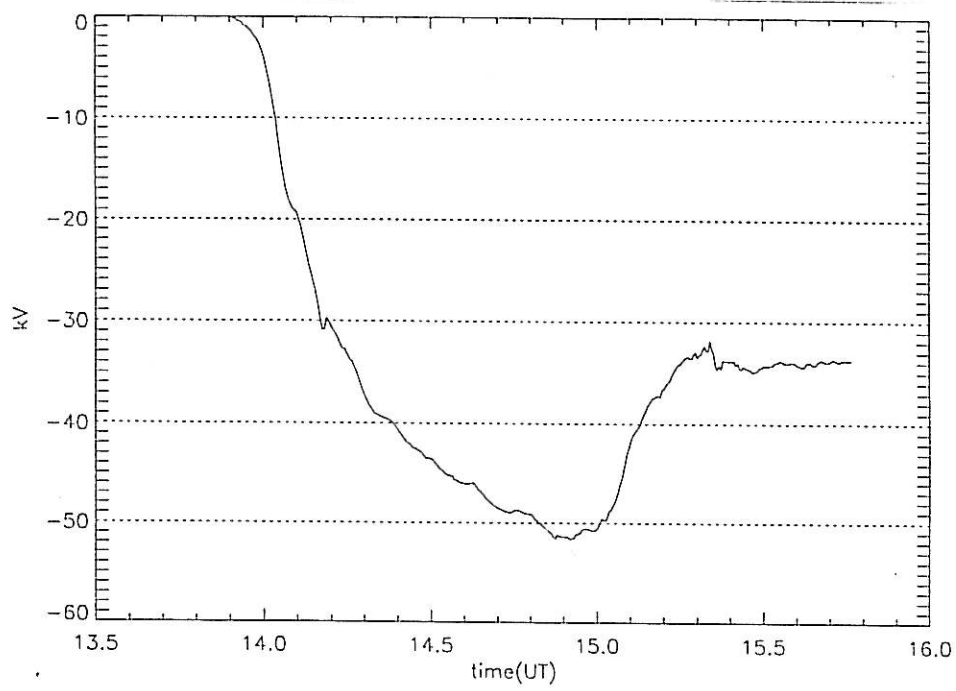
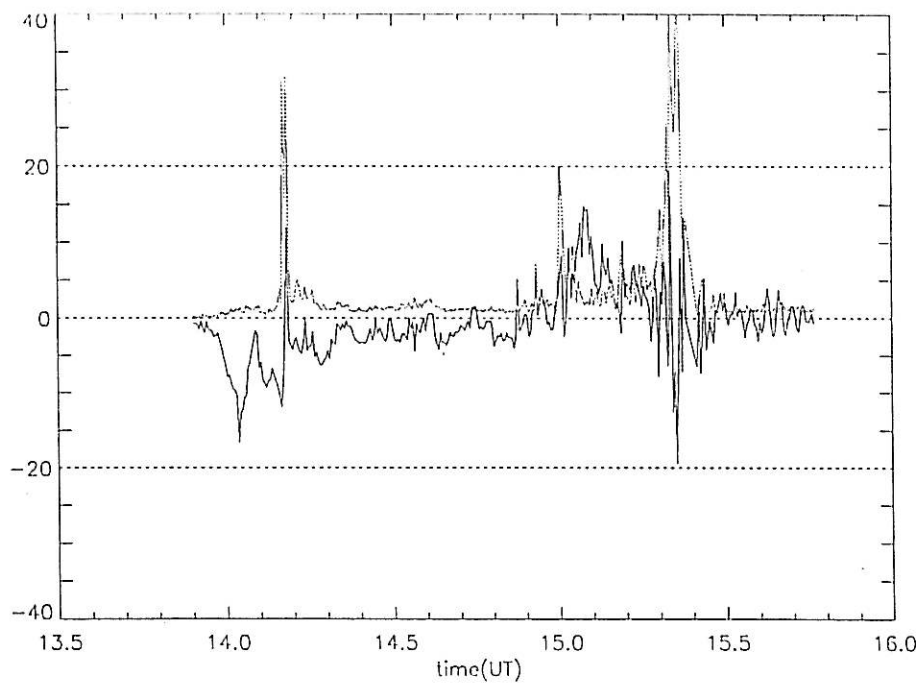




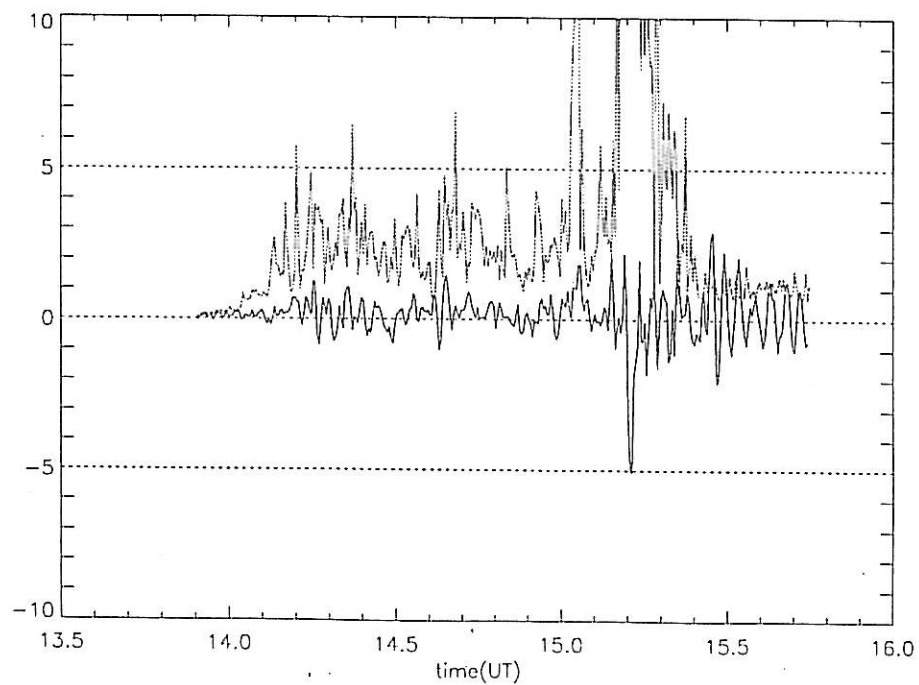
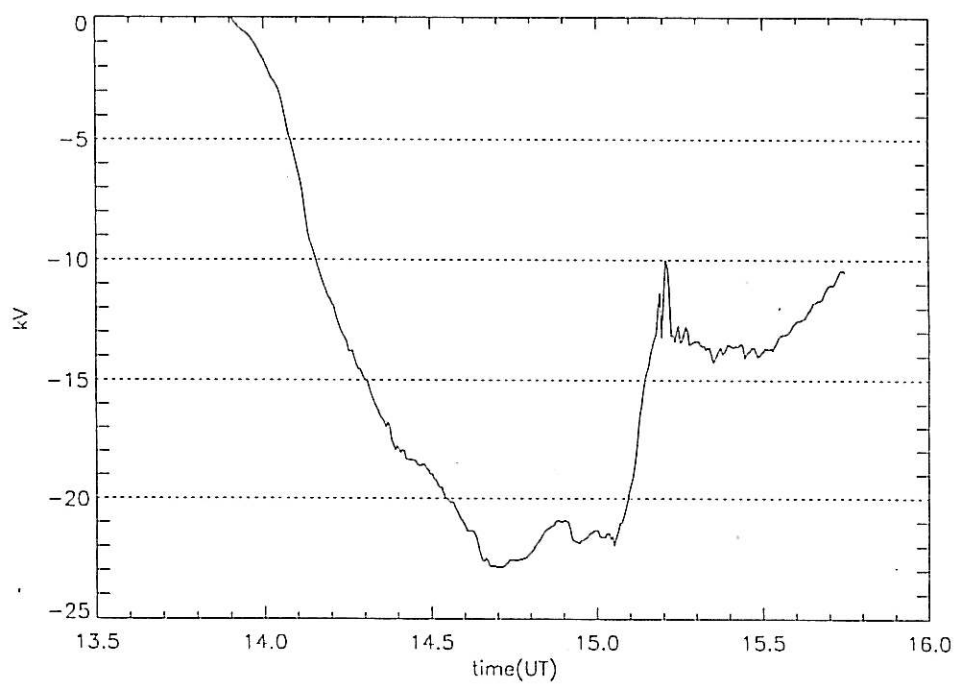
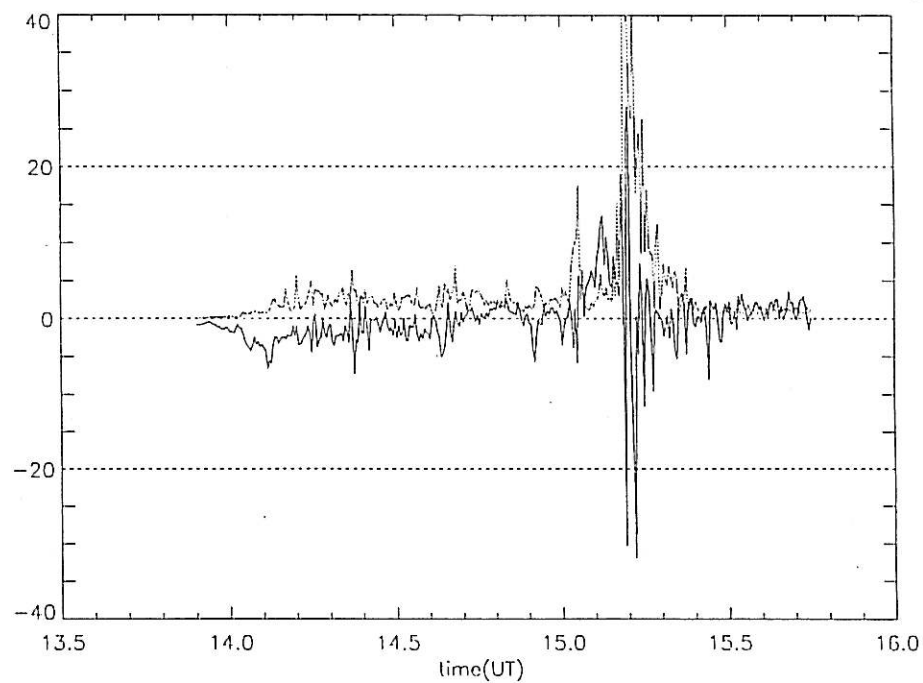






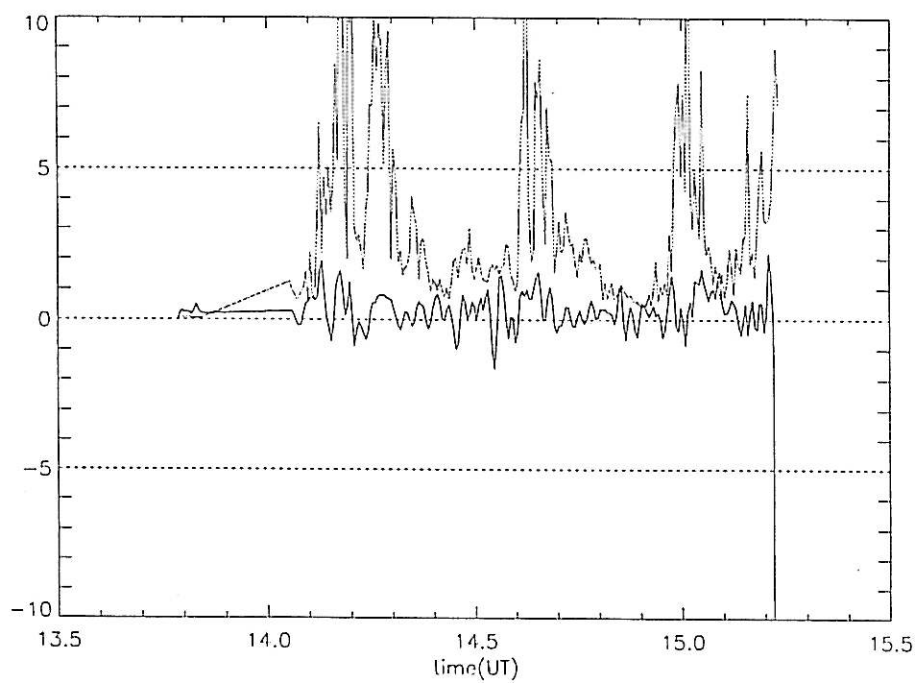
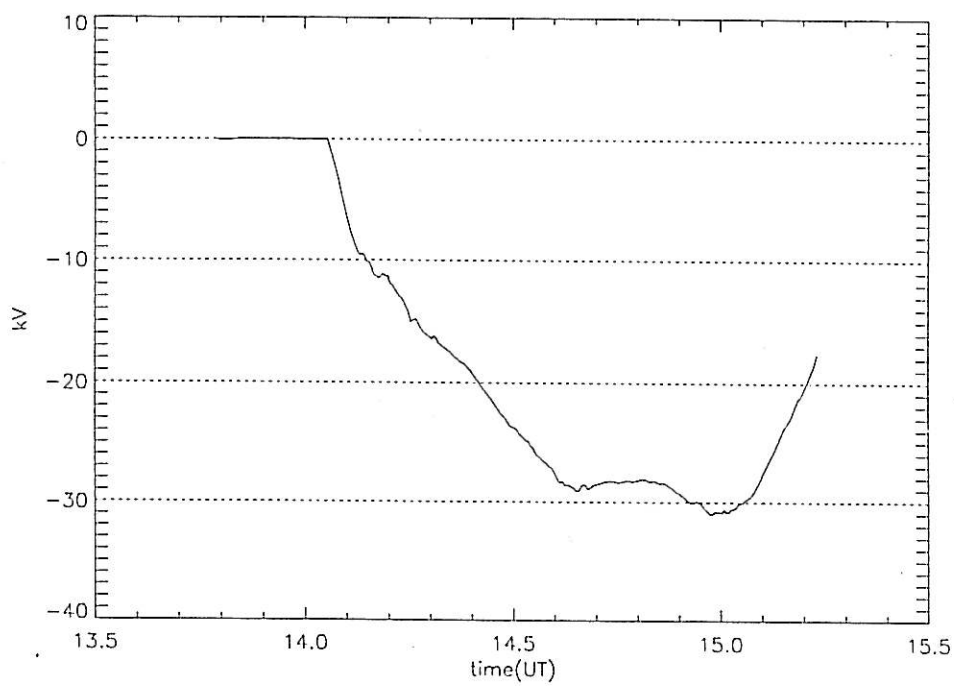
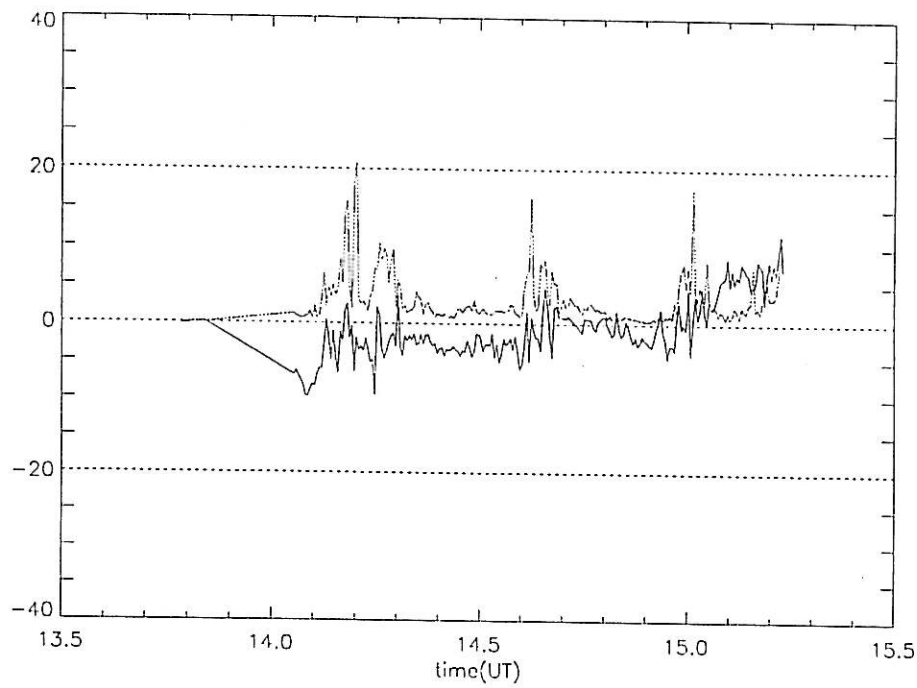




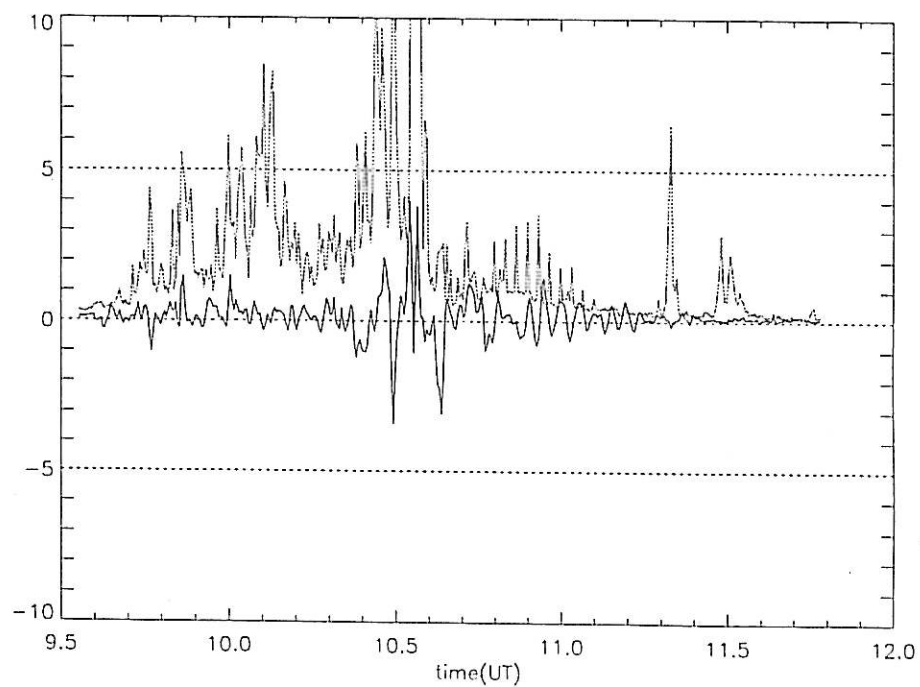
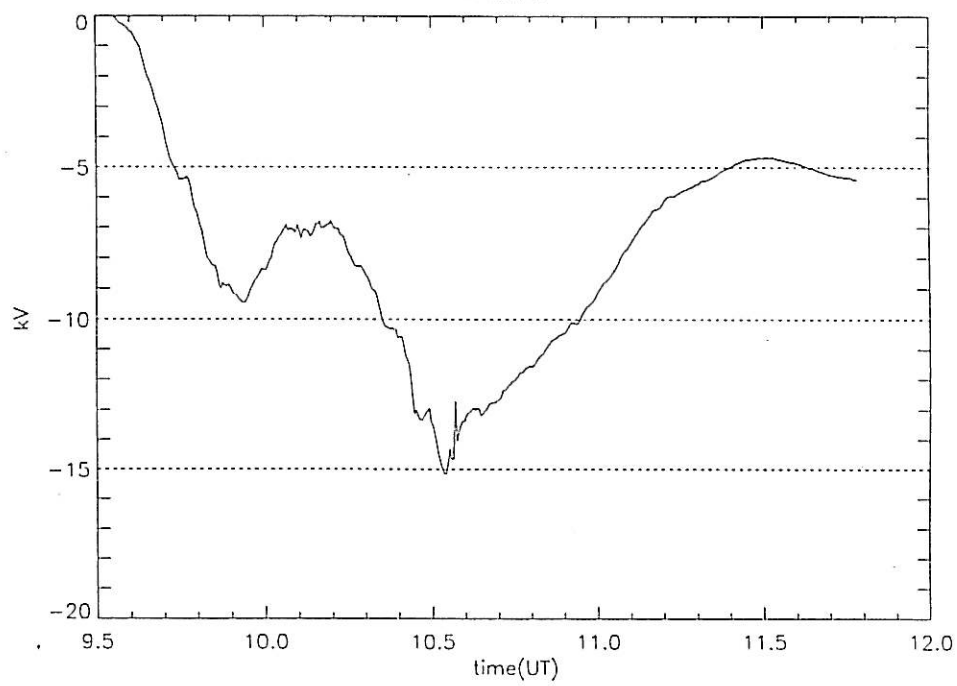
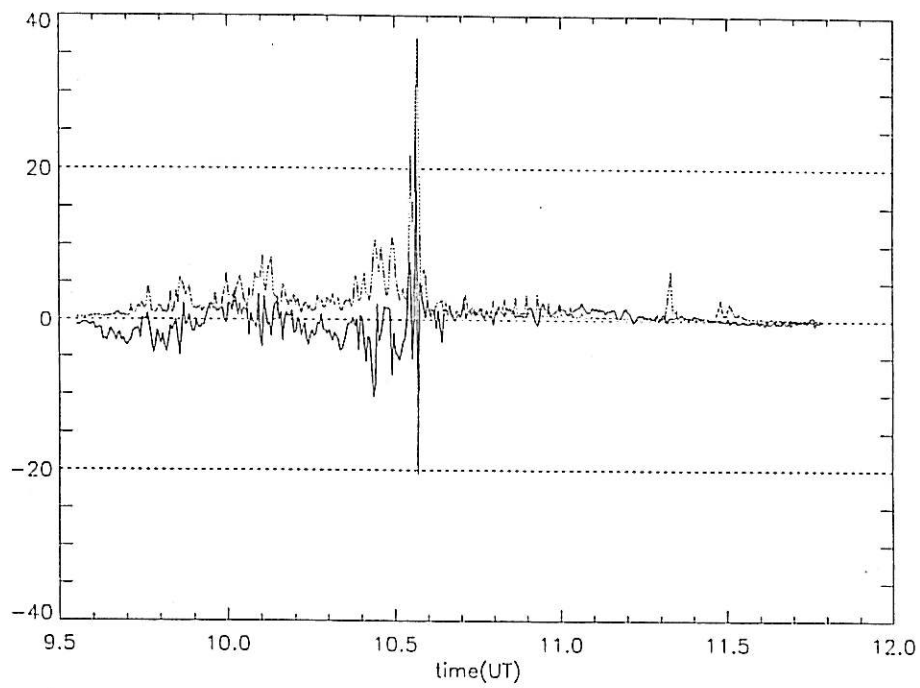




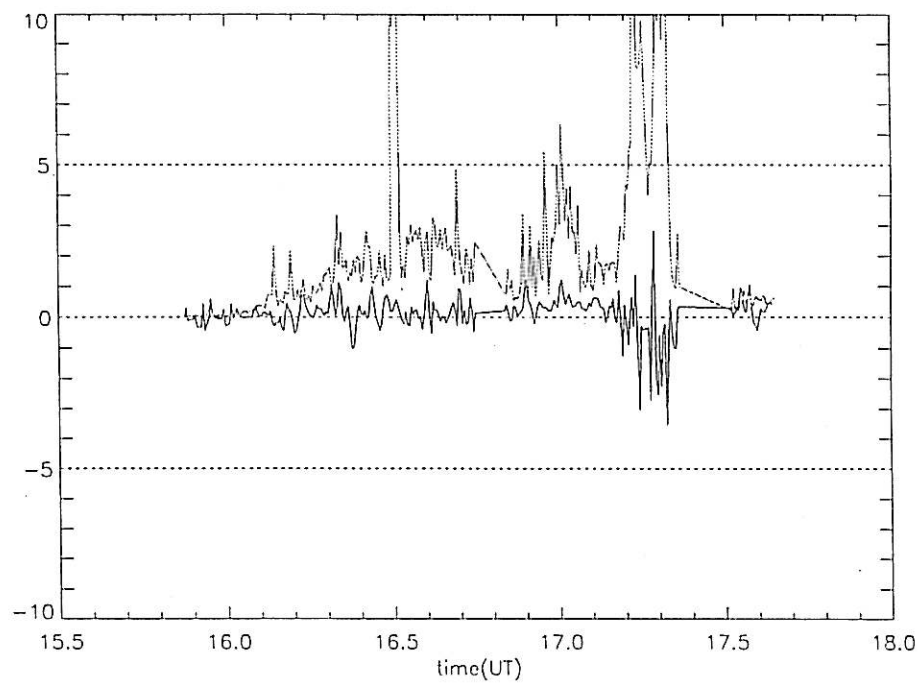
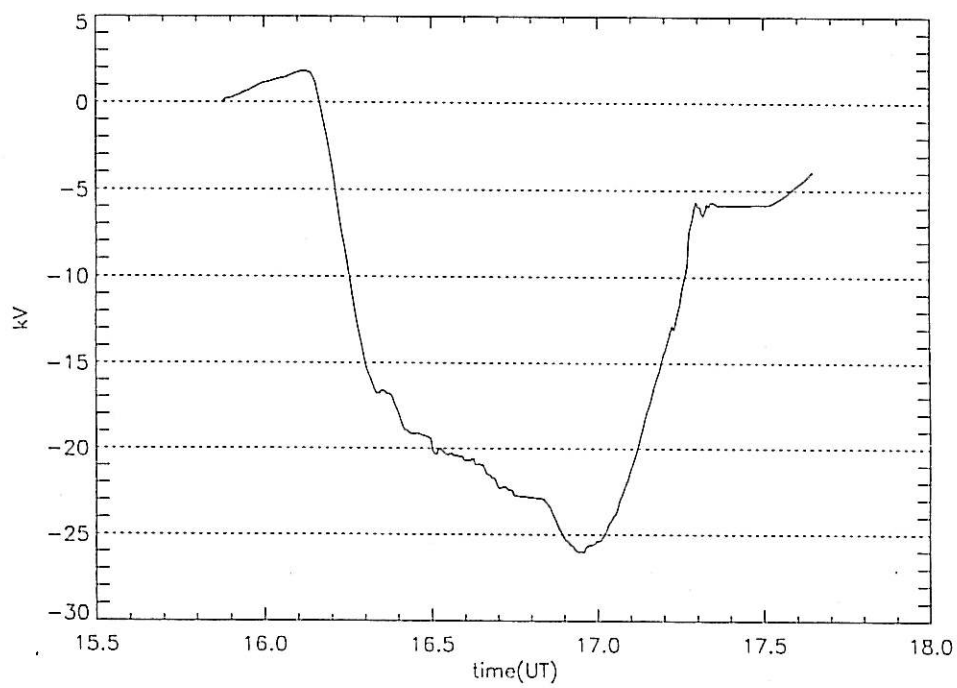
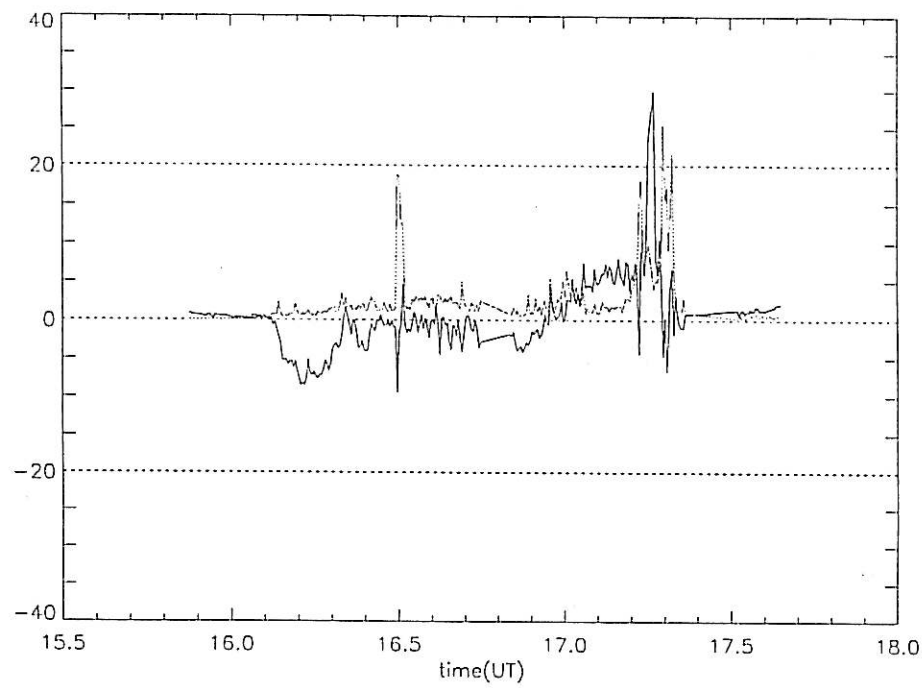




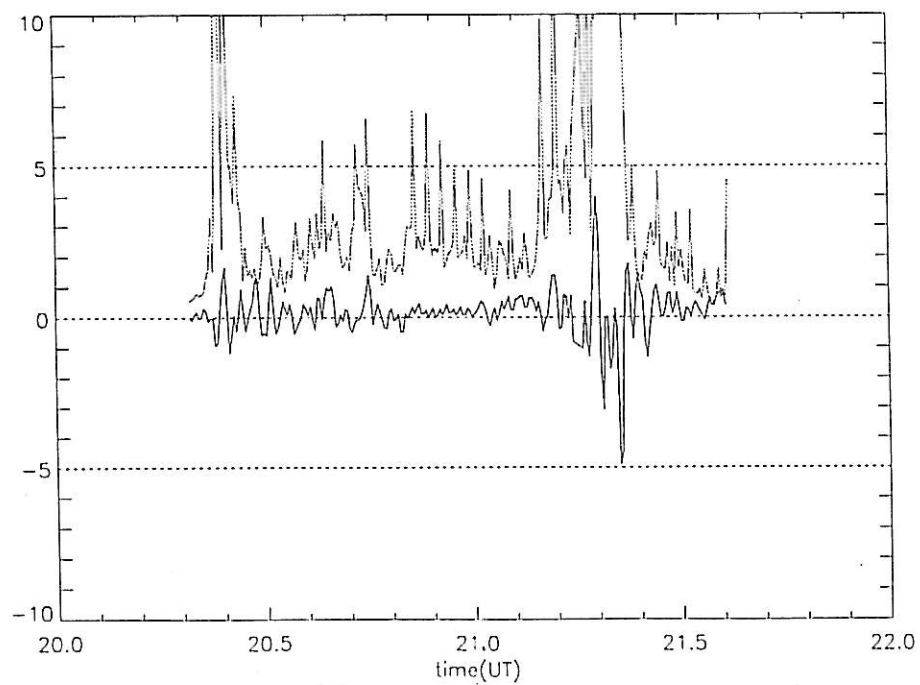
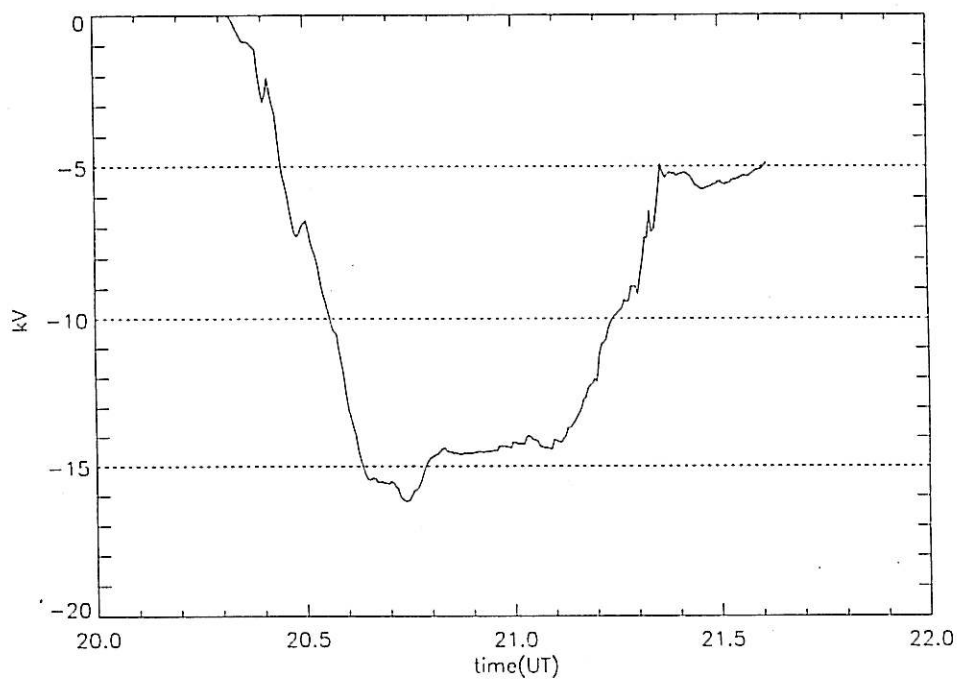
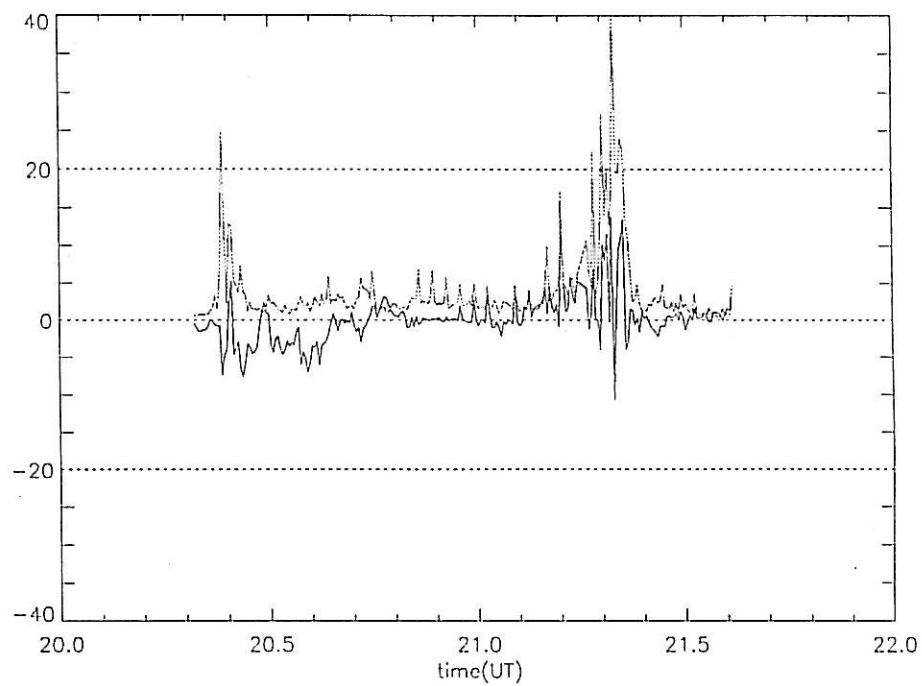






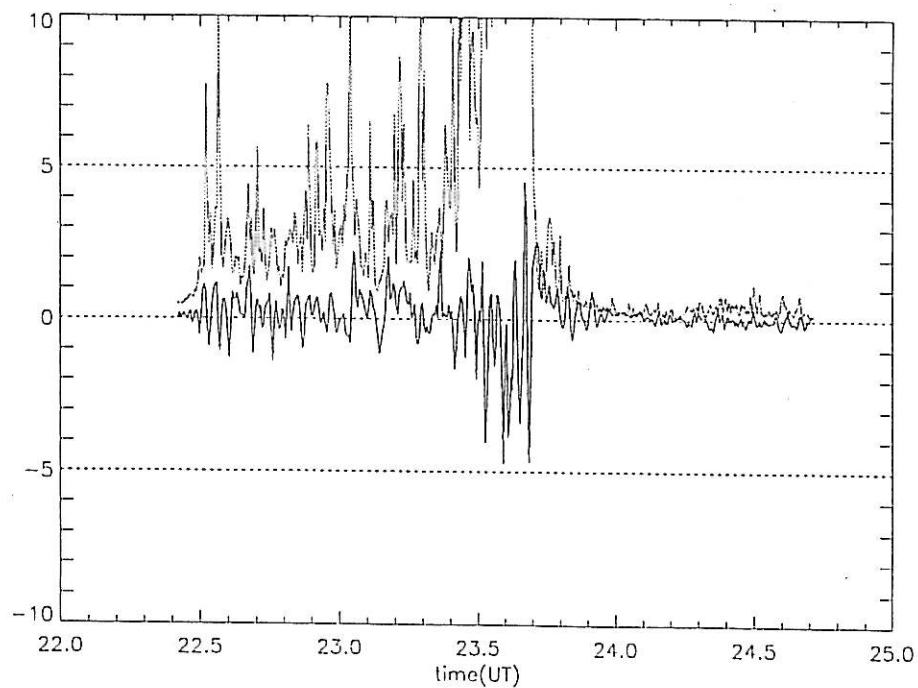
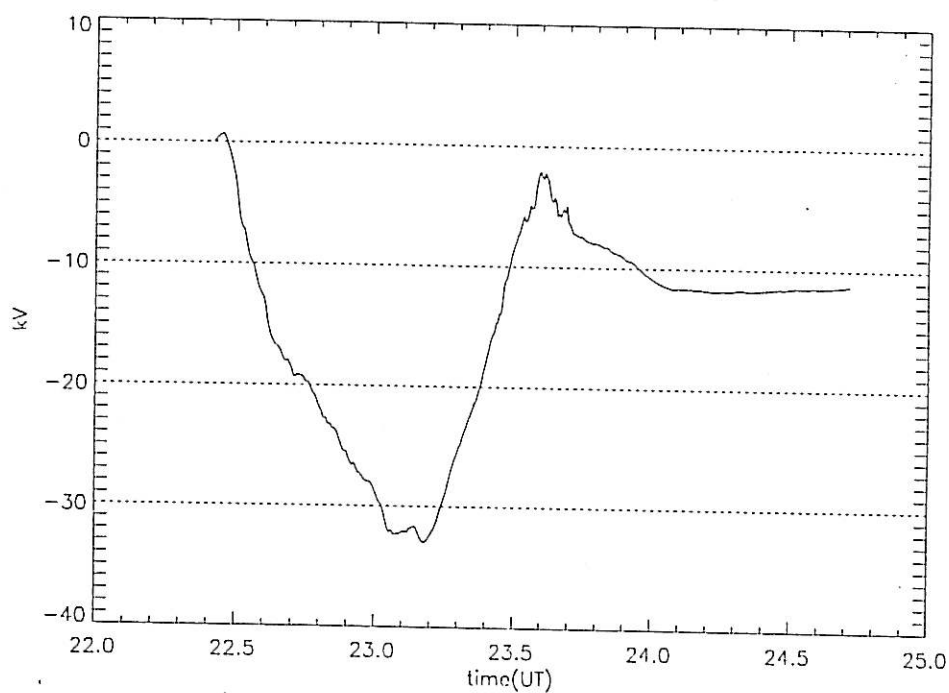
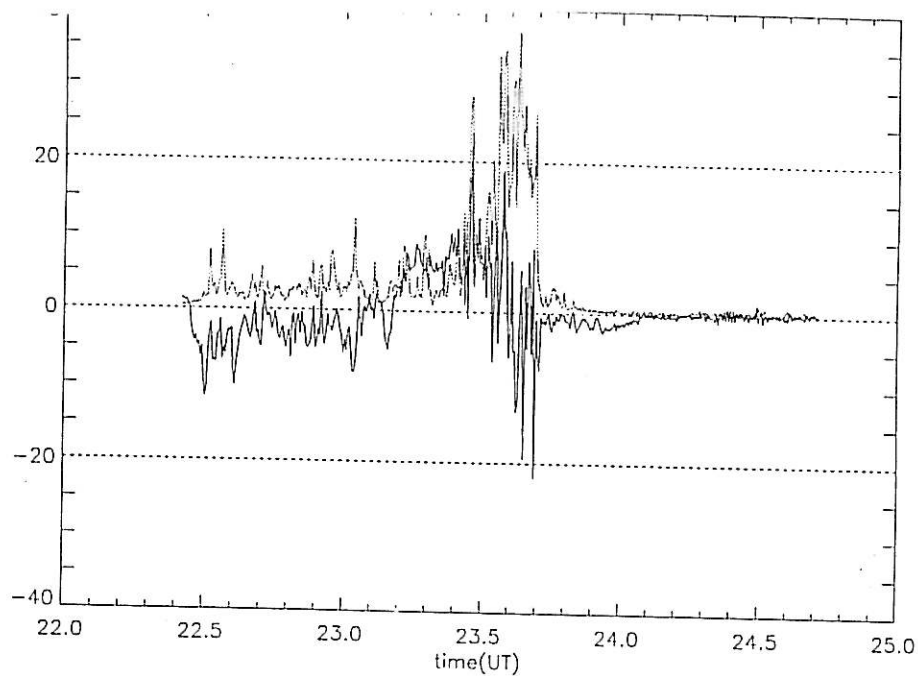




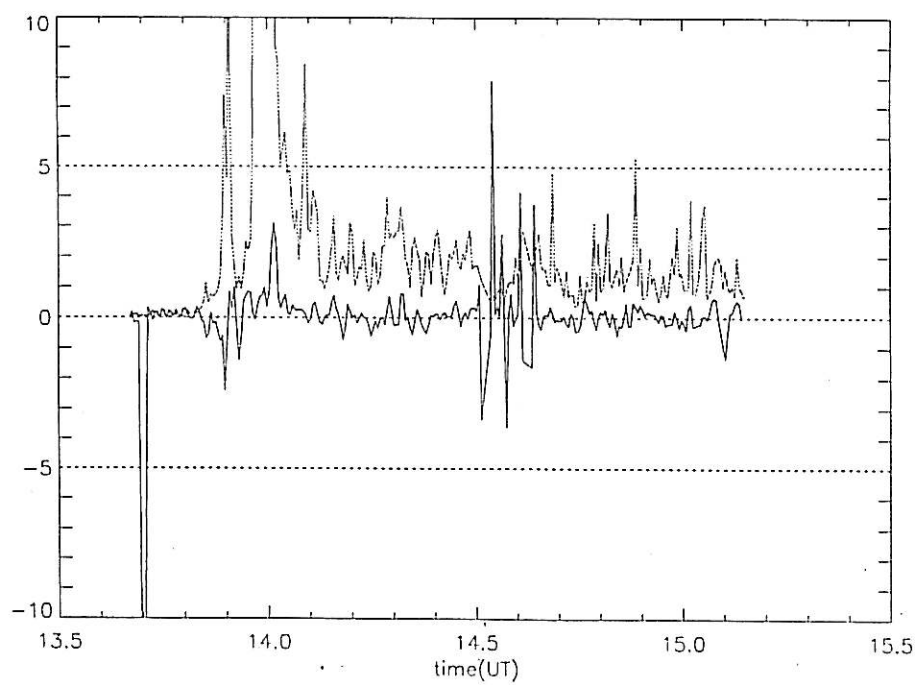
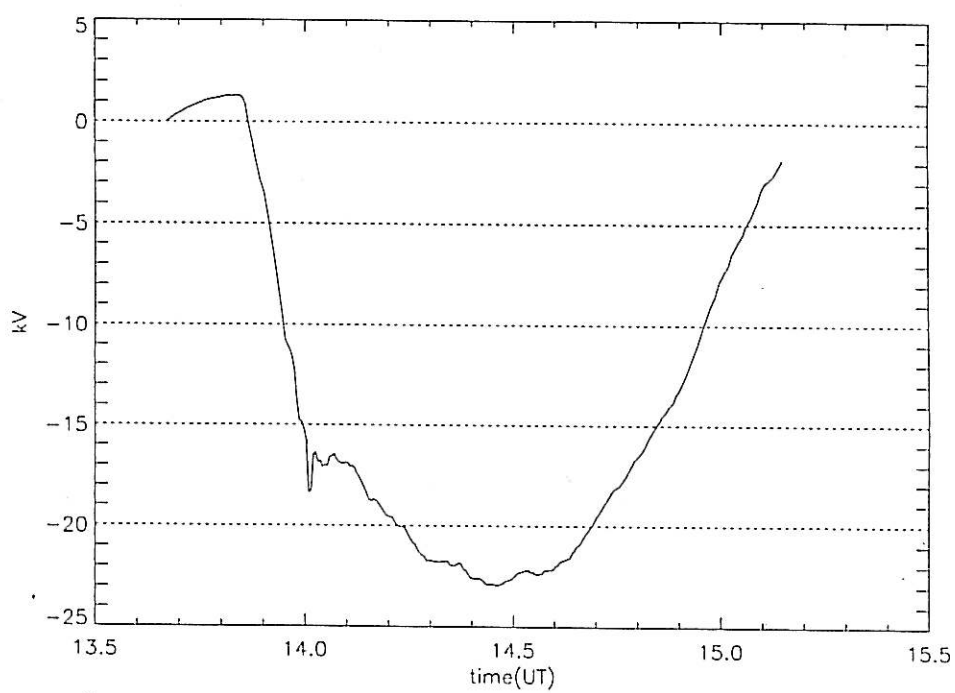
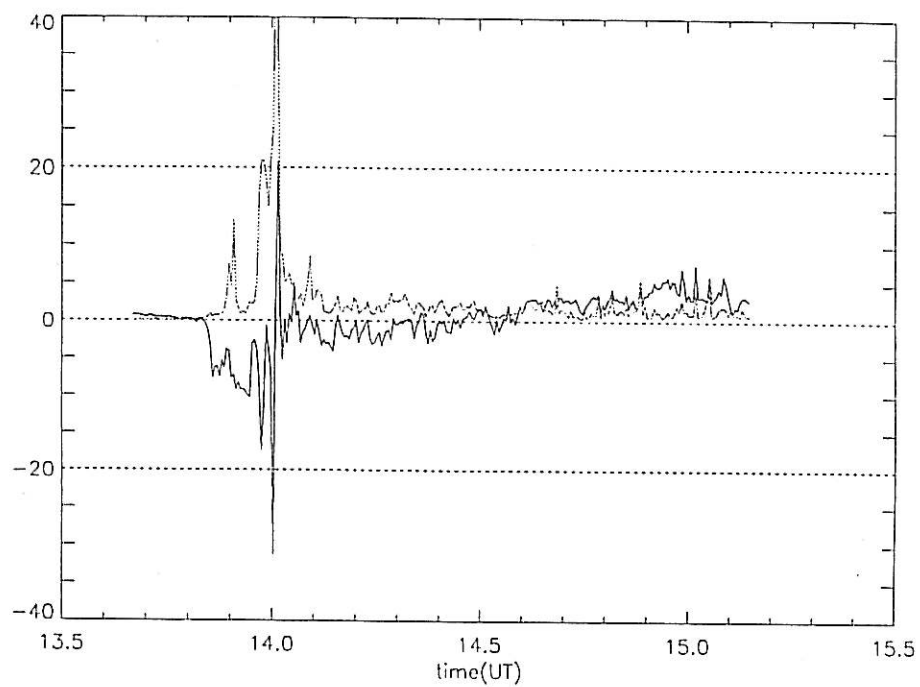




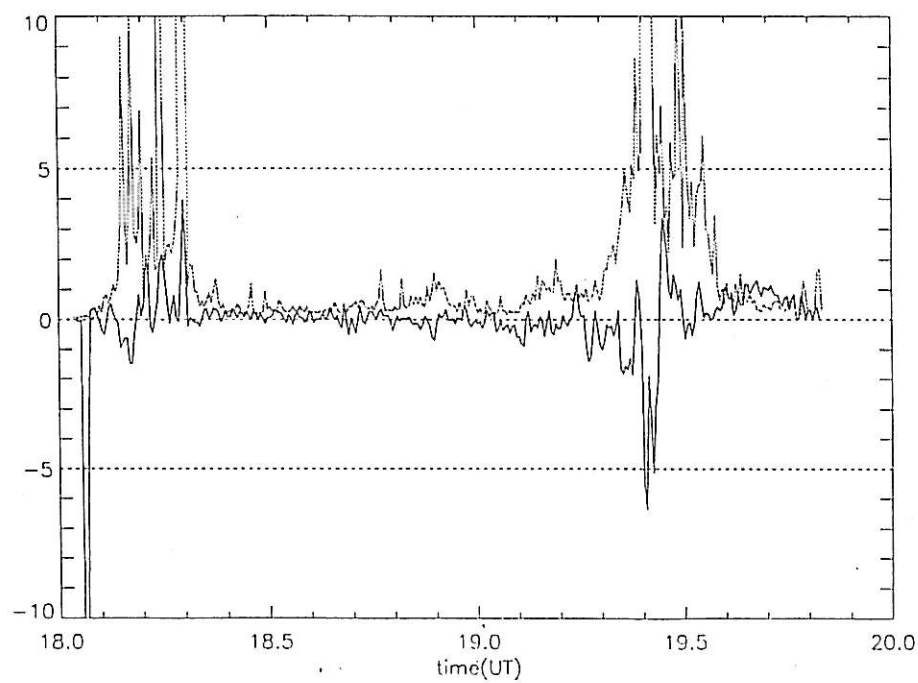
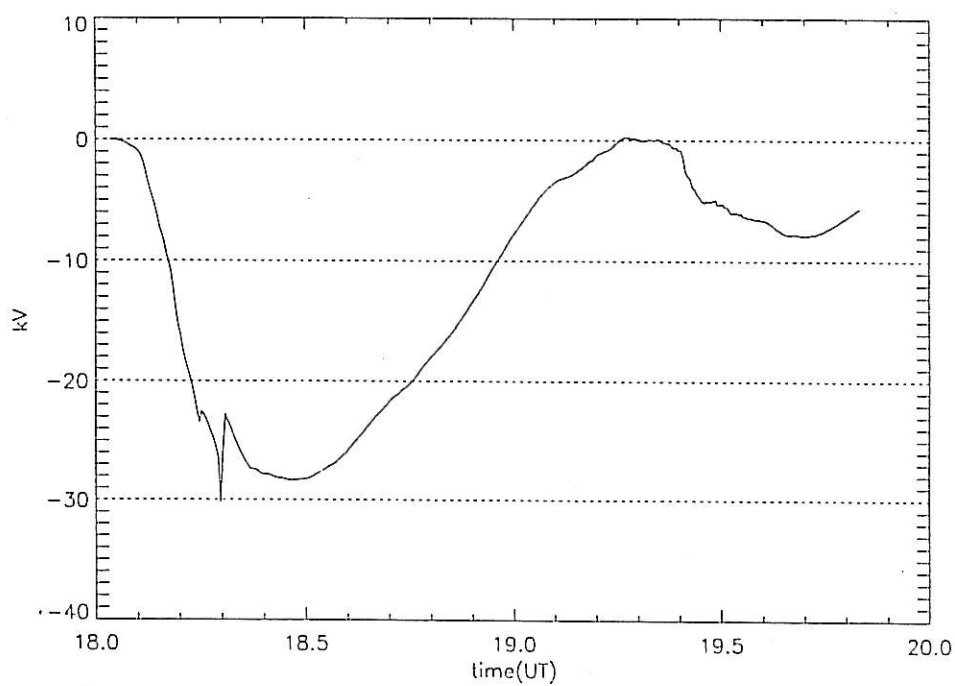
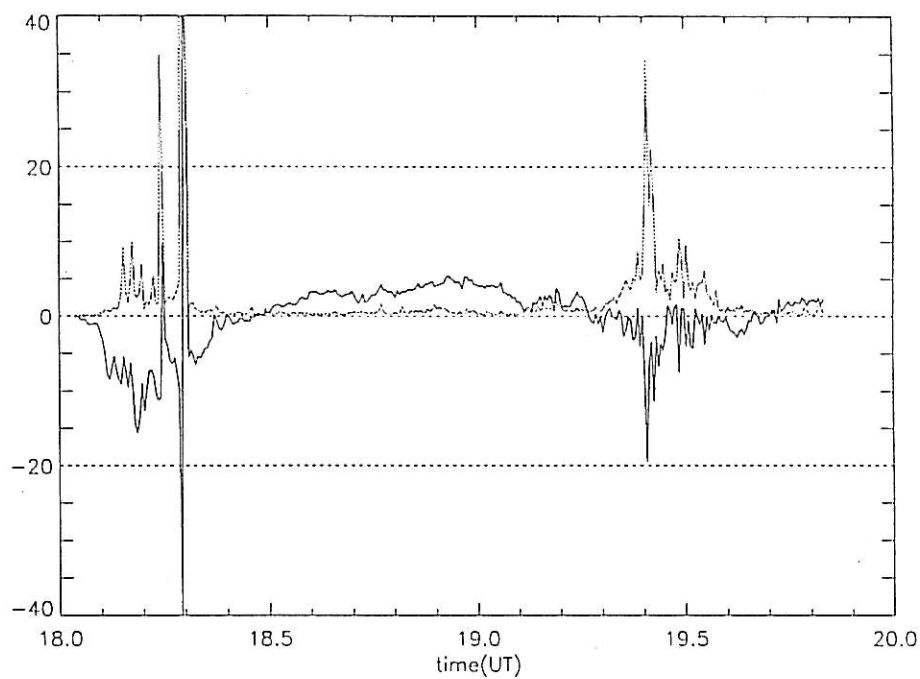




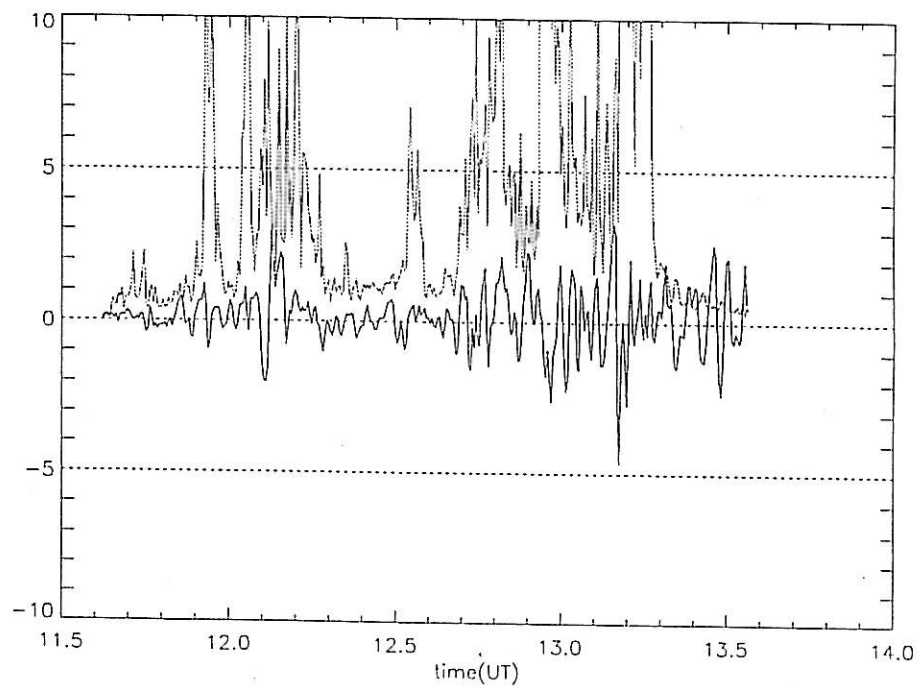
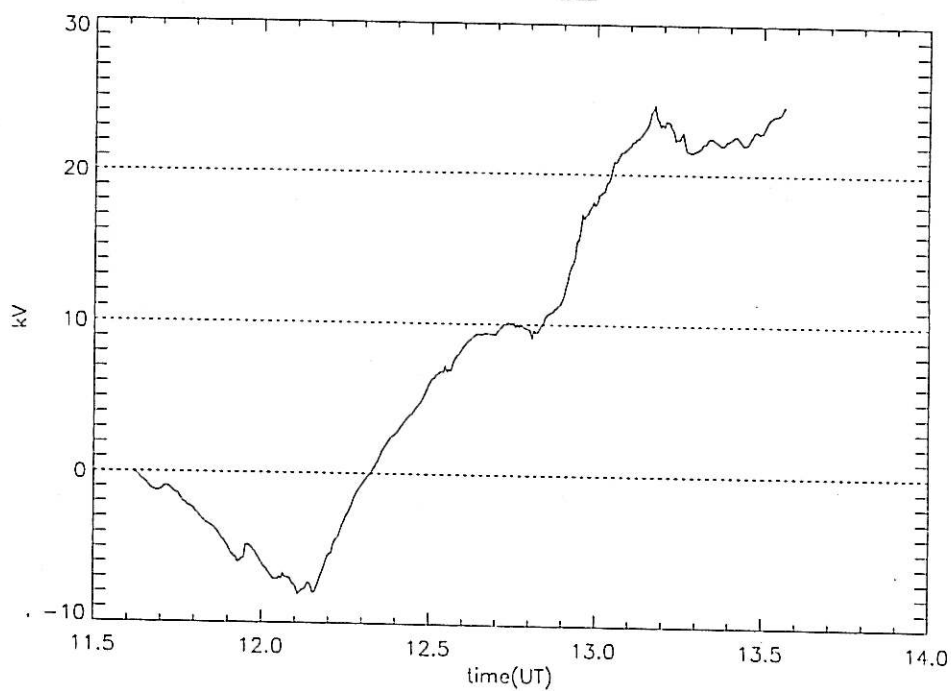
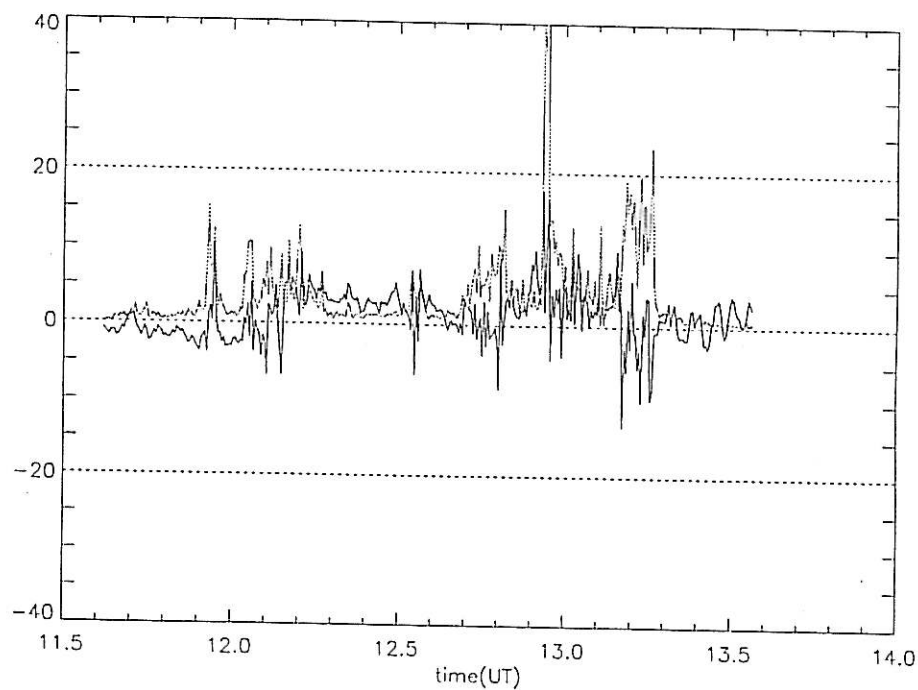






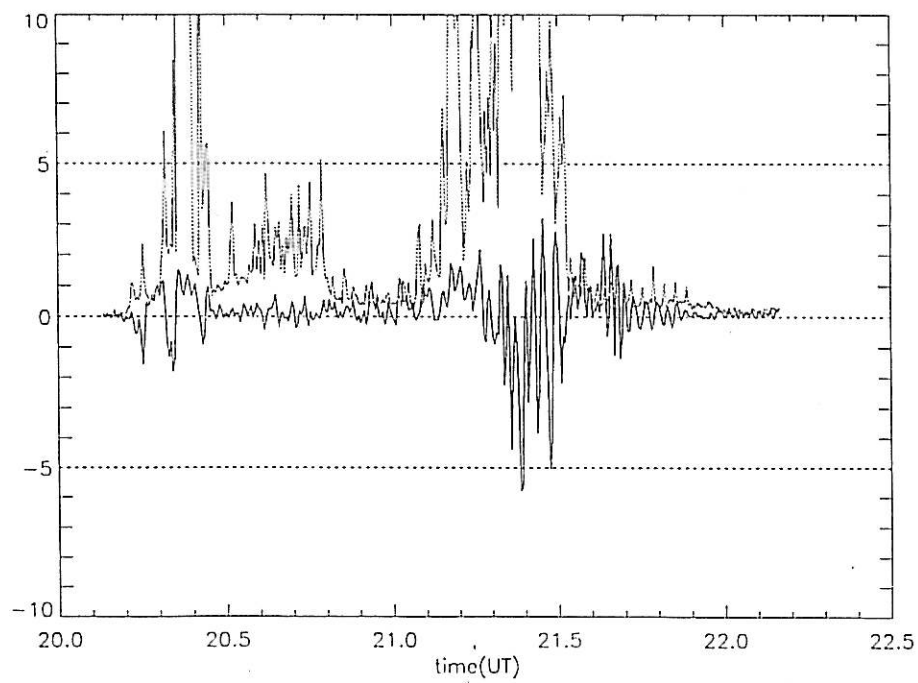
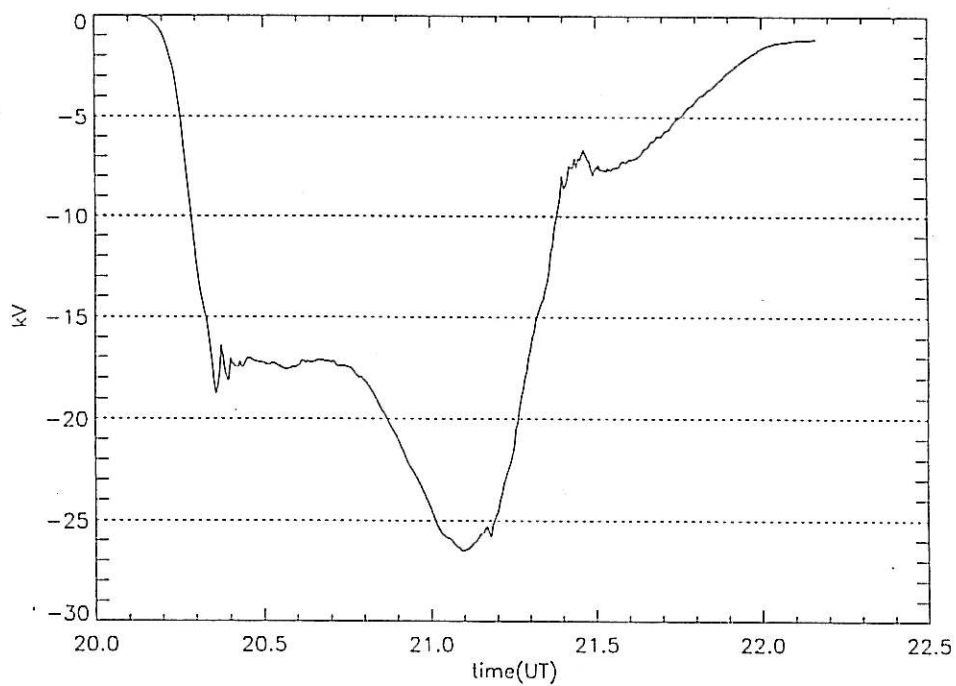
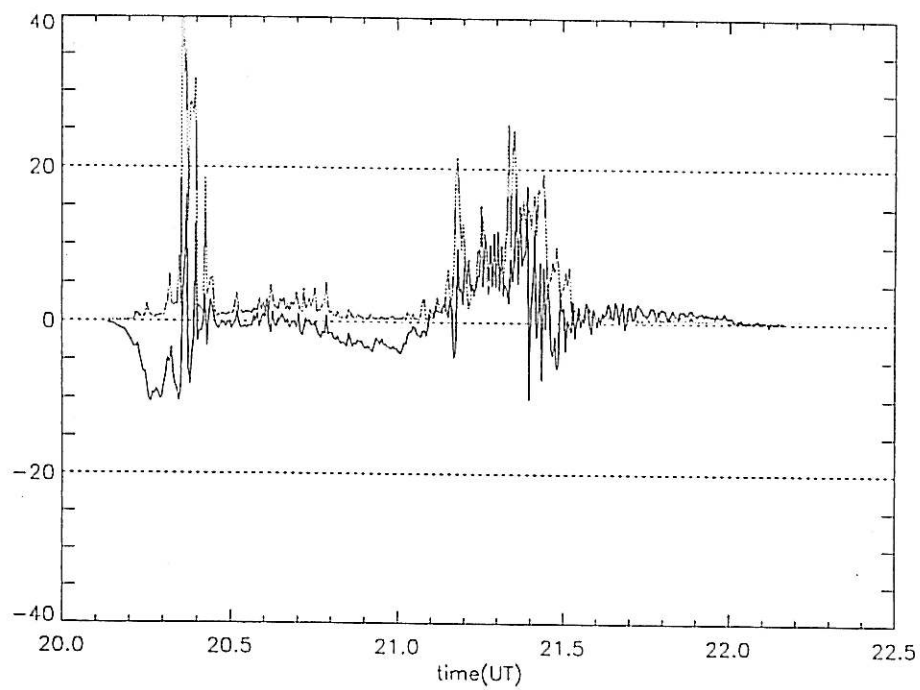




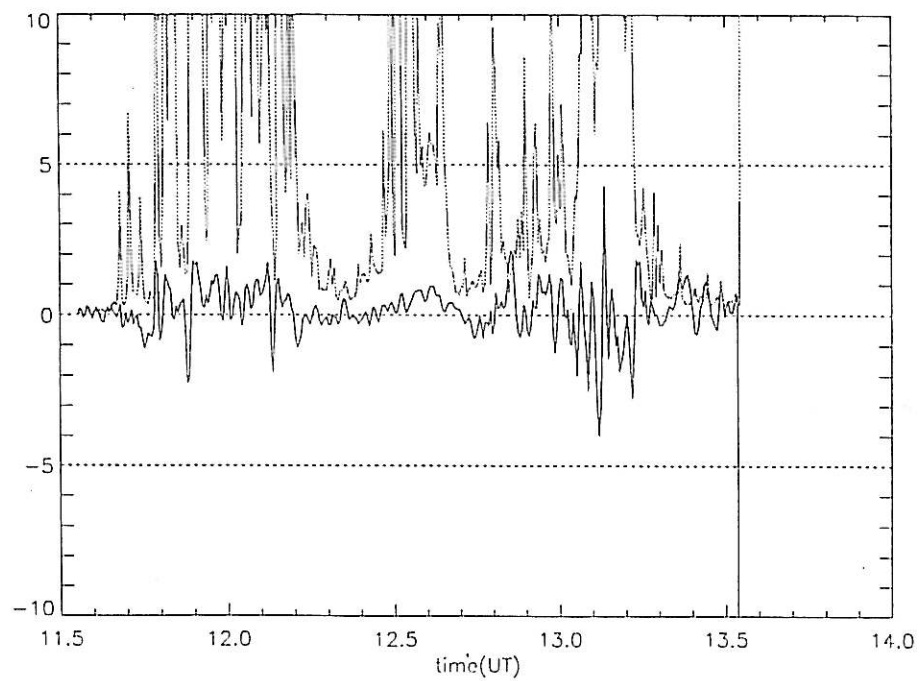
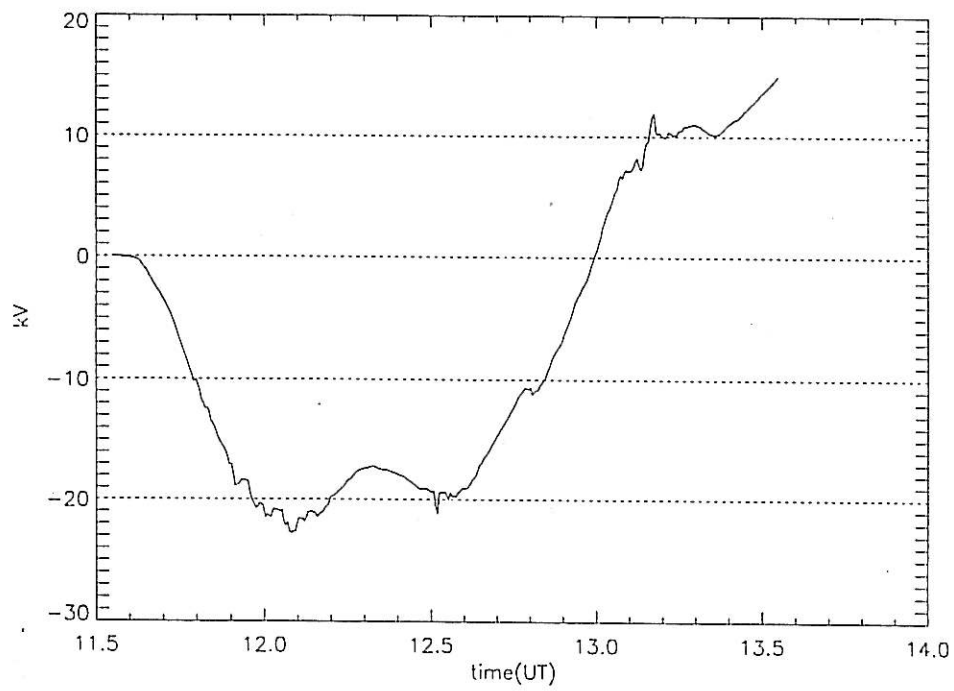
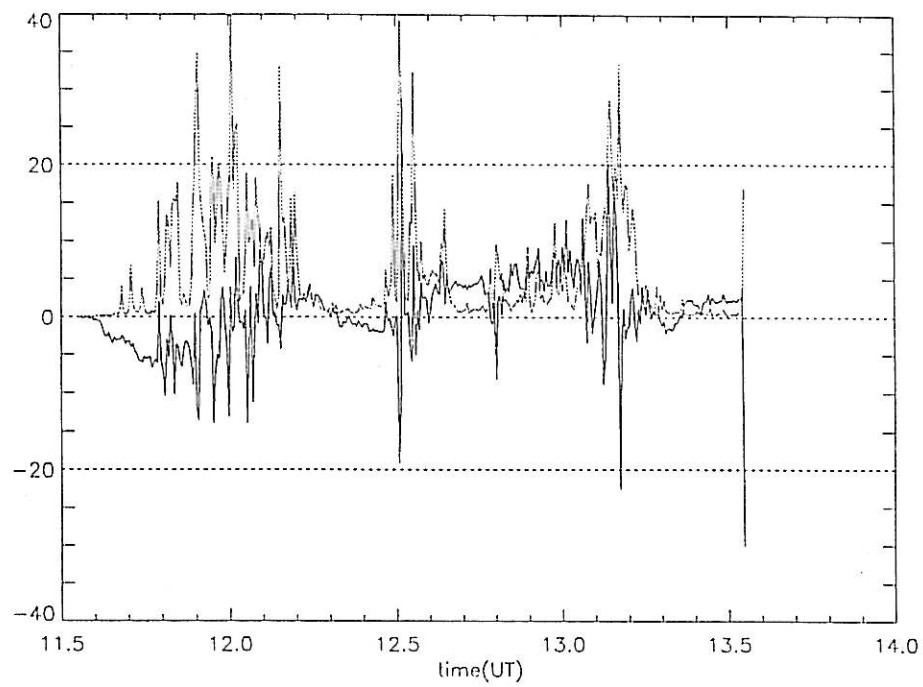




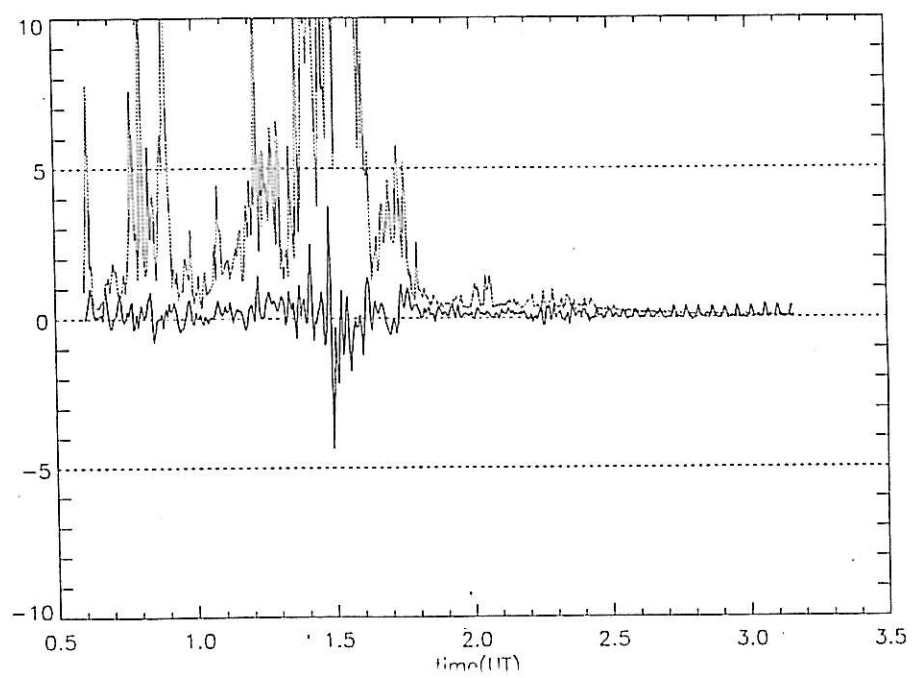
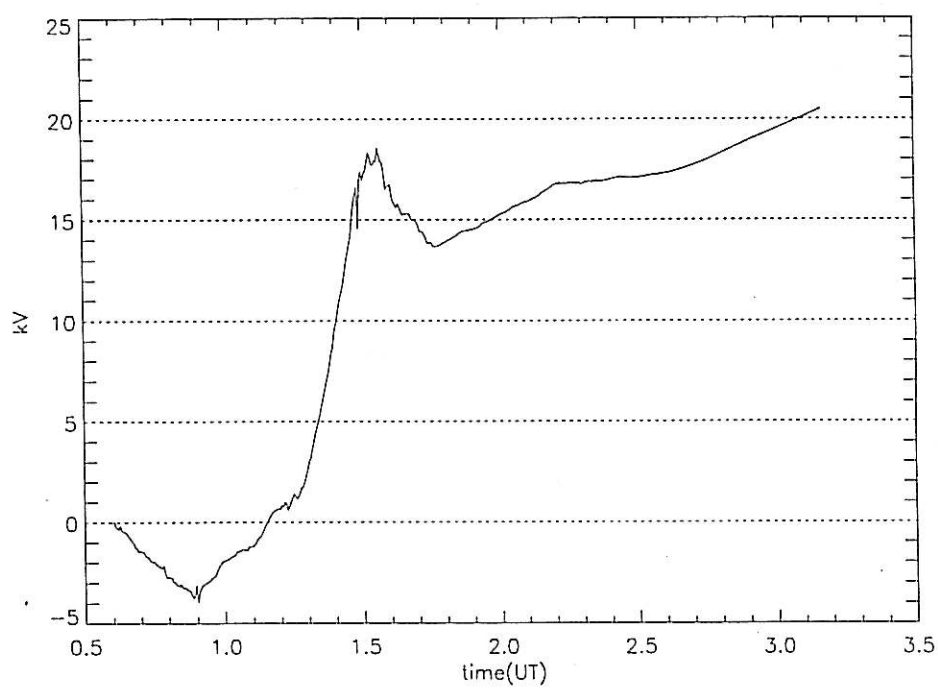
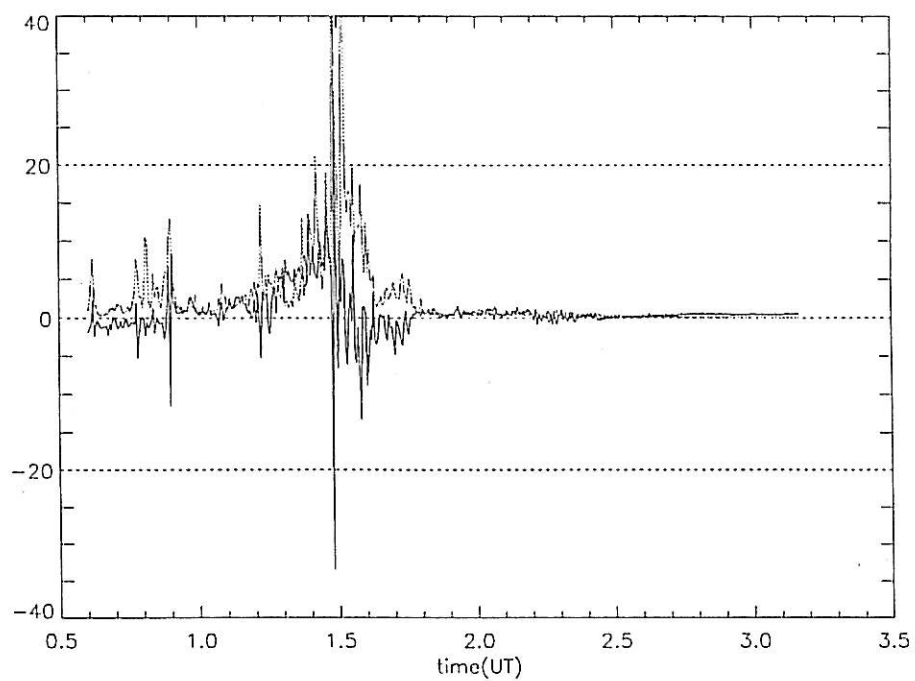




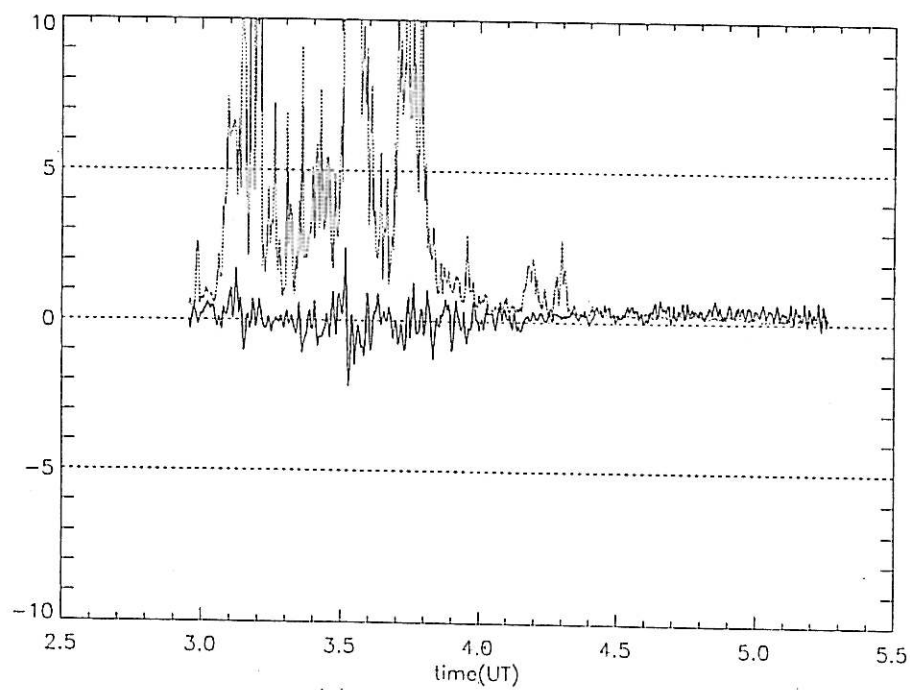
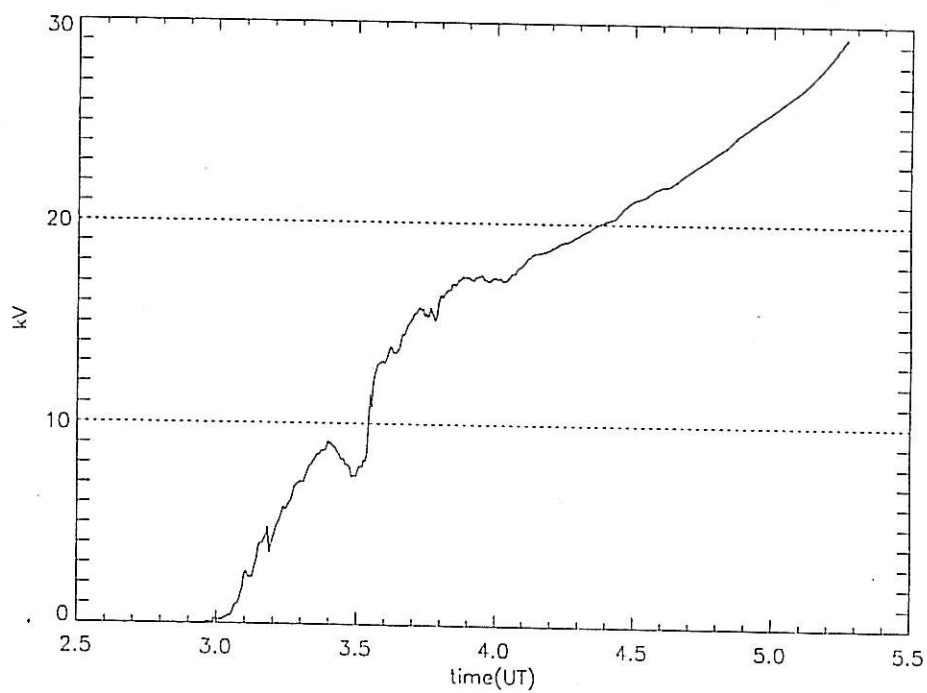
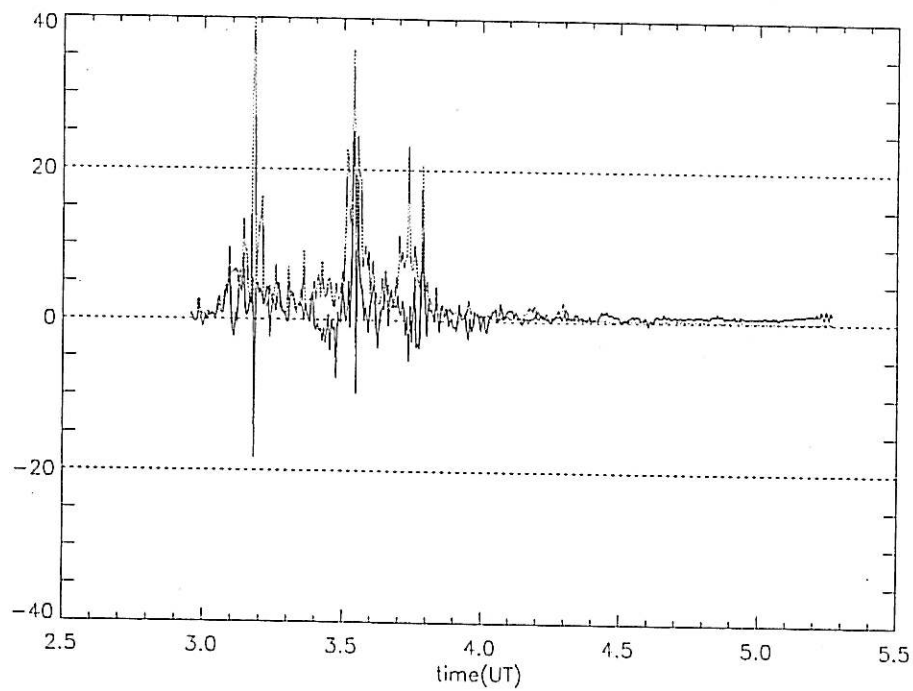






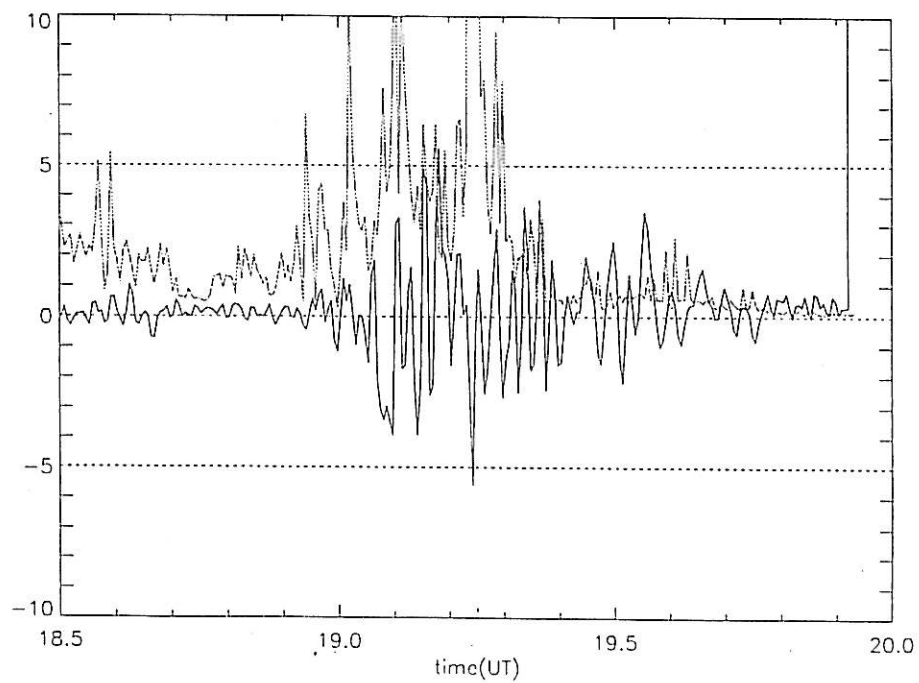
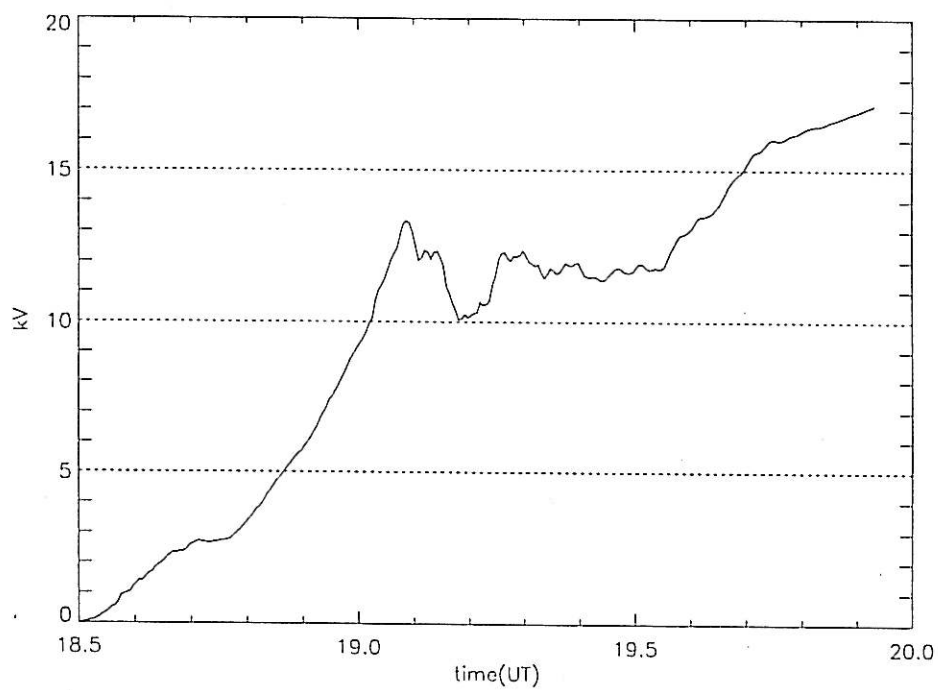
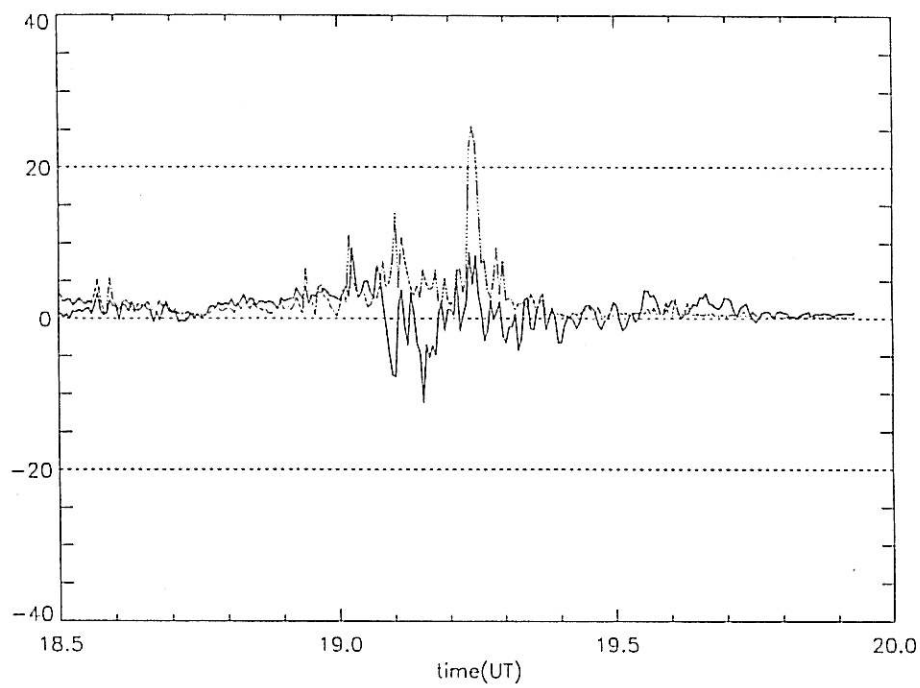




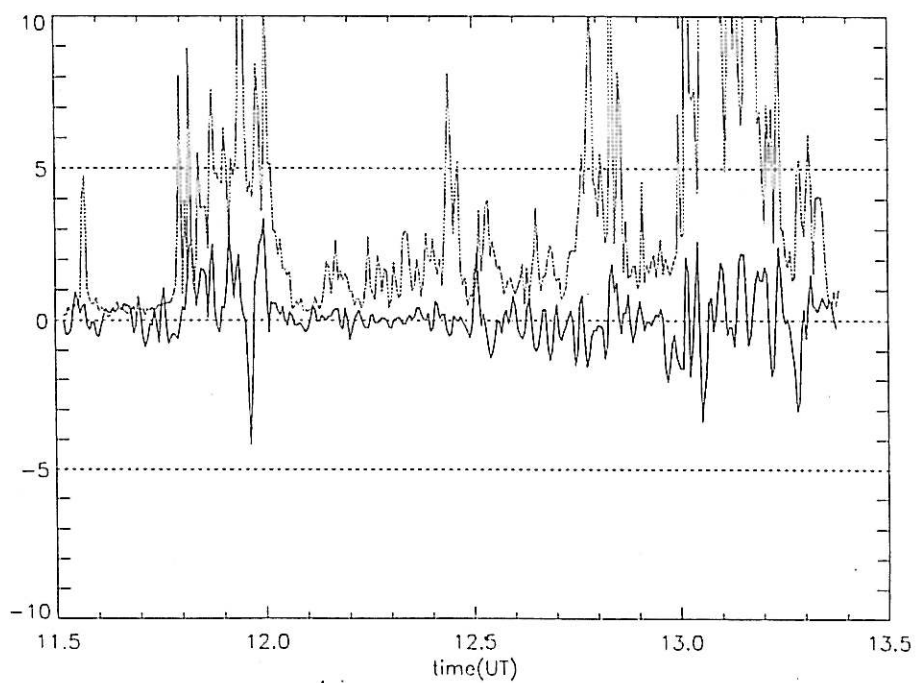
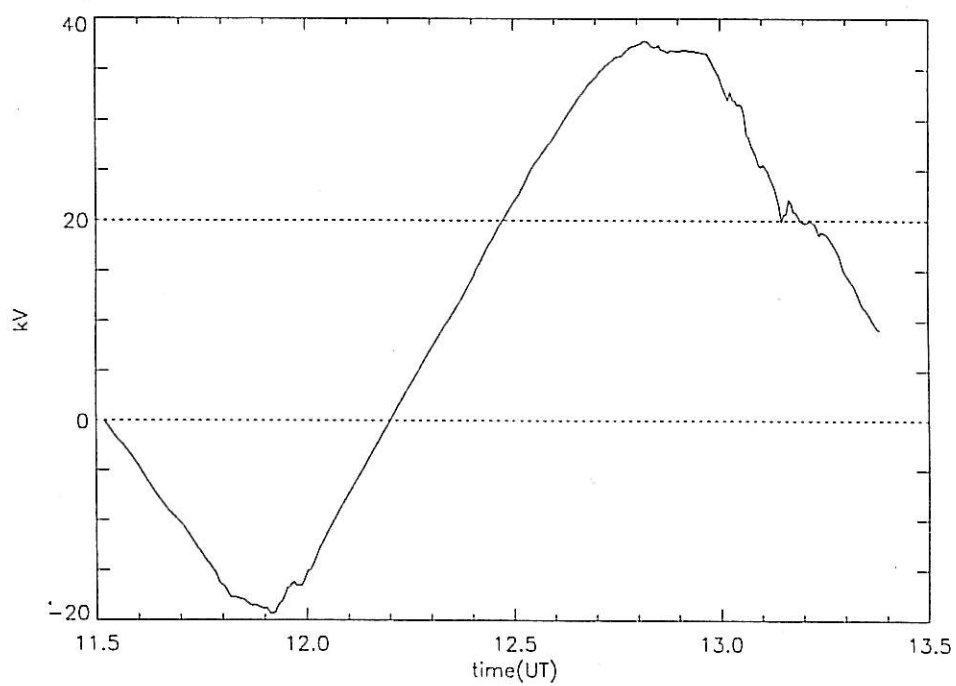
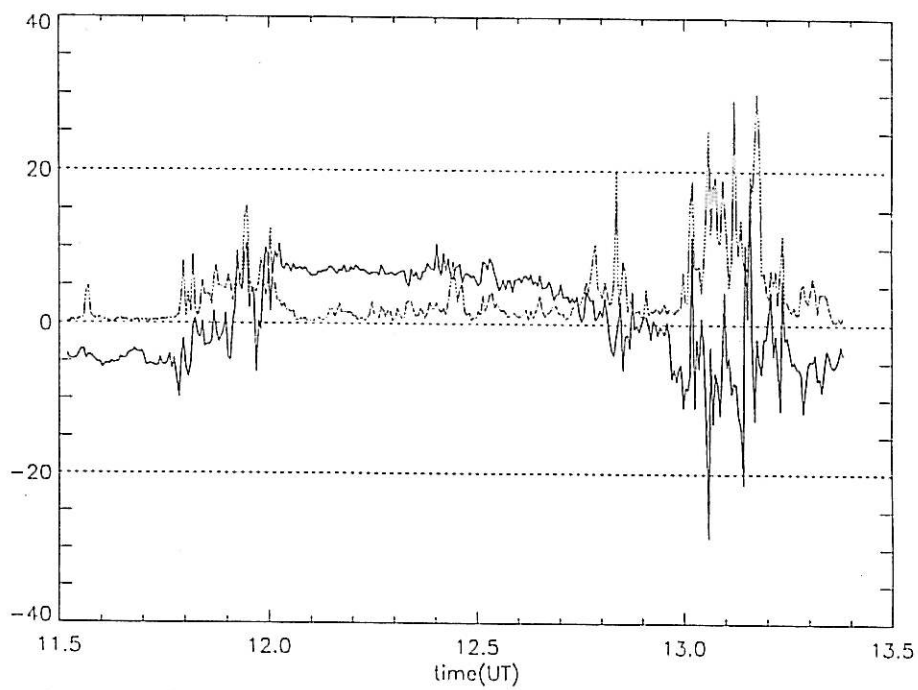




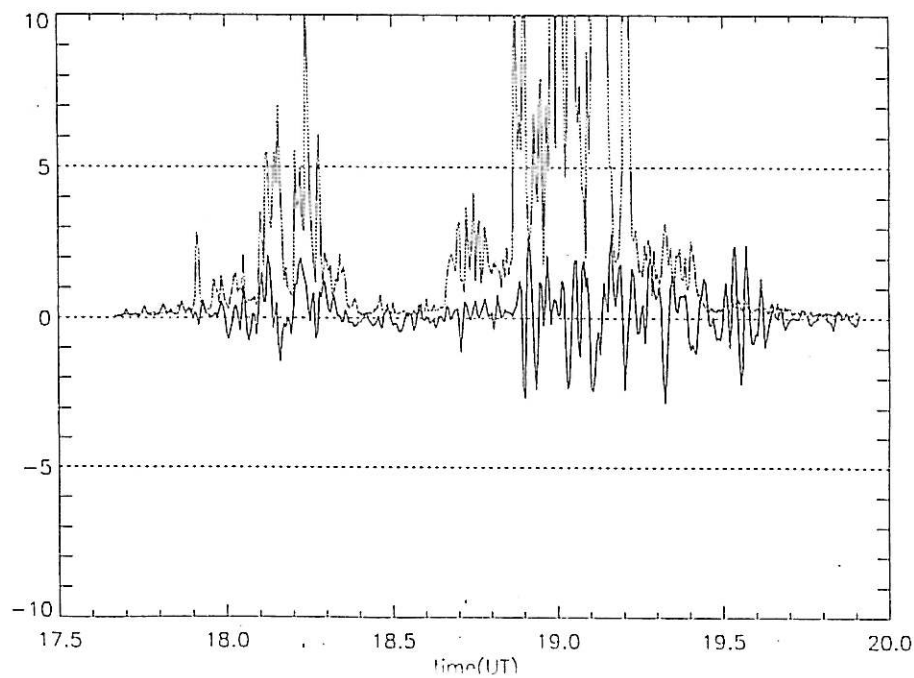
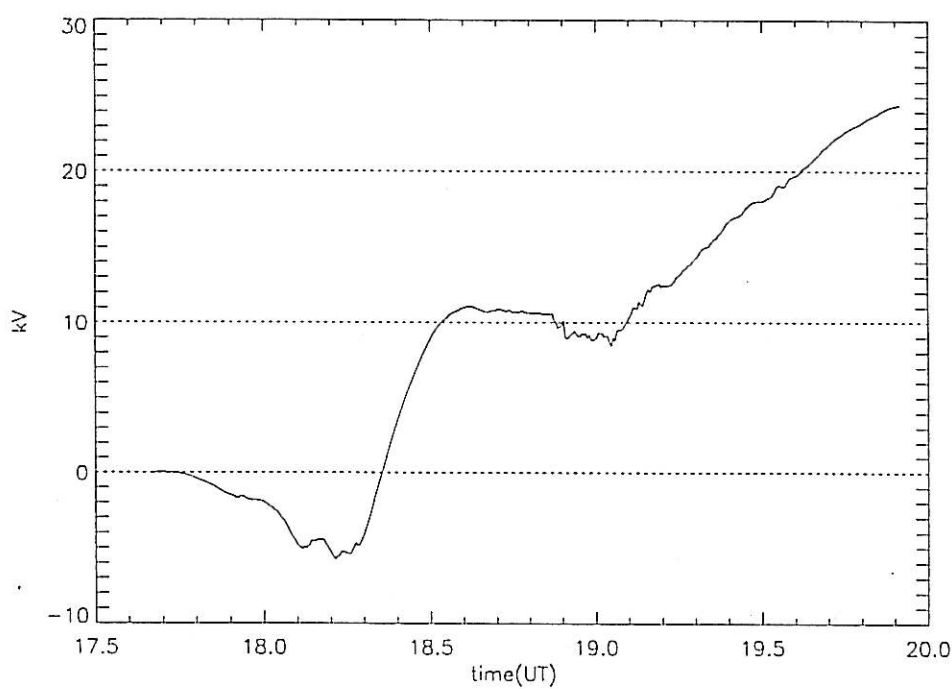
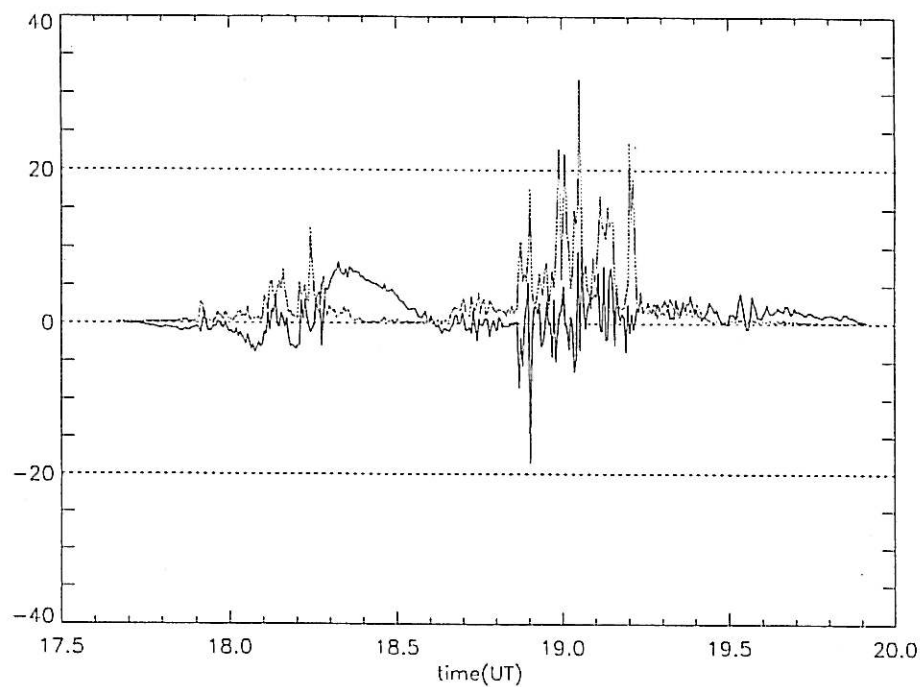




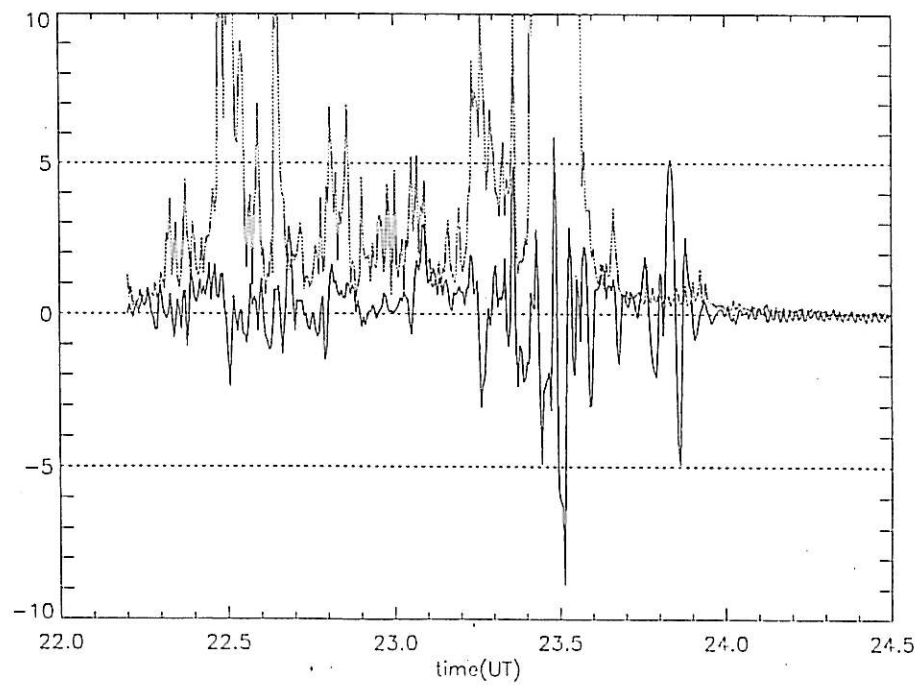
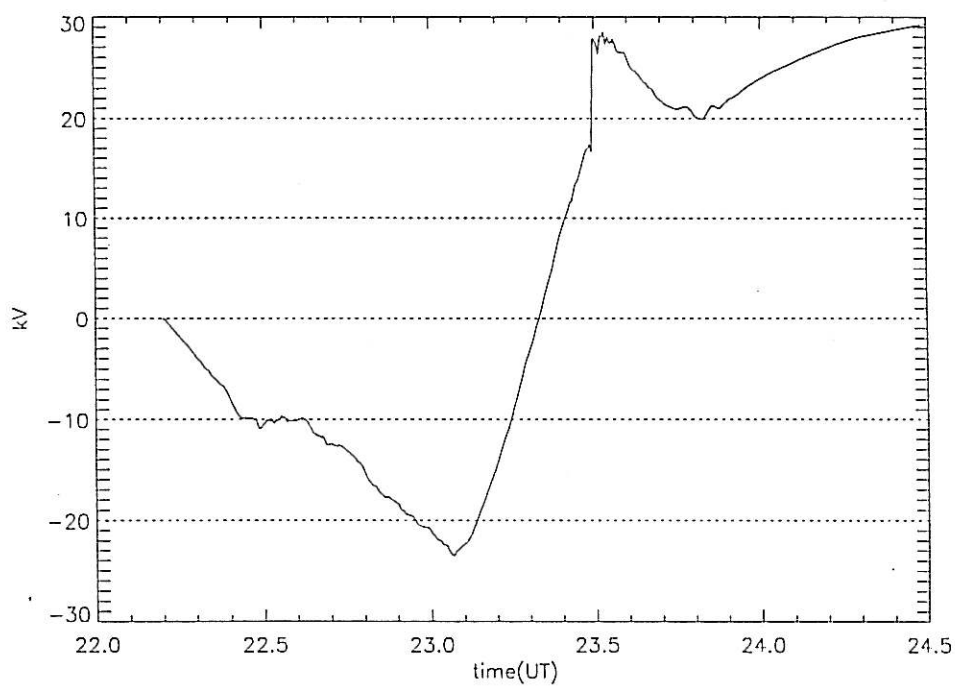
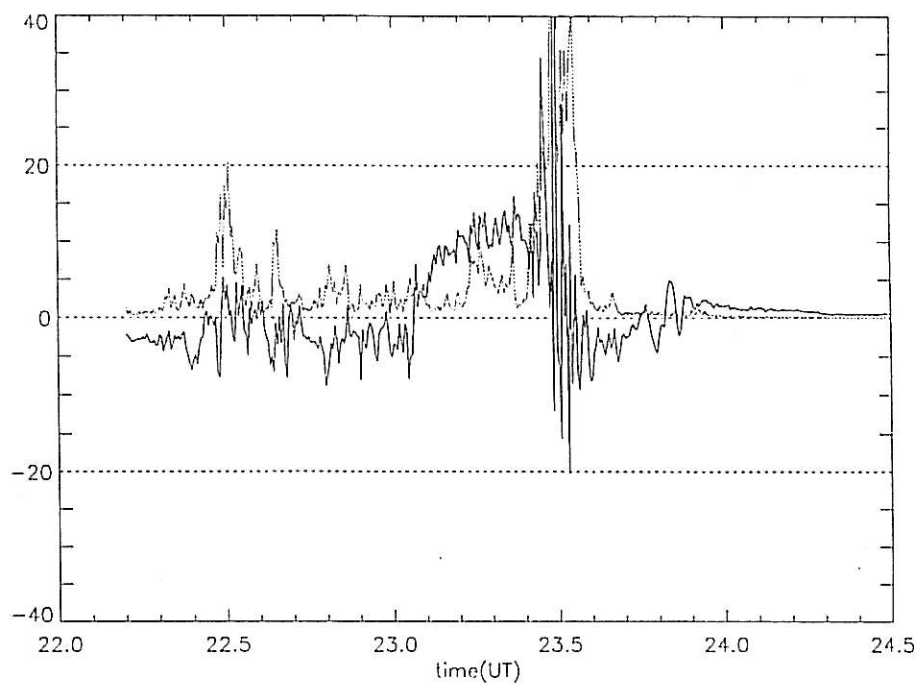






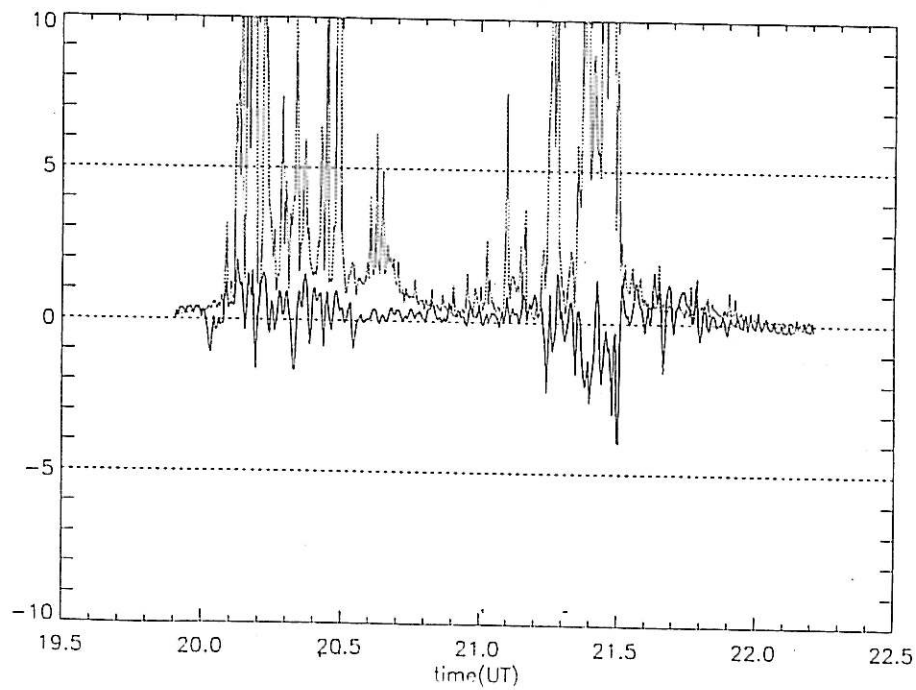
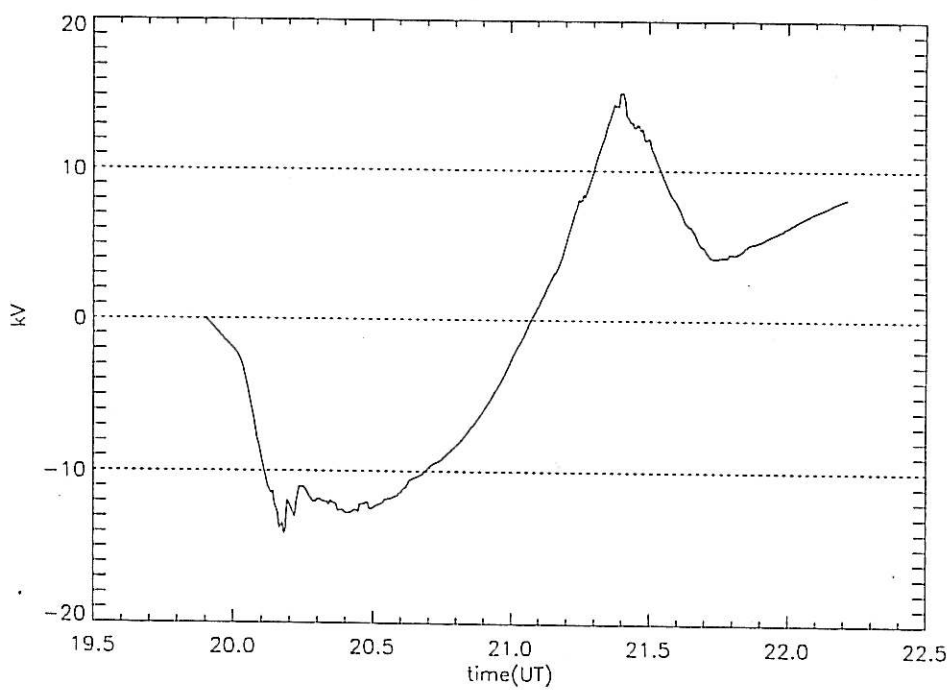
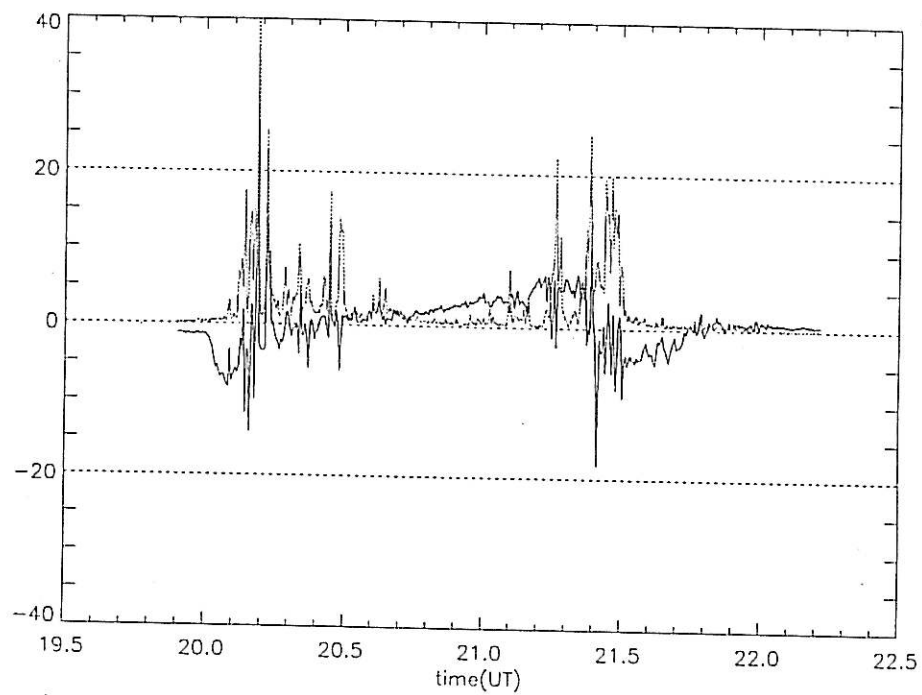




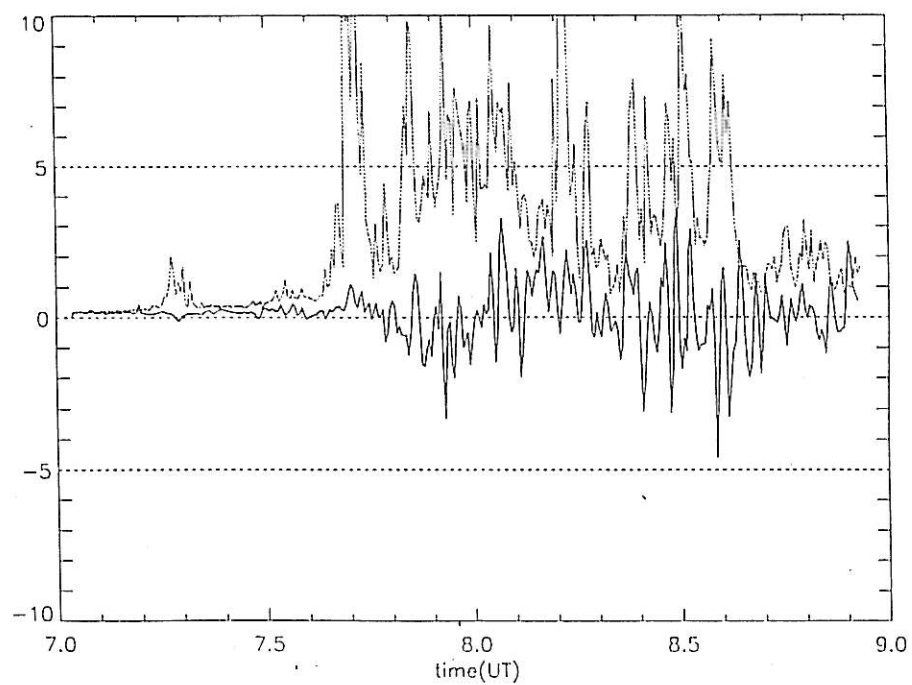
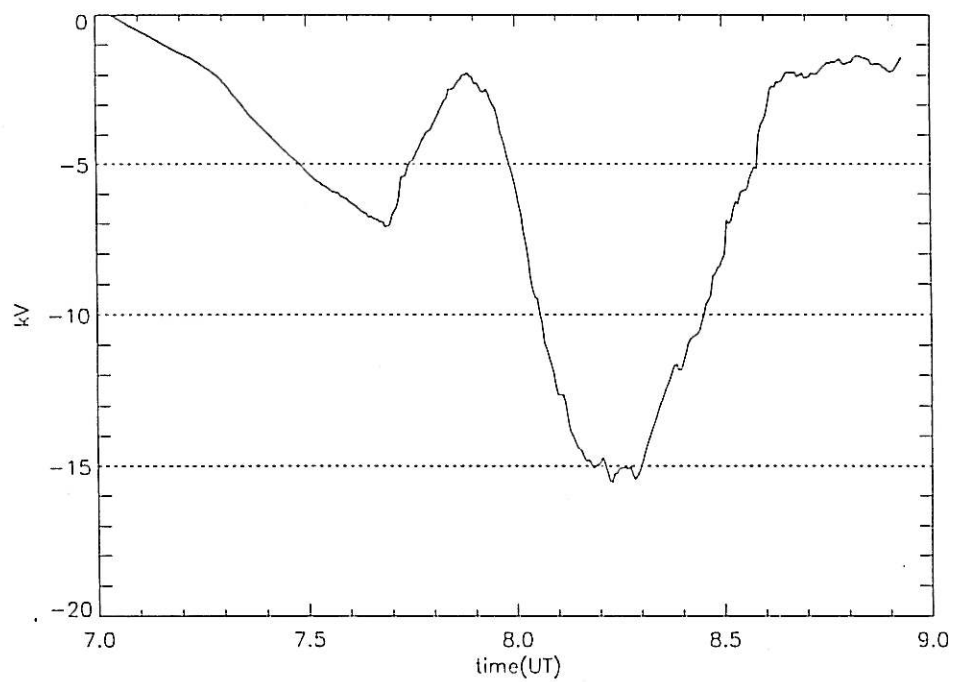
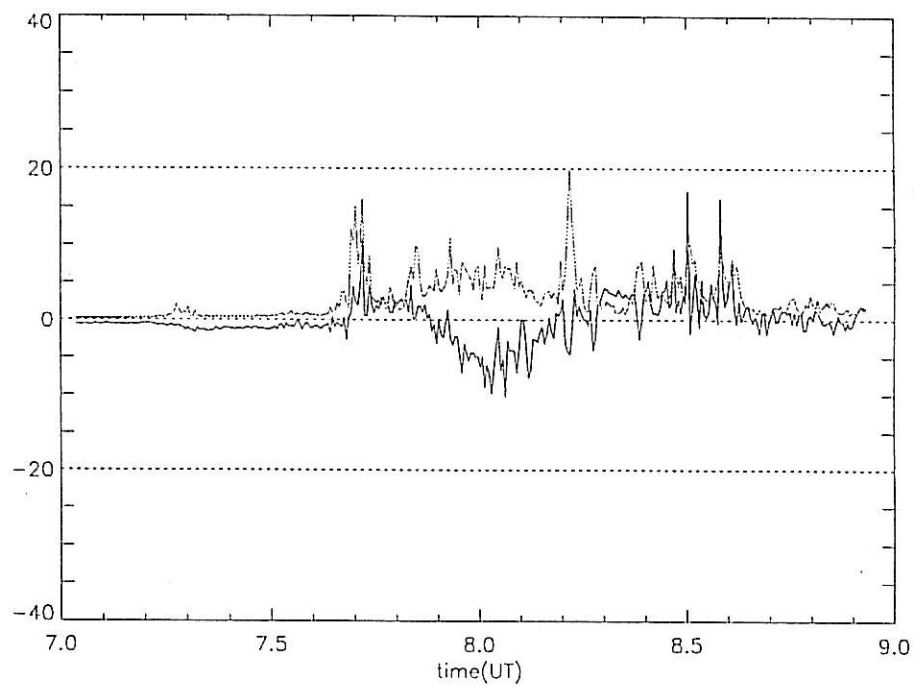




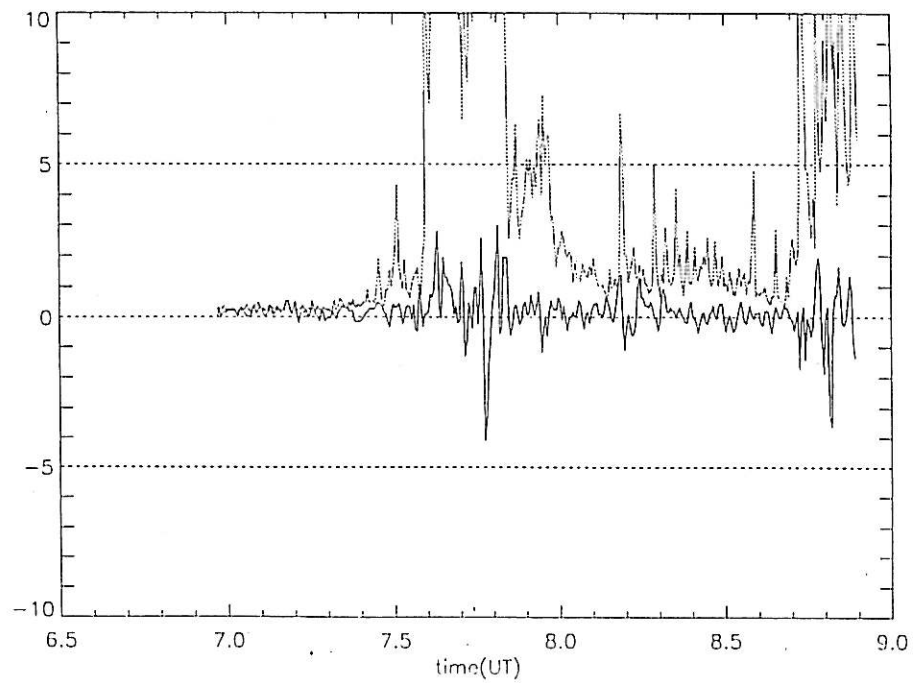
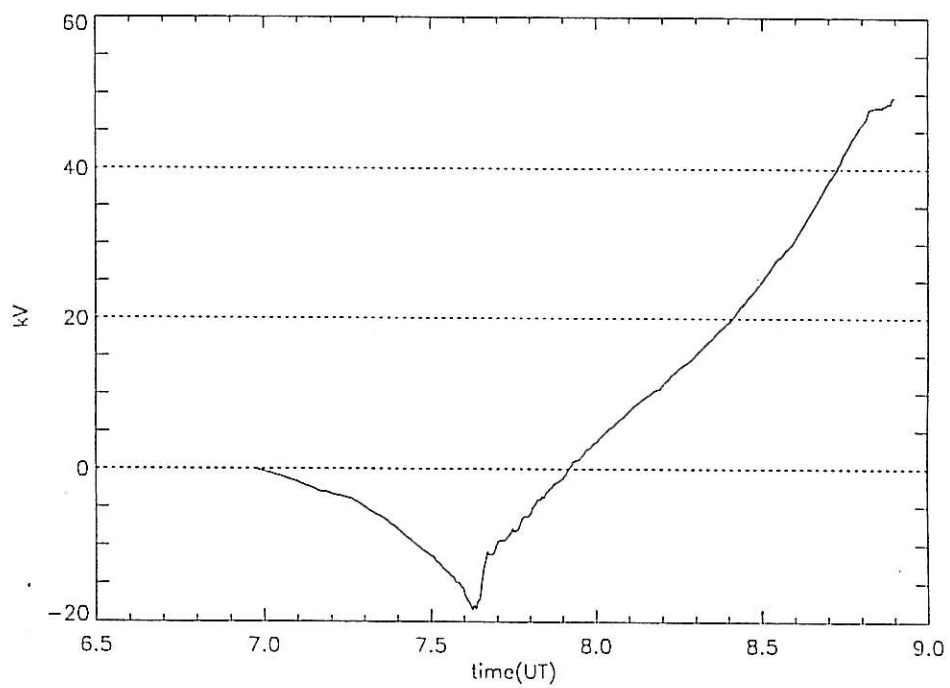
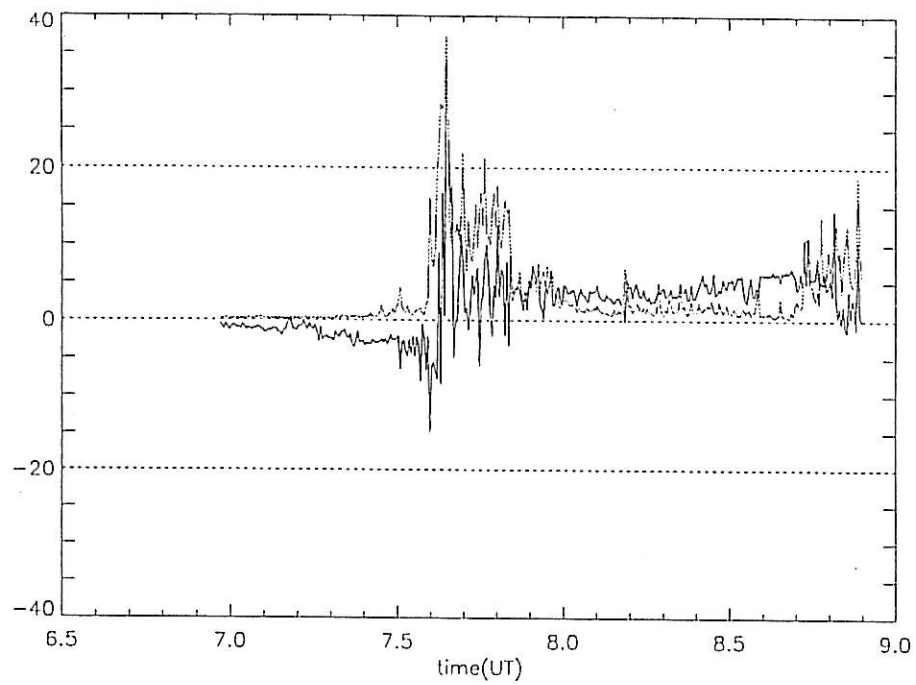




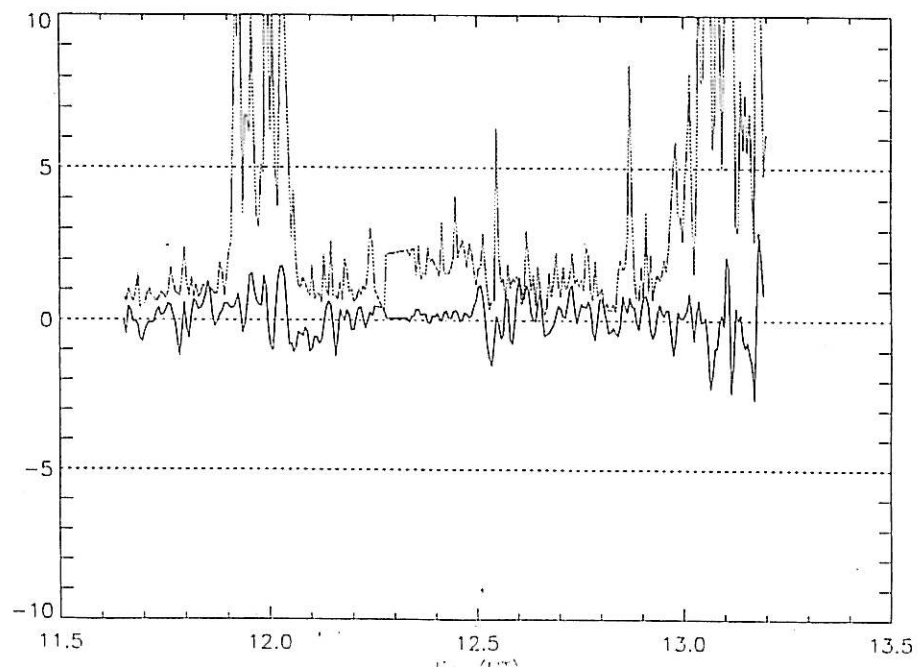
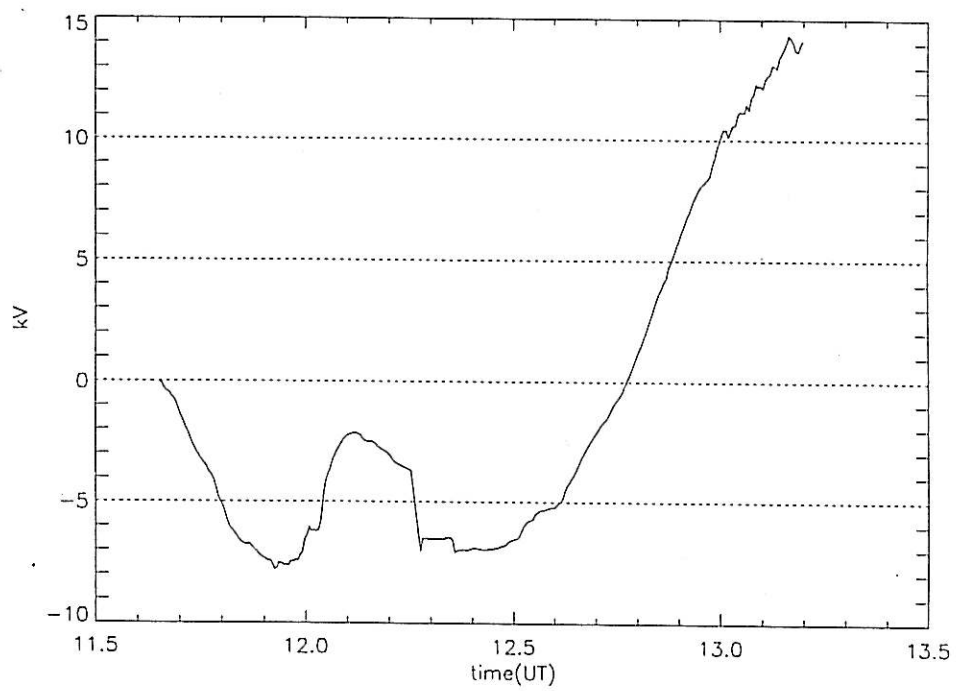
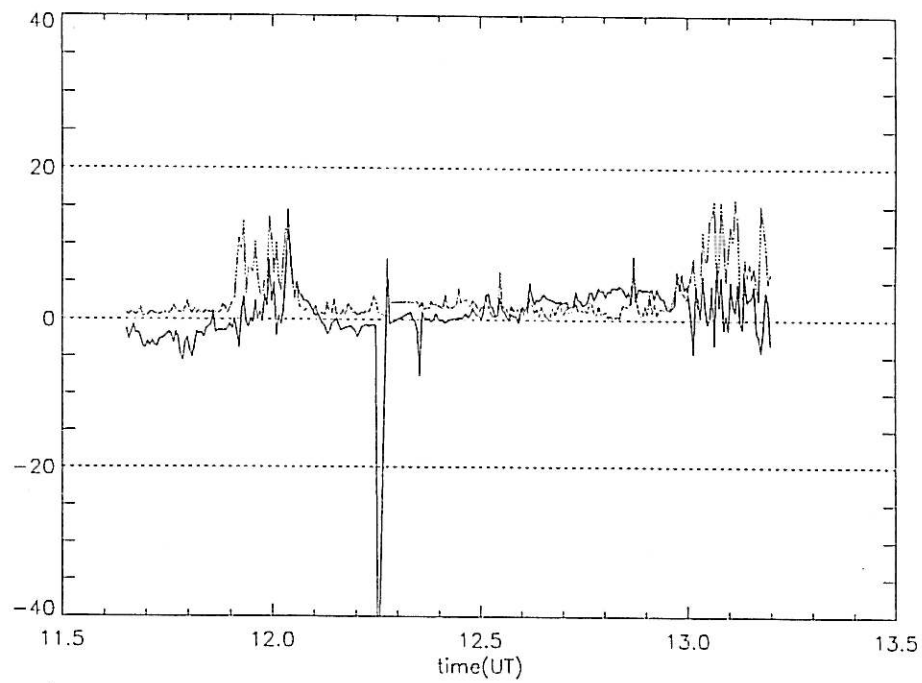






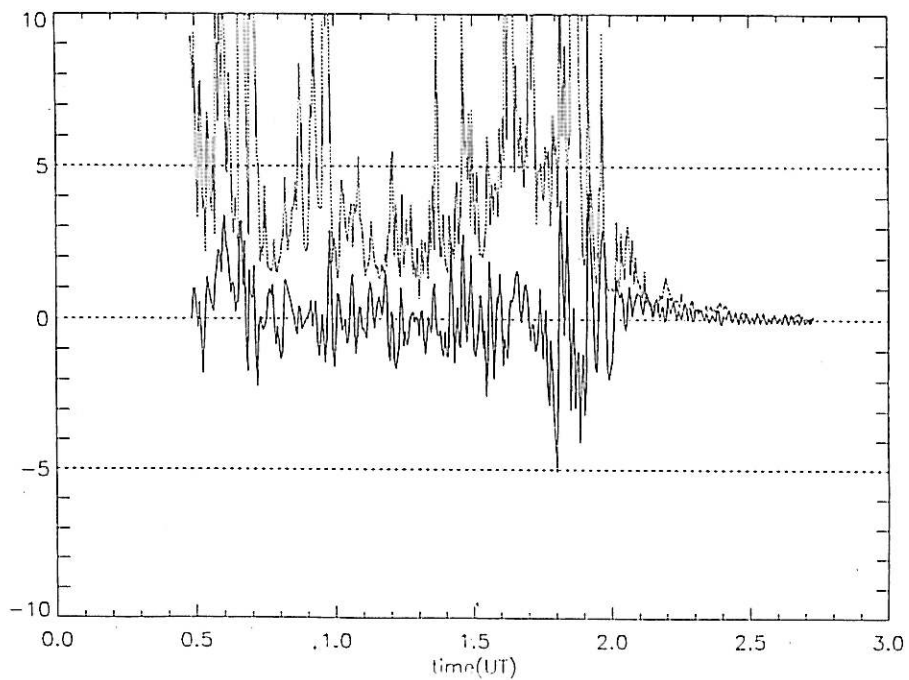
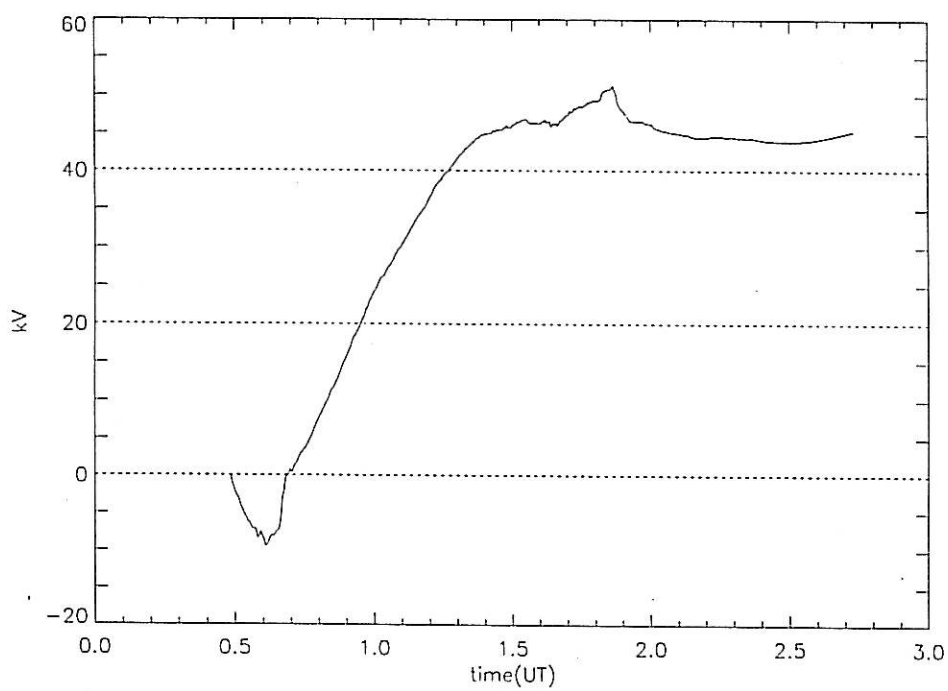
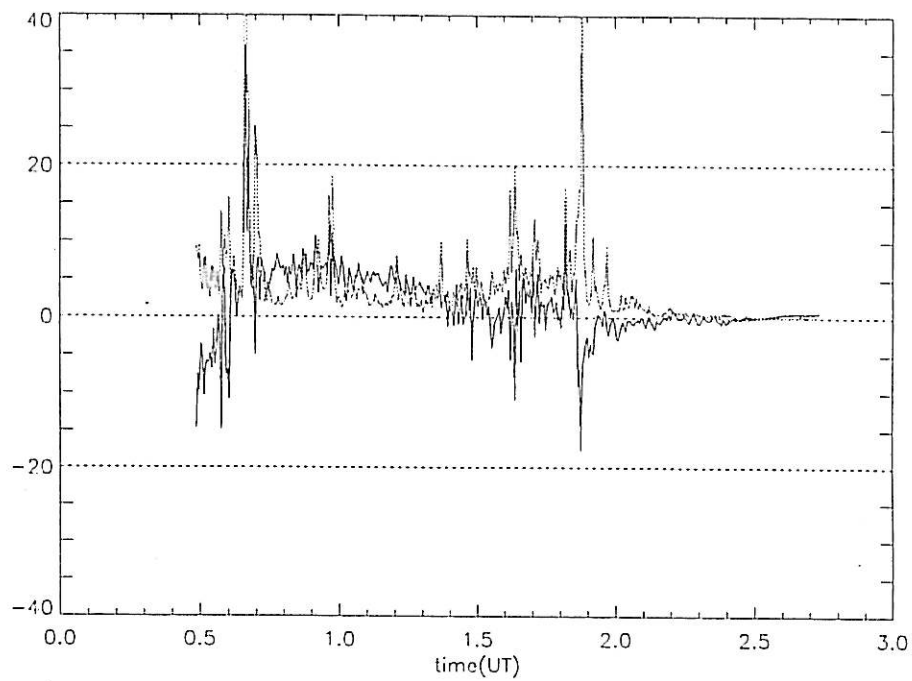




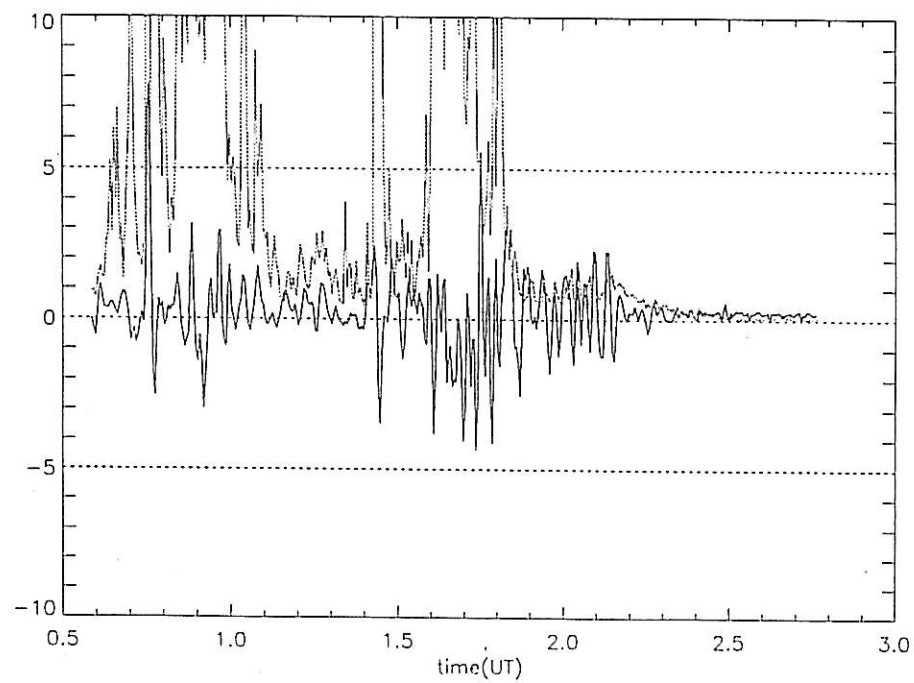
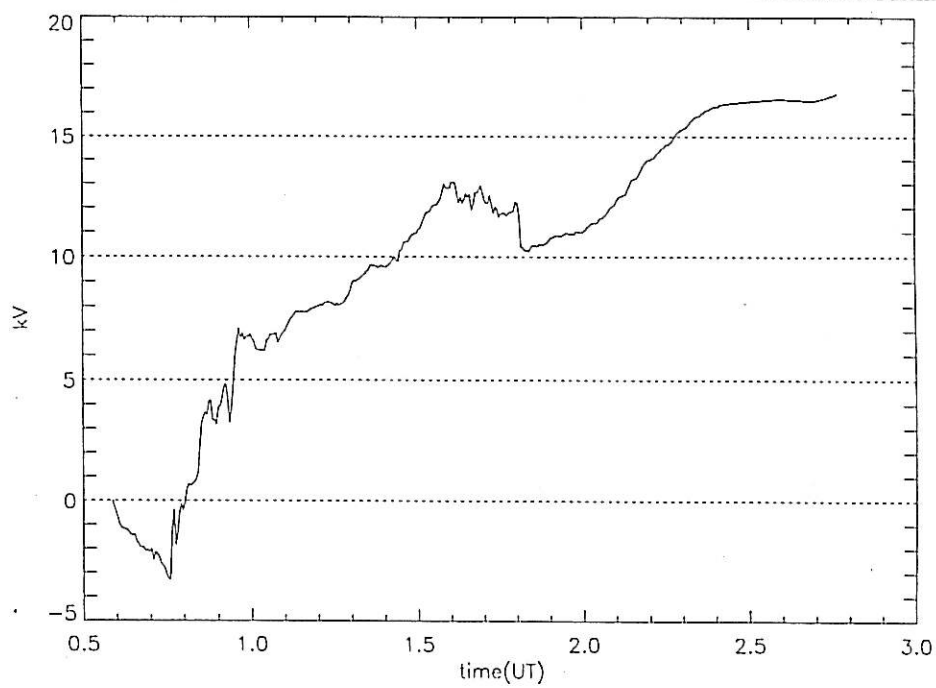
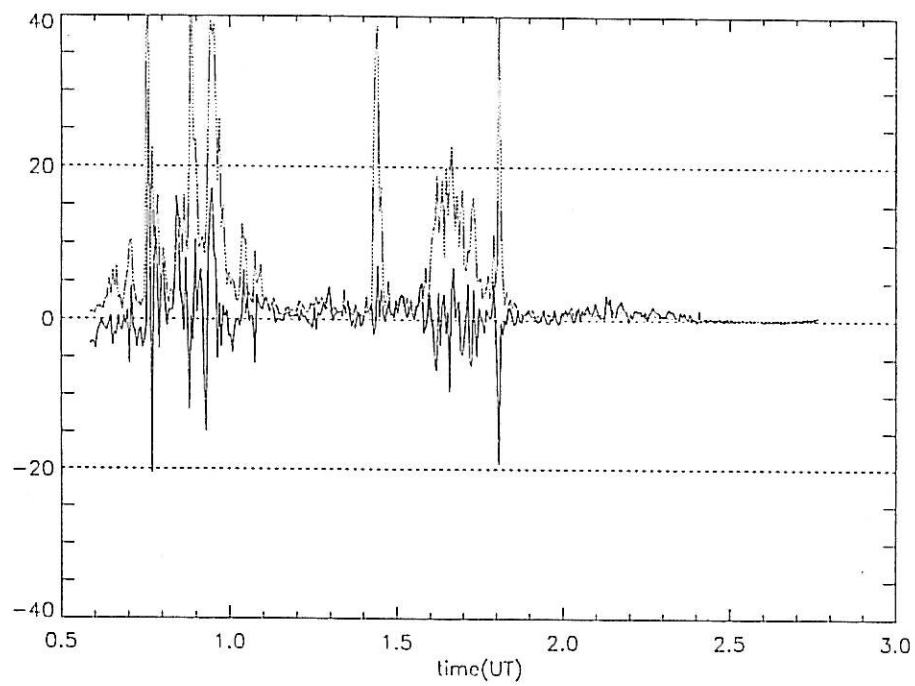




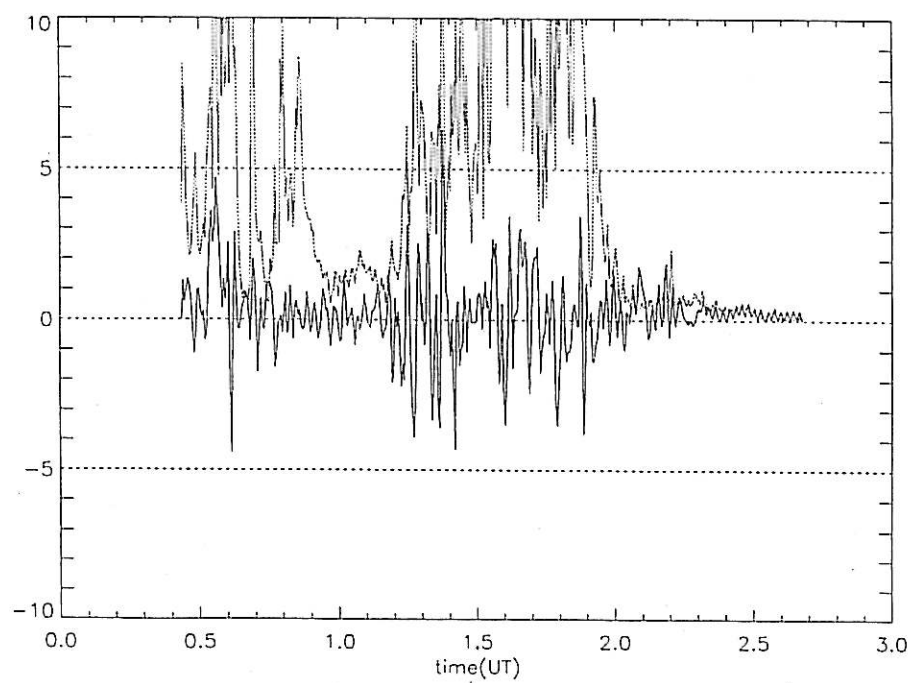
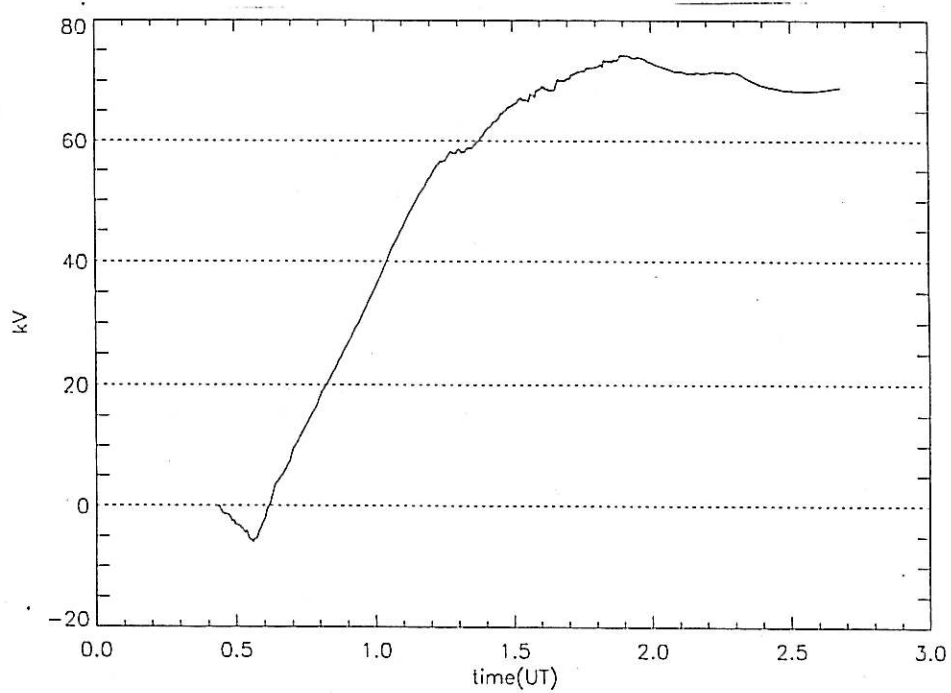
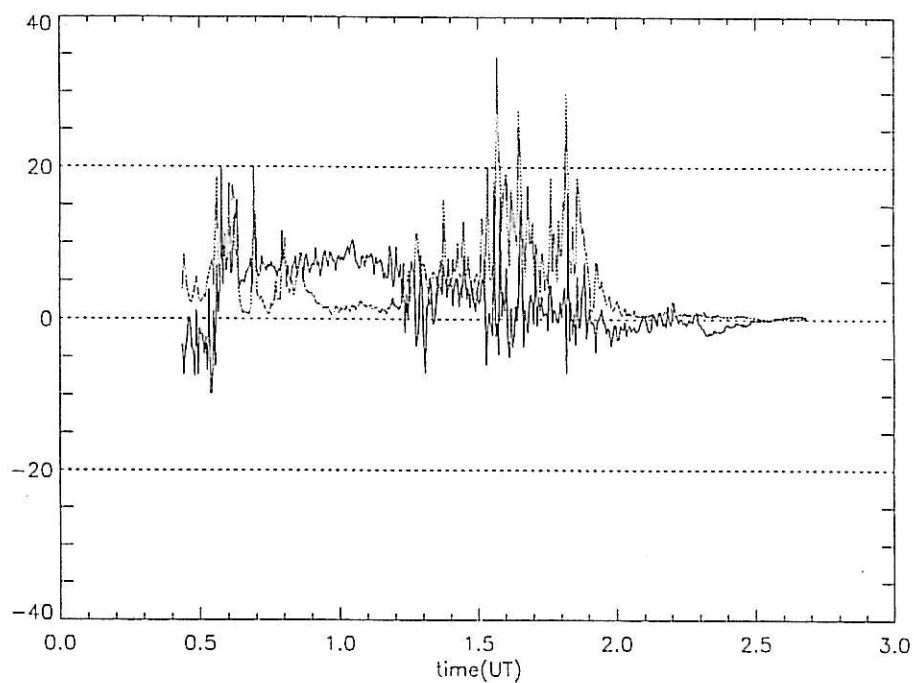




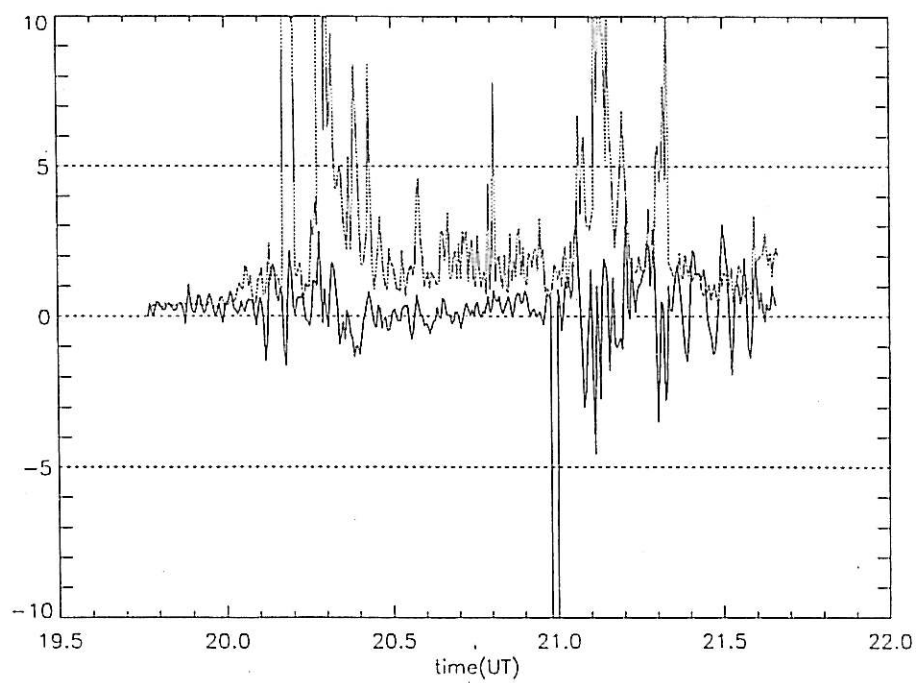
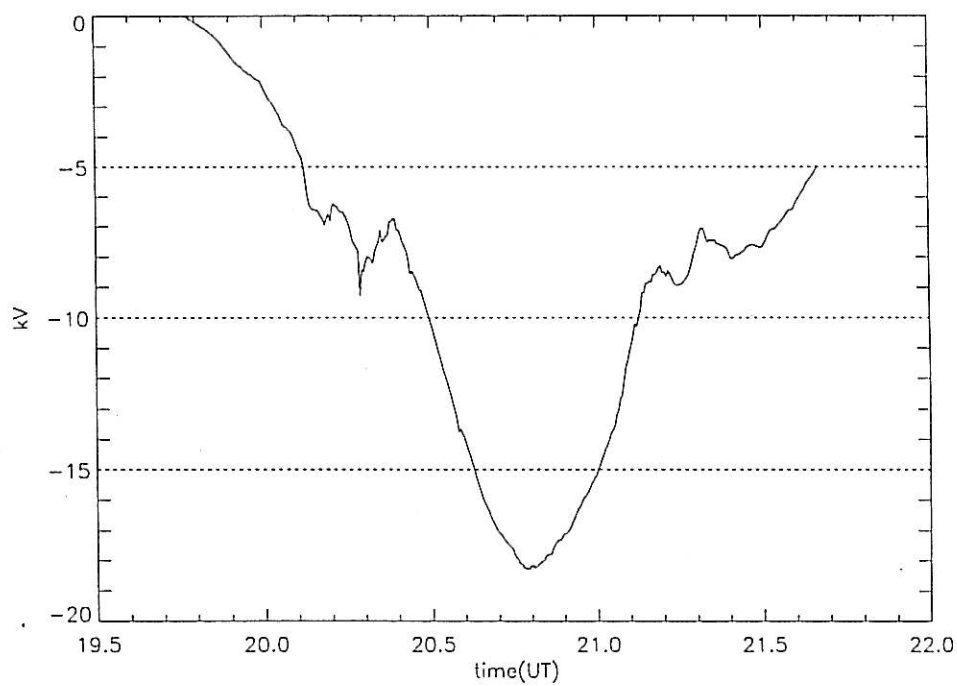
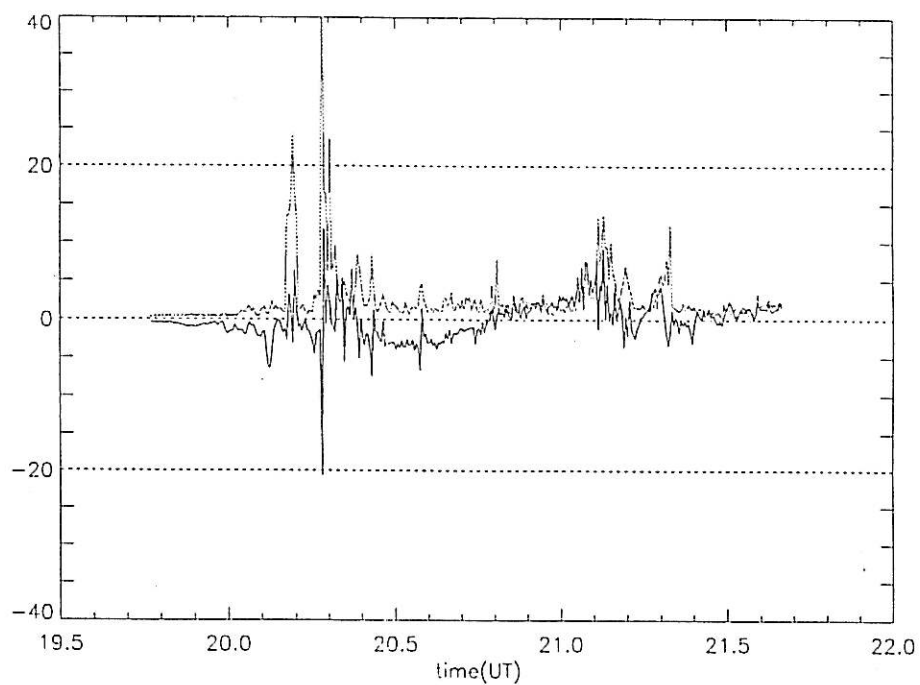






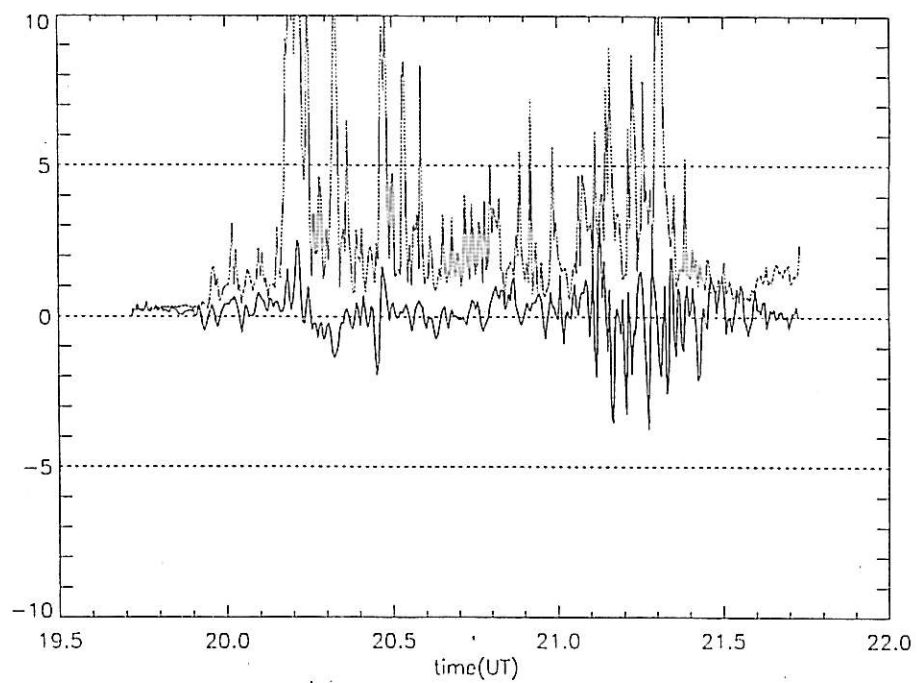
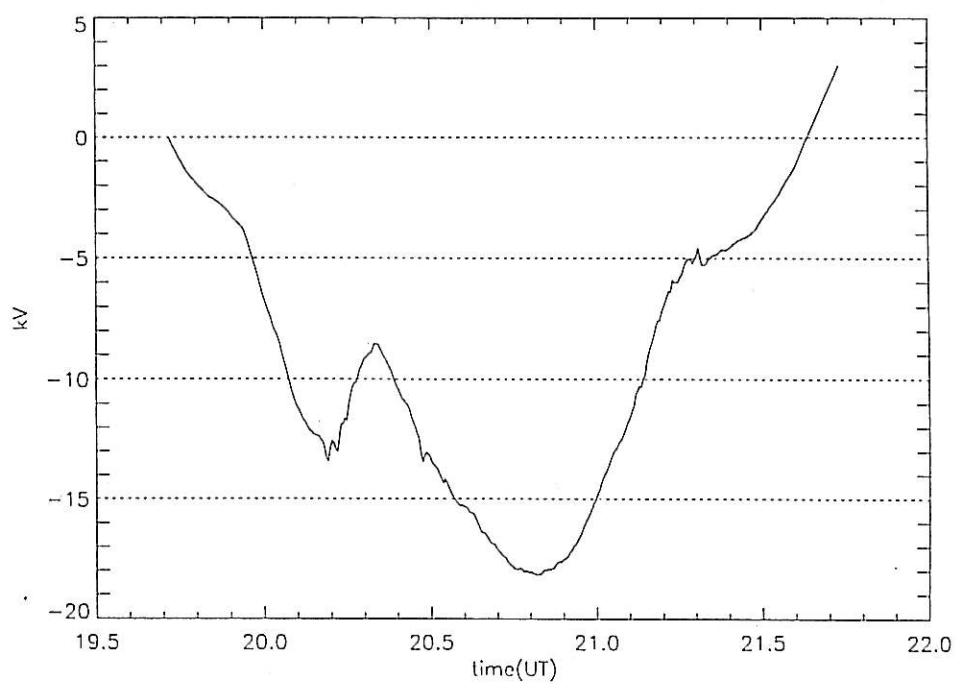
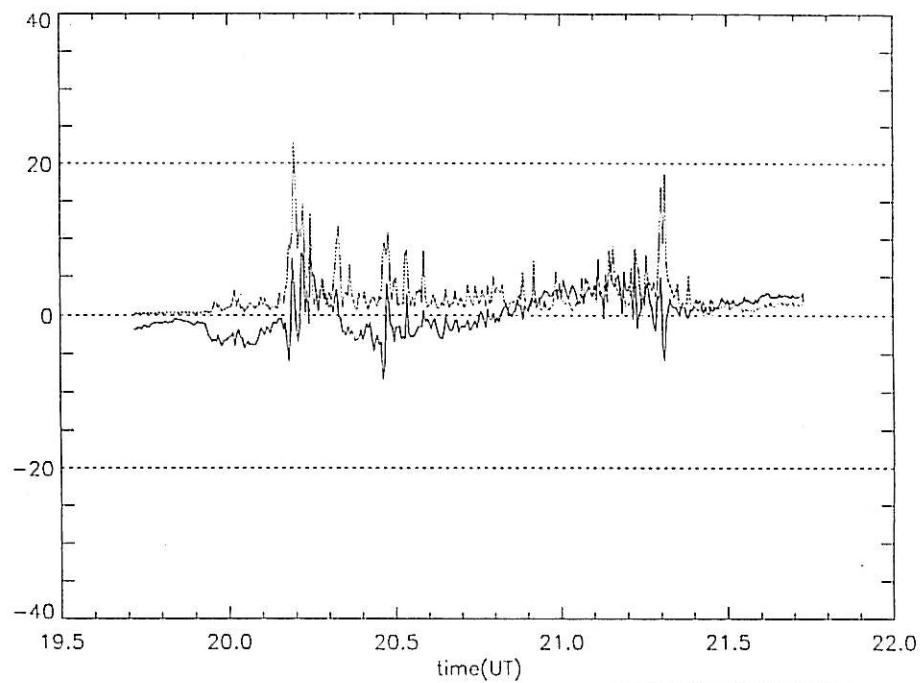




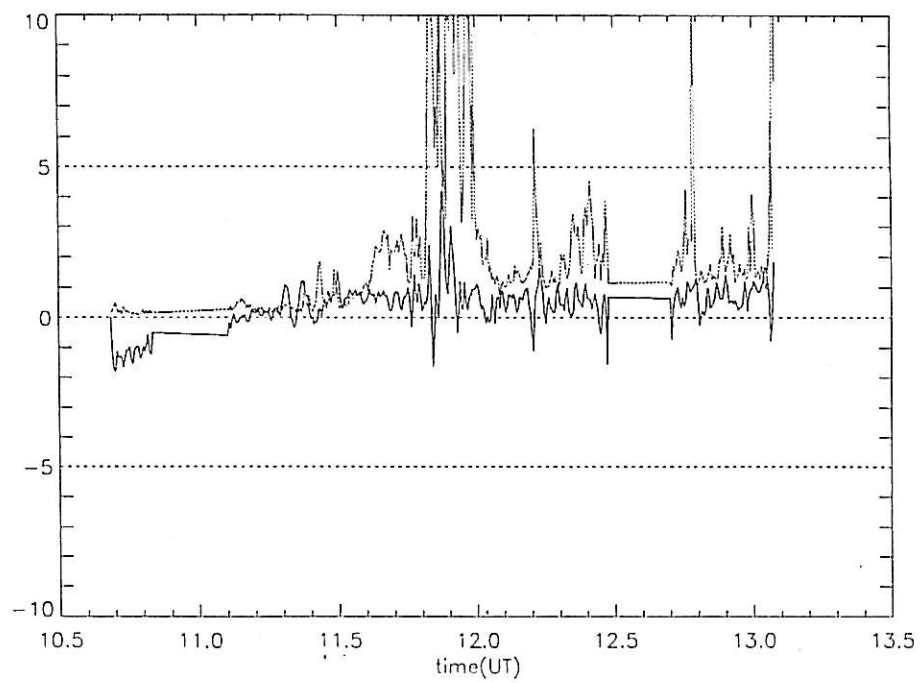
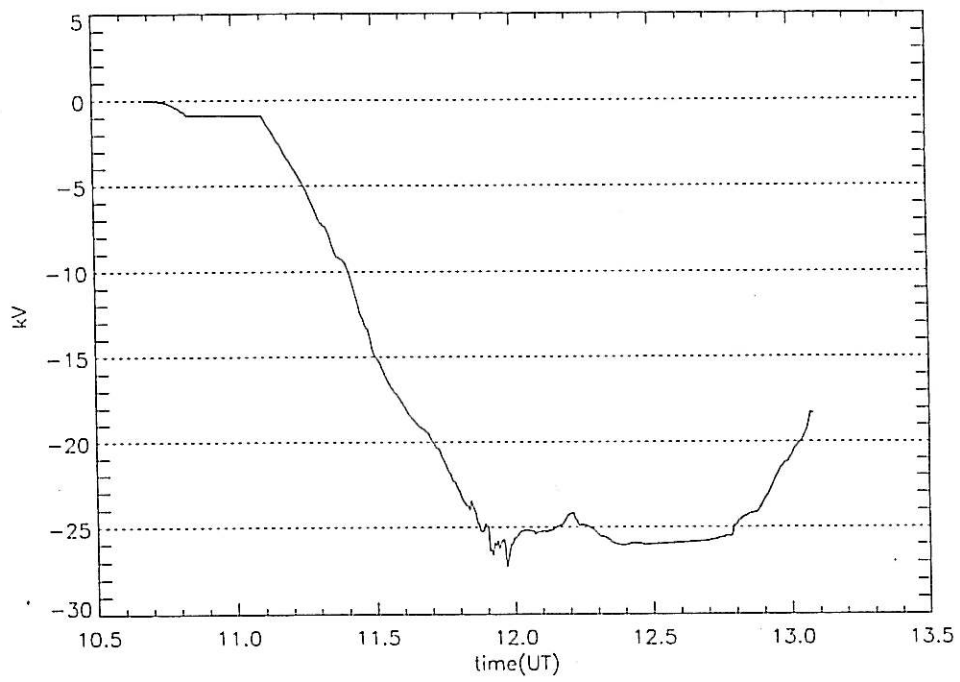
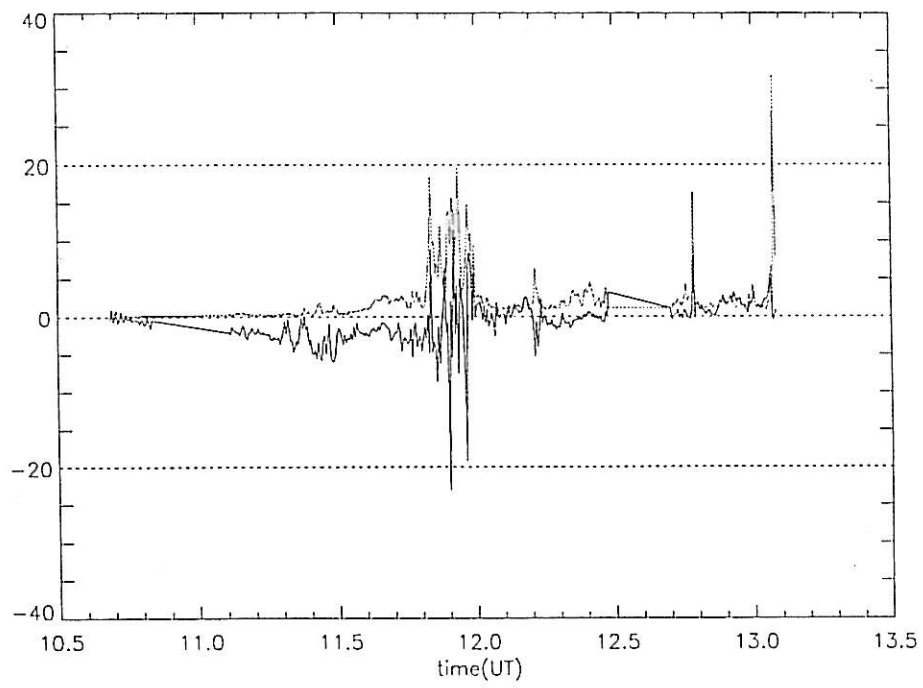




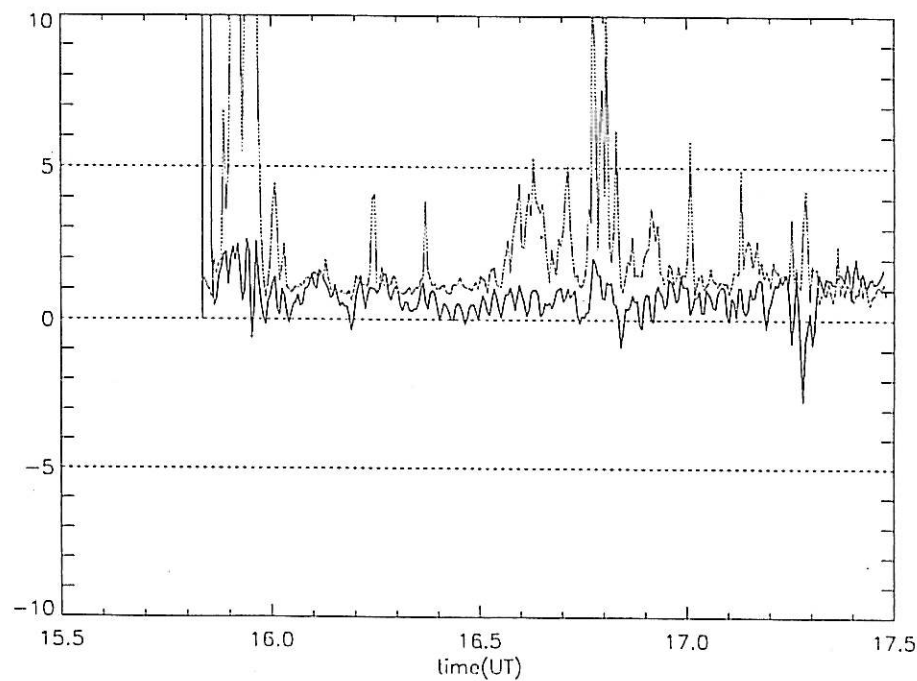
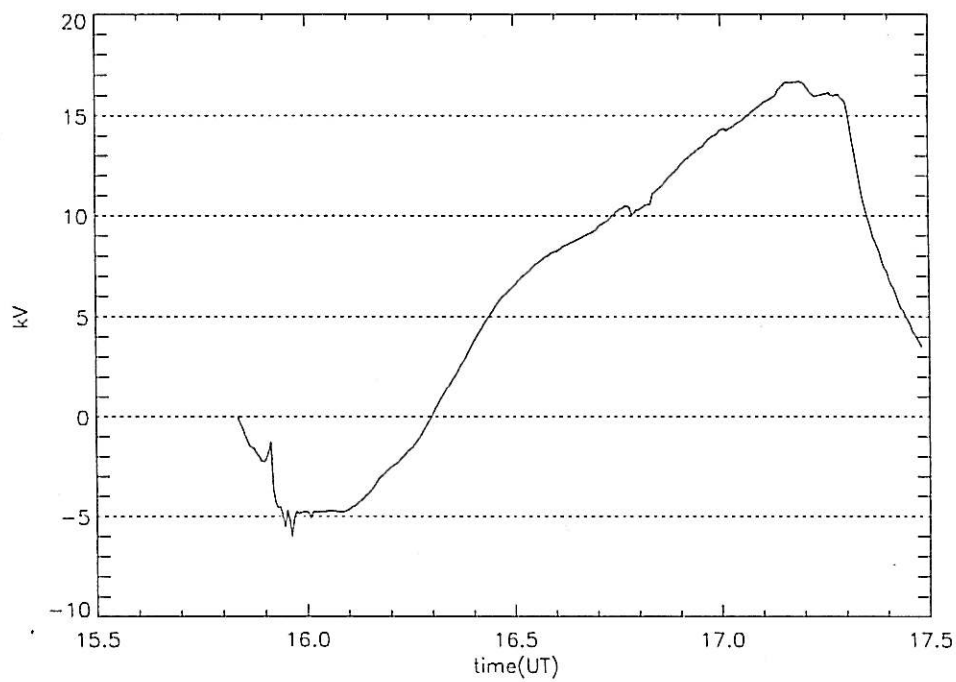
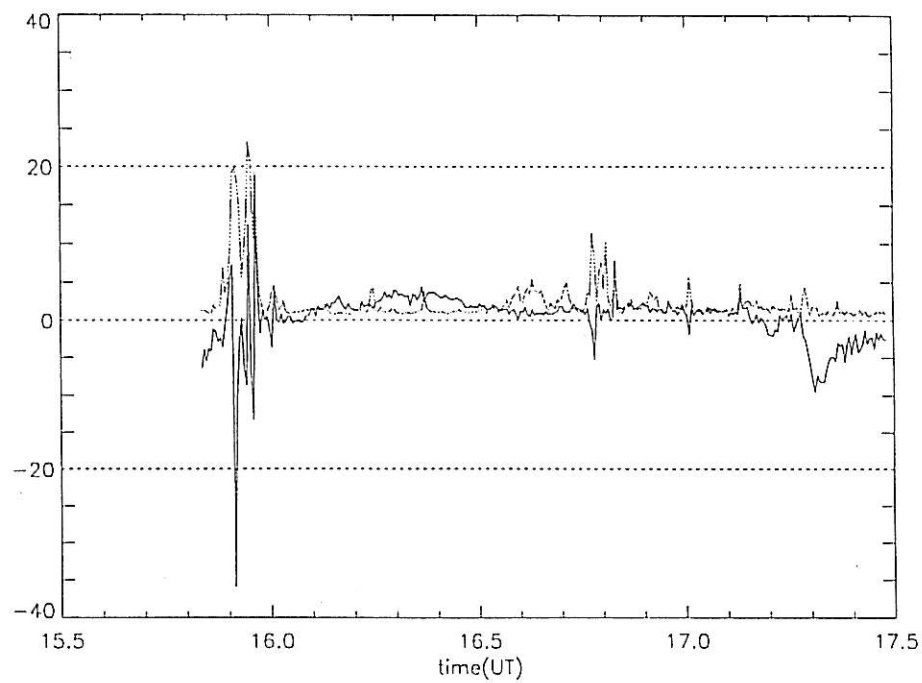




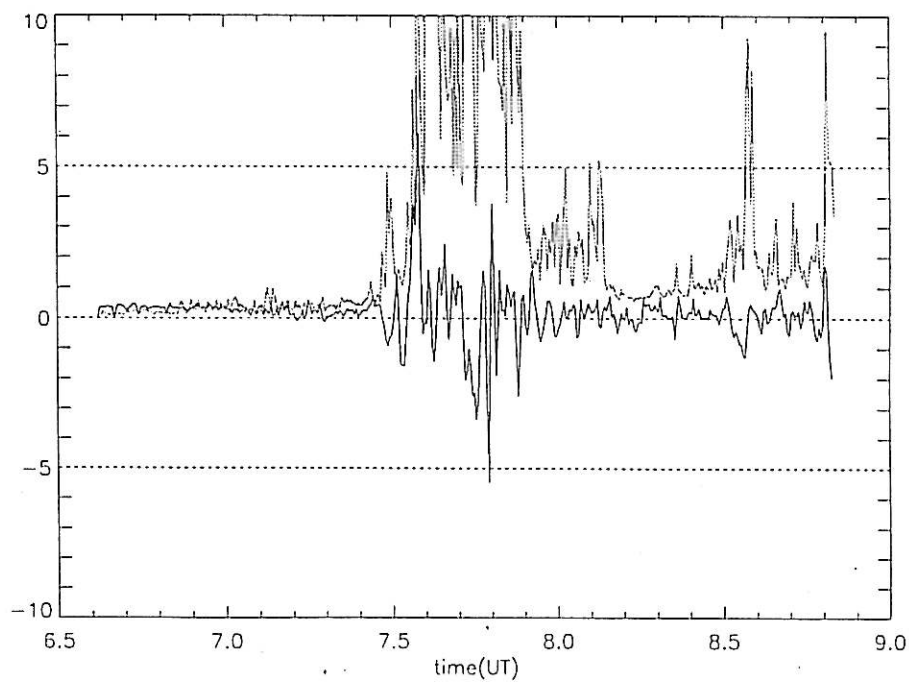
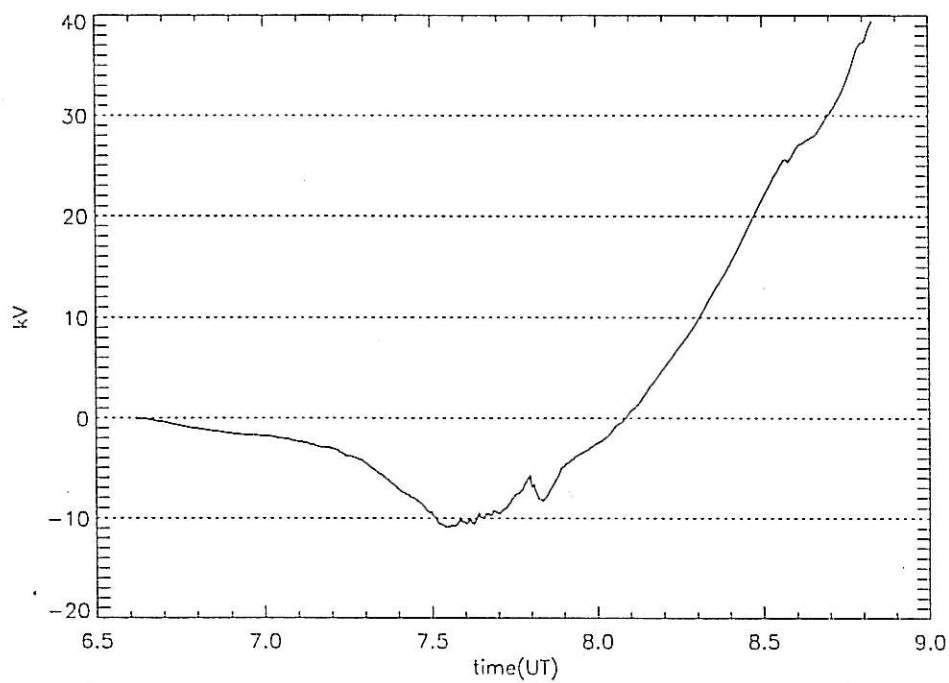
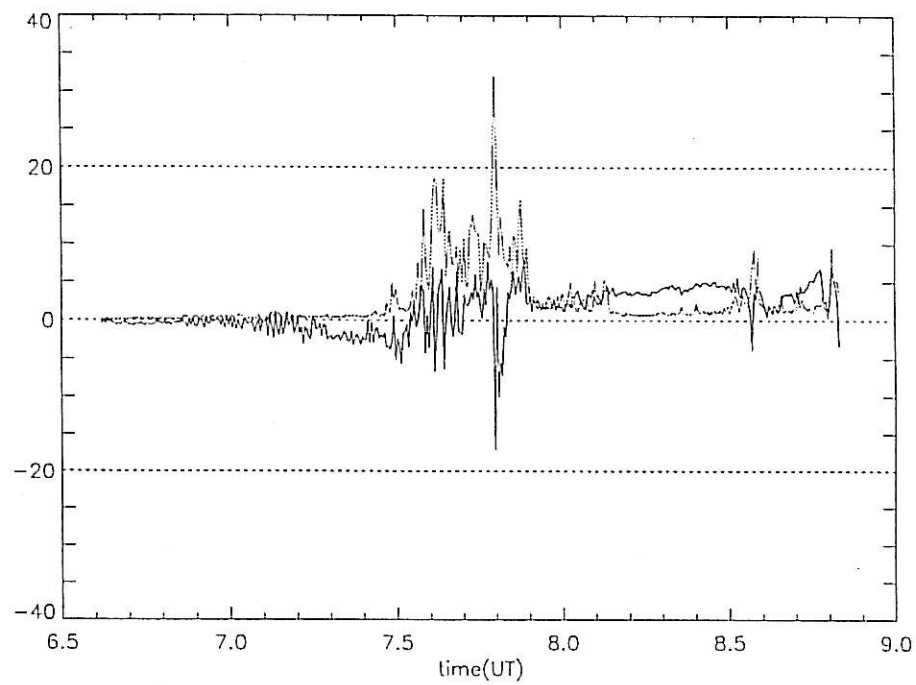






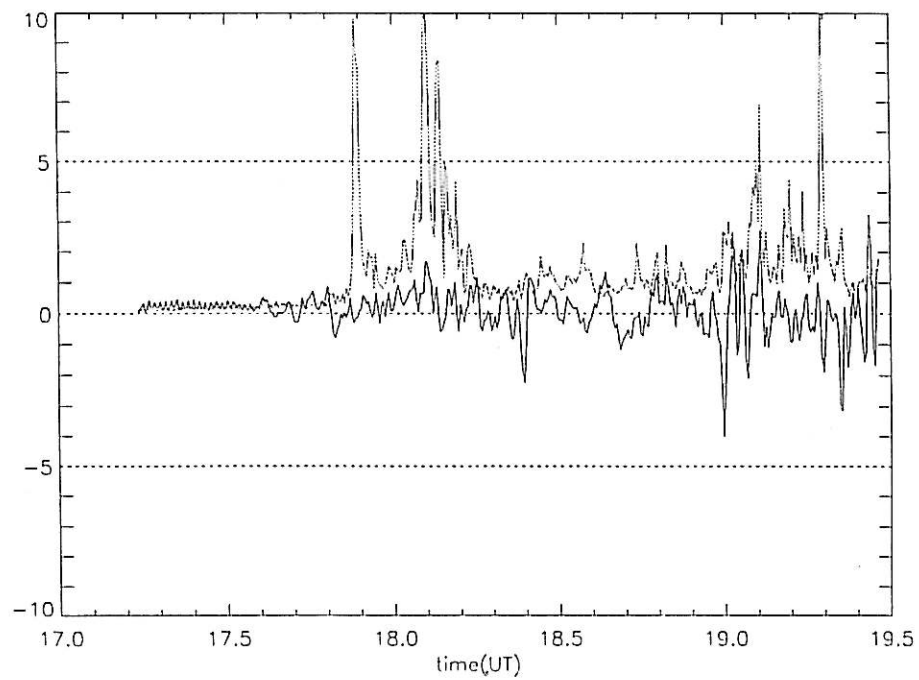
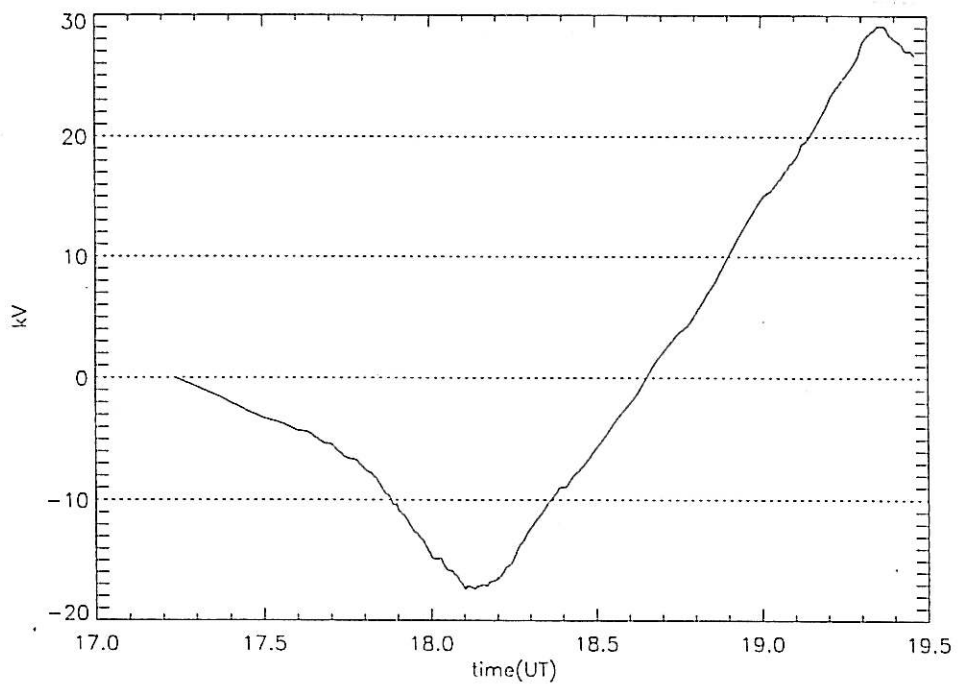
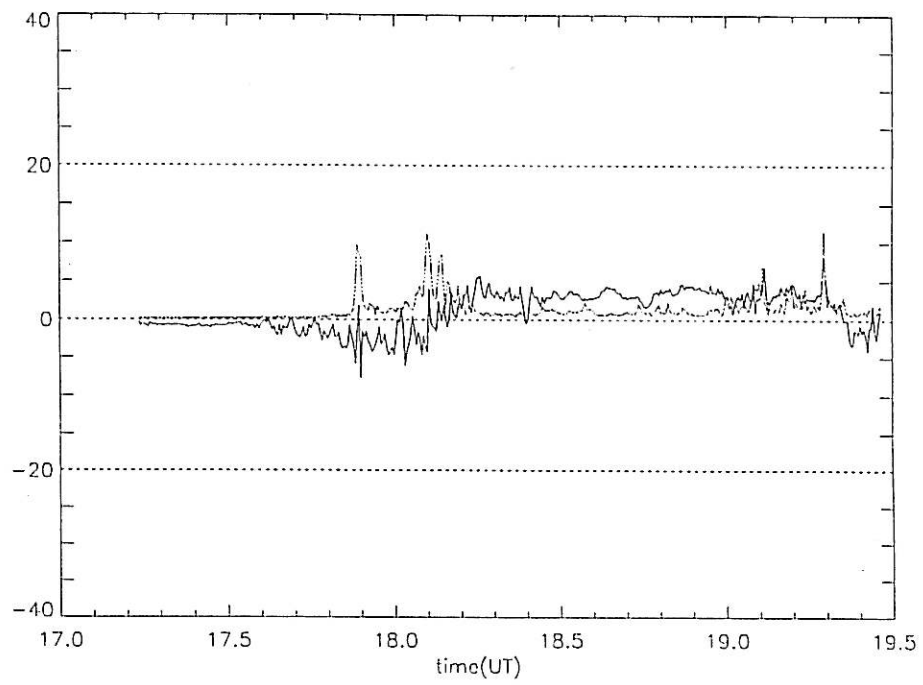




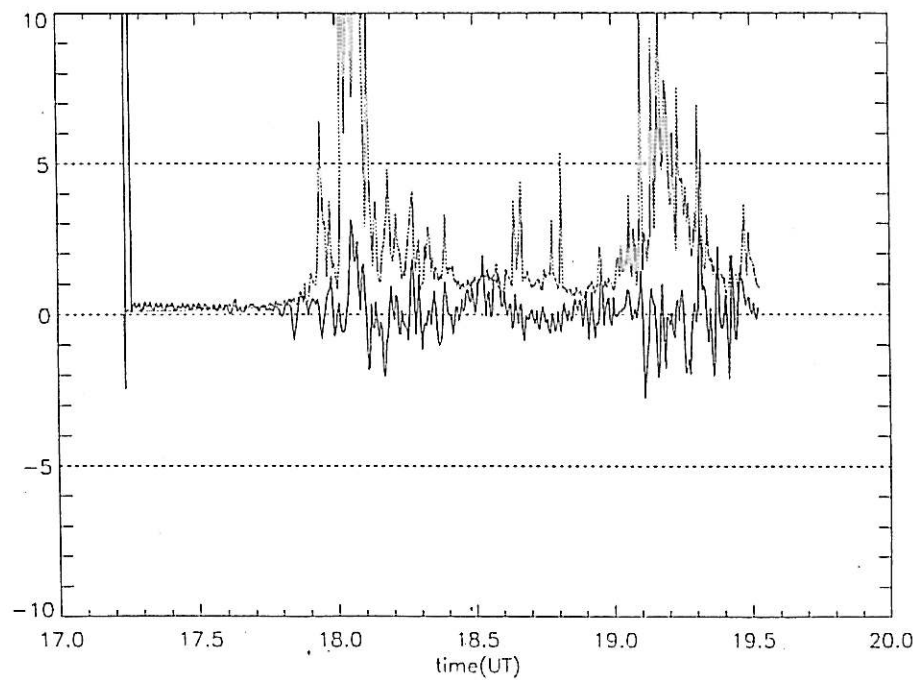
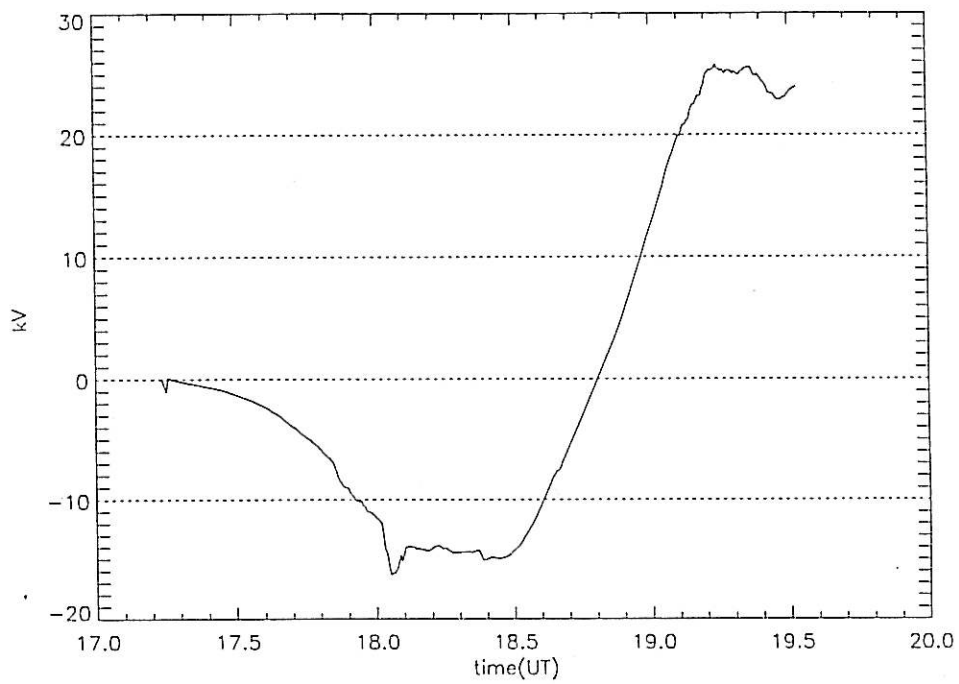
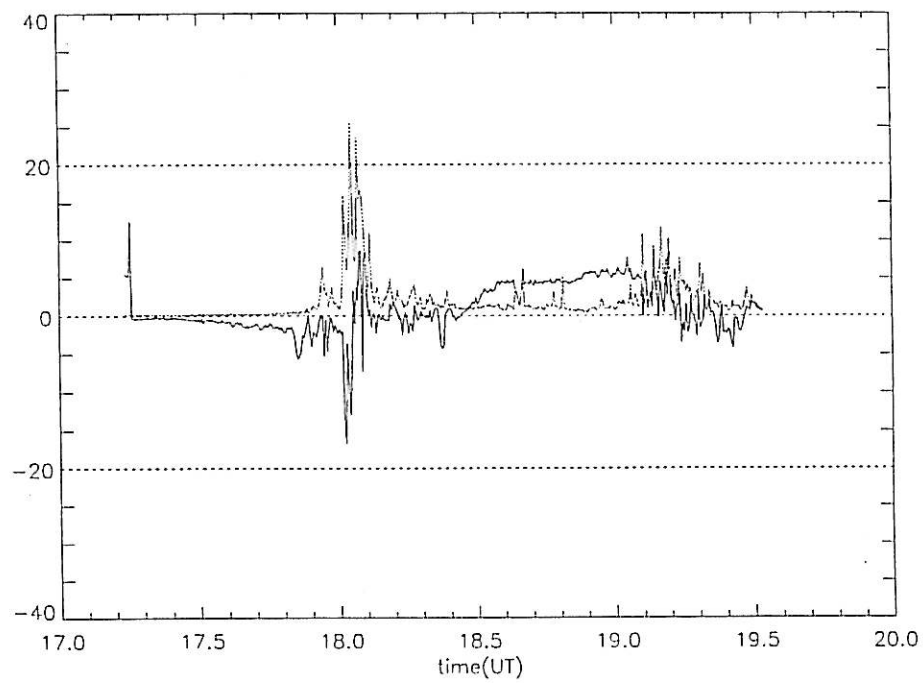




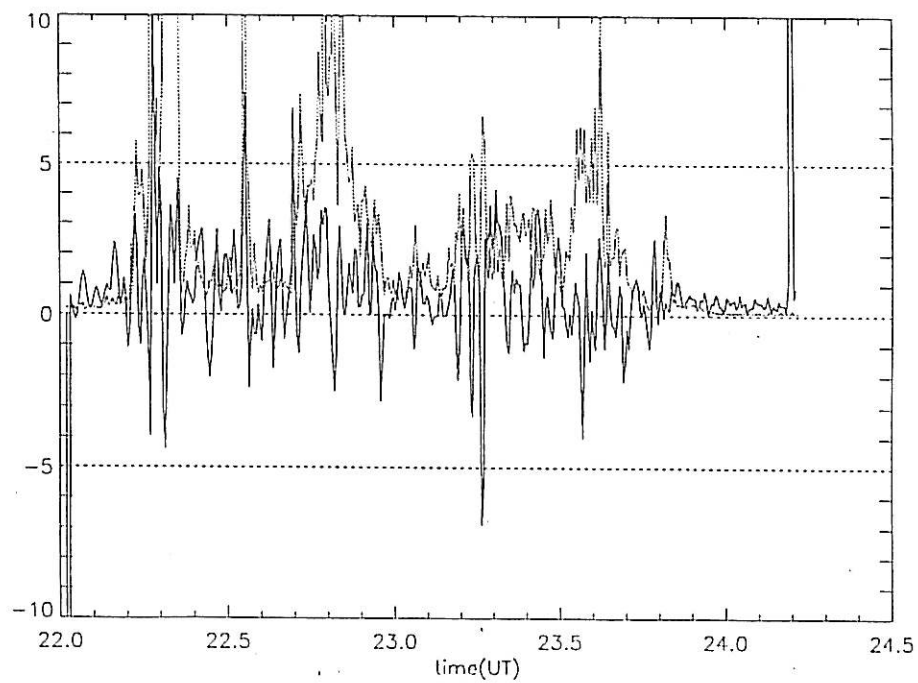
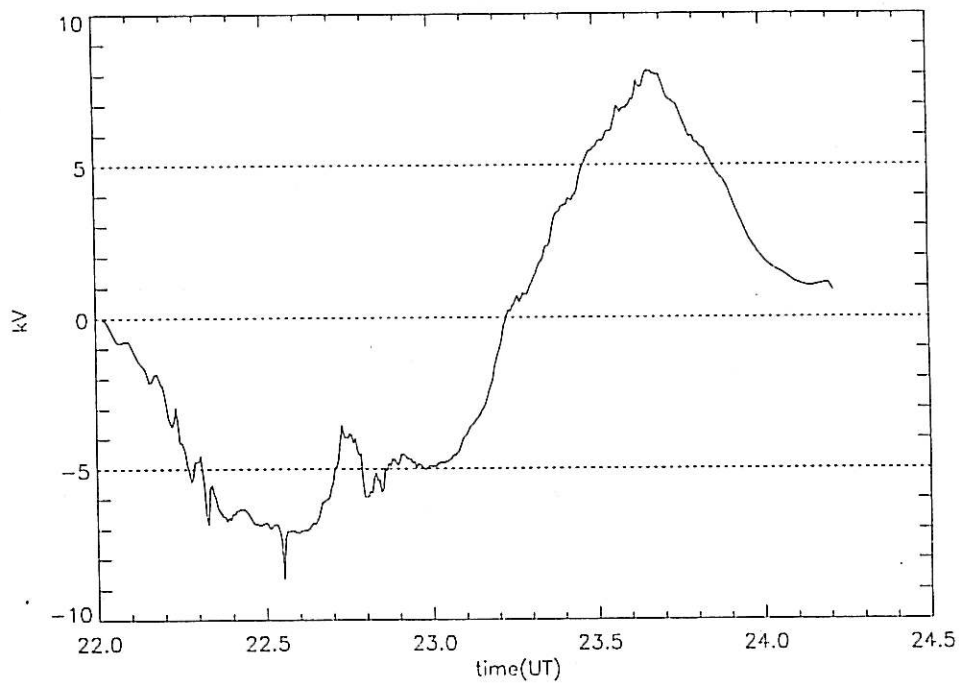
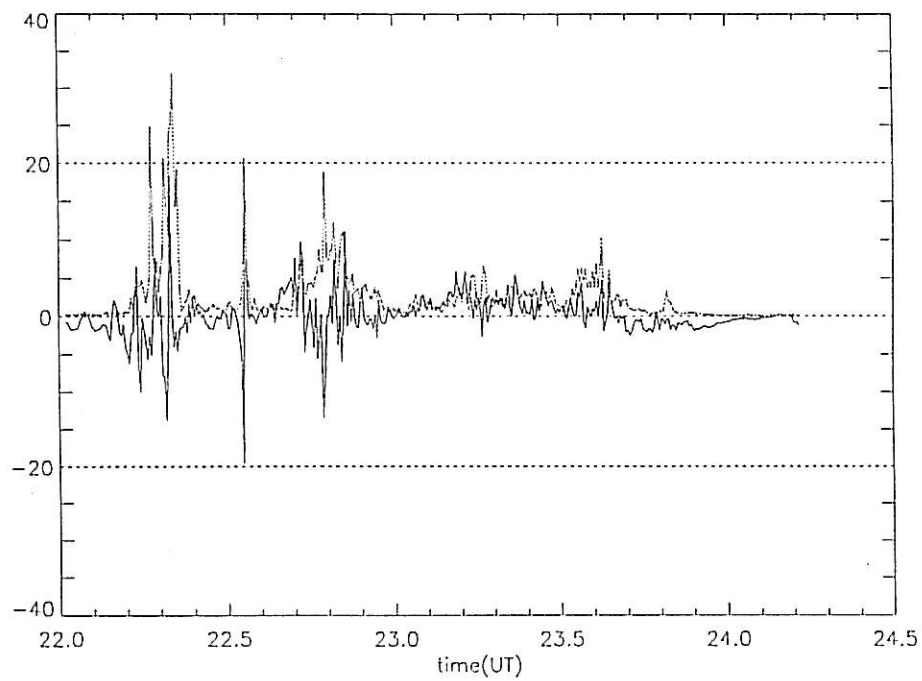




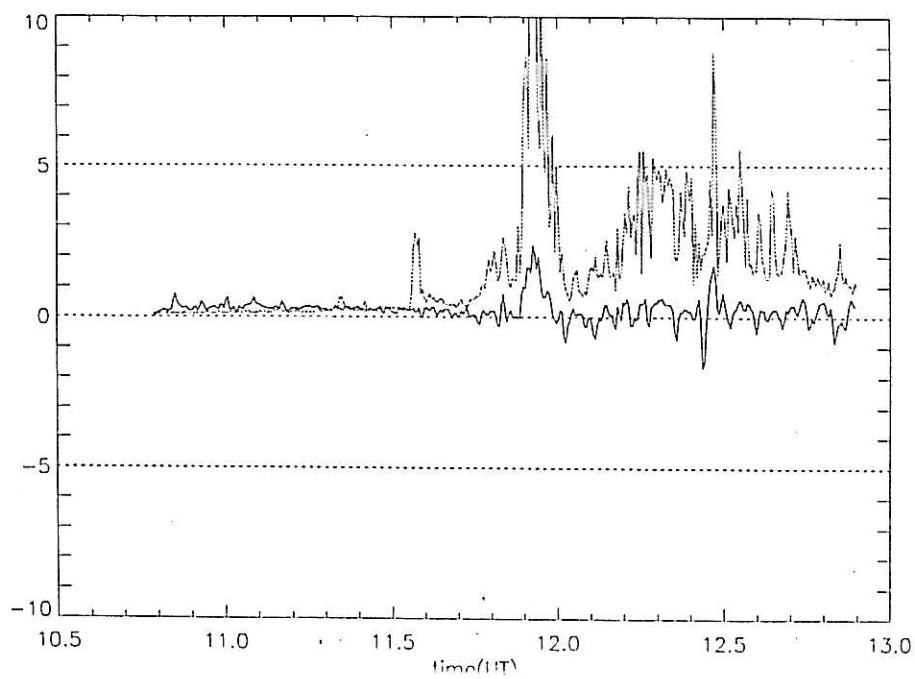
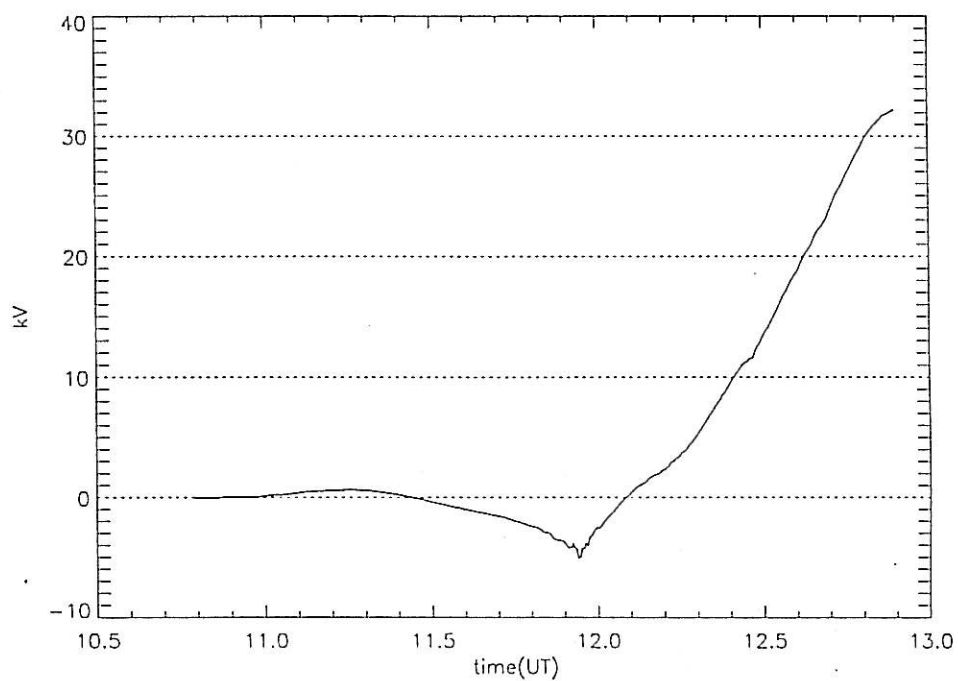
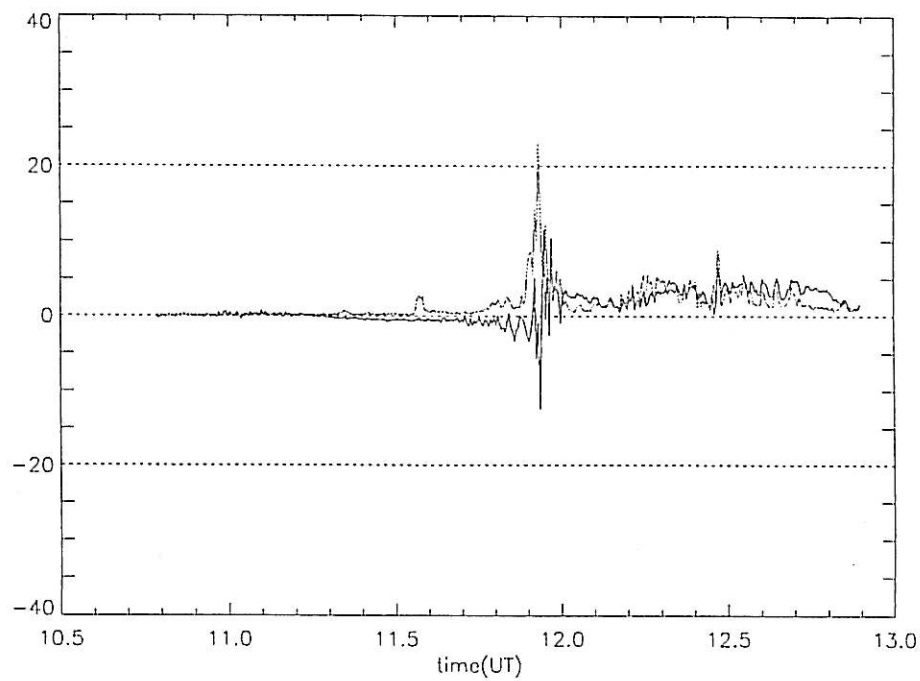






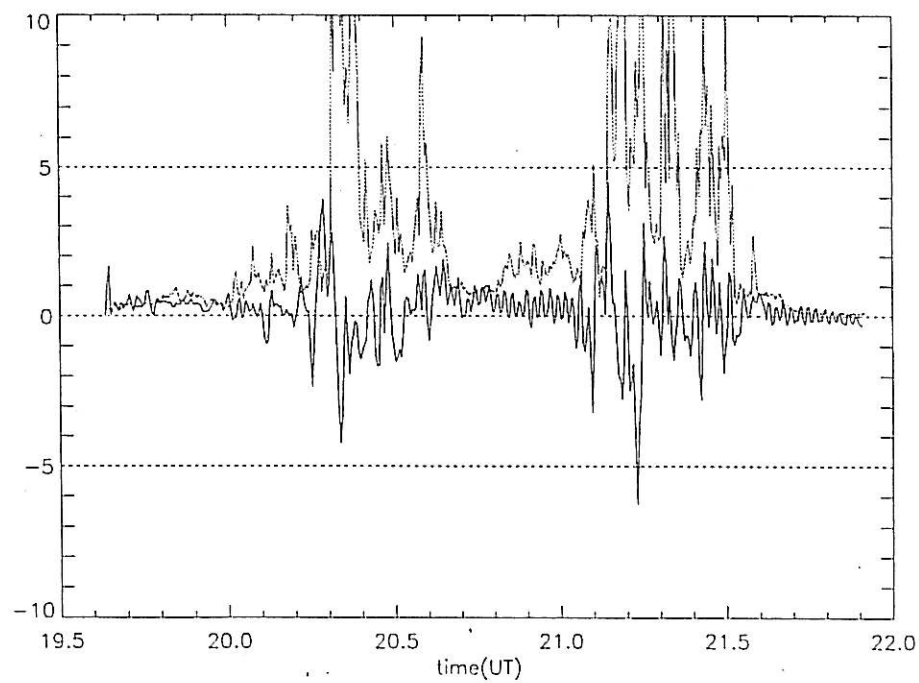
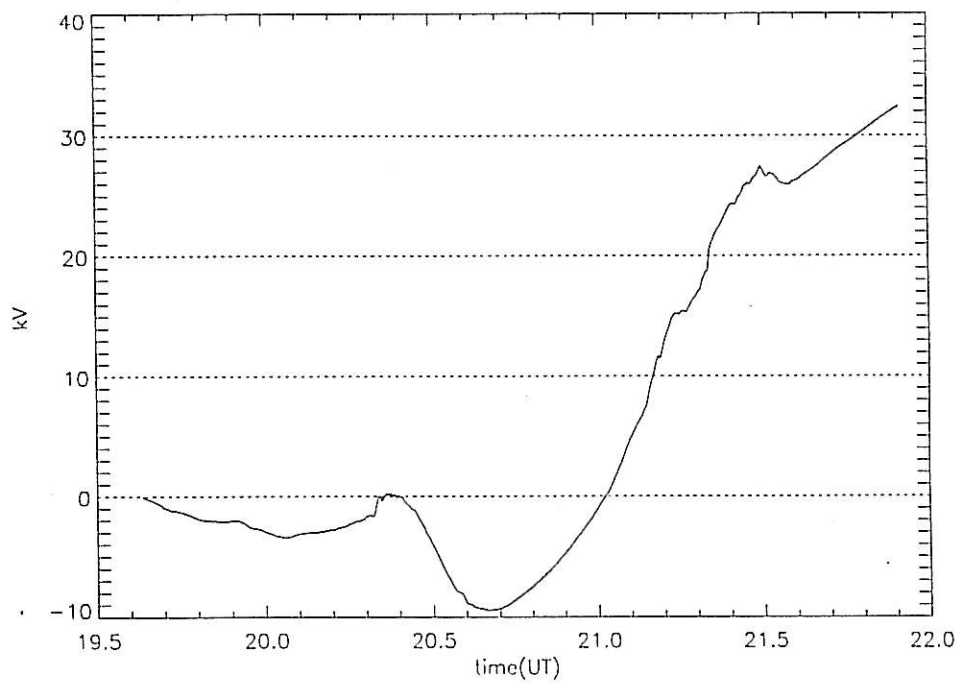
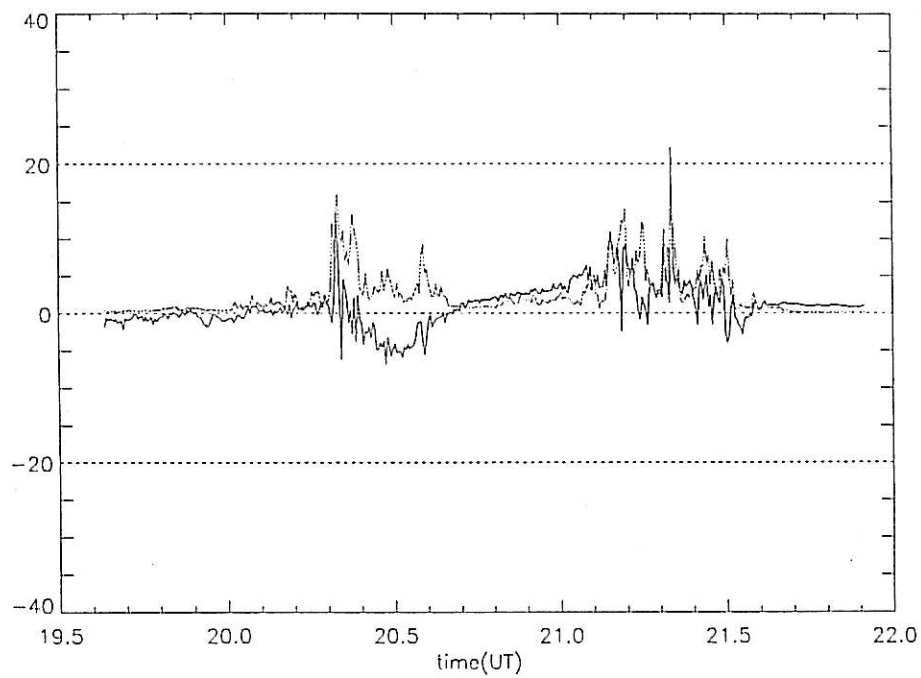




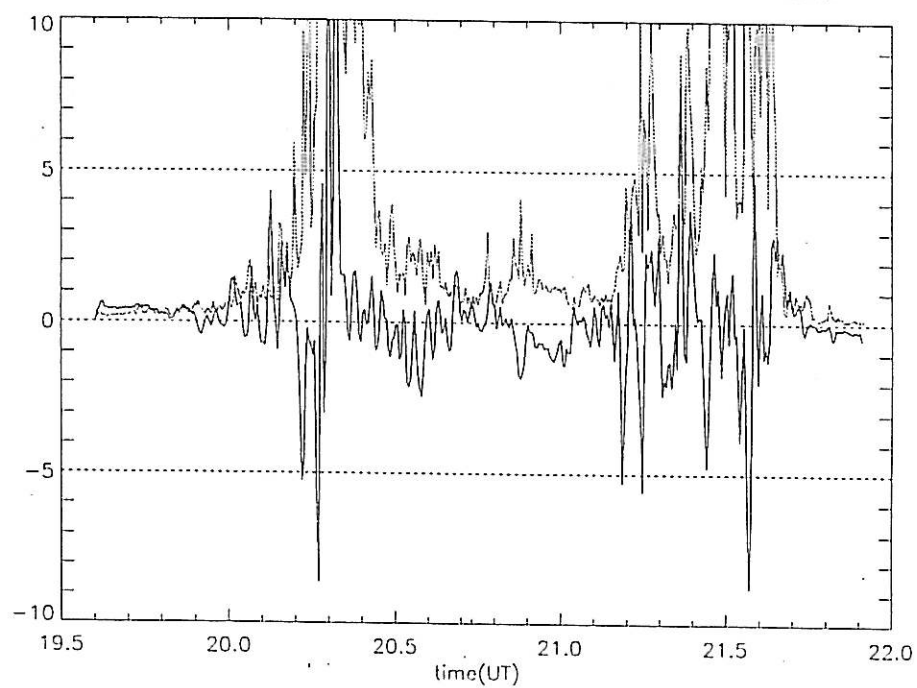
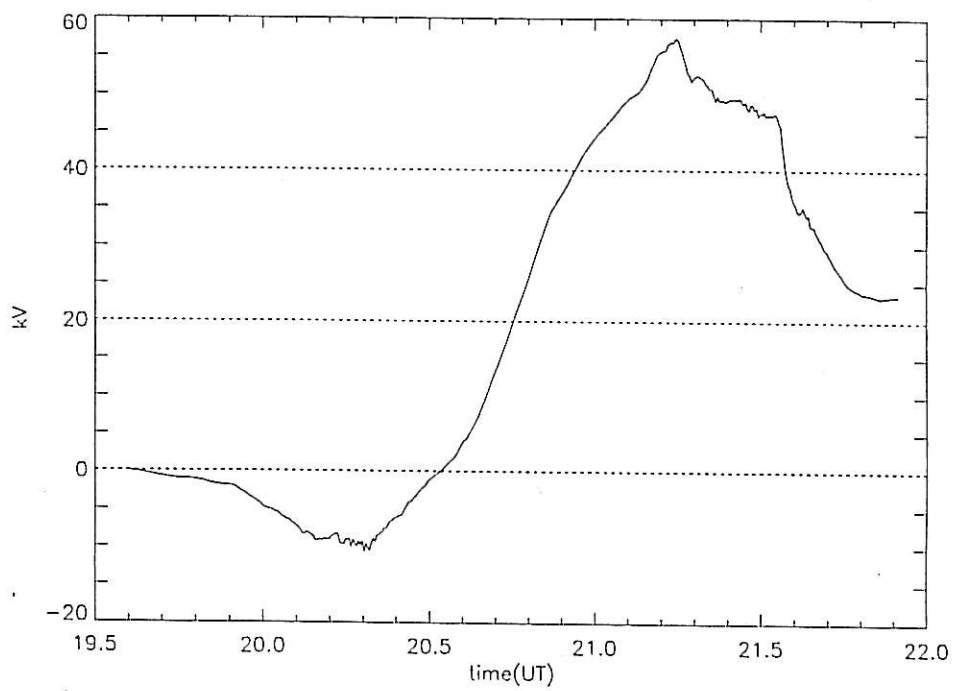
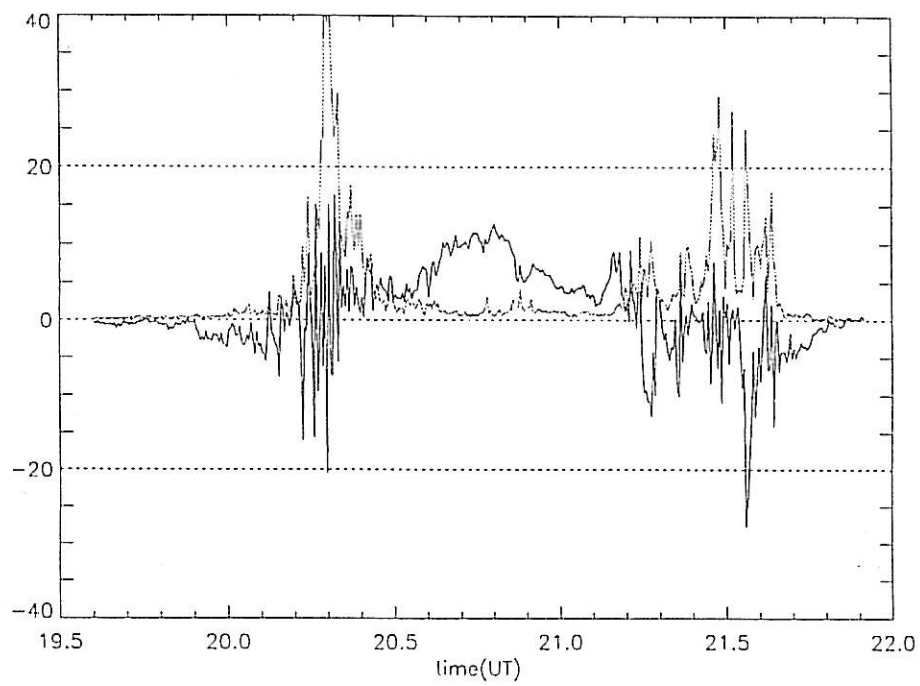




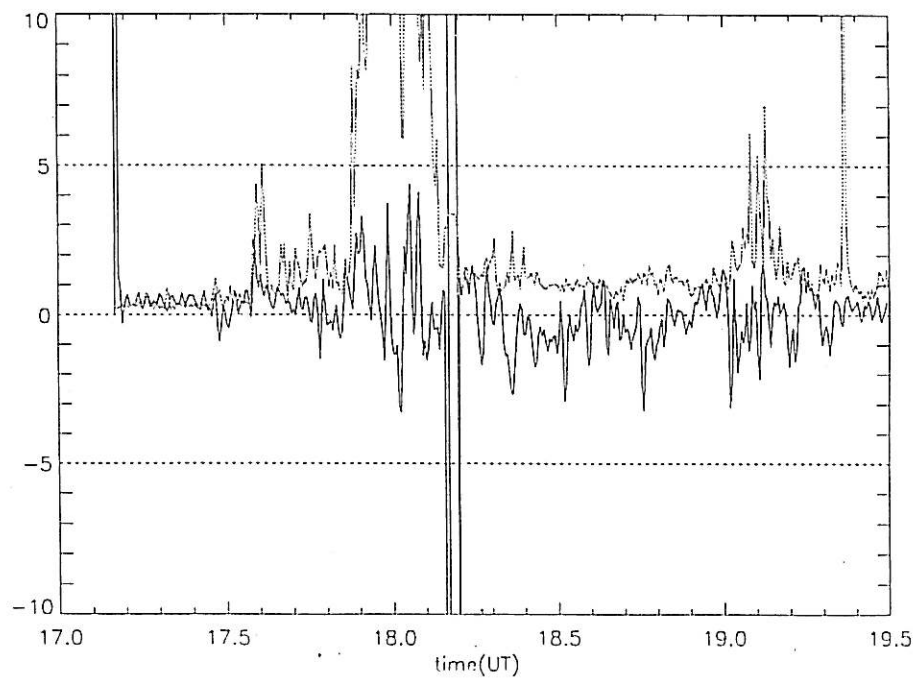
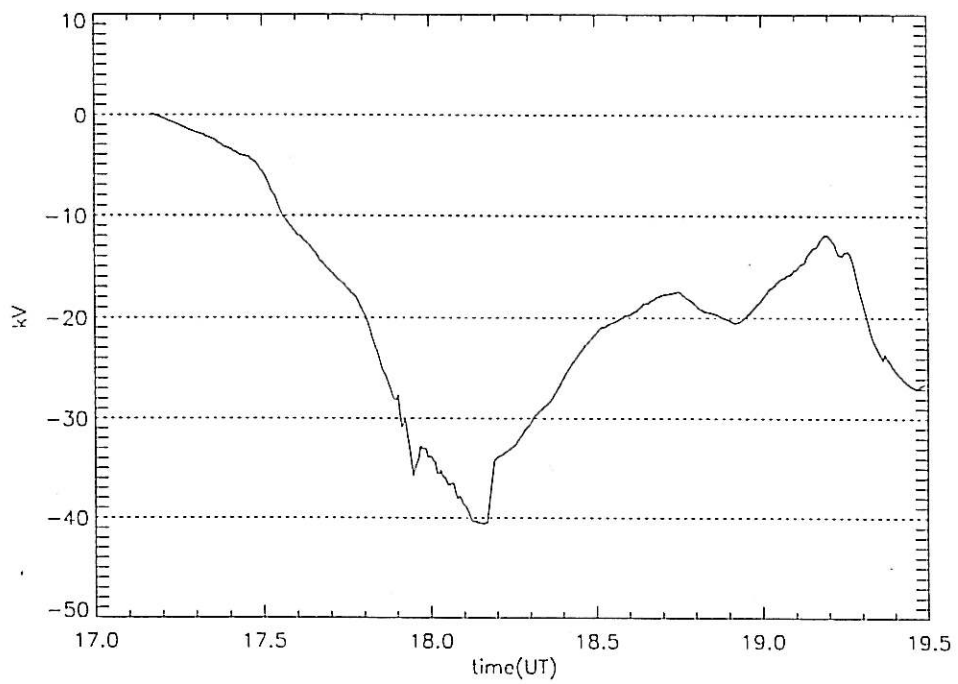
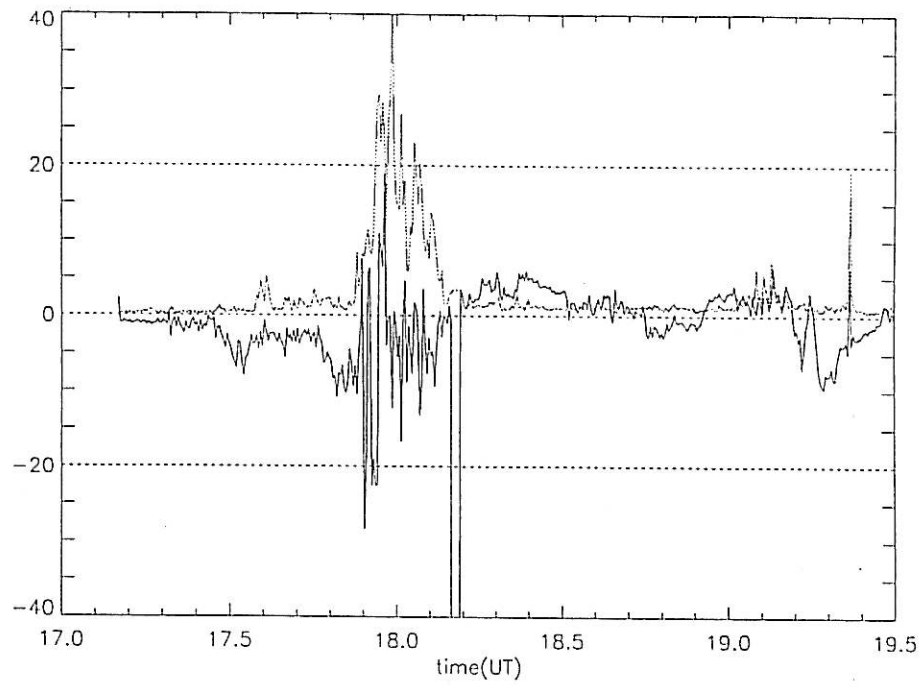










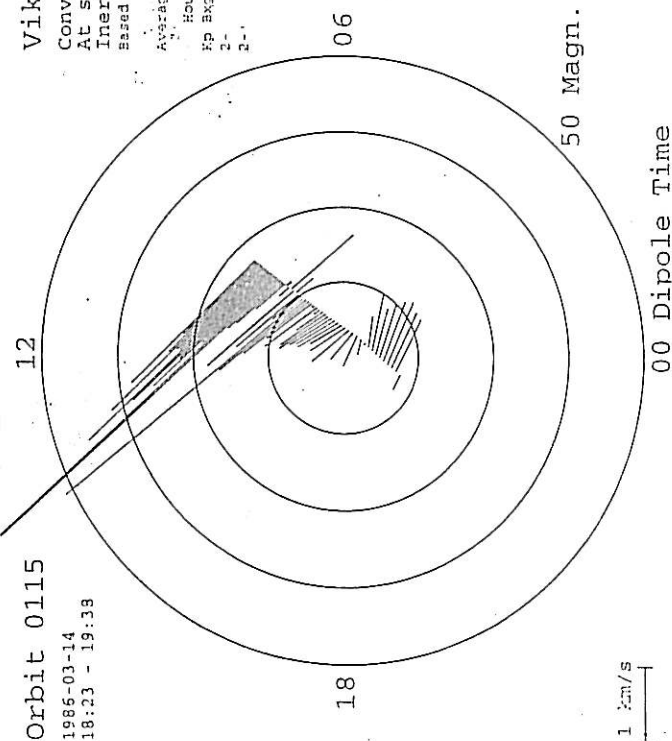




Orbit 0115  
1986-03-14  
18:23 - 19:38

Viking V1 Data  
Convection velocity  
At satellite  
Inertial frame  
Based on spin plane component of E

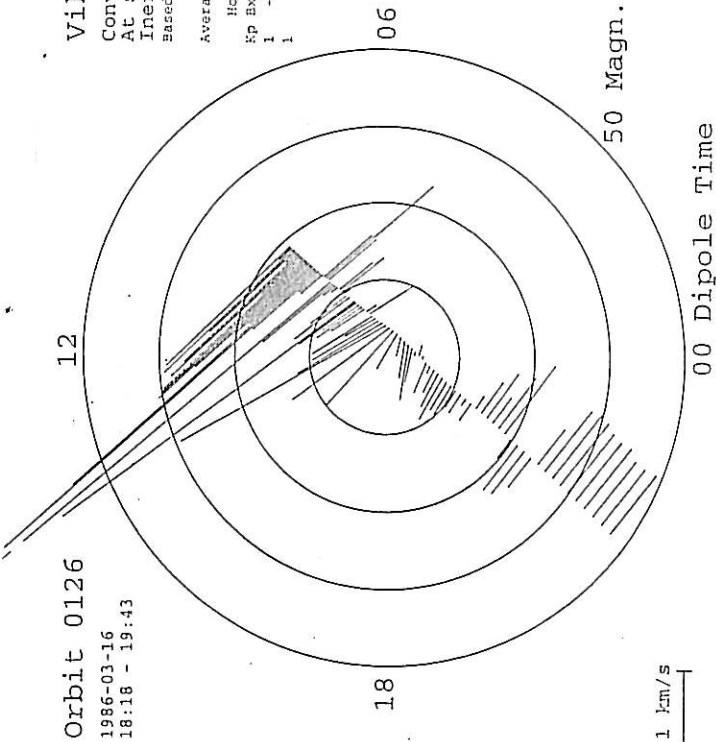
Averaging interval 60 seconds  
Hourly solar wind parameters:  
Kp Bzgm Bygm Bzgm Temp Dens Speed  
1 -5.6 1.3 -0.1 6.7 9.2 405.0  
2 -



Orbit 0126  
1986-03-16  
18:18 - 19:43

Viking V1 Data  
Convection velocity  
At satellite  
Inertial frame  
Based on spin plane component of E

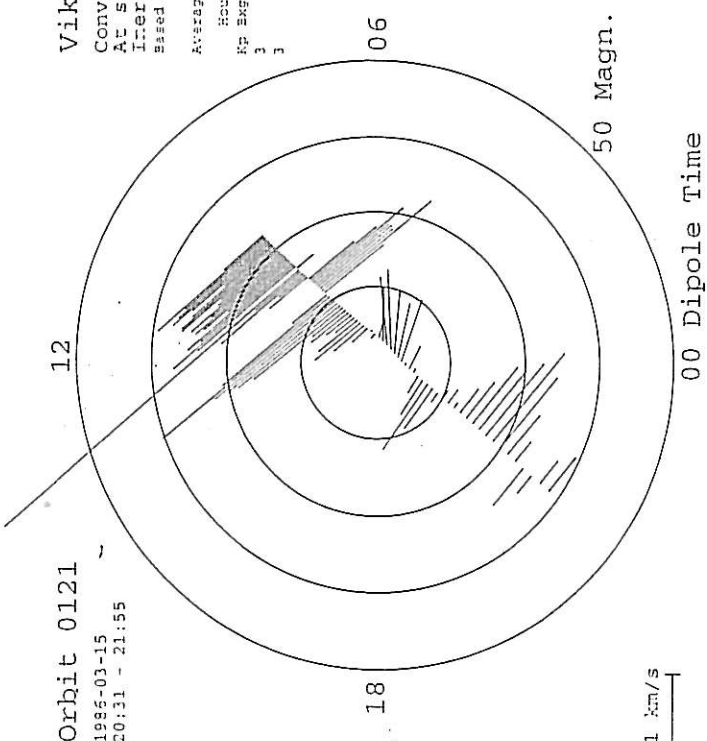
Averaging interval 60 seconds  
Hourly solar wind parameters:  
Kp Bzgm Bygm Bzgm Temp Dens Speed  
1 -5.6 1.3 -0.1 6.7 9.2 405.0  
2 -



Orbit 0121  
1986-03-15  
20:31 - 21:55

Viking V1 Data  
Convection velocity  
At satellite  
Inertial frame  
Based on spin plane component of E

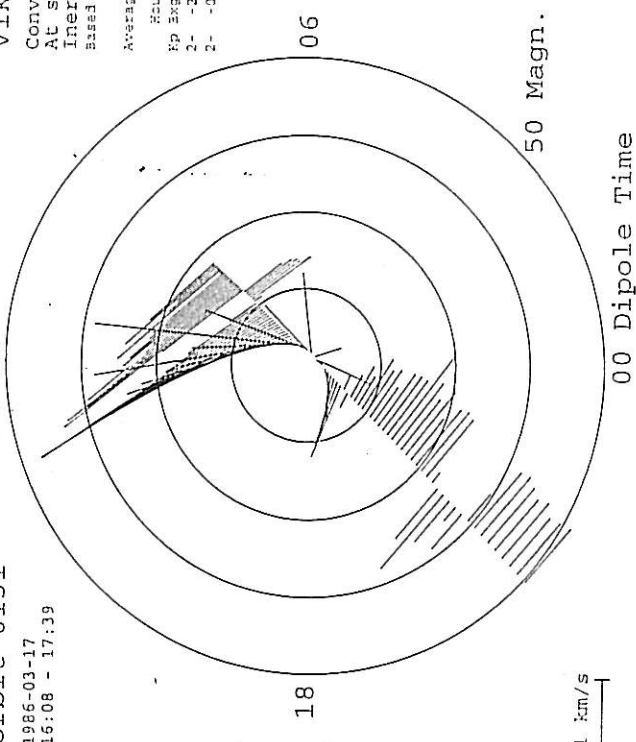
Averaging interval 60 seconds  
Hourly solar wind parameters:  
Kp Bzgm Bygm Bzgm Temp Dens Speed  
3 -2.2 -1.4 4.0 4.8 17.5 390.0  
2 -0.9 1.0 2.4 5.3 16.9 391.0



Orbit 0131  
1986-03-17  
16:08 - 17:39

Viking V1 Data  
Convection velocity  
At satellite  
Inertial frame  
Based on spin plane component of E

Averaging interval 60 seconds  
Hourly solar wind parameters:  
Kp Bzgm Bygm Bzgm Temp Dens Speed  
2 -2.2 -1.4 4.0 4.8 17.5 390.0  
2 -0.9 1.0 2.4 5.3 16.9 391.0







Orbit 0160

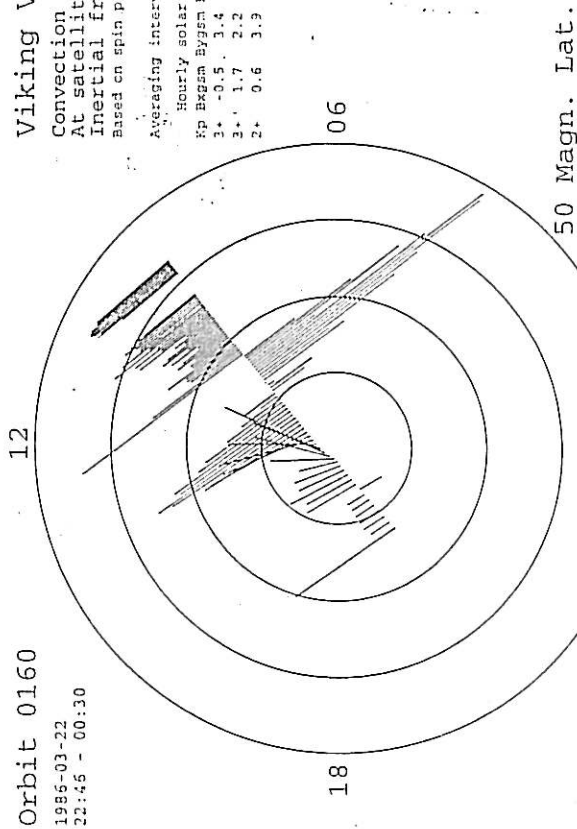
1986-03-22  
22:45 - 00:30

Viking V1 Data

Convection velocity  
At satellite  
Inertial frame  
Based on spin plane component of  $\Sigma$

Averaging interval 60 seconds

Hourly solar wind parameters:  
Rp Bxgsm Bygsm Bzgsm Temp Dens Speed  
3+ -0.5 3.4 2.4 14.8 5.4 618.0  
3- 1.7 2.2 1.8 14.6 5.2 635.0  
2+ 0.6 3.9 2.0 10.6 4.6 629.0



1 km/s

Orbit 0187

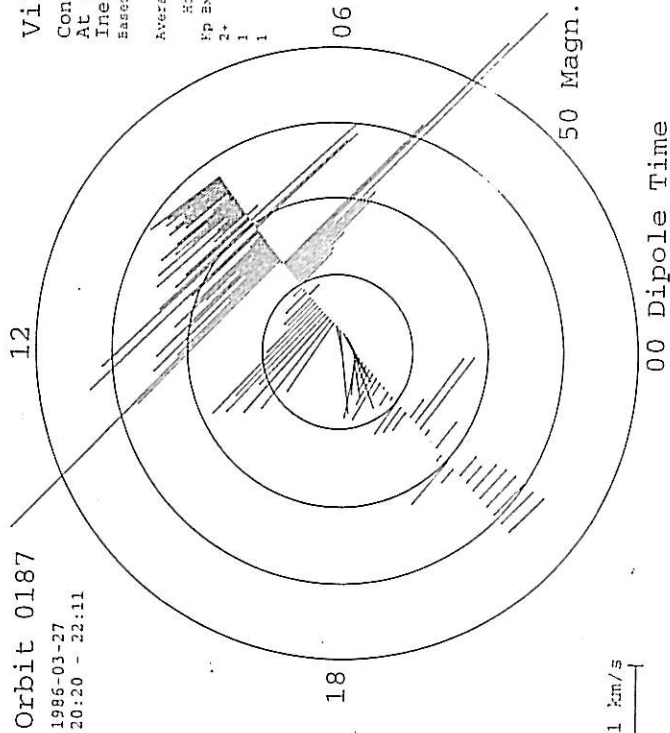
1986-03-27  
20:20 - 22:11

Viking V1 Data

Convection velocity  
At satellite  
Inertial frame  
Based on spin plane component of  $\Sigma$

Averaging interval 60 seconds

Hourly solar wind parameters:  
Rp Bxgsm Bygsm Bzgsm Temp Dens Speed  
2+ 7.7 3.5 611.0  
1 6.0 3.0 609.0



1 km/s

Orbit 0175

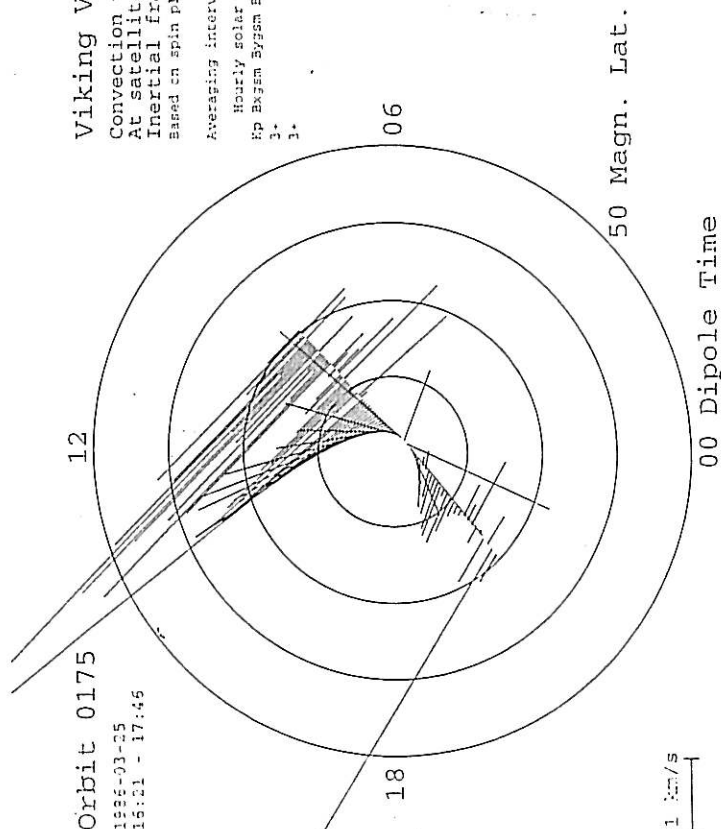
1986-03-25  
16:21 - 17:45

Viking V1 Data

Convection velocity  
At satellite  
Inertial frame  
Based on spin plane component of  $\Sigma$

Averaging interval 60 seconds

Hourly solar wind parameters:  
Rp Bxgsm Bygsm Bzgsm Temp Dens Speed  
3+ -0.5 3.4 2.4 14.8 5.4 618.0  
3- 1.7 2.2 1.8 14.6 5.2 635.0  
2+ 0.6 3.9 2.0 10.6 4.6 629.0



1 km/s

Orbit 0191

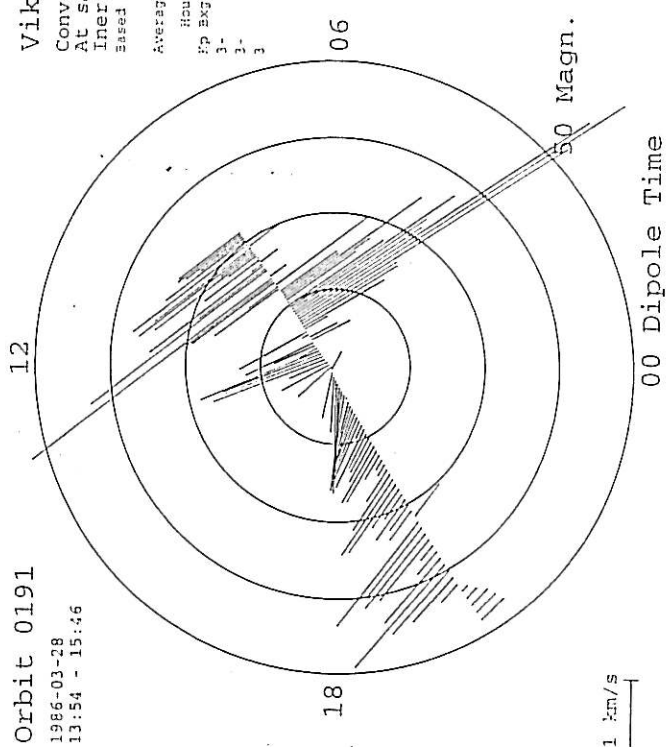
1986-03-28  
13:54 - 15:46

Viking V1 Data

Convection velocity  
At satellite  
Inertial frame  
Based on spin plane component of  $\Sigma$

Averaging interval 60 seconds

Hourly solar wind parameters:  
Rp Bxgsm Bygsm Bzgsm Temp Dens Speed  
3+ -0.5 3.4 2.4 14.8 5.4 618.0  
3- 1.7 2.2 1.8 14.6 5.2 635.0  
2+ 0.6 3.9 2.0 10.6 4.6 629.0

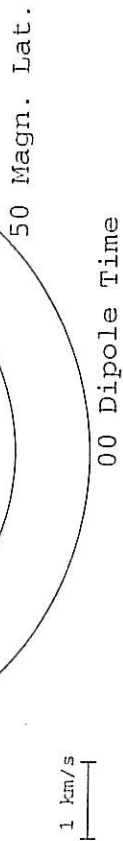


1 km/s



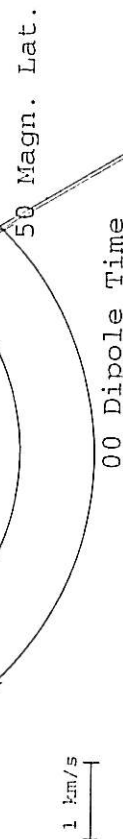
Viking V1 Data  
Convection velocity  
At satellite  
Inertial frame  
Based on spin plane component

Averaging interval 60 seconds  
Hourly solar wind parameters  
XP EXSM SYSM EXSM TSP DOTS  
1 +  
1 +  
1 +

Orbit 0252  
1986-04-09  
15:52 - 17:39

\* \* \*

Hourly solar wind parameters:  
velocity interval 60 seconds  
pressure 8 nPa  
density 5 cm<sup>-3</sup>



Viking V1 Data  
Convection velocity  
At satellite  
Inertial frame

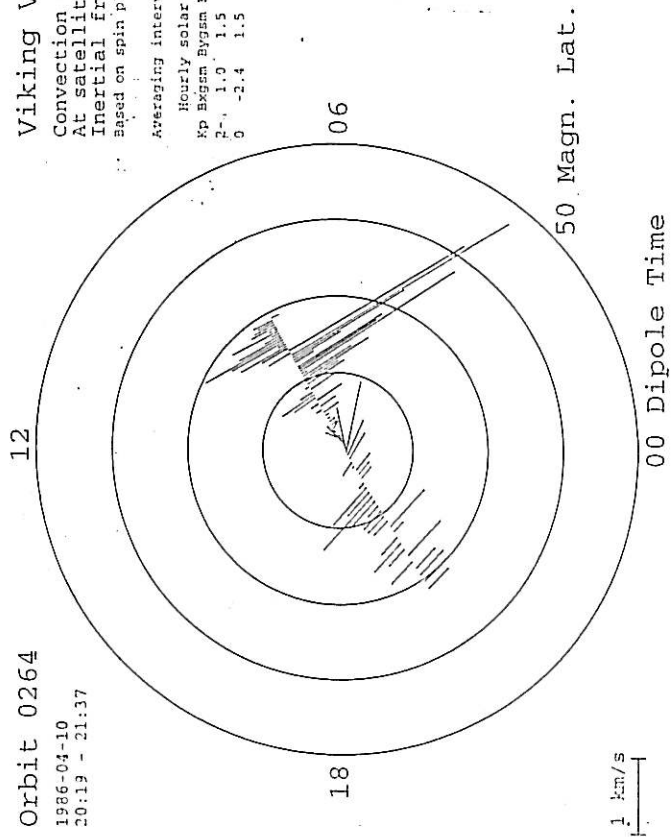
DATE	DESCRIPTION	AMOUNT
1911	...	...
1912	...	...
1913	...	...
1914	...	...
1915	...	...
1916	...	...
1917	...	...
1918	...	...
1919	...	...
1920	...	...
1921	...	...
1922	...	...
1923	...	...
1924	...	...
1925	...	...
1926	...	...
1927	...	...
1928	...	...
1929	...	...
1930	...	...
1931	...	...
1932	...	...
1933	...	...
1934	...	...
1935	...	...
1936	...	...
1937	...	...
1938	...	...
1939	...	...
1940	...	...
1941	...	...
1942	...	...
1943	...	...
1944	...	...
1945	...	...
1946	...	...
1947	...	...
1948	...	...
1949	...	...
1950	...	...
1951	...	...
1952	...	...
1953	...	...
1954	...	...
1955	...	...
1956	...	...
1957	...	...
1958	...	...
1959	...	...
1960	...	...
1961	...	...
1962	...	...
1963	...	...
1964	...	...
1965	...	...
1966	...	...
1967	...	...
1968	...	...
1969	...	...
1970	...	...
1971	...	...
1972	...	...
1973	...	...
1974	...	...
1975	...	...
1976	...	...
1977	...	...
1978	...	...
1979	...	...
1980	...	...
1981	...	...
1982	...	...
1983	...	...
1984	...	...
1985	...	...
1986	...	...
1987	...	...
1988	...	...
1989	...	...
1990	...	...
1991	...	...
1992	...	...
1993	...	...
1994	...	...
1995	...	...
1996	...	...
1997	...	...
1998	...	...
1999	...	...
2000	...	...
2001	...	...
2002	...	...
2003	...	...
2004	...	...
2005	...	...
2006	...	...
2007	...	...
2008	...	...
2009	...	...
2010	...	...
2011	...	...
2012	...	...
2013	...	...
2014	...	...
2015	...	...
2016	...	...
2017	...	...
2018	...	...
2019	...	...
2020	...	...
2021	...	...
2022	...	...
2023	...	...
2024	...	...
2025	...	...
2026	...	...
2027	...	...
2028	...	...
2029	...	...
2030	...	...
2031	...	...
2032	...	...
2033	...	...
2034	...	...
2035	...	...
2036	...	...
2037	...	...
2038	...	...
2039	...	...
2040	...	...
2041	...	...
2042	...	...
2043	...	...
2044	...	...
2045	...	...
2046	...	...
2047	...	...
2048	...	...
2049	...	...
2050	...	



Orbit 0264  
1986-04-10  
20:13 - 21:37

Viking V1 Data  
Convection velocity  
At satellite  
Inertial frame  
Based on spin plane component of E

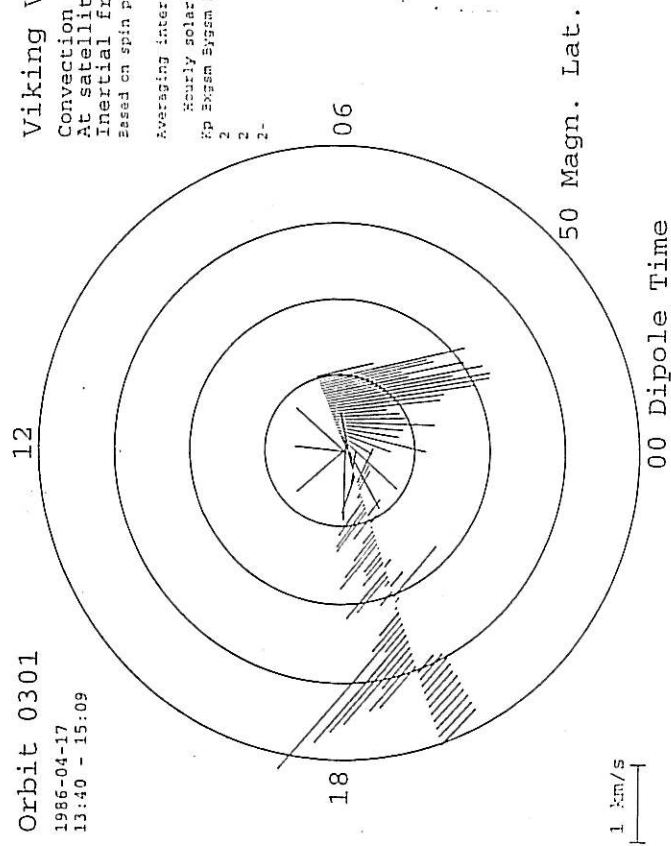
Averaging interval 60 seconds  
Hourly solar wind parameters:  
Kp Bzgm Bygsm Bzgm Temp Dens Speed  
2- 1.0 1.5 1.4 3.2 5.7 414.0  
0 -2.4 1.5 1.3 3.7 5.1 393.0



Orbit 0301  
1986-04-17  
13:40 - 15:09

Viking V1 Data  
Convection velocity  
At satellite  
Inertial frame  
Based on spin plane component of E

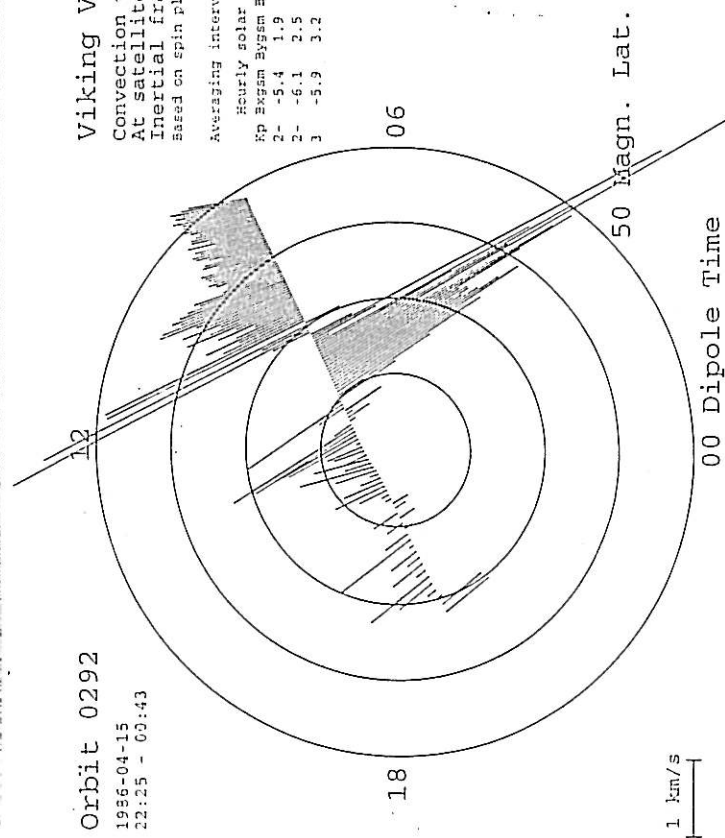
Averaging interval 60 seconds  
Hourly solar wind parameters:  
Kp Bzgm Bygsm Bzgm Temp Dens Speed  
2- 2 2 2 2 2 2



Orbit 0292  
1986-04-15  
22:25 - 00:43

Viking V1 Data  
Convection velocity  
At satellite  
Inertial frame  
Based on spin plane component of E

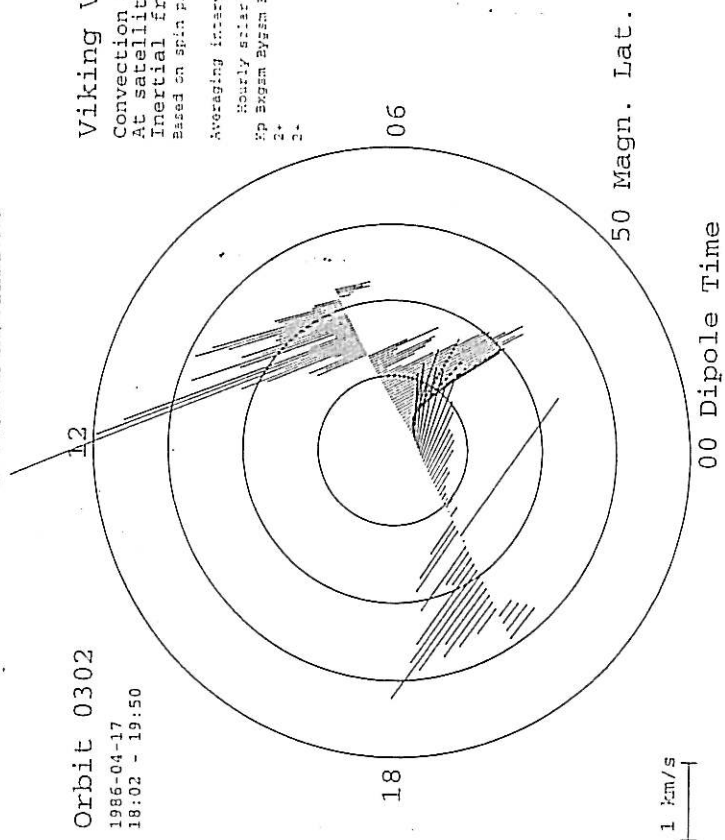
Averaging interval 60 seconds  
Hourly solar wind parameters:  
Kp Bzgm Bygsm Bzgm Temp Dens Speed  
2- -5.4 1.9 -4.5 10.7 7.5 431.0  
2- -6.1 2.5 -3.3 7.6 6.9 447.0  
3 -5.9 3.2 -1.2 6.8 7.4 454.0



Orbit 0302  
1986-04-17  
18:02 - 19:50

Viking V1 Data  
Convection velocity  
At satellite  
Inertial frame  
Based on spin plane component of E

Averaging interval 60 seconds  
Hourly solar wind parameters:  
Kp Bzgm Bygsm Bzgm Temp Dens Speed  
2- 2 2 2 2 2 2



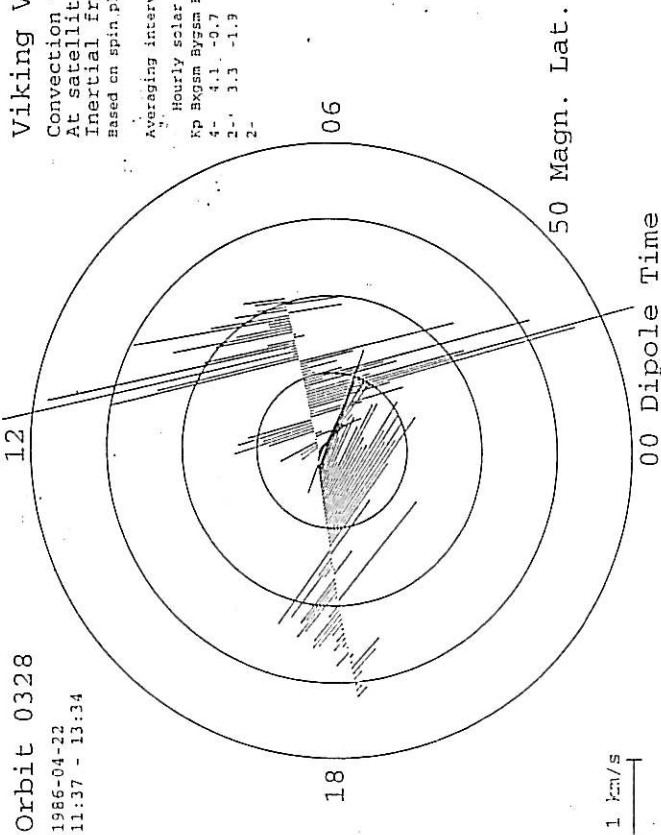


Orbit 0328  
1986-04-22  
11:37 - 13:34

Viking V1 Data  
Convection velocity  
At satellite  
Inertial frame  
Based on spin plane component of E

Averaging interval 60 seconds

Hourly solar wind parameters:  
Kp Bxgm Bygsm Bzgm Temp Dens Speed  
4- 4.1 -0.7 2.4 7.4 8.7 478.0  
2- 3.3 -1.3 1.3 6.6 8.6 471.0  
2- 2- 3.3 -1.3 1.3 6.6 8.6 471.0

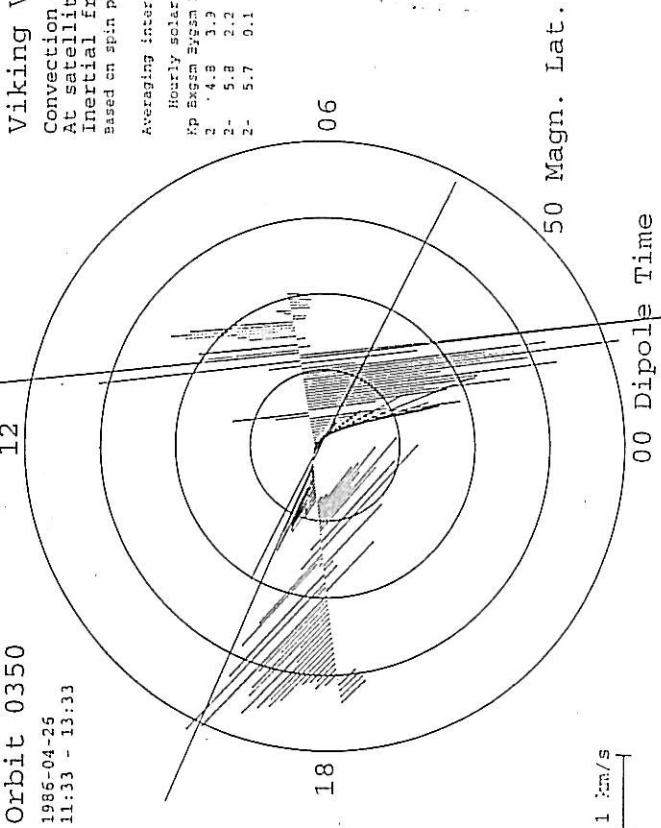


Orbit 0350  
1986-04-25  
11:33 - 13:33

Viking V1 Data  
Convection velocity  
At satellite  
Inertial frame  
Based on spin plane component of E

Averaging interval 60 seconds

Hourly solar wind parameters:  
Kp Bxgm Bygsm Bzgm Temp Dens Speed  
2- 4.8 3.9 -0.3 3.5 4.4 458.0  
2- 5.8 2.2 0.3 3.1 4.6 448.0  
2- 5.7 0.1 1.2 2.6 5.6 453.0

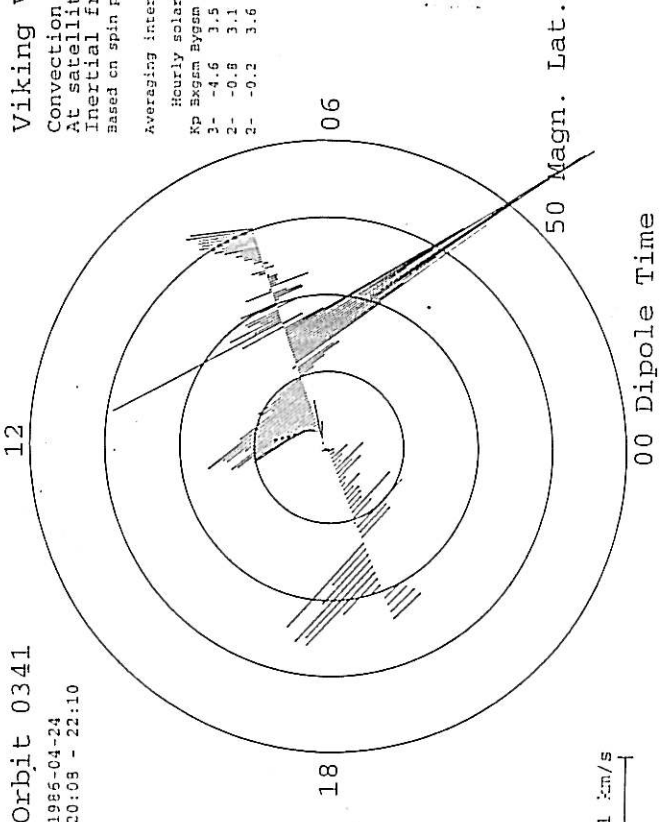


Orbit 0341  
1986-04-24  
20:08 - 22:10

Viking V1 Data  
Convection velocity  
At satellite  
Inertial frame  
Based on spin plane component of E

Averaging interval 60 seconds

Hourly solar wind parameters:  
Kp Bxgm Bygsm Bzgm Temp Dens Speed  
3- -4.6 3.5 3.1 11.3 4.3 574.0  
2- -0.8 3.1 3.3 15.8 4.7 614.0  
2- -0.2 3.6 3.4 15.5 5.0 610.0

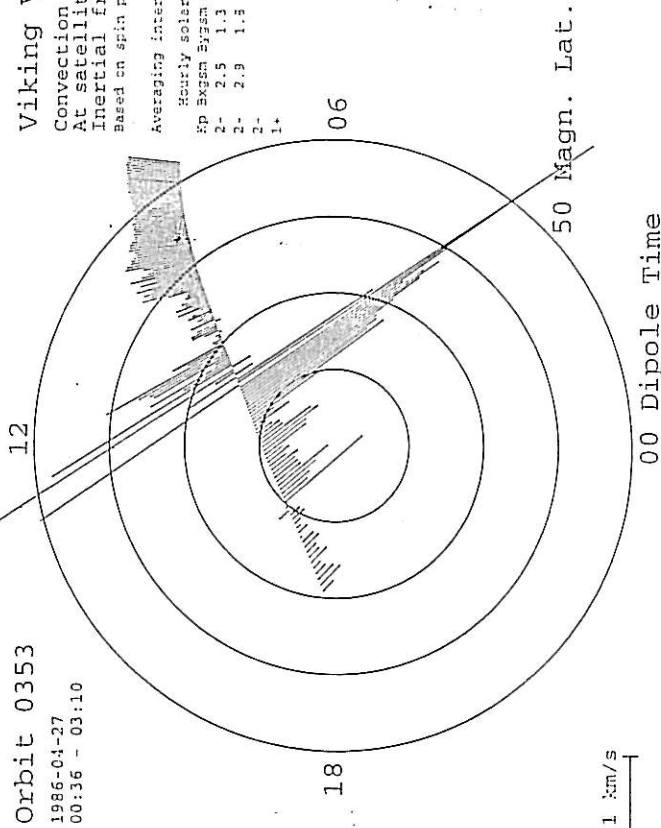


Orbit 0353  
1986-04-27  
00:36 - 03:10

Viking V1 Data  
Convection velocity  
At satellite  
Inertial frame  
Based on spin plane component of E

Averaging interval 60 seconds

Hourly solar wind parameters:  
Kp Bxgm Bygsm Bzgm Temp Dens Speed  
2- 2.5 1.3 0.5 2.3 6.9 395.0  
2- 2.9 1.3 0.2 1.7 5.3 397.0  
2- 2- 2.9 1.3 0.2 1.7 5.3 397.0



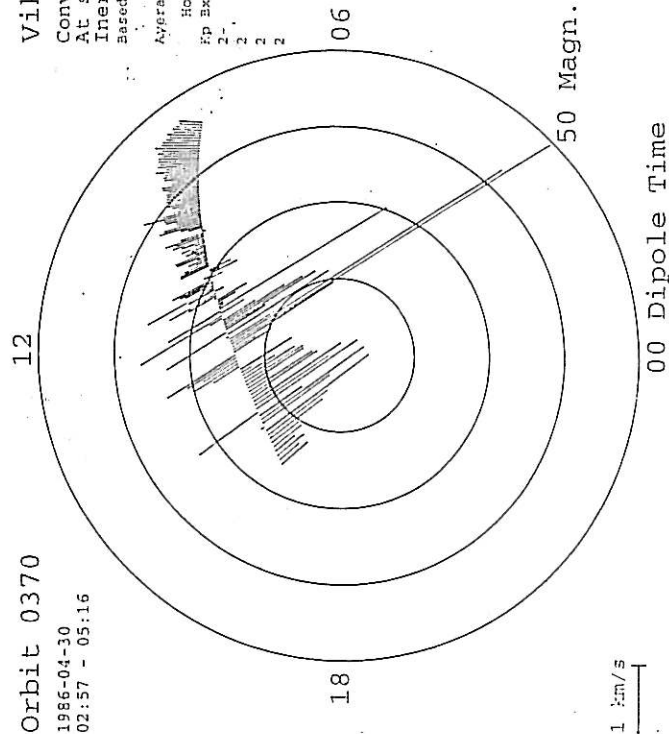




Orbit 0370  
1986-04-30  
02:57 - 05:16

Viking V1 Data  
Convection velocity  
At satellite  
Inertial frame  
Based on spin plane component of E

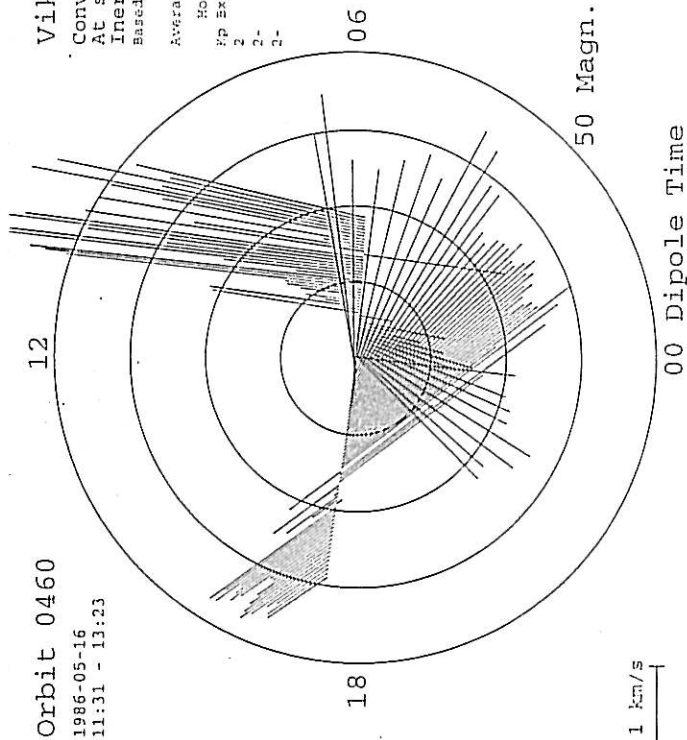
Averaging interval 60 seconds  
Hourly solar wind parameters:  
Kp Bzgm Bygsm Bzgm Temp Dens Speed  
2-  
2-  
2-  
2-



Orbit 0460  
1986-05-16  
11:31 - 13:23

Viking V1 Data  
Convection velocity  
At satellite  
Inertial frame  
Based on spin plane component of E

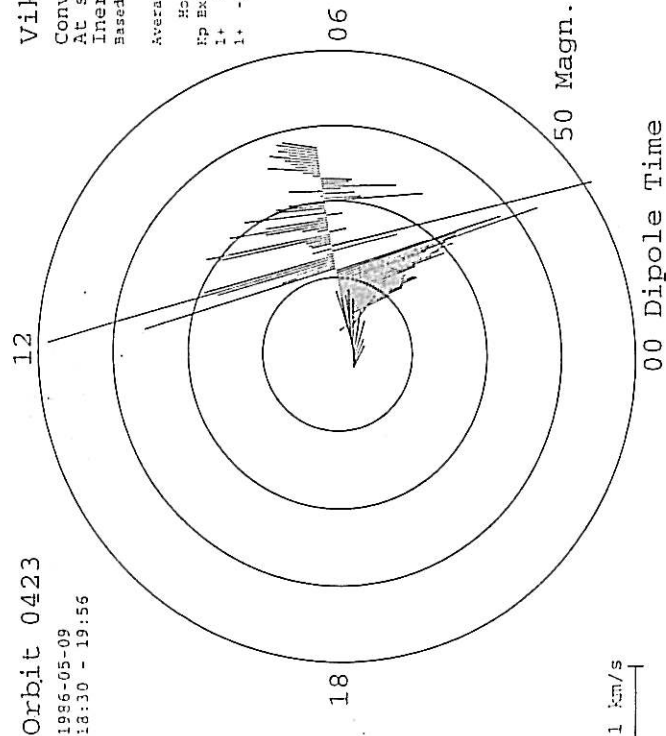
Averaging interval 60 seconds  
Hourly solar wind parameters:  
Kp Bzgm Bygsm Bzgm Temp Dens Speed  
2-  
2-  
2-  
2-



Orbit 0423  
1986-05-09  
18:30 - 19:56

Viking V1 Data  
Convection velocity  
At satellite  
Inertial frame  
Based on spin plane component of E

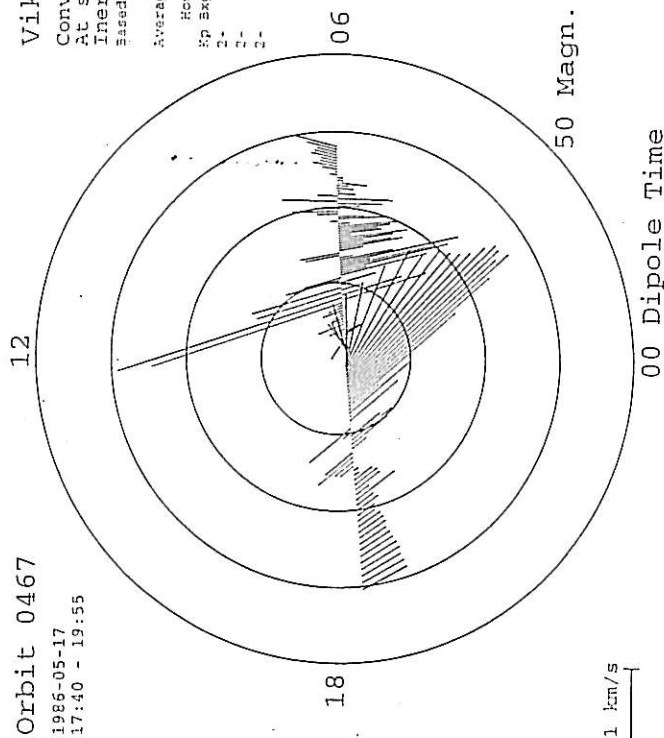
Averaging interval 60 seconds  
Hourly solar wind parameters:  
Kp Bzgm Bygsm Bzgm Temp Dens Speed  
1+ 0.2 0.3 2.3 3.5 16.5 403.0  
1+ -1.4 2.4 3.7 3.5 15.9 390.0



Orbit 0467  
1986-05-17  
17:40 - 19:55

Viking V1 Data  
Convection velocity  
At satellite  
Inertial frame  
Based on spin plane component of E

Averaging interval 60 seconds  
Hourly solar wind parameters:  
Kp Bzgm Bygsm Bzgm Temp Dens Speed  
2-  
2-  
2-  
2-



50 Magn. Lat.

50 Magn. Lat.

00 Dipole Time

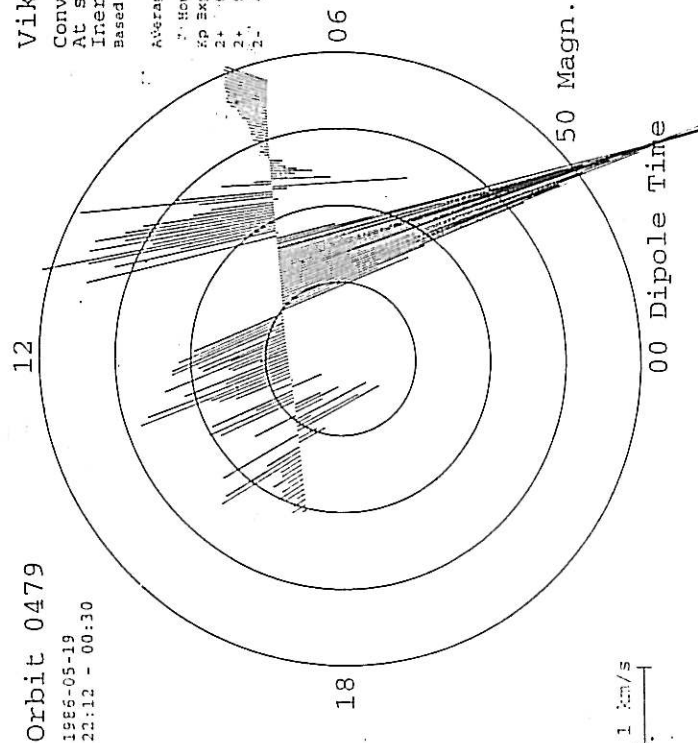
00 Dipole Time



Viking V1 Data  
Convection velocity  
At satellite  
Inertial frame  
Based on spin plane component of E

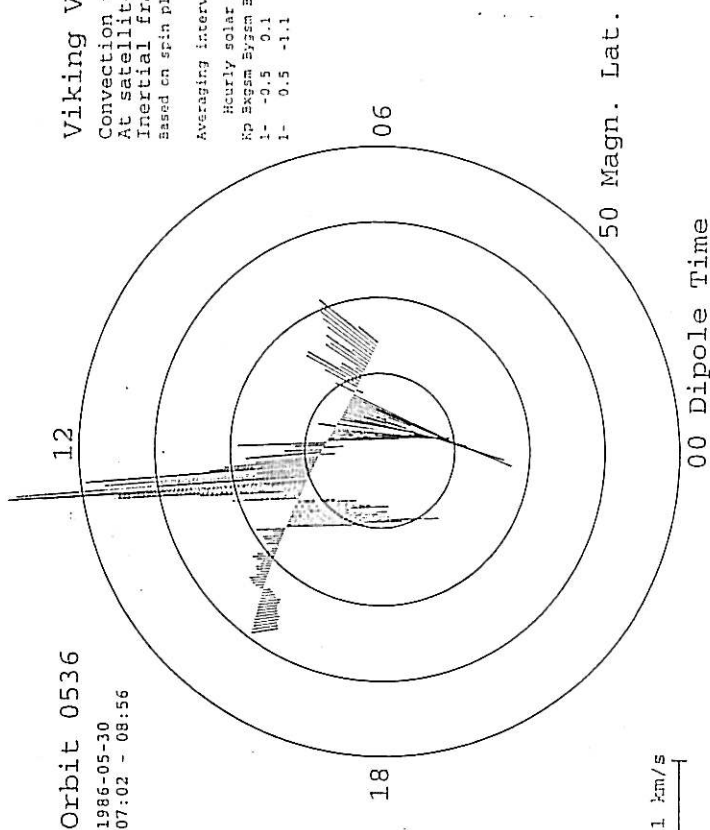
Orbit 0479  
1986-05-19  
22:12 - 00:30

Averaging interval 60 seconds  
Hourly solar wind parameters:  
Kp Bzsm Byzsm Bzsm Temp Dens Speed  
1- -5.7 1.9 -1.1 7.3 6.9 339.0  
2- -6.0 1.3 -0.4 3.9 8.1 422.0  
2- -2.3 0.9 0.2 4.4 12.3 376.0  
2- -0.3 0.3 0.3 3.5 12.5 376.0



Orbit 0536  
1986-05-30  
07:02 - 08:56

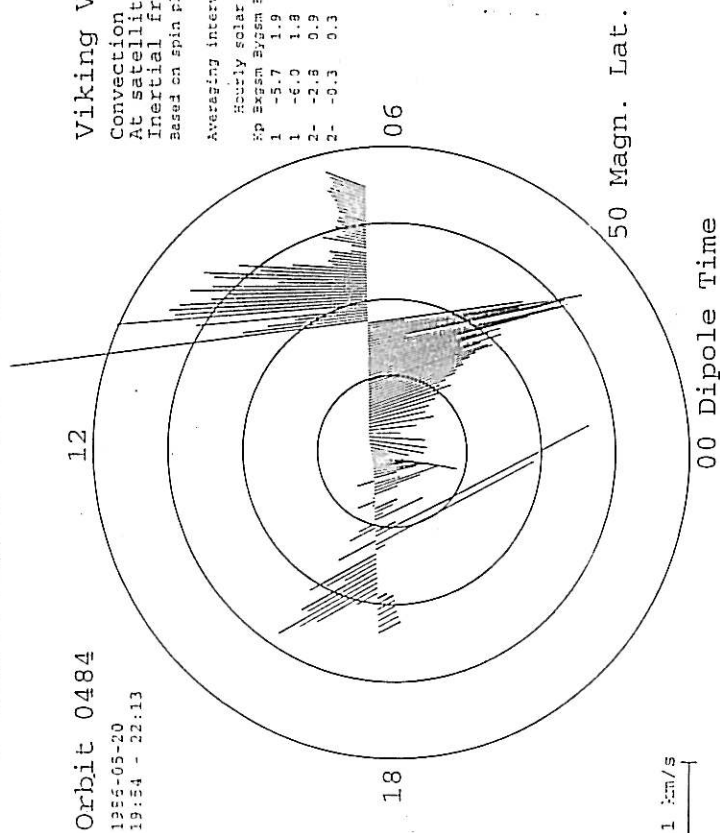
Averaging interval 60 seconds  
Hourly solar wind parameters:  
Kp Bzsm Byzsm Bzsm Temp Dens Speed  
1- -0.5 0.1 6.2 1.7 12.9 339.0  
1- 0.5 -1.1 5.3 1.5 13.7 339.0



Viking V1 Data  
Convection velocity  
At satellite  
Inertial frame  
Based on spin plane component of E

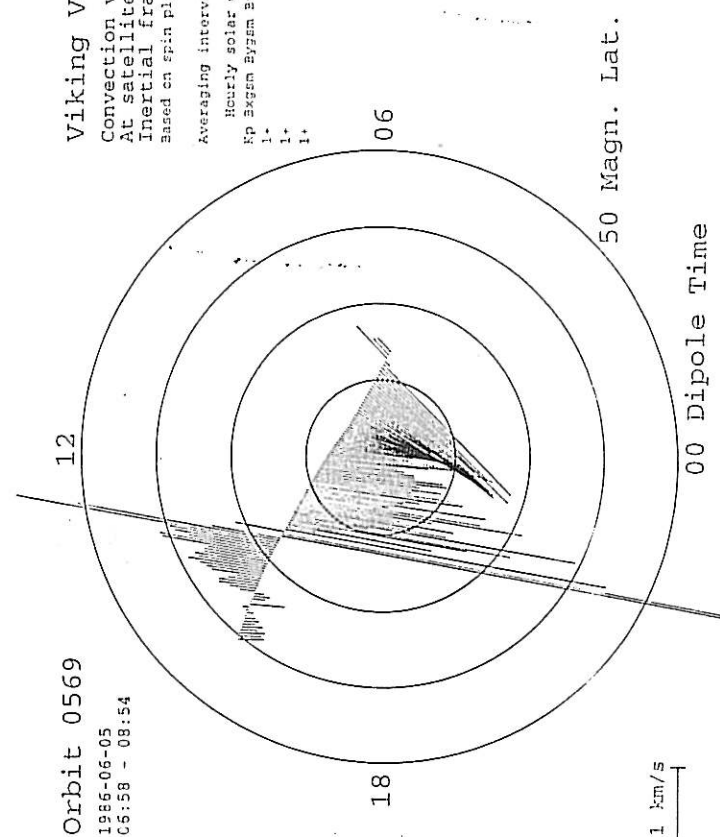
Orbit 0484  
1986-05-20  
19:54 - 22:13

Averaging interval 60 seconds  
Hourly solar wind parameters:  
Kp Bzsm Byzsm Bzsm Temp Dens Speed  
1- -5.7 1.9 -1.1 7.3 6.9 339.0  
1- -6.0 1.3 -0.4 3.9 8.1 422.0  
2- -2.3 0.9 0.2 4.4 12.3 376.0  
2- -0.3 0.3 0.3 3.5 12.5 376.0

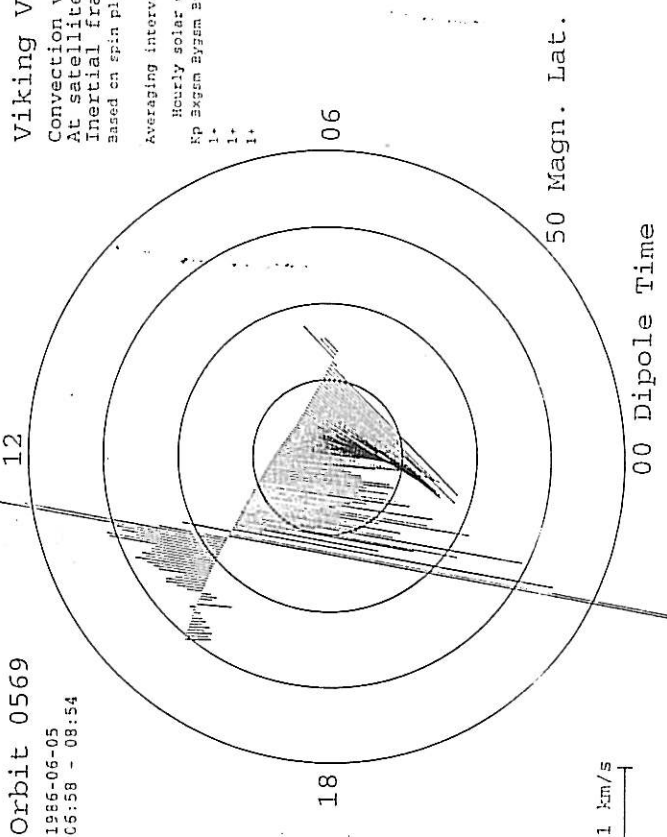


Orbit 0569  
1986-06-05  
06:58 - 08:54

Averaging interval 60 seconds  
Hourly solar wind parameters:  
Kp Bzsm Byzsm Bzsm Temp Dens Speed  
1- -0.5 0.1 6.2 1.7 12.9 339.0  
1- 0.5 -1.1 5.3 1.5 13.7 339.0



Viking V1 Data  
Convection velocity  
At satellite  
Inertial frame  
Based on spin plane component of E

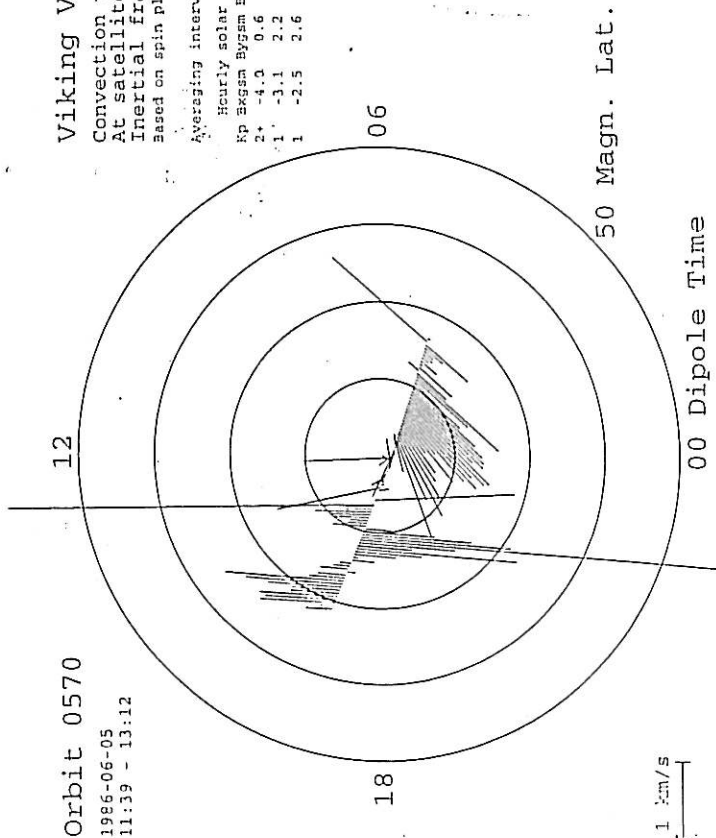




Orbit 0570  
1986-06-05  
11:39 - 13:12

Viking V1 Data  
Convection velocity  
At satellite  
Inertial frame  
Based on spin plane component of E

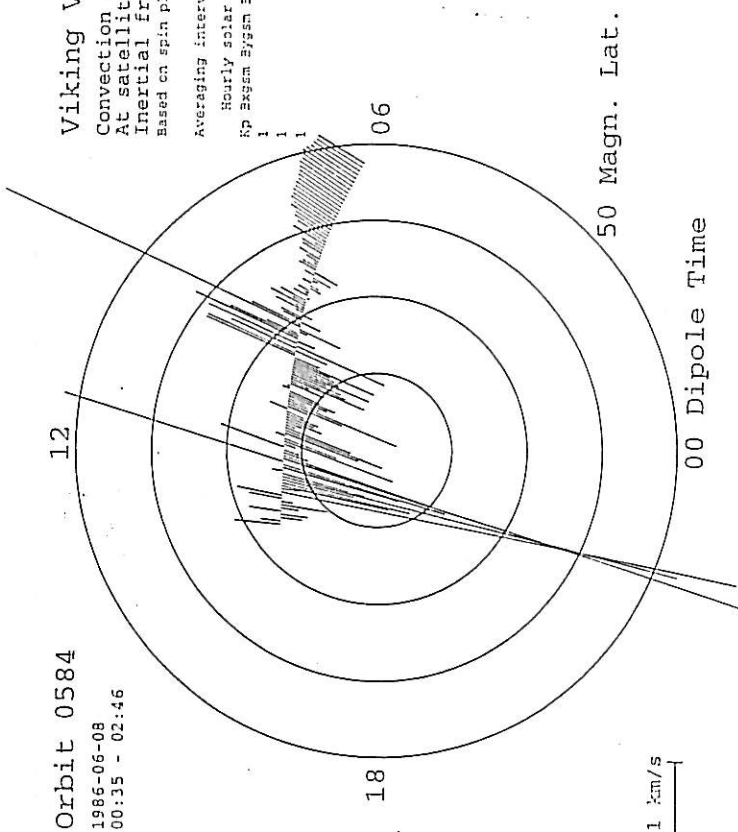
Averaging interval 60 seconds  
Hourly solar wind parameters:  
Kp Bzsm Bygsm Bzsm Temp Dens Speed  
2+ -4.0 0.6 1.4 2.0 10.7 389.0  
1 -3.1 2.2 1.5 2.4 11.3 382.0  
1 -2.5 2.6 1.6 2.7 12.2 373.0



Orbit 0584  
1986-06-08  
00:35 - 02:46

Viking V1 Data  
Convection velocity  
At satellite  
Inertial frame  
Based on spin plane component of E

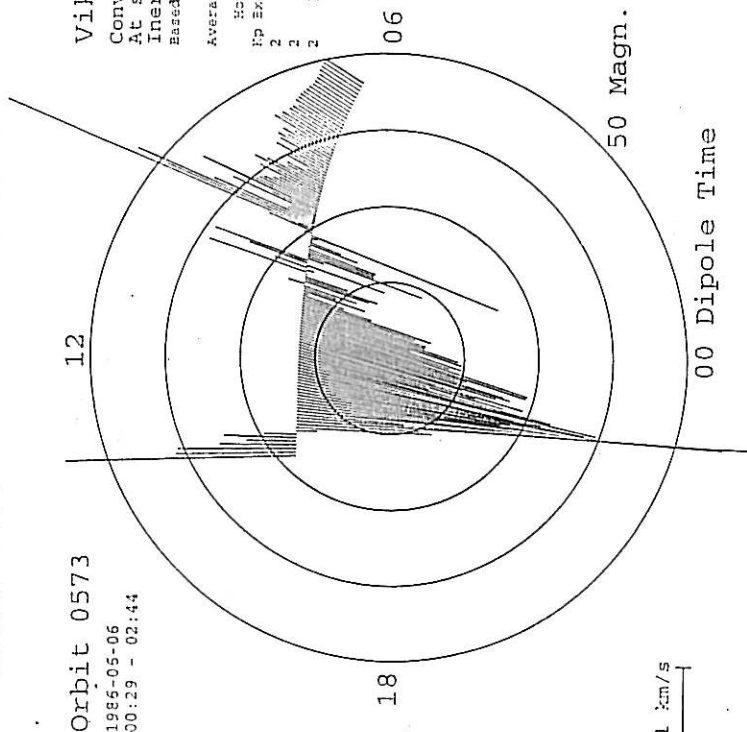
Averaging interval 60 seconds  
Hourly solar wind parameters:  
Kp Bzsm Bygsm Bzsm Temp Dens Speed  
1 1 1 1 1 1 1



Orbit 0573  
1986-05-06  
00:29 - 02:44

Viking V1 Data  
Convection velocity  
At satellite  
Inertial frame  
Based on spin plane component of E

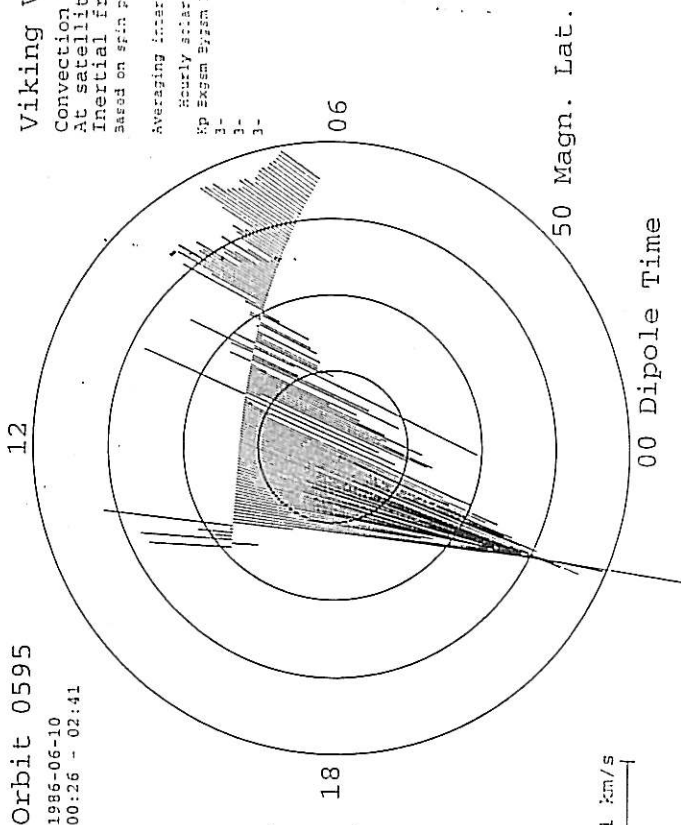
Averaging interval 60 seconds  
Hourly solar wind parameters:  
Kp Bzsm Bygsm Bzsm Temp Dens Speed  
2 2 2 3.1 -5.3 -2.7 3.2 9.8 378.0



Orbit 0595  
1986-06-10  
00:26 - 02:41

Viking V1 Data  
Convection velocity  
At satellite  
Inertial frame  
Based on spin plane component of E

Averaging interval 60 seconds  
Hourly solar wind parameters:  
Kp Bzsm Bygsm Bzsm Temp Dens Speed  
1- 1- 1- 1- 1- 1- 1-



50 Magn. Lat.

00 Dipole Time

50 Magn. Lat.

00 Dipole Time



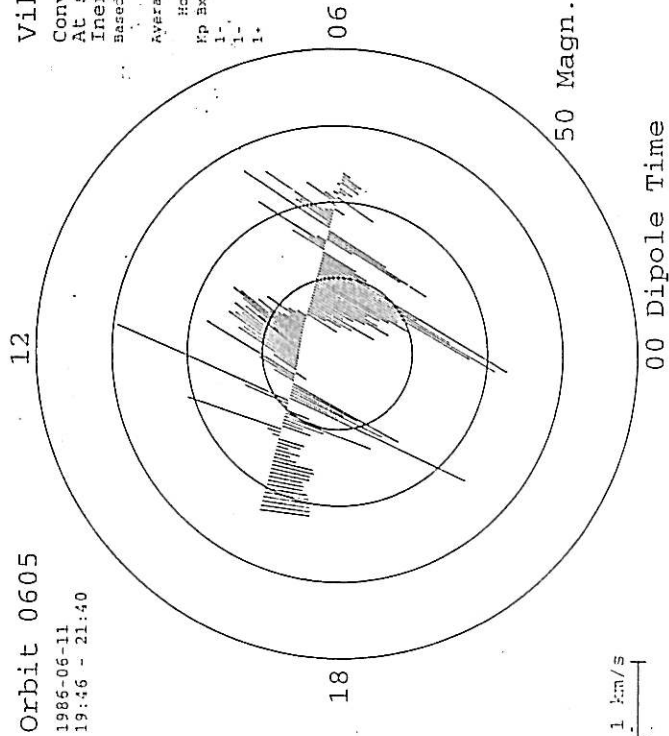
Orbit 0605

1986-06-11  
19:46 - 21:40

Viking V1 Data

Convection velocity  
At satellite  
Inertial frame  
Based on spin plane component of E

Averaging interval 60 seconds  
Hourly solar wind parameters:  
Kp Bzgm Bygsm Bzgm Temp Dens Speed  
1- 1- 1- 1- 1- 1- 1-  
1- 1- 1- 1- 1- 1- 1-



50 Magn. Lat.

00 Dipole Time

1 km/s

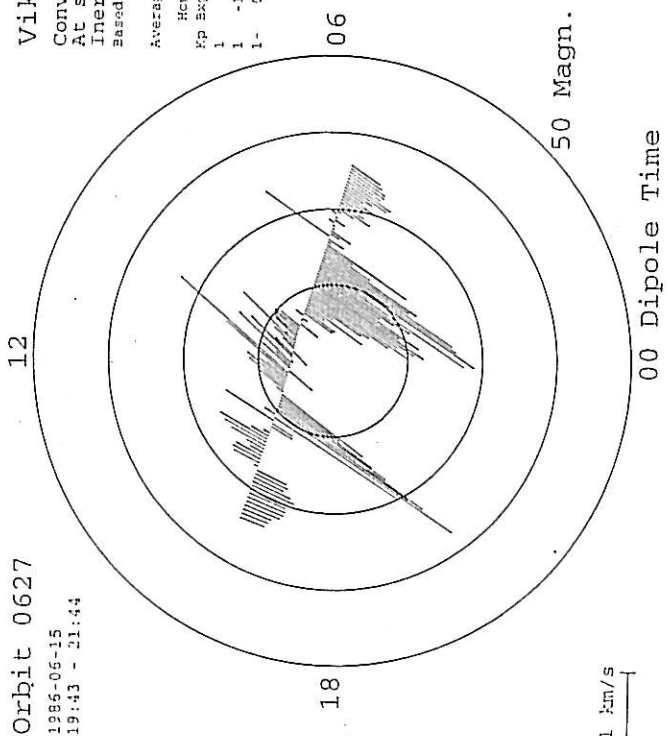
Orbit 0627

1986-06-15  
19:43 - 21:44

Viking V1 Data

Convection velocity  
At satellite  
Inertial frame  
Based on spin plane component of E

Averaging interval 60 seconds  
Hourly solar wind parameters:  
Kp Bzgm Bygsm Bzgm Temp Dens Speed  
1- -1.0 0.3 2.4 1.6 13.4 371.0  
1- 0.2 -0.3 1.1 1.9 14.8 375.0



50 Magn. Lat.

00 Dipole Time

1 km/s

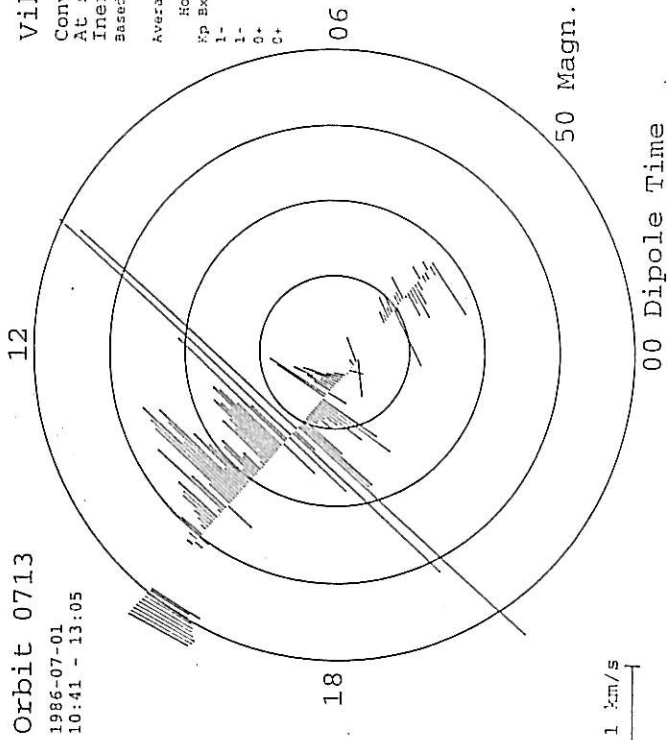
Orbit 0713

1986-07-01  
10:41 - 13:05

Viking V1 Data

Convection velocity  
At satellite  
Inertial frame  
Based on spin plane component of E

Averaging interval 60 seconds  
Hourly solar wind parameters:  
Kp Bzgm Bygsm Bzgm Temp Dens Speed  
1- 1- 1- 1- 1- 1- 1-  
1- 1- 1- 1- 1- 1- 1-



50 Magn. Lat.

00 Dipole Time

1 km/s

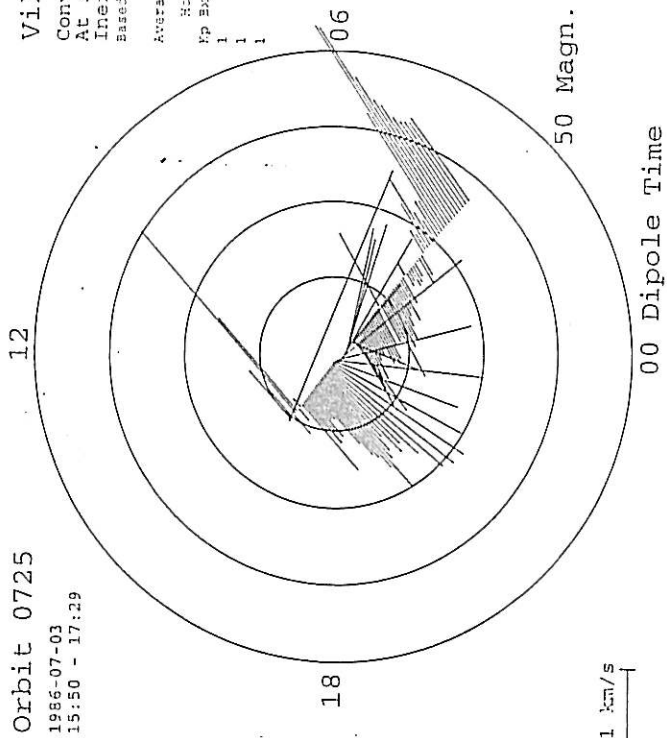
Orbit 0725

1986-07-03  
15:50 - 17:29

Viking V1 Data

Convection velocity  
At satellite  
Inertial frame  
Based on spin plane component of E

Averaging interval 60 seconds  
Hourly solar wind parameters:  
Kp Bzgm Bygsm Bzgm Temp Dens Speed  
1- 1- 1- 1- 1- 1- 1-  
1- 1- 1- 1- 1- 1- 1-



50 Magn. Lat.

00 Dipole Time

1 km/s

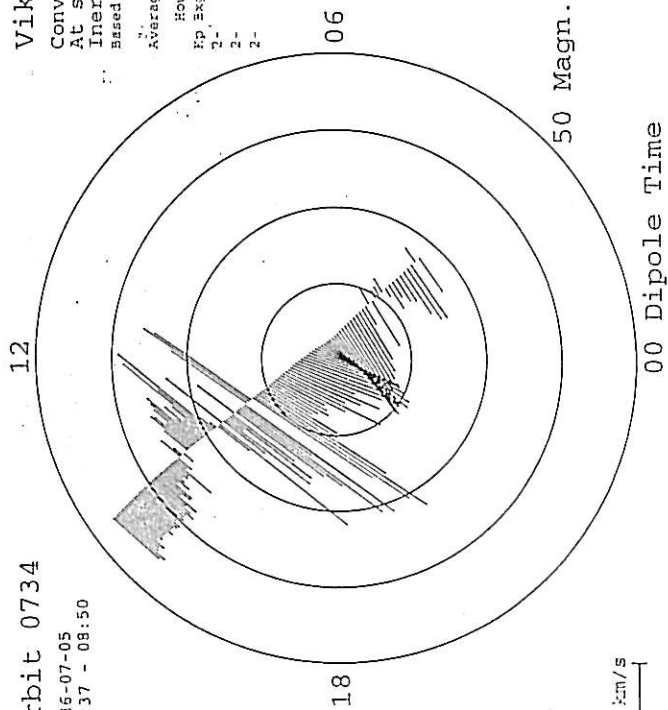




Orbit 0734  
1986-07-05  
06:37 - 08:50

Viking V1 Data  
Convection velocity  
At satellite  
Inertial frame  
Based on spin plane component of E

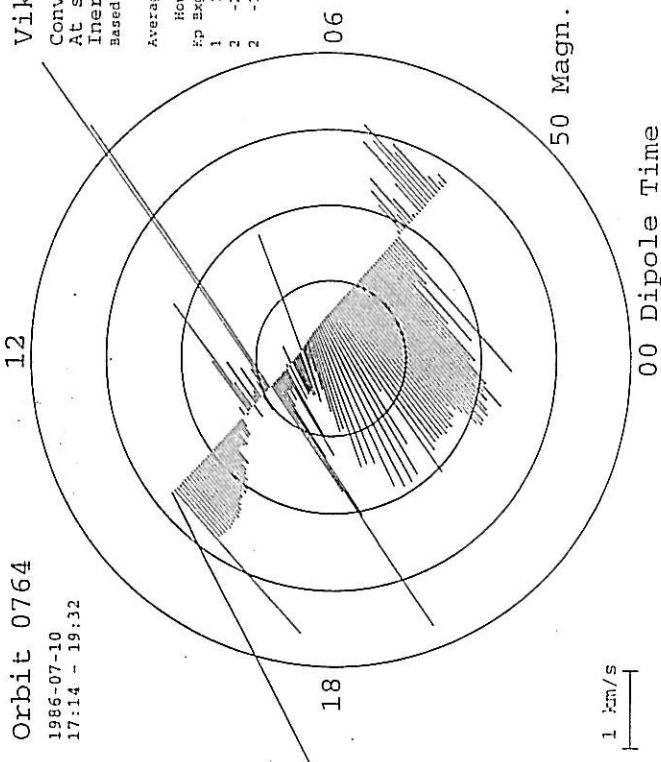
Averaging interval 60 seconds  
Hourly solar wind parameters:  
Kp Bzgm Bygm Bysm Temp Dens Speed  
1 1.5 2.6 -0.2 2.9 12.2 394.0  
2 -2.1 1.2 -0.1 3.1 13.0 394.0  
2 -1.2 -2.7 -0.6 2.7 12.9 390.0



Orbit 0764  
1986-07-10  
17:14 - 19:32

Viking V1 Data  
Convection velocity  
At satellite  
Inertial frame  
Based on spin plane component of E

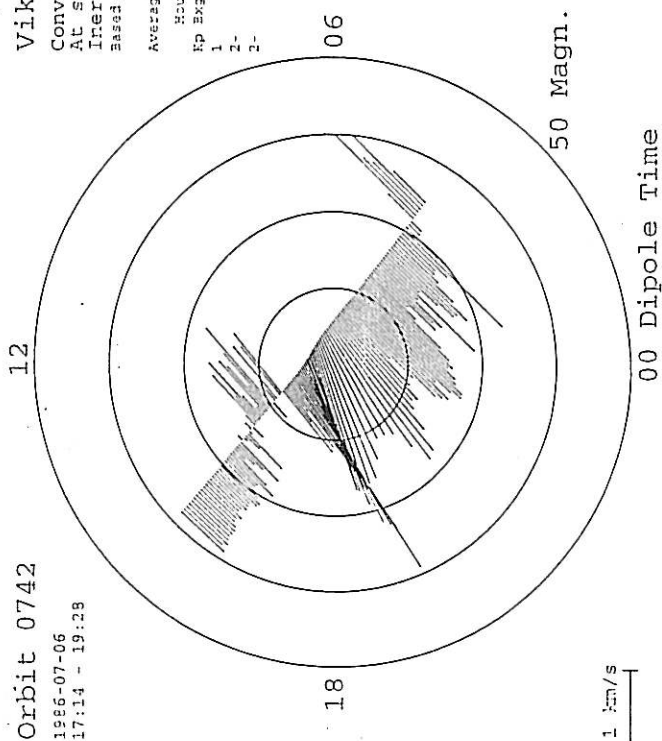
Averaging interval 60 seconds  
Hourly solar wind parameters:  
Kp Bzgm Bygm Bysm Temp Dens Speed  
1 1.5 2.6 -0.2 2.9 12.2 394.0  
2 -2.1 1.2 -0.1 3.1 13.0 394.0  
2 -1.2 -2.7 -0.6 2.7 12.9 390.0



Orbit 0742  
1986-07-06  
17:14 - 19:29

Viking V1 Data  
Convection velocity  
At satellite  
Inertial frame  
Based on spin plane component of E

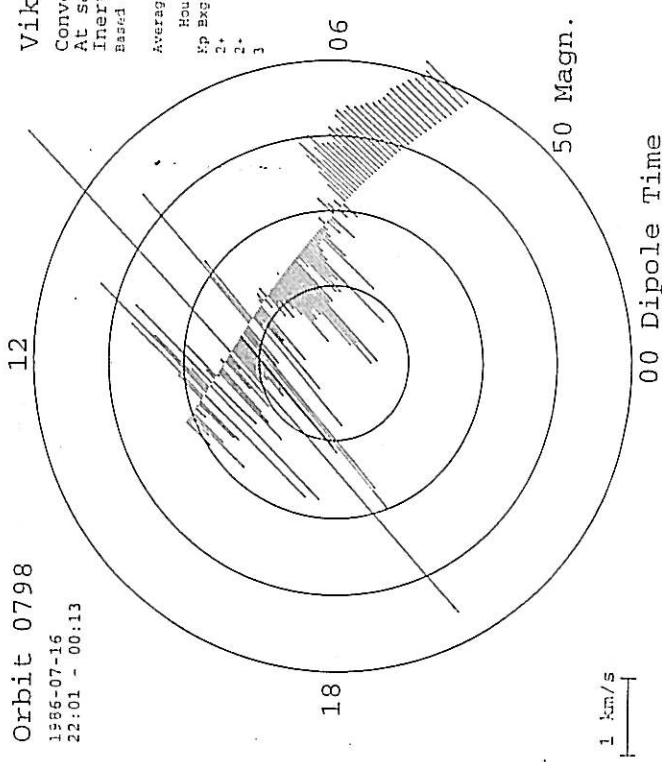
Averaging interval 60 seconds  
Hourly solar wind parameters:  
Kp Bzgm Bygm Bysm Temp Dens Speed  
1 1.5 2.6 -0.2 2.9 12.2 394.0  
2 -2.1 1.2 -0.1 3.1 13.0 394.0  
2 -1.2 -2.7 -0.6 2.7 12.9 390.0



Orbit 0798  
1986-07-16  
22:01 - 00:13

Viking V1 Data  
Convection velocity  
At satellite  
Inertial frame  
Based on spin plane component of E

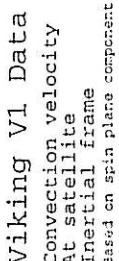
Averaging interval 60 seconds  
Hourly solar wind parameters:  
Kp Bzgm Bygm Bysm Temp Dens Speed  
1 1.5 2.6 -0.2 2.9 12.2 394.0  
2 -2.1 1.2 -0.1 3.1 13.0 394.0  
2 -1.2 -2.7 -0.6 2.7 12.9 390.0





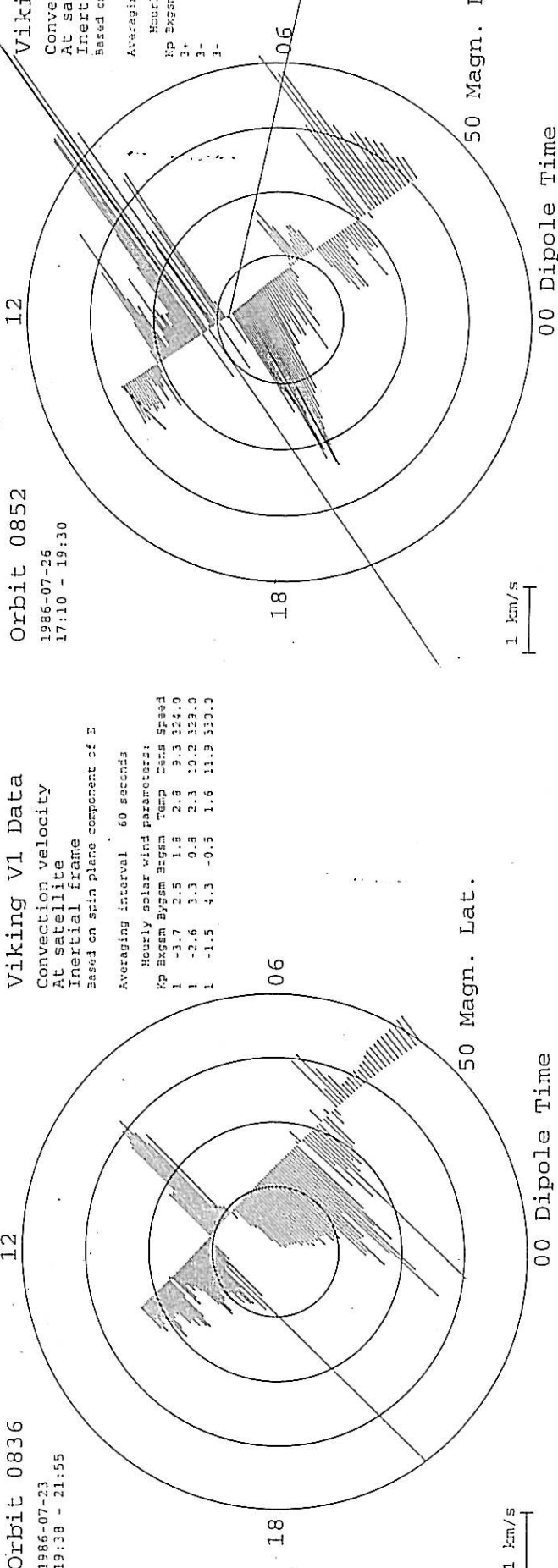
Orbit 0847  
1986-07-25  
19:36 - 21:55

Averaging interval		60 seconds	
Hourly solar wind	Parameters:		
Kp	Bxgsm	Bzgsm	Temp Dens
3+	3.9	5.2	2.6 17.3 7.0
3+	4.2	-2.1	-3.3 23.0 6.0
6-	5.6	-2.0	-4.0 30.5 7.0



Orbit 0852  
1986-07-26  
17:10 - 19:30

Averaging interval	60 seconds
Hourly solar wind parameters:	
Kp	Geom Bygem Bygem Temp Dens
3+	
3-	
1-	



Wiking V1 Data  
Convection velocity  
At satellite  
inertial frame  
measured on spin plane component

Orbit 0852  
1986-07-26  
17:10 - 19:30

Averaging interval	60 seconds
Hourly solar wind parameters:	
Kp	Geom Bygem Bygem Temp Dens
3+	
3-	
1-	







## References

- [1] H. Alfvén and C.-G.Fälthammar. *Cosmical Electrodynamics, Fundamental Principles*. Oxford University Press, 1963.
- [2] W.I. Axford and C.O.Hines. A unifying theory of high-latitude geophysical phenomena and geomagnetic storms. *Can.J.Phys.*, 39:1433, 1961.
- [3] K.D. Baker, L.P.Block, R.Kist, W.Kampa, N.Singh, and H.Thiemann. Studies of strong laboratory double layers and comparison with computer simulation. *J.Plasma Phys.*, 26:1, August 1981.
- [4] K. Birkeland. The Norwegian aurora polaris expedition 1902-3, vol.1. H.Aschehoug, Christiania, Norway, 1908. On the Cause of Magnetic Storms and the Origin of Terrestrial Magnetism.
- [5] L.P. Block. Ninth international conference on phenomena in ionized gases, Bucharest, Romania, invited review paper. Technical report, Preprint:Electron and Plasma Phys.,Royal Inst. of Techn., 100 44 Stockholm, Sweden, 1969.
- [6] L.P. Block. Potential double layers in the ionosphere. *Cosmic Electrodyn.*, 3:349, 1972.
- [7] L.P. Block. Double layers in the laboratory and above the aurora. In S.-I.Akasofu and J.R.Kan, editors, *Physics of Auroral Arc Formation, Geophysical Monograph 25*, page 218. AGU, Washington, D.C., 1981.
- [8] L.G. Blomberg and G.T.Marklund. High-latitude convection patterns for various large- scale field-aligned current configurations. *Geophys.Res.Lett.*, 18:717, 1991.
- [9] R. Boström. Ionosphere /magnetosphere coupling. *Magneto spheric Physics*, 1974. edited by B.M.McCormac,D.Reidel,Dordrecht, Netherlands.
- [10] J.L. Burch. Simultaneous plasma observations with DE 1 and DE 2. *Adv.Space Res.*, 8:353, 1988.
- [11] P. Carlqvist. Some theoretical aspects of electrostatic double layers. In P.J.Palmadesso and K.Papadopoulos, editors, *Wave Instabilities in Space Plasmas*. D.Reidel Publ.Company, 1979.





- [12] Y.T. Chiu, N.U.Crooker, and D.J.Gorney. Model of oval and polar cap arc configurations. *J.Geophys.Res.*, 90:5153, 1985.
- [13] N.U. Crooker. Antiparallel merging, the half-wave rectifier response of the magnetosphere, and convection, in magnetospheric boundary layers. In *Proceedings of the Chapman Conference, in Alpbach, Austria, June 1979*, Nevilly, France, 1979. European Space Agency. 1979(ESA-SP-148).
- [14] J.W. Dungey. Interplanetary magnetic field and the auroral zones. *Phys.Rev.Lett.*, 6:47, 1961.
- [15] T.E. Eastman, E.W.Hones Jr., S.J.Bame, and J.R.Asbridge. The magnetospheric boundary layer: Site of plasma momentum and energy transfer from the magnetosheath into the magnetosphere. *Geophys.Res.Lett.*, 3:685, 1976.
- [16] Y.I. Feldstein. Peculiarities in the auroral distribution and magnetic disturbance in high latitudes caused by the asymmetrical form of the magnetosphere. *Planet.Space Sci.*, 14:121, 1966.
- [17] L.A. Frank. Relationship of the plasma sheet, ring current, trapping boundary, and plasmapause near the magnetic equator and local midnight. *J.Geophys.Res.*, 76:2265, 1971.
- [18] L.A. Frank, J.D.Craven, D.A.Gurnett, S.D.Shawhan, D.R.Weimer, J.L.Burch, J.D.Winningham, C.R.Chappell, J.H.Waite, R.A.Heelis, N.C.Maynard, M.Sugiura, W.K.Peterson, and E.G.Shelley. The theta aurora. *J.Geophys.Res.*, 91:3177, 1986.
- [19] L.A. Frank, J.D.Craven, J.L.Burch, and J.D.Winningham. Polar views of the Earth's aurora with Dynamics Explorer. *Geophys.Res.Lett.*, 9:1001, 1982.
- [20] R.A. Hoffman, R.A.Heelis, and J.S.Prasad. A sun-aligned arc observed by DMSP and AE-C. *J.Geophys.Res.*, 90:9697, 1985.
- [21] T. Iijima and T.A.Potemra. The amplitude distribution of field-aligned currents at northern high latitudes observed by Triad. *J.Geophys.Res.*, 81:2165, 1976.



- [22] T. Iijima, T.A.Potemra, L.J.Zanetti, and P.F.Bythrow. Large-scale Birkeland currents in the dayside polar region during strongly northward IMF: A new Birkeland current system. *J.Geophys.Res.*, 89:7441, 1984.
- [23] T. Iijima and T.Shibaji. Global characteristics of northward IMF-associated (NBZ) field-aligned currents. *J.Geophys.Res.*, 92:2408, 1987.
- [24] A.S. Jursa, editor. *Handbook of Geophysics and the Space Environment*. (Distributed by National Technical Information Service, 5285 Port Royal Road, Springfield Virginia, USA), 1985. Air Force Geophysics Laboratory.
- [25] L.J. Lanzerotti. Earth's magnetic environment. *Sky and Telescope*, 76(4):360, October 1988.
- [26] W. Lennartsson. On the role of magnetic mirroring in the auroral phenomena. *Astrophys.Space Sci.*, 51:461, 1977.
- [27] L.R. Lyons, D.S.Evans, and R.Lundin. An observed relationship between magnetic field aligned electric fields and downward electron energy fluxes in the vicinity of auroral forms. *J.Geophys.Res.*, 84:457, 1979.
- [28] G.T. Marklund and L.G.Blomberg. On the influence of localized electric fields and field-aligned currents associated with polar arcs on the global potential distribution. *J.Geophys.Res.*, 96:13977, 1991.
- [29] F.S. Mozer, R.B.Torbert, U.V.Fahleson, C.-G.Fälthammar, A.Gonfalone, A.Pedersen, and C.T.Russell. Direct observation of a tangential electric field component at the magnetopause. *Geophys.Res.Lett.*, 6:305, 1979.
- [30] T. Obara, T.Mukai, H.Hayakawa, A.Nishida, K.Tsuruda, S.Machida, and H.Fukunishi. Akebono (EXOS D) observations of small-scale electromagnetic signatures relating to polar cap precipitation. *J.Geophys.Res.*, 98:11153, 1993.
- [31] W.G. Pilipp and G.Morfill. The formation of the plasma sheet resulting from plasma mantle dynamics. *J.Geophys.Res.*, 83:5670, 1978.



- [32] T.A. Potemra, L.J.Zanetti, P.F.Bythrow, A.T.Y.Lui, and T.Iijima. By-dependent convection patterns during northward interplanetary magnetic field. *J.Geophys.Res.*, 89:9753, 1984.
- [33] P.H. Reiff, H.L.Collin, J.D.Craven, J.L.Burch, J.D.Winningham, E.G.Shelley, L.A.Frank, and M.A.Friedman. Determination of auroral electrostatic potentials using high and low-altitude particle distributions. *J.Geophys.Res.*, 93:7441, 1988.
- [34] H. Rosenbauer, H.Grunwalt, M.D.Montgomery, G.Paschmann, and N.Sckopke. HEOS 2 plasma observations in the distant polar magnetosphere:the plasma mantle. *J.Geophys.Res.*, 80:2723, 1975.
- [35] N. Sckopke, G.Paschmann, H.Rosenbauer, and D.H.Fairfield. Influence of the interplanetary magnetic field on the area and thickness of the plasma mantle. *J.Geophys.Res.*, 81:2687, 1976.
- [36] M. Temerin, K.Cerny, W.Lotko, and F.S.Mozer. Observations of double layers and solitary waves in the auroral plasma. *Phys.Rev.Lett.*, 48:1175, 1982.
- [37] V.M. Vasyliunas. A survey of low-energy electrons in the evening sector of the magnetosphere with OGO 1 and OGO 3. *J.Geophys.Res.*, 73:2839, 1968.
- [38] V.M. Vasyliunas. Mathematical models of magnetospheric convection and its coupling to the ionosphere. *Particles and Fields in the Magnetosphere*, 1970. edited by B.M.McCormac,D.Reidel,Dordrecht, Netherlands.
- [39] V.M. Vasyliunas. Interaction between the magnetospheric boundary layers and the ionosphere. In *International Sydney Chapman Conference on Magnetospheric Boundary Layers, Alpbach, Austria*, Paris, 1979. European Space Agency. 1979(ESA-SP-148).
- [40] D.R. Weimer. Auroral E-fields from DE 1 and DE 2 at magnetically conjugate points. *Adv.Space Res.*, 8:373, 1988.
- [41] J.D. Winningham and W.J.Heikkila. Polar cap auroral electron fluxes observed with Isis 1. *J.Geophys.Res.*, 79:949, 1974.







